INVESTIGATIONS ON EFFICACY OF NEW COMBINATIONS OF HIGH TEMPERATURE NEUTRON SHIELD MATERIALS FOR OPTIMAL USE IN SODIUM COOLED FAST REACTORS

By

D. SUNIL KUMAR

Enrolment Number: PHYS 02 2008 04013

Indira Gandhi Centre for Atomic Research, Kalpakkam, India

A thesis submitted to the Board of Studies in Physical Sciences
In partial fulfillment of the requirements
For the degree of

Doctor of Philosophy
of

HOMI BHABHA NATIONAL INSTITUTE

MUMBAI, INDIA

(August, 2014)

Homi Bhabha National Institute
Recommendations of the Viva Voce Committee

As members of the Viva Voce Board, we certify that we have read the dissertation prepared by **Mr. D. Sunil Kumar** entitled **"Investigations on effective new combinations of high temperature neutron shield materials for optimal use in sodium cooled fast reactors"** and recommend that it may be accepted as fulfilling the thesis requirement for the Degree of Doctor of Philosophy.

Chairman – B. Venkatraman	**Date:** 9/3/15
Convener/Guide – R. S. Keshavamurthy	**Date:** 9/3/15
External Examiner - K. V. Subbaiah	**Date:** 9/3/15
Member – K. Velusamy	**Date:** 9/3/2015
Member – K. Devan	**Date:** 9/3/2015

Final approval and acceptance of this thesis is contingent upon the candidate's submission of the final copies of the thesis to HBNI.

I hereby certify that I have read this thesis prepared under my direction and recommend that it may be accepted as fulfilling the thesis requirement.

Date: 9/3/15
Place: Kalpakkam

R.S. Keshavamurthy
(R.S. Keshavamurthy)
Guide

STATEMENT BY AUTHOR

This dissertation has been submitted in partial fulfillment of requirements for an advanced degree at Homi Bhabha National Institute (HBNI) and is deposited in the Library to be made available to borrowers under rules of the HBNI. Brief quotations from this dissertation are allowable without special permission, provided that accurate acknowledgement of source is made. Requests for permission for extended quotation from or reproduction of this manuscript in whole or in part may be granted by the Competent Authority of HBNI when in his or her judgment the proposed use of the material is in the interests of scholarship. In all other instances, however, permission must be obtained from the author.

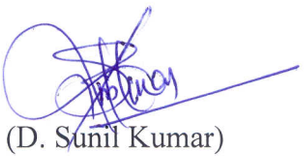

(D. Sunil Kumar)

DECLARATION

I, hereby declare that the investigation presented **in** the thesis has been carried out by me. The work is original and has not been submitted earlier as a whole or in part for a degree / diploma at this or any other Institution / University.

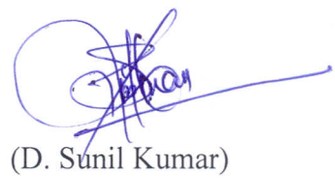

(D. Sunil Kumar)

List of Publications arising from the thesis

Journal Papers

1. D. Sunil Kumar, R.S. Keshavamurthy, P. Mohanakrishnan, S.C. Chetal, “A feasibility study of ferro-boron as in-core shield material in fast breeder reactors”, in the International Journal – Nuclear Engineering and Design, Volume 240, (2010), Pages 2972-2980.

2. D. Sunil Kumar, R.S. Keshavamurthy, P. Mohanakrishnan, S.C. Chetal, “Axial and radial shield optimization for CFBRs with ferro-boron”, in the International Journal Nuclear Engineering and Design, Volume 265 (2013), Pages 1159– 1165.

Conference Papers

1. D.Sunil Kumar,R.S.Keshavamurthy and P.Mohanakrishnan, “Reduction of Radial Shields in PFBR Using Ferro-Boron”, National Symposium on Radiation Physics, NSRP-18, Udaipur, Nov. 19-21 (2009).
2. D.Venkatasubramanian, AdishHaridas,D. Sunil Kumar, R.S. Keshavamurthy,P. Mohanakrishnan,“Experimental Measurements of Neutron Attenuation through Ferro-boron Slabs in the South End Neutron Beam of KAMINI Reactor”, 2009. National Symposium on Radiation Physics, NSRP-18, Udaipur, Nov. 19-21,(2009).
3. R. S. Keshavamurthy, S. Raju, S. Anthonysamy, S. Murugan, D. Sunil Kumar, V. RajanBabu, S. C. Ravi Chandar, C. N. Venkiteswaran, S. C. Chetal, “Experimental and Theoretical Investigations of Ferro-Boron as In-vessel Shield Material in FBRs”, FR-13 Paris March 3-7 (2013).

Other Publications

1. D. Sunil Kumar , Sujoy Sen, R.S. Keshavamurthy, P. Mohanakrishnan, “Comparison of FBTR hybrid core and Mark-II (carbide) core design and neutron irradiation in in-vessel shields”, Annals of Nuclear Energy, Volume 35 (2008), Pages 937–946.

DEDICATED TO MY PARENTS

ACKNOWLEDGEMENTS

Foremost, I would like to express my profound sense of reverence to my supervisor Prof.R.S.Keshavamurthy, for his constant guidance, support, enthusiasm and untiring help during the course of my PhD. His guidance from the beginning of my career has helped me in learning fundamentals and preparation of the thesis.

My sincere gratitude to Dr.P.Mohanakrishnan for full support and encouragement during the period of my thesis work.

I would like to thank my doctoral committee members Prof. B. Venkatraman, Prof. K. Velusamy, and Prof. K. Devan and also my earlier doctoral committee members Prof.R.Indira and Prof.C.P. Reddy for their encouragement and suggestions for the successful completion of the thesis work.

I would like to express my deep thanks to Prof. B. V. R. Tata, Dean Academics- Physics, for his help and advice which helped me to submit the thesis in time.

I am thankful to Dr. P.R. Vasudeva Rao, present Director, IGCAR, Shri. S.C. Chetal and Dr. Baldev Raj former Directors of IGCAR for allowing me to use the facilities for the research work. I am also thankful to Dr. P. Chellapandi, Director, RDG, Shri. P. Puthiyavinayagam Associate Director, CDG and Shri. A. John Arul, Head RSDD for their kind encouragement to my studies.

I thank the task force members on Advanced Shield Materials for Future FBRs, Shri.S.Raju, Shri.V.Rajan Babu, Dr.S.Anthonysamy, Shri.S.Clement Ravichandar, Dr.S.Murugan and Shri.C.N.Venkiteswaran for useful interactions during this study. I am thankful to Shri.D.Venkatasubramanian and Shri.Adish Haridas for useful discussions on experiments and data presented in the study. I gratefully acknowledge the help from Shri. Sujoy Sen and Dr.V.Gopalakrishnan for providing all the cross section data required for the studies.

As part of my PhD program, I have undergone course work on nuclear reactor physics. This has helped me in providing good background as a prelude to my thesis work and my heartful thanks to all the teachers in this occasion.

There are many friends with whom I interacted during my course work and thesis work. I thank Shri.Rajeev Ranjan Prasad, Shri.A.Riyas, Smt.M.M.Shanthi, Dr.G.Pandikumar, Smt.T.Sathiyasheela, Shri.G.Raghukumar, Shri.D.Naga Sivayya and Shri.V.L.Anuraj for their valuable help during this period. I thank Shri.M.L.Jayalal and Shri.R.Jehadeesan for giving excellent support to use cluster facility to carry out intensive computer calculations.

I am indebted to Shri. M.Asok Kumar, Shri.M.S.Sridharan, Shri.M.Ramakrishnan and Smt.V.Bhuvana for their moral support and encouragement during the period of this work. I express my sincere thanks to Shri.K.Krishnaprasad, Shri.G.Padmanabhan, Smt. Neethu Henna Stephan, Dr.A.Jasmine Sudha, Dr.L.Thilagam, Dr.O.Annalekshmi and Shri.B.Anoop for their valuable suggestions and support during this study.

I am grateful to my school and college teachers, especially Dr.A.K.Gopalakrishnan Nair, who laid the seeds of enthusiasm in my pursuit of knowledge.

I would like to express my appreciation to all my colleagues in IGCAR who directly or indirectly supported me in this work.

Above all, I would like to thank my wife Praveena for her personal support to this work and also for taking full care of our children Naveen and Namith while I was busy with preparation of the thesis. I gratefully acknowledge the keen interest shown by Shri. S.G.Arun, my brother-in-law, in the thesis work. My parents and brother have given me support throughout as always, for which my mere expression of thanks does not suffice.

SYNOPSIS

Fast Breeder Reactors are an important part of energy planning in India. They use highly enriched fuel and the neutrons are not moderated so that excess neutrons produced in fast fissions become available for breeding fissile material in fertile material blankets. As a result, they have high and energetic neutron flux leaking out of blankets. Hence large shields are provided around fast reactor core and blankets. Out of the total subassemblies in the Prototype Fast Breeder Reactor (PFBR), which is under construction in Kalpakkam, about 60 % are shielding subassemblies. Reduction in shield assemblies will lead to cost saving and thereby reactor vessel size can also be decreased. The development of alternative cost effective shield materials meeting the stringent technical specifications for use inside FBRs has always been considered one of the major challenges in the science and technology of fast reactors. The incident neutron spectrum is very hard with negligible thermal component and has anisotropic angular distribution and hence higher order anisotropy in cross section has to be considered. As a consequence, reduction of the neutron flux to acceptable levels has always been a challenging problem. Ideal shield materials which absorb both fast and slow neutrons at equally high rates do not exist. One has to take recourse to materials which bring down energy of neutrons by elastic and inelastic scattering along with those which absorb. One should also take care of resonance structure in cross sections. Hence large numbers of energy groups have to be used in the calculations. The calculations span an energy range of 0.025 eV to 14 MeV and attenuation through more than 40 mean free paths of shield thickness. The energy behaviour of these neutron interaction cross sections for materials is complex and this makes the shield optimization interesting and challenging.

Shield optimization involves trials with different combinations of shield materials with varying thickness. Number of possible combinations increase with new prospective materials becoming available. This has led to investigations of new combinations of shield materials to come out with optimal solutions which form the subject matter of this thesis. Through many scoping studies Ferro-Boron is identified as an alternative shield material for fast reactor shielding applications. Experiments carried out to measure its neutron attenuation characteristics in KAMINI reactor are presented.

It is recognized that reduction of reactor vessel size is linked to reduction in cost in future FBRs planned in India. The critical parameter for determining the size of the reactors has been the volume of the shields provided around the core and blankets, which is actually represented by the number of shield rows provided. Studies on reduction of number of rows are presented to show that a) Activation of secondary sodium activity, for a given number of radial shield rows, is determined more by axial streaming of neutrons towards regions around IHX window, b) Provision of axial shields would decrease the secondary sodium activity. However, it may have undesirable consequences on the crucial aspect of neutron monitoring, particularly at low power. Neutron detector counts should not be lower than reference case values: To achieve this, many axial shield configurations are studied to arrive at the right solutions. c) The choice of Fe-B as radial shield results in economy of the use of shield material. One row of shields can be reduced. The weight reduction of the outer rows of in-vessel shields is by about 50 % of PFBR outer shields and the cost is down to approximately 17 % of the shields in the reference case and d) The best axial shield configuration is where axial SS shielding is provided over core-1 and axial B_4C shielding is provided over blanket and reflector subassemblies. This increases the detector counts by about 50 % for without affecting secondary sodium activity. The reduction of number

of rows of radial shields makes it possible to bring the IHX closer to the core, and hence reduction of reactor vessel size.

The thesis deals with another problem of radiation damage to grid plate of the Fast Breeder Test Reactor (FBTR), currently in operation in Kalpakkam. Life of FBTR is critically linked to radiation damage suffered by grid plate. Currently, the lower axial shield provided in FBTR is stainless steel. Several lower axial shield options were considered in the thesis. The main conclusions of the study are a) Life of FBTR can be extended by the use of alternate lower axial shield materials. b) Out of the different materials studied B_4C shows the greatest reduction. However, reactivity loss is also maximum in that case. In addition, the consequences of helium production in the case of B_4C may result in some modification of the lower axial part of the subassembly, such as providing a plenum, c) Use of Tungsten Carbide reduces radiation damage by more than 50 % and the consequent reactivity loss is also not very significant.

CONTENTS

LIST OF TABLES

LIST OF FIGURES

List of Abbreviations

Initials	Full Form
BTE	Boltzman Transport Equation
CFBR	Commercial Fast Breeder Reactor
DPA	Displacement Per Atom
DTA	Differential Thermal Analysis
FBTR	Fast Breeder Test Reactor
HTFC	High Temperature Fission Chamber
IHX	Intermediate Heat Exchanger
KAMINI	Kalpakkam Mini Reactor
MOX	Metal Oxide Fuel
NR	Neutron Radiography
PFBR	Prototype fast Breeder Reactor
PKA	Primary Knock on Atom
SCP	Safety Control Plate
SGB	Steam Generator Building
SS	Stainless Steel

Chapter-1

INTRODUCTION

1.1 Background and Motivation

Fast Breeder Reactors are an important part of India's nuclear power programme. They use highly enriched fuel in their cores to produce power which comes mostly from fast neutron induced fissions. These are also used to breed fissile material in blankets (Walter and Reynolds, 1981). But, leaking neutrons from core and blankets have energies that peak around 10-100 keV and have anisotropic angular distribution. Hence reduction of the neutron flux to acceptable levels has always been a challenging problem. Ideal shield materials which absorb both fast and slow neutrons at equally high rates do not exist. One has to take recourse to materials which bring down energy of neutrons by elastic and inelastic scattering along with those which absorb. Calculations for shields are also challenging as one should take care of resonance structure in cross sections. Hence large number of groups have to be used in the calculations which span an energy range of 0.025 eV to 14 MeV and attenuation through more than 40 mean free paths of shield thickness. The energy behavior of these neutron interaction cross sections for materials is complex and this makes the shield optimization interesting and challenging.

Shield optimization involves trials with different combinations of shield materials with varying thickness. Number of possible combinations increase with new prospective materials becoming available. This has led to investigations of new combinations of shield materials to come out with optimal solutions which form the subject matter of this thesis. It presents scoping calculations to identify prospective shield materials, neutron attenuation experiments carried out to measure its effectiveness and material properties. The methodology of computations adopted and nuclear data used are presented. The reference case used in the present studies is the shield

configuration of Prototype Fast Breeder Reactor (PFBR) (Chetal et al., 2006, Puthiyavinayagam et al., 2006), which is is a 500 MWe sodium cooled pool type reactor (Fig.1.1) due to be commissioned in Kalpakkam. It has two core zones with 21 % and 28 % Pu enriched mixed (U, Pu) oxide fuel arranged in 181 fuel subassemblies surrounded by 2 rows of depleted UO_2 blankets. The core plan and the core subassembly sketch are given in Figs.1.2-1.3. In pool type of fast reactors, intermediate heat exchangers (IHXs), in which the primary sodium exchanges heat with the secondary sodium and pumps, are immersed in the pool of liquid sodium contained in the reactor vessel itself. Therefore, sodium becomes radioactive and the secondary sodium passing through IHXs also gets activated. It is obvious that without adequate shielding around the core, this activation can lead to an unacceptable large dose in the steam generator building.Hence fast reactors are generally characterized by large in-vessel shields, which incidentally contribute to the reactor vessel size. PFBR is provided with 9 rows of shields of which 6 rows are Stainless Steel (SS) and 3 rows are B_4C.

1.2 In-vessel Shielding in Fast Reactors

Stainless steel was used as shielding material in a variety of fast reactors, such as RAPSODIE, JOYO, FBTR, BOR-60, FFTF and FERMI (IAEA, 2006; Masayuki Naganuma et al., 2008). However, EBR-II used graphite and borated graphite, while SS/borated graphite was used in DFR. In PHENIX (Cabrillat et al., 1983) Graphite/SS was used in the radial direction. In addition, B_4C was added in the axial direction because of the superior neutron absorption properties of boron. In SUPER PHENIX (Gourdon et al., 1990) too, B_4C shielding was provided in the axial direction. B_4C was also considered for radial shielding in the reactors SPX2, EFR and DFBR. The PFBR, has been designed with 3 outermost rows of B_4C, in addition to 6 rows of

Table - 1.1: Experimental fast reactors -radial shields

Plant	Shield
Rapsodie (France)	Stainless steel
KNK-II (Germany)	iron
FBTR (India)	stainless steel
PEC (Italy) (not built)	B_4C
JOYO (Japan)	Stainless steel
DFR (UK)	Steel and Borated Graphite, top plugs only borated Graphite
BOR-60 (Russian Federation)	Stainless Steel
EBR-II (USA)	Graphite and Borated Graphite
Fermi (USA)	Stainless Steel
CEFR (China)	SS + B_4C

Table - 1.2: Demonstration or prototype fast reactors -radial shields

Plant	Shield
Phénix (France)	Graphite and Stainless Steel
SNR-300 (Germany)	Stainless Steel
PFBR (India)	SS + B_4C
MONJU (Japan)	SS
PFR (UK)	Graphite
CRBRP (USA) (not built)	SS-316
BN-350 (Kazakhstan)	SS
BN-600 (Russian Federation)	Graphite and SS
ALMR (USA) (not built)	304 SS + B_4C
KALIMER-150 (Republic of Korea) (Under construction)	304 SS + B_4C covered by SS
SVBR-75/100 (Russian Federation) (Planned)	SS+ B_4C
BREST-OD-300 (Russian Federation) (Planned)	SS

Table - 1.3: Commercial size reactors -radial shields

Plant	Shield
Super-Phénix 1 (France)	SS
Super-Phénix 2 (France)	SS + Boron
SNR 2 (Germany) (not built)	Steel
DFBR (Japan) (not built)	SS + B_4C
CDFR (UK) (not built)	Steel
BN-1600 (Russian Federation) (design stage)	Stainless Steel
BN-800 (Russian Federation) (planned)	SS + graphite and borated graphite
EFR (not built)	SS + B_4C pins and blocks
ALMR (USA) (not built)	304 + B_4C covered by SS
BN-1800 (Russian Federation) (design stage)	SS+graphite and borated graphite
BREST-1200 (Russian Federation)	SS
JSFR-1500 (Japan) (planned)	SS + Zr-H

Table - 1.4: Experimental fast reactors -axial shields

Plant	Shield
BOR-60 (Russian Federation)	SS
BR-10 (Russian Federation)	SS, B_4C
CEFR (China)	SS

Table - 1.5: Demonstration or prototype fast reactors -axial shields

Phénix (France)	SS,B_4C
PFBR (India)	SS,B_4C
MONJU (Japan)	SS
BN-350 (Kazakhstan)	SS
BN-600 (Russian Federation)	SS
ALMR (USA)	SS
KALIMER-150 (Republic of Korea)	SS
SVBR-75/100 (Russian Federation)	SS,B_4C
BREST-OD-300 (Russian Federation)	SS

Table - 1.6: Commercial size reactors -axial shields

Super-Phénix 1 (France)	SS + B_4C pins
DFBR (Japan)	B_4C
BN-1600 (Russian Federation)	SS
BN-800 (Russian Federation)	SS
EFR (not built)	SS + B_4C
SVBR-75/100 (Russian Federation)	SS+ B_4C
BN-1800 (Russian Federation)	SS
BREST-1200 (Russian Federation)	SS
JSFR-1500 (Japan)	SS + B_4C

SS. Axial SS and B_4C shields, integrated with the fuel subassembly, are also provided to control streaming of neutrons towords IHX.

The radial and axial shield materials in different fast reactors like experimental reactors, Demonstration or Prototype Fast Reactors and Commercial Size Reactors are given in Tables 1.1 to 1.6.

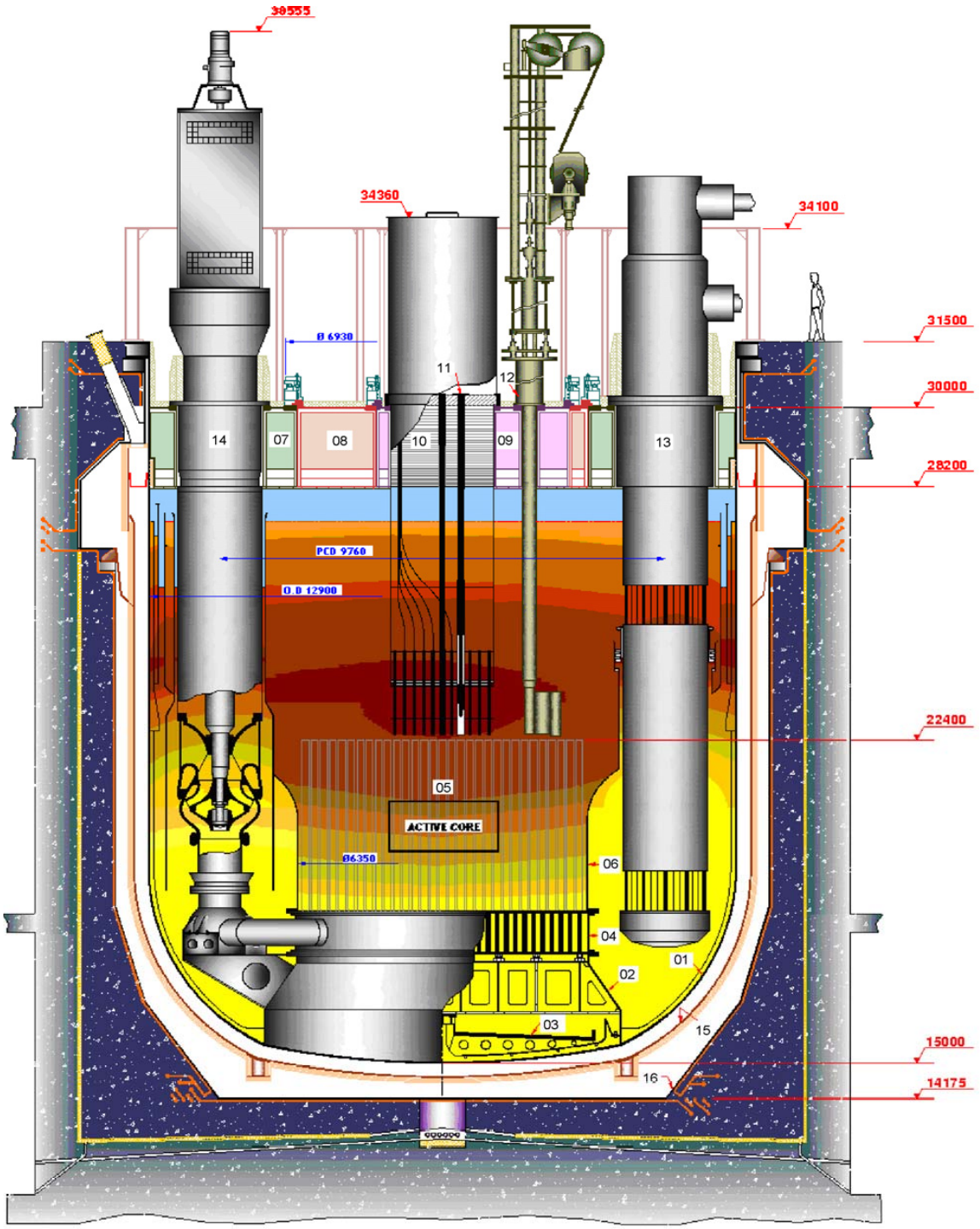

Fig-1.1: PFBR reactor assembly

(01) Main vessel, (02) core support structure, (03) core catcher, (04) grid plate, (05) core, (06) inner vessel, (07) roof slab, (08) large rotatable plug, (09) small rotatable plug, (10) control plug, (11) control and safety rod mechanism, (12) in-vessel transfer machine, (13) intermediate heat exchanger, (14) primary sodium pump, (15) safety vessel and (16) reactor vault.

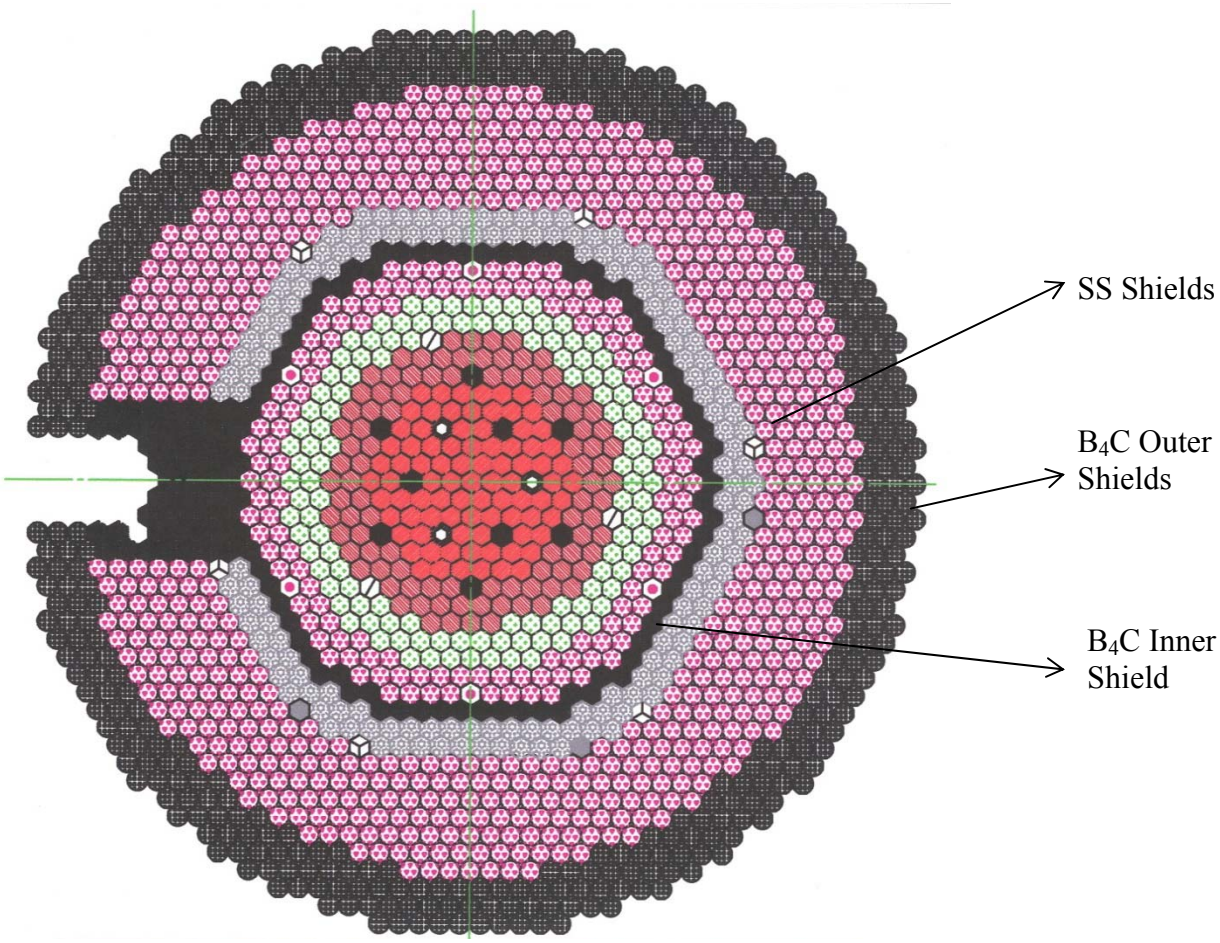

Fig-1.2: Core plan of PFBR

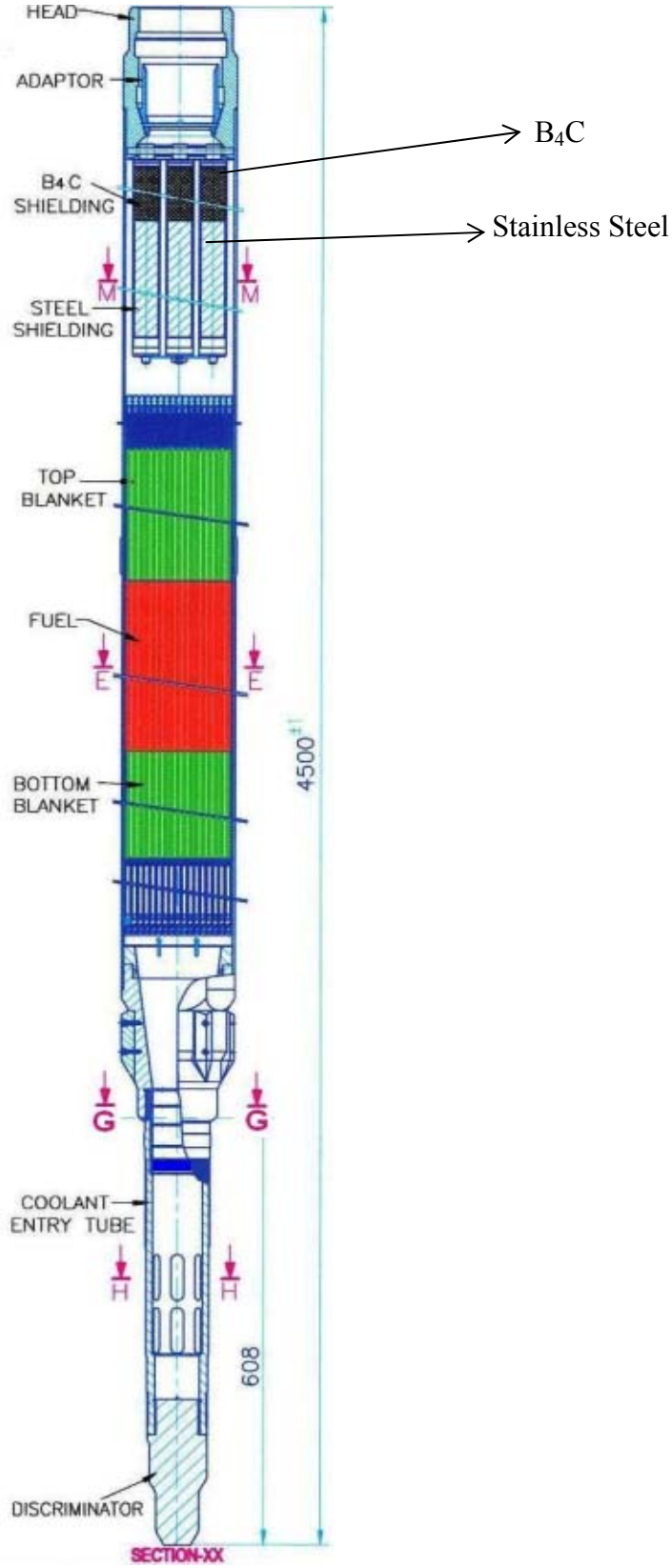

Fig-1.3: PFBR core subassembly

1.3 Specific objectives of the thesis

Shielding provided around the core and blankets of Fast Breeder Reactors have large volume and weight because of the hard nature and high values of neutron flux leaking out of core and blankets. Shield optimization problems involve studies with varieties of shield material combinations. These require computer intensive transport calculations as they have to take care of neutron scattering and slowing down of energetic neutrons in a larger volume. The specific objectives of the thesis are

- Identification of novel shield material through several scoping calculations
- Experimental measurements of its effectiveness
- Full reactor shield calculations to show that the material has the same level of radiological effectiveness as the reference case (PFBR) and is cheaper
- Achievement of reduction of shields as they are linked to reduction in cost and reactor vessel size. Several axial shield configurations tried to achieve the same without affecting neutron monitoring at the control plug location
- Alternate lower axial shields for Fast Breeder Test Reactor (FBTR), currently in operation in Kalpakkam, to reduce radiation damage to grid plate within the dimensional constraints. Radiation damage to grid plate is the most critical parameter in limiting the life of the reactor.

1.4 Organization of the report

Chapter 1 gives introduction to the problem and summarizes the need for such investigations.The shield configuration in PFBR is taken as the reference case, for evaluating alternate shielding options. The criterion adopted is that the alternate options should be cheaper and have the same level of radiological safety as the reference case. It is clear that such an

alternative, if realised, can lead to potential cost saving both due to a reduction in vessel size and in the number of shield assemblies. It is with this design imperative, several potential shield material combinations were considered in our investigations for their efficacy.

Chapter 2 describes the methodology and calculations for the reference case. A brief introduction to particle transport equation and solving it for deep penetration shield problems are presented.Approaches to solve transport equation are discussed from the point of view of computation time, geometry modelling and computation of desired parameters. The rationale for carrying out the calculations using Discrete Ordinate Method to solve neutron transport problem is described. The available multigroup nuclear data suitable for use in the calculations are presented. DLC-37 (Plaster et al., 1975) cross sections in 100 neutron energy groups as well as IGC-S3 (Devan et al., 2002; Devan et al., 2003) cross sections in 175 groups are used for studies on PFBR. The differences arising from the use of DLC-37 and IGC-S3 are shown to be not very significant for PFBR. However, rest of the calculations are carried out using IGC-S3 because of its employing more recent evaluated data in superior energy group structure viz., neutron data in 175 energy groups in the range from 1.0E-5 eV to 19.6 MeV.

Computation of secondary sodium activation requires that the transport of neutrons is calculated to the end of reactor vessel. The geometry of IHX is not amenable to 2-D calculations in cylindrical geometry which happens to be the geometry of the reactor core. A new method of accomodating the IHX geometry is presented. Results of calculation for PFBR, taking its 2D RZ geometry,taken as the reference case is presented. Contours of sodium capture rates in the IHX region are presented. The spectral shapes at various axial positions along IHX are arrived at to help in understanding the neutron streaming paths towards IHX. Detector fluxes are computed for various locations such as control plug location, undervessel, core centre etc.

locations. Comparison of flux values and neutron spectrum at various locations are done with 100 and 175 neutron group stuctures are presented. Secondary sodium activity comparison is also made with different group structures.

Chapter 3 describes scoping studies to identify prospective shield materials that could be effective with respect to cost and volume reduction. From the preliminary literature survey, the basic shield materials identified for scoping studies are SS, boron carbide, Ferro-Boron, Borated Steel, tungsten carbide, gadolinium, gadolinium oxide, calcium boride, gadolinium boride, silicon boride, iron boride, aluminium boride and zirconium boride. Transport calculations using 2- dimensional transport code DORT (Rhoads and Childs, 1988; Mynatt, 1967) are carried out for the core and blanket surrounded by the candidate shield material in the radial direction. In this scoping study, single material is assumed in all the shield rows. The reference case is the PFBR shield configuration described in the previous sections. The calculations show that a) All borides are as effective or even more effective than the reference case. Their efficacy essentially depends on the boron atom density. b) Many of the absorbers like Gadolinium are not as effective for leaking fast neutrons as the reference shield combination. This is clearly due to low absorption cross sections for fast neutrons and c) tungsten and tantalum are found to be very effective than the reference case. The other factors to be considered are availability and cost as compared to the reference case. The cost is very high in the case of tungsten and tantalum compounds. In the case of borides of Al, Gd, Si, Zr and Ca, availability itself is in doubt though many of them show good prospects. The only new material other than traditional boron carbide and SS is Ferro-Boron (Sunil Kumar and anthonysamy, et al., 2010). The studies show that, as a single material, it is a prospective material though not as effective as the reference case. It also happens to be commercially available in large quantities and cheap. Hence Experimental studies

of neutron attenuation in Ferro-Boron using KAMINI reactor were undertaken (Venkatasubramanian et al., 2009; Keshavamurthy et al., 2011). The chapter describes the measurements for Ferro-Boron with different boron content along with standard materials like B_4C and SS. Results are compared and shown that Ferro-Boron is as effective as shown in the calculations. Since it is not possible to use KAMINI reactor to study the attenuation behaviour of neutrons leaking from blanket regions, studies are confined to outer in-vessel shield regions and sodium region where the neutron spectra are somewhat similar to the neutron spectra from the KAMINI beam tubes. Comparison of attenuation shows that for fast neutron attenuation Ferro-Boron is as good as Boron Carbide. Effectiveness of this material as a neutron shield is studied by foil activation analysis by putting these materials in aluminium boxes in KAMINI south beam tube. The type of spectrum in KAMINI can also be very useful in studying the effectiveness of different shield materials around IHX, in reducing secondary sodium activation.

Chapter 4 describes studies done for the Ferro-Boron as shield material l for in-vessel fast reactor applications. Ferro-boron is a binary alloy of iron with boron content up to 15% to 18% which is a low cost boron additive for steel and other ferrous metals. Recent out of pile measurements of its high temperature properties, material characteristics and interactions with SS at high temperatures (Arun Kumar Rai et al., 2011; Raju et al., 2011) show feasibility of using the material in high temperature environment. Though, the efficacy of Ferro-Boron as a neutron shield material identified based on scoping calculations and neutron attenuation experiments in KAMINI reactor, detailed reactor physics analyses and transport calculations using realistic combinations of Ferro-Boron, are necessary to achieve the same level of radiological safety as the reference case combination. In the transport calculations, Ferro-Boron containing about 17 wt.% of boron is used. All the radial rows of shield assemblies in the

reference case is replaced with Ferro-Boron. The calculations span an energy range of 1.0E-05 eV to 19.6 MeV and attenuation through more than 40 mean free paths of shield thickness. The volume fraction of the Ferro-Boron taken is as that of the B_4C volume fraction in the outer shield assemblies. Comparison of neutron fluxes and reaction rates are carried out for the two cases. Secondary sodium activity and thereby the dose rate in the steam generator are studied which is one of the major deciding factors for the effectiveness of the shield. Also the control plug detector counts are studied by calculating the U-235 equivalent and B-10 equivalent fluxes where the detector can go upto blanket regions in the radial direction. Calculations showed that the secondary sodium activity and the detector counts in the control plug detector are almost same as that of the PFBR case. The major portion of the secondary sodium activity contribution is due to the leakage of neutrons from the upper axial shields and hence there is not much change in the secondary sodium activity between the two cases. Though Ferro-Boron has much lower boron atom densities as compared to Boron Carbide, its effectiveness has stemmed from the fact that boron is spread throughout the shield region in the proposed core. The total shield material weight is lower by about 50 tonnes. Another advantage is the lower radioactive waste generation over a period of irradiation because of the absence of cobalt in Ferro-Boron as impurity (Keshavamurthy et al., 2013). Ferro-boron is much less expensive as compared to SS and B_4C and the cost and weight of shielding is shown to be significantly lower.

Chapter 5 describes the axial and radial shield optimization studies done for fast reactor applications towards reduction of number of shield subassemblies. The reduction of number of rows of radial shields makes it possible to bring the IHX closer to the core, and hence reduction of reactor vessel size. This chapter also gives a description of the detectors used in fast reactors. The axial shields in FBRs play an important role in the counts in the control plug detectors where

these counts are important especially in the low power operations of the reactor. Lower axial shields give more counts in the detector location but the penalty one has to pay is that secondary sodium activity will go up. Therefore optimization studies are required for axial and radial shield configuration. Many axial and radial shield optimization studies are made with the criteria that there should be no increase of the secondary sodium activity and no decrease in the flux at detector locations in the control plug. Design calculations are performed with eight rows of Ferro-Boron assemblies instead of nine rows of shield assemblies and results show an increase in secondary sodium activity. Further studies show that reduction of one row of radial subassemblies is possible only if B_4C is kept in the axial shields of blanket subassemblies (Sunil Kumar et al., 2013). Many axial shield configurations are tested for the flux at detector location secondary sodium activity. These studies include the replacement of a) axial B_4C in the core -1 and core -2 assemblies of PFBR with SS, b) core-1 subassemblies alone with SS, c) replacement of B_4C with Ferro-Boron, d) replacement of both SS and B_4C with Ferro-Boron. These modifications are introduced in core -1 and core-2 subassemblies separately and together also.

Chapter 6 describes the radiation damage studies made for Fast Breeder Test Reactor (FBTR) for the proposed hybrid core (Sunil Kumar et al., 2008). FBTR uses mixed (U, Pu)C fuel with Pu content going up to 70 %. Use of mixed (U, Pu)O_2 would reduce the Pu content to 44 % (Sengupta, 2006). Hybrid core has both (U, Pu)C and (U, Pu)O_2 fuel assemblies. Due to restrictions of the size of core cover plate, MOX fuel assemblies have longer fissile columns. Hence the lower positions of these subassemblies are closer to the grid plate. Hence a new calculation of radiation damage is necessitated to check if displacement per atom (*dpa*) of the top of the grid plate will be higher below the MOX fuel region. Modelling of FBTR core with Mark-I core at the centre and oxide core at the periphery is done in 2-dimensional geometry and the

transport calculations are carried out towards estimating the *dpa* at grid plate. Standard 2-D code DORT and IGC-S3 cross section set is used for the purpose. Calculations of *dpa* are carried out using the available 100 energy group cross sections for *dpa* (Gopalakrishnan, 1994) and fluxes collapsed into 100 energy groups. Results of *dpa* are compared with the values for existing core. Comparisons are also made for various fluxes and spectra at different locations. Calculations have shown that the hybrid core is safe for operation from radiation damage point of view, as the *dpa* decreases radially on the grid plate surface.

As a part of the extension of life of FBTR, studies are done towards reduction of the *dpa* on the grid plate by replacing the SS shields below the core subassemblies with more effective shields. The candidate shield materials are Ferro-Boron, tungsten, tungsten carbide, molybdenum, boron carbide and combinations of these shield materials. All the calculations are done through transport methods. The studies show that tungsten, tungsten carbide and boron carbide are quite effective. boron carbide gives the highest reduction in *dpa*. However, problems due to helium production and reduction in reactivity have to be tackled. The pros and cons of using the material combinations are presented.

Chapter 7 gives summary and scope for future work. There is recently an immense interest in metal reactors (Beldev Raj, 2005; Chetal, 2009), lead cooled reactors and accelerator driven systems all having their own characteristic neutron spectra. Optimization studies of shield thickness, which is of perennial interest in effective shield combinations of new materials such as Ferro-Boron with known materials like B_4C and SS, will be pursued.

Chapter – 2

METHODOLOGY AND CALCULATIONS FOR THE REFERENCE CASE

2.1 Introduction

Boltzmann Transport Equation (BTE) is the most accurate representation of neutron flow in a reactor. But solving this equation is difficult. Because of its complexity, the equation is solved by deterministic numerical methods or stochastic methods like Monte Carlo. Currently, the popular deterministic methods are based on discrete ordinates, S_N approximations (Stevens, 1970; Lewis and Miller, 1993). In this chapter, we describe briefly the BTE with notations and methods used to solve the equation in section 2.2 and gives details of cross sections employed in section 2.3 In section 2.4, 2-D R-Z calculations are presented for the reference case, viz., PFBR using the two cross section sets DLC-37 and IGC-S3. All the relevant fluxes and reaction rates are generated. These will provide reference values for studies to be presented in future chapters. Computation of secondary sodium activity is undertaken in section 2.5. Geometry of IHX cannot be treated accurately in 2-D codes. A methodology devised to calculate activity of secondary sodium in IHX is presented in this section. The last section gives the chapter summary.

2.2 Boltzman Transport Equation

The linear Boltzmann equation describes the angular, energy and spatial variations of the particle distribution. The neutron (or photon) transport equation is derived from particle balance on an infinitesimal volume using only a few assumptions that remove unimportant phenomena, such as neutron-neutron interactions. The particle flux $\Phi(\mathbf{r}, E, \Omega, t)$ for particles with energy E and direction Ω is given by the linear Boltzmann Transport Equation (BTE) or, simply, the transport equation

$$\frac{1}{V(E)}\frac{\partial\Phi(r,E,\Omega,t)}{\partial t} = -\Omega.\nabla\Phi(r,E,\Omega,t) - \sum_t (r,E)\,\Phi(r,E,\Omega,t)$$

$$+ \frac{\chi(E)}{4\pi}\int_{E'} dE'\,\vartheta\sum_f(r,E')\int_{\Omega'} d\Omega'\Phi(r,E',\Omega',t) +$$

$$\int_{E'} dE'\int_{\Omega'} d\Omega'\sum_s(r,\Omega'.\Omega,E'\to E)\Phi(r,E',\Omega',t) \qquad (2.1)$$

where, Φ is the neutron angular flux, and Σ_t, Σ_f and Σ_s respectively are the macroscopic total, fission and scattering cross sections of the medium respectively. The neutron transport equation is a balance equation for angular neutron density n(**r**, E, Ω, t), which is the expected number of neutrons per unit volume, per unit energy interval per unit solid angle per unit time around the phase space point $(\boldsymbol{r}, E, \Omega)$ at time t. The angular neutron density is related to the angular neutron flux Φ(**r**,E,Ω,t) and the neutron velocity by the equation;

$$\Phi(r,E,\Omega,t) = n(r,E,\Omega,t)\times v \qquad (2.2)$$

The equation 2.1 gives the net rate of change of neutron angular density as a balance equation of neutrons getting accumulating and leaving the phase space volume per unit time. The terms in the RHS of equation gives the rate of gain or loss of neutrons from the phase space volume.

1st term - loss of neurons due to leakage.

2nd term - removal of neutrons from phase space due to interactions.

3rd term - the gain of neutrons in the phase space due to total fissions in the medium

4th term - gain of neutrons in the phase space due to interactions from other energies and solid angles.

χ (E) is the fraction of total fission neutrons that belongs to an unit energy interval around E and obtained by fission neutron spectrum and ν is the average number of neutrons

released per fission. $\Sigma_s(r; \Omega'.\Omega; E' \rightarrow E)$ is the differential macroscopic scattering cross section and refers to the scattering cross-section for the differential scattering of neutrons from initial energy and solid angle (E', Ω') to final energy and direction (E,Ω).

Unfortunately, the transport equation cannot be solved analytically except for idealistic cases. Numerical solutions must be used for all practical shielding analyses (Bell and Glasstone, 1985; Duderstadt and Hamilton, 1976, Lamarsh 1983). The energy multi-group approximation is almost always used in which the group averaged cross sections depend on an assumed energy spectrum of the radiation. Even with an energy multi-group approximation, numerical solutions are still computationally intensive (Kenneth Shultis et al., 2005).

2.2.1 Discretes Ordinates Method

The most widely used deterministic transport approach is the discrete-ordinates method(Carson, 1965; Carson, 1970; Lathrop, 1965; Mynatt et al., 1966; Stacey, 2001). In this method a spatial and directional mesh is created for the problem geometry, and the multi-group form of the transport equation is then integrated over each spatial and directional cell. The solution of the approximating algebraic equations is then accomplished by introducing another approximation that relates the cell-centered flux densities to those on the cell boundaries, and an iterative procedure between the source (scattered particles and true source particles) and flux density calculation is then used to calculate the fluxes at the mesh nodes (Carlson and Lathrop, 1968; Duderstadt and Martin, 1979; Lewis and Miller, 1984). Discrete ordinates calculations can be computationally expensive because of the usually enormous number of mesh nodes and the fact that the convergence of an iterative solution is often very slow. A subject of great interest in the last thirty years has been the development of numerous methods to accelerate convergence of the iterations. Without convergence acceleration schemes, discrete ordinate solutions would be

computationally be impractical for many shielding problems. An excellent description of the various acceleration schemes that have been used is provided by Adams and Larsen (2002).

Although discrete-ordinates methods are widely used by shielding analysts, these methods do have their limitations. Most restrictive is the requirement that the problem geometry must be one of the three basic geometries (rectangular, spherical, or cylindrical) with boundaries and material interfaces placed perpendicular to a coordinate axis. Problems with irregular boundaries and material distributions are difficult to solve accurately with the discrete-ordinates method. Also, in multidimensional geometries, the discrete-ordinates method often produces spurious oscillations in the flux densities (the ray effect) as an inherent consequence of the angular discretization (Lathrop, 1971; 1968). Finally, the discretization of the spatial and angular variables (John F. Crew and Gabriel Zamonsky, 1999; 2000) introduces numerical truncation errors, and it is necessary to use sufficiently fine angular and spatial meshes to obtain flux densities that are independent of the mesh size. For multidimensional situations in which the flux density is very anisotropic in direction and in which the medium is many mean-free path lengths in size, typical of many shielding problems, the computational effort to obtain an accurate discrete ordinates solution can become very large. However, unlike Monte Carlo calculations, discrete-ordinates methods can treat very deep penetration problems, i.e., the calculation of fluxes and doses at distances many mean-free-path lengths from a source.

2.2.2 Monte Carlo method

By simulating the random nature of the particle interactions with the medium, particle tracks are generated. Here one needs complete mathematical expressions of the probability relationships that govern the track length of an individual particle between interaction points, the choice of an interaction type at each such point, the choice of a new energy and new direction if

the interaction is of a scattering type, and the possible production of additional particles (Hammersley and Handscomb, 1964, Spanier and Gelbard, 1969). These are all stochastic variables, and in order to make selections of specific values for these variables, one need a complete understanding of the various processes a particle undergoes in its lifetime from the time it is given birth by the source until it is either absorbed or leaves the system under consideration.

2.3 Cross Sections for Shielding Applications

A complete and validated data set of nuclear data is required for estimating various reactor parameters as close to the actual simulation as possible. Cross-section gives neutron-nuclear interaction probability, and is a quantity needed to be input to the BTE.

For reactor physics calculations, cross-section data is required up to about 15 MeV. To solve the transport equation deterministically, multi-group cross sections are used. These are obtained by dividing the energy range into suitable number of groups (or energy bins) and defining average cross-sections in these groups without affecting the net reaction rates. The transport equation is suitably converted to a multi-group transport equation. The selection of the number of groups and the group limits depends on manageability with respect to computer time and memory availability, the energy region of importance with respect to the flux spectrum, and other specific needs.

The shield materials, substantially away from the core, see neutrons with substantial directional orientation, and require anisotropy in neutron fluxes and scattering cross-sections taken into account. Cross-section variation in energy is required in more detail and hence finer group-widths are used for multigrouping. Further, as shielding is concerned with neutrons, as well as gammas, effects in radiation and heating of the materials, interaction and production rates of both neutrons and gammas are to be considered. Such considerations have given rise to

neutron-gamma coupled cross-section set. Appropriate energy groups are defined for neutrons as well as for photons. This set includes cross-sections for the neutron interactions, neutron production (transfer between two neutron groups), photon production in neutron interactions (transfer from a neutron group to a gamma group), 'photo-atomic' interactions, and for photon production in photon interactions (transfer between two gamma groups). Gamma absorption is mainly in the photoelectric effect, and gamma production is in the Compton effect, and in the (threshold reaction of) electron-positron pair production that subsequently results in the production of 2 photons. Gamma producing neutron reactions include fission, inelastic, (n,γ), etc. Anisotropy involved is accounted for by Legendre expansion coefficients of reasonably high order (say 5). Photonuclear interactions are not considered.

2.3.1 100 group cross sections

We have made use of DLC-37 cross section set available in 100 neutron + 21 gamma energy groups (Plaster et al; 1975). It has been created from ENDF/B-IV (Garber, 1975) basic data. Neutron energy boundaries are 1.0E-04 eV to14.918 MeV and in the case of gammas it is 1.0E+04 eV to 1.4E+07 eV. Below 1eV, four groups are available for neutrons. The group energy structure for neutrons and gammas are given in Tables 2.1 and 2.2.

2.3.2 175 group cross sections

We have also made use of the more recent IGC-S3 (175 neutron groups and 42 gamma groups) (Devan et al; 2002) cross section set. It has been created from ENDF/B-VI (McLane et al., 1997; Rose, 1991) basic data. Energy boundaries of neutron energies are 1.0E-05 eV to19.6 MeV and in the case of gammas it is 1.0 keV to 50 MeV. Below 1eV, six groups are available. The energy boundaries of neutrons and gamma groups is in VITAMIN-J structure highly suited

to shielding calculations (Satori,1990) and are given in Table 2.3 and 2.4. Also the isotopes present are given in the Table 2.5. Total 104 isotopes are introduced in IGC-S3 cross section set.

Table - 2.1: 100 Group energy limits for neutrons in DLC- structure

Group No	Upper limit (eV)	Group No	Upper limit (eV)	Group No	Upper Limit (eV)	Group No	Upper limit (eV)
1	1.49E+07	27	1.11E+06	53	5.25E+04	79	7.89E+01
2	1.35E+07	28	1.00E+06	54	4.09E+04	80	6.14E+01
3	1.22E+07	29	9.07E+05	55	3.18E+04	81	4.79E+01
4	1.11E+07	30	8.21E+05	56	2.48E+04	82	3.73E+01
5	1.00E+07	31	7.43E+05	57	1.93E+04	83	2.90E+01
6	9.05E+06	32	6.72E+05	58	1.50E+04	84	2.26E+01
7	8.19E+06	33	6.08E+05	59	1.17E+04	85	1.76E+01
8	7.41E+06	34	5.50E+05	60	9.12E+03	86	1.37E+01
9	6.70E+06	35	4.98E+05	61	7.10E+03	87	1.07E+01
10	6.07E+06	36	4.50E+05	62	5.53E+03	88	8.32E+00
11	5.49E+06	37	4.08E+05	63	4.31E+03	89	6.48E+00
12	4.97E+06	38	3.69E+05	64	3.35E+03	90	5.04E+00
13	4.49E+06	39	3.34E+05	65	2.61E+03	91	3.93E+00
14	4.07E+06	40	3.02E+05	66	2.03E+03	92	3.06E+00
15	3.68E+06	41	2.73E+05	67	1.58E+03	93	2.38E+00
16	3.33E+06	42	2.47E+05	68	1.23E+03	94	1.86E+00
17	3.01E+06	43	2.24E+05	69	9.61E+02	95	1.45E+00
18	2.73E+06	44	2.02E+05	70	7.49E+02	96	1.13E+00
19	2.47E+06	45	1.83E+05	71	5.83E+02	97	8.76E-01
20	2.23E+06	46	1.66E+05	72	4.54E+02	98	6.83E-01
21	2.02E+06	47	1.50E+05	73	3.54E+02	99	5.32E-01
22	1.83E+06	48	1.36E+05	74	2.75E+02	100	4.14E-01**
23	1.65E+06	49	1.23E+05	75	2.14E+02	** Lower energy limit of 175th group is 1.0E-04 eV	
24	1.50E+06	50	1.11E+05	76	1.67E+02		
25	1.35E+06	51	8.65E+04	77	1.30E+02		
26	1.22E+06	52	6.74E+04	78	1.01E+02		

Table - 2.2: 21 Group energy limits for photons

Group No.	Upper limit (eV)	Group No.	Upper limit (eV)	Group No.	Upper Limit (eV)
1	1.40E+07	9	5.50E+06	17	1.50E+06
2	1.20E+07	10	5.00E+06	18	1.00E+06
3	1.00E+07	11	4.50E+06	19	4.00E+05
4	8.00E+06	12	4.00E+06	20	2.00E+05
5	7.50E+06	13	3.50E+06	21	1.00E+05
6	7.00E+06	14	3.00E+06	** Lower energy limit for 21st group is 10 keV	
7	6.50E+06	15	2.50E+06		
8	6.00E+06	16	2.00E+06		

Table- 2.3: 175 Group energy limits for neutrons in VITAMIN-J structure

Group No	Upper limit (eV)	Group No	Upper limit (eV)	Group No	Upper Limit (eV)	Group No	Upper limit (eV)
1	1.9640E+07	46	2.3457E+06	91	2.2371E+05	136	2.7465E+03
2	1.7333E+07	47	2.3069E+06	92	2.1280E+05	137	2.6126E+03
3	1.6905E+07	48	2.2313E+06	93	2.0242E+05	138	2.4852E+03
4	1.6487E+07	49	2.1225E+06	94	1.9255E+05	139	2.2487E+03
5	1.5683E+07	50	2.0190E+06	95	1.8316E+05	140	2.0347E+03
6	1.4918E+07	51	1.9205E+06	96	1.7422E+05	141	1.5846E+03
7	1.4550E+07	52	1.8268E+06	97	1.6573E+05	142	1.2341E+03
8	1.4191E+07	53	1.7377E+06	98	1.5764E+05	143	9.6112E+02
9	1.3840E+07	54	1.6530E+06	99	1.4996E+05	144	7.4852E+02
10	1.3499E+07	55	1.5724E+06	100	1.4264E+05	145	5.8295E+02
11	1.2840E+07	56	1.4957E+06	101	1.3569E+05	146	4.5400E+02
12	1.2523E+07	57	1.4227E+06	102	1.2907E+05	147	3.5358E+02
13	1.2214E+07	58	1.3534E+06	103	1.2277E+05	148	2.7536E+02
14	1.1618E+07	59	1.2873E+06	104	1.1679E+05	149	2.1445E+02
15	1.1052E+07	60	1.2246E+06	105	1.1109E+05	150	1.6702E+02
16	1.0513E+07	61	1.1648E+06	106	9.8037E+04	151	1.3007E+02
17	1.0000E+07	62	1.1080E+06	107	8.6517E+04	152	1.0130E+02
18	9.5123E+06	63	1.0026E+06	108	8.2500E+04	153	7.8893E+01
19	9.0484E+06	64	9.6164E+05	109	7.9500E+04	154	6.1442E+01
20	8.6071E+06	65	9.0718E+05	110	7.2000E+04	155	4.7851E+01
21	8.1873E+06	66	8.6294E+05	111	6.7379E+04	156	3.7267E+01
22	7.7880E+06	67	8.2085E+05	112	5.6562E+04	157	2.9023E+01
23	7.4082E+06	68	7.8082E+05	113	5.2475E+04	158	2.2603E+01
24	7.0469E+06	69	7.4274E+05	114	4.6309E+04	159	1.7603E+01
25	6.7032E+06	70	7.0651E+05	115	4.0868E+04	160	1.3710E+01
26	6.5924E+06	71	6.7206E+05	116	3.4307E+04	161	1.0677E+01
27	6.3763E+06	72	6.3928E+05	117	3.1828E+04	162	8.3153E+00
28	6.0653E+06	73	6.0810E+05	118	2.8500E+04	163	6.4760E+00
29	5.7695E+06	74	5.7844E+05	119	2.7000E+04	164	5.0435E+00
30	5.4881E+06	75	5.5023E+05	120	2.6058E+04	165	3.9279E+00
31	5.2205E+06	76	5.2340E+05	121	2.4788E+04	166	3.0590E+00
32	4.9659E+06	77	4.9787E+05	122	2.4176E+04	167	2.3824E+00
33	4.7237E+06	78	4.5049E+05	123	2.3579E+04	168	1.8554E+00
34	4.4933E+06	79	4.0762E+05	124	2.1875E+04	169	1.4450E+00
35	4.0657E+06	80	3.8774E+05	125	1.9305E+04	170	1.1254E+00
36	3.6788E+06	81	3.6883E+05	126	1.5034E+04	171	8.7642E-01
37	3.3287E+06	82	3.3373E+05	127	1.1709E+04	172	6.8256E-01
38	3.1664E+06	83	3.0197E+05	128	1.0595E+04	173	5.3158E-01
39	3.0119E+06	84	2.9850E+05	129	9.1188E+03	174	4.1399E-01
40	2.8650E+06	85	2.9720E+05	130	7.1017E+03	175	1.0000E-01**
41	2.7253E+06	86	2.9452E+05	131	5.5308E+03	** Lower energy limit of 175th group is 1.0E-05 eV	
42	2.5924E+06	87	2.8725E+05	132	4.3074E+03		
43	2.4660E+06	88	2.7324E+05	133	3.7074E+03		
44	2.3852E+06	89	2.4724E+05	134	3.3546E+03		
45	2.3653E+06	90	2.3518E+05	135	3.0354E+03		

Table - 2.4: 42 Group energy limits for photons

Group No.	Upper limit (eV)	Group No.	Upper limit (eV)	Group No.	Upper Limit (eV)
1	5.00E+07	17	3.00E+06	33	2.00E+05
2	3.00E+07	18	2.50E+06	34	1.50E+05
3	2.00E+07	19	2.00E+06	35	1.00E+05
4	1.40E+07	20	1.66E+06	36	7.50E+04
5	1.20E+07	21	1.50E+06	37	7.00E+04
6	1.00E+07	22	1.34E+06	38	6.00E+04
7	8.00E+06	23	1.33E+06	39	4.50E+04
8	7.50E+06	24	1.00E+06	40	3.00E+04
9	7.00E+06	25	8.00E+05	41	2.00E+04
10	6.50E+06	26	7.00E+05	42	1.00E+04 **
11	6.00E+06	27	6.00E+05	** Lower energy limit for 42nd group is 1 keV	
12	5.50E+06	28	5.12E+05		
13	5.00E+06	29	5.10E+05		
14	4.50E+06	30	4.50E+05		
15	4.00E+06	31	4.00E+05		
16	3.50E+06	32	3.00E+05		

Table - 2.5: List of nuclides in IGC-S3

Nuclide	MAT No.	Nuclide	MAT No.	Nuclide	MAT No.	Nuclide	MAT No
H1	125	V	2300	Ag107	4725	Np237	9346
H2	128	Cr	2400	Ag109	4731	Np238	9349
H3	131	Cr50	2425	Ag111	4737	Np239	9352
He3	225	Cr52	2431	Cd	4800	Pu236	9428
He4	228	Cr53	2434	Hf	7200	Pu238	9434
Li6	325	Cr54	2437	Ta181	7328	Pu239	9437
Li7	328	Mn55	2525	W	7400	Pu240	9440
Be9	425	Fe	2600	Nb193##	4125	Pu241	9443
B10	525	Fe54	2625	Re185	7525	Pu242	9446
B11	528	Fe56	2631	Re187	7531	Am241**	9543
C	600	Fe57	2634	Au197	7925	Am242	9546
N14	725	Fe58	2637	Pb	8200	Am242m	9547
N15	728	Co59	2725	Pb204**	8225	Am243	9549
O16	825	Ni	2800	Pb206	8231	Cm241	9628
O17	828	Ni58	2825	Pb207	8234	Cm242	9631
F19	925	Ni60	2831	Pb208	8237	Cm243	9634
Na23	1125	Ni61	2834	Th230	9034	Cm244	9637
Mg	1200	Ni62	2837	Th232	9040	Cm245	9640
Al27	1325	Ni64	2843	Pa233	9137	Cm246	9643
Si	1400	Cu	2900	U232**	9219	Cm247	9646
P31	1525	Cu63	2925	U233	9222	Cm248	9649
S	1600	Cu65	2931	U234	9225	Cf249	9852
Cl	1700	Ga	3100	U235	9228	Cf250	9855
K	1900	Zr	4000	U236	9231	Cf251	9858
Ca	2000	Mo	4200	U237	9234	Cf252	9861
Ti	2200	Rh103	4525	U238	9237	Cf253	9864

** From JENDL-3.2

From JEF-2

2.3.3 Displacement cross-sections

Neutrons can cause displacement of atoms of the material being irradiated, which could subsequently cause a displacement cascade, leading to defects and changes in the mechanical properties, like ductility, of the material. Such changes have a bearing on the life of the material inside the reactor. Radiation damage caused by neutrons is characterized by displacement per atom (*dpa)*. As the name suggests, this represents the number of atomic displacements caused by the irradiation over a given time, and is given by

$$\text{dpa} = t\int \sigma_D(E)\phi(E)dE \, .$$

where t is the time of irradiation. The flux is a function of spatial location in a reactor and so is the *dpa*. The total displacement cross-section, $\sigma_D(E)$ may itself be defined in terms of its partials as

$$\sigma_D(E) = \sum_x \sigma_{Dx}(E) \, .$$

$$\sigma_{Dx}(E) = \int_{E_d}^{E_T\,max} \sigma_x(E)\ P_x(E,E_T)\ \nu(E_T)\ dE_T \, .$$

P is the PKA (Primary Knock-on Atom) spectrum, which represents the probability that a neutron of energy E transfers an energy E_T to the target atom, upon collision. $\nu(E_T)$ gives the number of displacements caused by the PKA in the sequential sharing of the energy E_T. $\sigma_\chi$is the cross-section for the reaction process x, in which the energy was transferred. The energy transfer obviously depends on the type of reaction, though most contribution is from elastic scattering. The extent of damage is correlated to the *dpa*, by material science studies, and so *dpa* is used to fix upper limits on time or irradiation, or fluence that a reactor material should face, to be within

the permissible damage level. Code like SPECTER (Lawrence R Greenwood and Robert K Smither, 1985) give multigroup displacement cross-sections σ_{Dg}, from which *dpa* is obtained as

$$\text{dpa} = t\sum_{g}\sigma_{Dg}\phi_{g} .$$

2.4 2D Transport Calculations- Reference Case

The in-vessel bulk shield problems in fast reactors are deep penetration problems. Therefore our calculations are performed using 2D deterministic transport code available with us, DORT (Rhoads and Childs, 1988) in RZ geometry which extends upto reactor vault radially and bottom concrete below the reactor vessel to top shield. The calculation also gives full flux distribution. The 2D RZ calculation model is given in Fig.2.1. After many trials with mesh widths, we chose the mesh structure: 571 meshes along the radial direction and 718 meshes along axial direction. The criterion was stability of results with increase in mesh size. The criterion used for flux convergence is 1.0E-04 and that for the fission convergence is 1.0E-03. This convergence was obtained in almost all the groups for all the spatial mesh points. Vacuum boundary condition is used at the bottom, top and right ends; where as reflective boundary condition is used at the left end. Again, after several trial calculations, the angular approximation S_8 and the order of scattering cross section anisotropy P_3 were found to be adequate in the sense that increasing the orders gave the same results. Identical mesh structures were used for both the computations using IGC-S3 and DLC-37.

2.4.1 Neutron flux distributions

For the equilibrium core the different types of neutron fluxes calculated radially are given in Table 2.6 and 2.7 for IGC-S3 and DLC-37 cross section sets. The radial variation of total flux, U235 equivalent flux, sodium equivalent flux and fast flux above 0.1 MeV are shown in Figs.2.2, 2.3, 2.4 and 2.5 respectively.

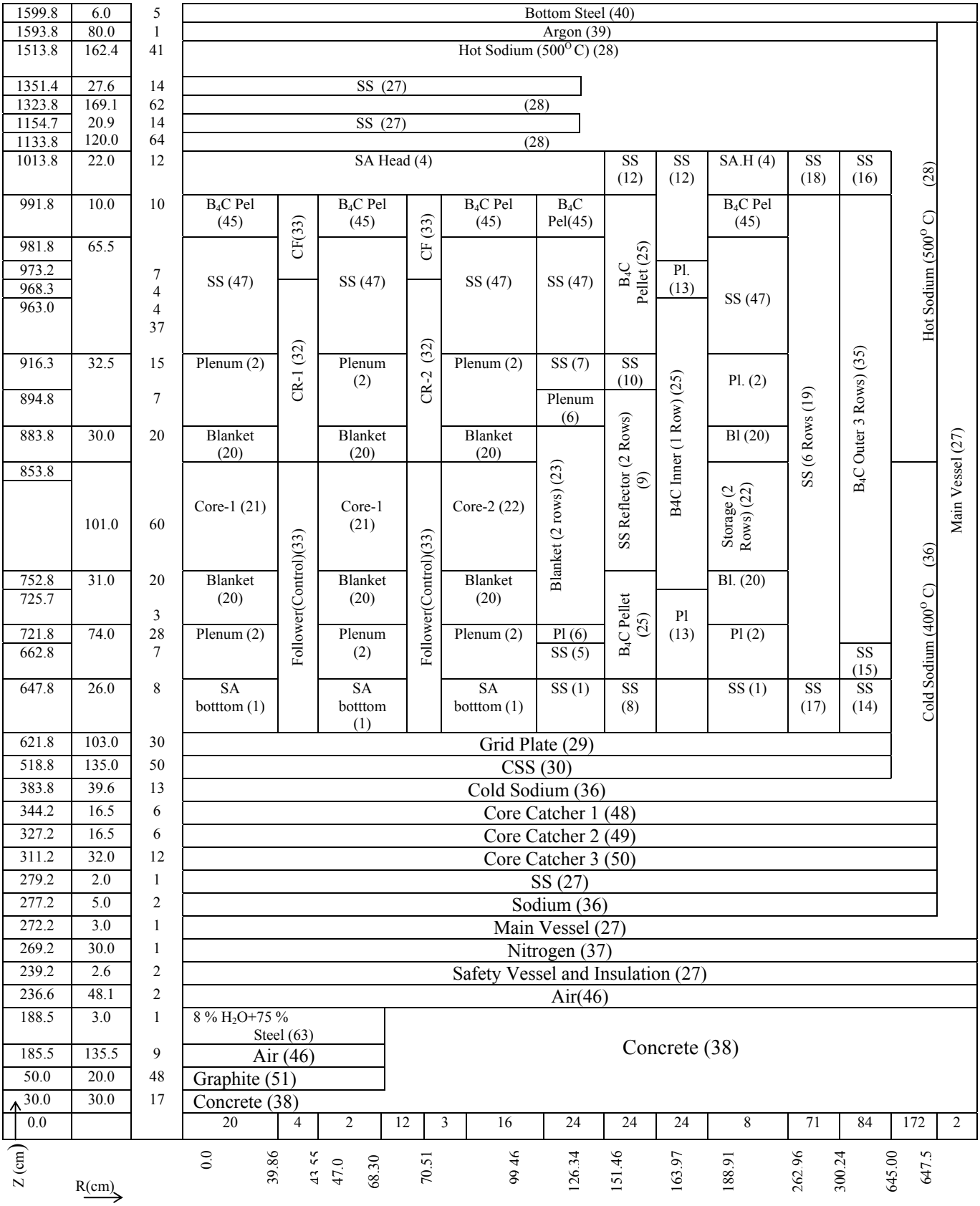

Fig-2.1: 2D R-Z Calculation model of PFBR

The various types of neutron fluxes along axial direction is shown in Tables 2.8 and 2.9 for IGC-S3 and DLC-37. The axial variation of total flux, U235 equivalent flux and fast flux above 0.1 MeV are shown in Fig. 2.6, 2.7 and 2.8 respectively. The contour plots of total neutron flux, U235 equivalent flux, sodium equivalent flux and fast flux (> 0.1 MeV) are given in Fig.2.9, 2.10, 2.11 and 2.12 respectively. Central radial variation of sodium equivalent flux in the IHX region after shields is shown in Fig. 2.13 and axial variation of sodium equivalent fluxes at left boundary, Midpoint and right boundary of IHX are plotted in Figs. 2.14, 2.15 and 2.16. DLC 37 is a 100 neutron group cross section set. There is only one group to represent thermal flux, viz., 100^{th} group whose upper boundary is 0.41 eV. In contrast, IGC-S3 is a 175 group neutron cross section set which has thermal flux represented by 6 energy groups below 0.41 eV. As we progress towards interior points in concrete, the spectrum is more thermalised. Hence there is a greater variation in fluxes and ratios. However, differences are not high in in-vessel shields in fast reactors since the neutron spectra in neutron shields in the reactor vessel are much harder and thermal flux component does not significantly contribute to reaction rates.

The definitions of equivalent fluxes are given in the appendix.

2.4.2 Detector location flux distributions

Tables 2.10 and 2.11 show the average U235 equivalent fluxes and B-10 equivalent fluxes at the control plug detector position using IGC-S3 and DLC-37 cross section sets.

2.4.3 Gamma flux and dose distributions

The total gamma flux contours are given in Fig.2.17. The radial and axial gamma fluxes are shown in Figs.2.18 and 2.19.

Table - 2.6: Neutron fluxes (n/cm^2/s) along radial direction

No	Region	Radius (cm)	mesh	Total Neutron Flux			U235- Eq. Flux		
				DLC-37	IGC-S3	Ratio	DLC-37	IGC-S3	Ratio
1	Core Centre	0.00E+00	1	8.00E+15	8.00E+15	1.00	2.99E+13	2.85E+13	0.95
2	Core-1 (39.6 cm)	3.79E+01	20	7.24E+15	7.23E+15	1.00	2.85E+13	2.71E+13	0.95
3	CR Follower (3.69 cm)	4.26E+01	24	7.15E+15	7.14E+15	1.00	2.85E+13	2.72E+13	0.95
4	Core-1 (Outer) (24.75 cm)	6.65E+01	38	6.40E+15	6.36E+15	0.99	2.40E+13	2.27E+13	0.95
5	CR Follower (2.21cm)	6.98E+01	41	6.31E+15	6.27E+15	0.99	2.37E+13	2.25E+13	0.95
6	Core-2 (28.95 cm)	9.77E+01	57	3.52E+15	3.52E+15	1.00	1.30E+13	1.24E+13	0.95
7	Blanket (26.88 cm)	1.25E+02	81	7.78E+14	8.00E+14	1.03	4.02E+12	4.08E+12	1.01
8	SS Reflector (25.12 cm)	1.50E+02	105	8.28E+13	9.28E+13	1.12	6.10E+11	7.00E+11	1.15
9	B_4C Inner (12.51cm)	1.63E+02	129	1.14E+13	1.26E+13	1.11	4.26E+10	4.53E+10	1.06
10	Storage (24.94 cm)	1.86E+02	137	6.73E+12	7.46E+12	1.11	2.87E+10	3.10E+10	1.08
11	SS (74.05 cm)	2.62E+02	208	2.96E+10	4.01E+10	1.35	3.05E+08	4.42E+08	1.45
12	B_4C Outer (37.28 cm)	3.00E+02	292	2.09E+07	2.64E+07	1.26	1.37E+05	1.64E+05	1.20
13	(Sodium) (344.76 cm)	6.43E+02	464	2.42E+04	3.10E+04	1.28	6.05E+03	5.00E+03	0.83
14	Main Vessel (2.5 cm)	6.46E+02	466	1.24E+04	1.63E+04	1.31	2.51E+03	2.03E+03	0.81
15	Nitrogen (30 cm)	6.48E+02	467	1.01E+04	1.33E+04	1.32	1.99E+03	1.62E+03	0.81
16	Safety Vessel (3.5 cm)	6.79E+02	469	4.32E+03	5.71E+03	1.32	1.07E+03	9.09E+02	0.85
17	Nitrogen (28 cm)	6.81E+02	470	3.26E+03	4.20E+03	1.29	1.14E+03	9.84E+02	0.86
18	CS Liner (0.6 cm)	7.09E+02	471	2.98E+03	3.84E+03	1.29	1.25E+03	1.17E+03	0.94
19	Conc (10.0 cm)	7.19E+02	477	1.45E+03	1.53E+03	1.06	1.35E+03	1.35E+03	1.00
20	Conc (15.0 cm)	7.22E+02	479	1.08E+03	1.08E+03	1.00	1.05E+03	1.01E+03	0.96
21	Conc (20.0 cm)	7.28E+02	482	6.89E+02	6.39E+02	0.93	6.81E+02	6.23E+02	0.91
22	Conc (25.0 cm)	7.33E+02	485	4.35E+02	3.76E+02	0.86	4.33E+02	3.72E+02	0.86
23	Conc (30.0 cm)	7.38E+02	488	2.74E+02	2.20E+02	0.80	2.73E+02	2.19E+02	0.80
24	Conc (35.0 cm)	7.42E+02	490	2.02E+02	1.54E+02	0.76	2.01E+02	1.53E+02	0.76
25	Conc (40.0 cm)	7.47E+02	493	1.27E+02	9.04E+01	0.71	1.27E+02	9.03E+01	0.71
26	Conc (45.0 cm)	7.53E+02	496	8.05E+01	5.32E+01	0.66	8.05E+01	5.32E+01	0.66
27	Conc (50.0 cm)	7.58E+02	499	5.08E+01	3.13E+01	0.62	5.08E+01	3.13E+01	0.62
28	Conc (75.0 cm)	7.83E+02	513	6.05E+00	2.70E+00	0.45	6.05E+00	2.70E+00	0.45
29	Conc (100.0 cm)	8.09E+02	527	7.32E-01	2.34E-01	0.32	7.32E-01	2.34E-01	0.32
30	Conc (125.0 cm)	8.32E+02	540	1.02E-01	2.50E-02	0.25	1.02E-01	2.50E-02	0.25
31	Conc (150.0 cm)	8.57E+02	554	1.26E-02	2.25E-03	0.18	1.26E-02	2.25E-03	0.18
32	Conc (175.0 cm)	8.82E+02	568	1.14E-03	1.58E-04	0.14	1.14E-03	1.58E-04	0.14
33	Conc (180.0 cm)	8.88E+02	571	3.45E-04	5.22E-05	0.15	3.45E-04	5.22E-05	0.15

Table - 2.7: Neutron fluxes (n/cm^2/s) along radial direction

	Region	Radius (cm)	mesh	Fast Flux (> 0.1 MeV)			Na Eq. Flux		
				DLC-37	IGC-S3	Ratio	DLC-37	IGC-S3	Ratio
1	Core Centre	0.00E+00	1	5.31E+15	4.76E+15	0.90	2.90E+13	2.61E+13	0.90
2	Core-1 (39.6 cm)	3.79E+01	20	4.68E+15	4.16E+15	0.89	2.71E+13	2.42E+13	0.89
3	CR Follower (3.69 cm)	4.26E+01	24	4.59E+15	4.08E+15	0.89	2.68E+13	2.34E+13	0.87
4	Core-1 (Outer) (24.75 cm)	6.65E+01	38	4.29E+15	3.83E+15	0.89	2.24E+13	1.98E+13	0.88
5	CR Follower (2.21cm)	6.98E+01	41	4.24E+15	3.78E+15	0.89	2.17E+13	1.89E+13	0.87
6	Core-2 (28.95 cm)	9.77E+01	57	2.32E+15	2.08E+15	0.90	1.29E+13	1.17E+13	0.91
7	Blanket (26.88 cm)	1.25E+02	81	3.77E+14	3.32E+14	0.88	5.26E+12	5.05E+12	0.96
8	SS Reflector (25.12 cm)	1.50E+02	105	3.77E+13	3.38E+13	0.90	6.73E+11	7.16E+11	1.06
9	B_4C Inner (12.51cm)	1.63E+02	129	6.70E+12	6.25E+12	0.93	4.89E+10	5.02E+10	1.03
10	Storage (24.94 cm)	1.86E+02	137	4.24E+12	4.23E+12	1.00	2.94E+10	3.00E+10	1.02
11	SS (74.05 cm)	2.62E+02	208	9.69E+09	8.95E+09	0.92	3.20E+08	4.25E+08	1.33
12	B_4C Outer (37.28 cm)	3.00E+02	292	7.13E+06	6.99E+06	0.98	1.62E+05	1.84E+05	1.14
13	(Sodium) (344.76 cm)	6.43E+02	464	5.60E+00	5.92E+00	1.06	6.71E+03	5.96E+03	0.89
14	Main Vessel (2.5 cm)	6.46E+02	466	3.97E+00	4.15E+00	1.05	2.88E+03	2.56E+03	0.89
15	Nitrogen (30 cm)	6.48E+02	467	3.36E+00	3.36E+00	1.00	2.30E+03	2.06E+03	0.90
16	Safety Vessel (3.5 cm)	6.79E+02	469	2.12E+00	2.24E+00	1.06	1.20E+03	1.09E+03	0.91
17	Nitrogen (28 cm)	6.81E+02	470	1.62E+00	1.68E+00	1.04	1.23E+03	1.12E+03	0.91
18	CS Liner (0.6 cm)	7.09E+02	471	1.49E+00	1.61E+00	1.08	1.33E+03	1.29E+03	0.97
19	Conc (10.0 cm)	7.19E+02	477	1.72E-01	1.46E-01	0.85	1.36E+03	1.36E+03	1.00
20	Conc (15.0 cm)	7.22E+02	479	9.18E-02	7.05E-02	0.77	1.05E+03	1.02E+03	0.97
21	Conc (20.0 cm)	7.28E+02	482	3.97E-02	2.69E-02	0.68	6.82E+02	6.24E+02	0.91
22	Conc (25.0 cm)	7.33E+02	485	2.00E-02	1.18E-02	0.59	4.33E+02	3.72E+02	0.86
23	Conc (30.0 cm)	7.38E+02	488	1.05E-02	5.77E-03	0.55	2.73E+02	2.19E+02	0.80
24	Conc (35.0 cm)	7.42E+02	490	7.00E-03	3.72E-03	0.53	2.01E+02	1.53E+02	0.76
25	Conc (40.0 cm)	7.47E+02	493	4.04E-03	2.01E-03	0.50	1.27E+02	9.04E+01	0.71
26	Conc (45.0 cm)	7.53E+02	496	2.32E-03	1.12E-03	0.48	8.05E+01	5.32E+01	0.66
27	Conc (50.0 cm)	7.58E+02	499	1.37E-03	6.43E-04	0.47	5.08E+01	3.13E+01	0.62
28	Conc (75.0 cm)	7.83E+02	513	1.35E-04	5.64E-05	0.42	6.05E+00	2.70E+00	0.45
29	Conc (100.0 cm)	8.09E+02	527	1.38E-05	5.40E-06	0.39	7.32E-01	2.34E-01	0.32
30	Conc (125.0 cm)	8.32E+02	540	1.66E-06	6.22E-07	0.37	1.02E-01	2.50E-02	0.25
31	Conc (150.0 cm)	8.57E+02	554	1.72E-07	6.12E-08	0.36	1.26E-02	2.25E-03	0.18
32	Conc (175.0 cm)	8.82E+02	568	1.60E-08	5.52E-09	0.35	1.14E-03	1.58E-04	0.14
33	Conc (180.0 cm)	8.88E+02	571	6.96E-09	2.35E-09	0.34	3.45E-04	5.22E-05	0.15

Table - 2.8: Neutron fluxes (n/cm^2/s) along axial direction

No	Region	Height (cm)	mesh	Total Neutron Flux			U235- Eq. Flux		
				DLC-37	IGC-S3	Ratio	DLC-37	IGC-S3	Ratio
1	Concrete (30 cm)	2.82E+01	17	5.34E+04	6.06E+04	1.13	5.30E+04	5.97E+04	1.13
2	Graphite 5 cm above concrete	3.54E+01	29	9.95E+04	1.32E+05	1.33	9.67E+04	1.26E+05	1.30
3	Graphite 12.5 cm above concrete	4.25E+01	47	1.54E+05	2.17E+05	1.41	1.40E+05	1.87E+05	1.34
4	Graphite(20 cm)	4.96E+01	65	1.73E+05	2.43E+05	1.40	1.23E+05	1.44E+05	1.17
5	Air (10.0 cm)	5.00E+01	66	1.79E+05	2.53E+05	1.41	1.33E+05	1.62E+05	1.22
6	Air (135.5 cm)	1.65E+02	74	4.00E+05	6.09E+05	1.52	2.15E+05	2.53E+05	1.18
7	Steel+H_2O (2.0 cm)	1.86E+02	75	5.40E+05	8.75E+05	1.62	1.79E+05	2.00E+05	1.12
8	Air (48.5 cm)	2.12E+02	77	8.39E+05	1.42E+06	1.69	2.14E+05	2.65E+05	1.24
9	Safety vessel and Insulation (4.0)	2.38E+02	79	2.60E+06	4.44E+06	1.71	3.24E+05	4.06E+05	1.25
10	Nitrogen (30.0)	2.39E+02	80	2.72E+06	4.64E+06	1.71	3.19E+05	4.08E+05	1.28
11	Main Vessel (3.0)	2.69E+02	81	4.69E+06	8.01E+06	1.71	5.72E+05	7.34E+05	1.28
12	Na (5.0)	2.75E+02	83	8.21E+06	1.39E+07	1.69	1.01E+06	1.31E+06	1.30
13	SS (2.0)	2.77E+02	84	1.10E+07	1.84E+07	1.67	1.43E+06	1.81E+06	1.27
14	CCR-3 (31.5)	3.09E+02	96	3.73E+07	6.21E+07	1.66	4.87E+06	6.23E+06	1.28
15	CCR-2 (16.5)	3.25E+02	102	6.73E+07	1.12E+08	1.66	7.90E+06	1.02E+07	1.29
16	CCR-1 (16.0)	3.41E+02	108	2.02E+08	3.30E+08	1.63	2.50E+07	3.19E+07	1.28
17	Sodium (39.6)	3.81E+02	121	4.95E+08	8.14E+08	1.64	5.61E+07	7.41E+07	1.32
18	CSS (135.0)	5.16E+02	171	4.32E+10	6.79E+10	1.57	1.93E+09	2.89E+09	1.50
19	Grid Plate(100.0)	6.18E+02	201	1.43E+13	1.86E+13	1.30	3.71E+11	4.95E+11	1.33
20	SA bottom (26.0)	6.41E+02	208	5.66E+13	6.92E+13	1.22	1.31E+12	1.65E+12	1.26
21	Plenum (75.0cm)	7.20E+02	244	6.74E+14	7.22E+14	1.07	5.06E+12	5.45E+12	1.08
22	Blanket (30.0cm)	7.51E+02	267	3.37E+15	3.42E+15	1.01	1.39E+13	1.36E+13	0.98
23	Core Centre	8.02E+02	297	8.00E+15	8.00E+15	1.00	2.99E+13	2.85E+13	0.95
24	Core (103 cm)	8.52E+02	327	3.37E+15	3.41E+15	1.01	1.36E+13	1.32E+13	0.97
25	Blanket (30 cm)	8.82E+02	347	5.87E+14	6.14E+14	1.05	3.42E+12	3.51E+12	1.03
26	Plenum (31.5 cm)	9.15E+02	369	1.90E+14	2.08E+14	1.09	2.19E+12	2.46E+12	1.12
27	SS (65.5 cm)	9.81E+02	421	1.59E+12	2.04E+12	1.28	2.00E+10	2.70E+10	1.35
28	B_4C (10.0 cm)	9.91E+02	431	3.68E+11	4.61E+11	1.25	2.16E+09	2.67E+09	1.24
29	SA Head (22cm)	1.01E+03	443	1.58E+11	2.12E+11	1.34	3.47E+09	4.48E+09	1.29
30	Lattice Plate #	1.06E+03	467	6.69E+10	9.03E+10	1.35	2.97E+09	3.64E+09	1.23
31	Core Cover Plate $	1.14E+03	514	2.28E+09	3.33E+09	1.46	1.34E+08	1.80E+08	1.34
32	Sodium	1.51E+03	638	2.29E+05	2.70E+05	1.18	8.64E+04	6.29E+04	0.73
33	Argon (80.0 cm)	1.51E+03	639	2.29E+05	2.70E+05	1.18	8.42E+04	6.09E+04	0.72
34	Bottom Steel (6.0 cm)	1.60E+03	644	3.43E+04	4.27E+04	1.24	1.14E+04	8.69E+03	0.76
35	Concrete (119.0 cm)	1.72E+03	712	7.80E-06	3.46E-06	0.44	2.50E-06	5.65E-07	0.23
36	Top Steel (5.0 cm)	1.72E+03	716	1.61E-06	8.32E-07	0.52	1.68E-07	3.56E-08	0.21
37	Air (100.0 cm)	1.77E+03	718	1.17E-06	5.84E-07	0.50	1.08E-07	2.09E-08	0.19

45 cm above SA head; $130 cm above SA head

Table - 2.9: Neutron fluxes (n/cm^2/s) along axial direction

No	Region	Height (cm)	mesh	Fast Flux (> 0.1 MeV)			Na Eq. Flux		
				DLC-37	IGC-S3	Ratio	DLC-37	IGC-S3	Ratio
1	Concrete (30 cm)	2.82E+01	17	9.86E-01	1.10E+00	1.12	5.30E+04	5.98E+04	1.13
2	Graphite 5 cm above concrete	3.54E+01	29	4.28E+00	5.96E+00	1.39	9.69E+04	1.27E+05	1.31
3	Graphite 12.5 cm above concrete	4.25E+01	47	2.59E+01	4.69E+01	1.81	1.40E+05	1.89E+05	1.35
4	Graphite(20 cm)	4.96E+01	65	1.43E+02	2.74E+02	1.92	1.25E+05	1.48E+05	1.18
5	Air (10.0 cm)	5.00E+01	66	1.39E+02	2.51E+02	1.81	1.35E+05	1.66E+05	1.23
6	Air (135.5 cm)	1.65E+02	74	5.13E+02	6.82E+02	1.33	2.21E+05	2.66E+05	1.20
7	Steel+H_2O (2.0 cm)	1.86E+02	75	9.21E+02	1.17E+03	1.27	1.90E+05	2.21E+05	1.16
8	Air (48.5 cm)	2.12E+02	77	1.49E+03	1.71E+03	1.15	2.31E+05	2.97E+05	1.29
9	Safety vessel and Insulation (4.0)	2.38E+02	79	3.50E+03	3.50E+03	1.00	3.74E+05	4.97E+05	1.33
10	Nitrogen (30.0)	2.39E+02	80	3.75E+03	3.66E+03	0.98	3.74E+05	5.07E+05	1.36
11	Main Vessel (3.0)	2.69E+02	81	5.78E+03	5.93E+03	1.03	6.64E+05	9.03E+05	1.36
12	Na (5.0)	2.75E+02	83	9.37E+03	9.54E+03	1.02	1.17E+06	1.59E+06	1.36
13	SS (2.0)	2.77E+02	84	1.19E+04	1.20E+04	1.01	1.64E+06	2.20E+06	1.34
14	CCR-3 (31.5)	3.09E+02	96	5.78E+04	5.49E+04	0.95	5.43E+06	7.29E+06	1.34
15	CCR-2 (16.5)	3.25E+02	102	1.41E+05	1.29E+05	0.91	8.61E+06	1.16E+07	1.35
16	CCR-1 (16.0)	3.41E+02	108	4.74E+05	3.94E+05	0.83	2.65E+07	3.53E+07	1.33
17	Sodium (39.6)	3.81E+02	121	2.66E+06	2.25E+06	0.85	5.80E+07	7.90E+07	1.36
18	CSS (135.0)	5.16E+02	171	2.98E+09	2.80E+09	0.94	1.65E+09	2.44E+09	1.48
19	Grid Plate(100.0)	6.18E+02	201	2.66E+12	2.39E+12	0.90	3.00E+11	3.81E+11	1.27
20	SA bottom (26.0)	6.41E+02	208	1.25E+13	1.09E+13	0.87	1.04E+12	1.23E+12	1.18
21	Plenum (75.0cm)	7.20E+02	244	2.63E+14	2.31E+14	0.88	5.26E+12	5.12E+12	0.97
22	Blanket (30.0cm)	7.51E+02	267	2.01E+15	1.80E+15	0.90	1.50E+13	1.37E+13	0.91
23	Core Centre	8.02E+02	297	5.31E+15	4.76E+15	0.90	2.90E+13	2.61E+13	0.90
24	Core (103 cm)	8.52E+02	327	2.06E+15	1.85E+15	0.90	1.42E+13	1.30E+13	0.92
25	Blanket (30 cm)	8.82E+02	347	2.52E+14	2.23E+14	0.88	3.95E+12	3.73E+12	0.94
26	Plenum (31.5 cm)	9.15E+02	369	6.59E+13	5.81E+13	0.88	1.80E+12	1.87E+12	1.04
27	SS (65.5 cm)	9.81E+02	421	4.68E+11	4.13E+11	0.88	1.80E+10	2.22E+10	1.23
28	B_4C (10.0 cm)	9.91E+02	431	1.23E+11	1.04E+11	0.85	2.65E+09	3.01E+09	1.14
29	SA Head (22cm)	1.01E+03	443	2.92E+10	2.46E+10	0.84	2.70E+09	3.32E+09	1.23
30	Lattice Plate #	1.06E+03	467	4.69E+09	3.86E+09	0.82	2.29E+09	2.75E+09	1.20
31	Core Cover Plate $	1.14E+03	514	6.62E+07	5.79E+07	0.87	1.35E+08	1.79E+08	1.33
32	Sodium	1.51E+03	638	7.05E+00	5.33E+00	0.76	9.49E+04	7.55E+04	0.80
33	Argon (80.0 cm)	1.51E+03	639	7.20E+00	6.19E+00	0.86	9.28E+04	7.35E+04	0.79
34	Bottom Steel (6.0 cm)	1.60E+03	644	3.68E+00	3.01E+00	0.82	1.27E+04	1.07E+04	0.84
35	Concrete (119.0 cm)	1.72E+03	712	1.61E-06	6.43E-07	0.40	2.55E-06	5.98E-07	0.23
36	Top Steel (5.0 cm)	1.72E+03	716	6.58E-07	2.65E-07	0.40	1.75E-07	3.97E-08	0.23
37	Air (100.0 cm)	1.77E+03	718	5.54E-07	2.37E-07	0.43	1.12E-07	2.33E-08	0.21

45 cm above SA head; $130 cm above SA head

Table - 2.10: U235 equivalent flux (average) (n/cm^2/s) over 30 cm height for different radial distances for detector in lattice plate for equilibrium core

Radius (cm)	Radial Mesh	DLC-37	IGC-S3
0.0	1	3.29E+09	4.06E+09
50	28	2.92E+09	3.59E+09
100	57	2.00E+09	2.43E+09
125	80	1.47E+09	1.76E+09
150	104	1.02E+09	1.20E+09
200	148	4.59E+08	5.15E+08
235	181	2.53E+08	2.74E+08

Table - 2.11: B-10 equivalent flux (average) (n/cm^2/s) over 100 cm height for different radial distances for detector in lattice plate for equilibrium core

Radius (cm)	Radial Mesh	DLC-37	IGC-S3
0.0	1	1.68E+09	2.01E+09
50	28	1.52E+09	1.80E+09
100	57	1.12E+09	1.31E+09
125	80	8.89E+08	1.03E+09
150	104	6.85E+08	7.80E+08
200	148	3.69E+08	4.07E+08
235	181	2.25E+08	2.42E+08

2.4.4 Neutron and gamma spectra

The neutron spectra at core centre, B_4C exit, IHX left, IHX middle and IHX exit along central radial direction are shown in Figs.2.20, 2.21, 2.22, 2.23 and 2.24 respectively. Radially along the primary sodium top, the spectrum at the beginning of IHX positions is given in Fig. 2.25. Axially the neutron spectra plots are given in Figs. 2.26 and 2.27 for top and bottom detector positions.

The comparison of 42 group and 21 group gamma spectrum are given in Fig. 2.28, 2.29 and 2.30 for core centre, top detector and bottom detector positions. In the lower range there is a large variation of spectra values in the gammas as shown in figures. Here in all the plots ratio is

given between the collapsed IGC-S3 and DLC-37 values. The number of groups of gammas in the lower energy range below 20 keV is 6 in the case of DLC-37 whereas it is 9 in the case of IGC-S3. The gamma production data in IGC-S3 is based on recent ENDF-BVI whereas DLC-37 gamma production data is based on ENDF- BIV which differs considerably from ENDF-BVI data. Hence considerable differences in spectral shapes exist.

2.4.5 Helium production

The helium production calculated in the central axial and radial directions are given in Tables 2.12 and 2.13. Table 2.14 gives the helium production due to (n,α) reactions of each element in the D-9 steel at core centre. Helium production contribution is more due to Ni (n, α) reaction (51 % of the total) and then comes boron (30 %). The net variation in helium production at core centre is 9 % between the values calculated using these two cross section sets.

Table - 2.12: Maximum helium production in steel in various regions along axial direction through the core centre

	Region	Mesh	IGC-S3		DLC-37	
			2y	40y	2y	40y
1	*Safety Vessel*	79	-	3.37E-05	-	2.41E-05
2	*Reactor Vessel*	81	-	6.12E-05	-	4.29E-05
3	*CSS*	171	-	1.51E-01	-	9.58E-02
4	*Grid Plate*	201	-	2.05E+01	-	1.47E+01
5	SA Bottom	208	3.15E+00	-	2.39E+00	-
6	Plenum	224	7.35E+00	-	5.94E+00	-
7	Blanket (Lower)	267	2.51E+01	-	2.64E+01	-
8	Core-1	297	6.97E+01	-	7.59E+01	-
9	Blanket (Upper)	347	4.24E+00	-	4.03E+00	-
10	Plenum	369	3.20E+00	-	2.70E+00	-
11	SS	421	4.18E-02	-	2.91E-02	-
12	B_4C	431	2.67E-03	-	2.01E-03	-
13	*SA Head Top*	443	-	1.61E-01	-	1.21E-01
14	*Lattice Plate* #	467	-	1.68E-01	-	1.33E-01
15	*Core Cover Plate* $	514	-	1.04E-02	-	7.51E-03

** Load factor is taken as 75 %
# 45 cm above SA head; $130 cm above SA head

Table - 2.13: Maximum helium production in steel in various regions along radial direction through the core centre

	Region	Mesh	IGC-S3		DLC-37	
			2y	40y	2y	40y
1	Core- 1	1	6.97E+01	-	7.59E+01	-
2	Core- 1 Exit	38	5.48E+01	-	5.99E+01	-
3	Core- 2	57	3.07E+01	-	3.34E+01	-
4	Radial Blanket	81	5.82E+00	-	5.71E+00	-
5	*SS Reflector*	105	-	1.69E+01	-	1.39E+01
6	*B_4C Inner*	129	-	1.47E+00	-	1.46E+00
7	Storage	137	-	1.24E+00	-	1.19E+00
8	*SS*	208	-	1.28E-02	-	8.23E-03
9	*B_4C Outer*	292	-	3.65E-06	-	2.99E-06
10	*IHX Left*	336	-	1.96E-05	-	1.85E-05
11	*IHX Right*	436	-	1.58E-06	-	1.66E-06
12	*RV*	466	-	1.74E-07	-	1.87E-07
13	*SV*	469	-	7.45E-08	-	7.79E-08

** Load factor is taken as 75 %

- In Table 13 and 14, regions given in Italics letters are 316LN Steel and other regions are with D9 Steel

Table - 2.14: Helium production contribution due to each element for the entire spectrum at the core centre for two years

(n , α) reactions due to	Helium Production due to each element		% Contribution of Helium Production due to each element	
	IGC-S3	DLC-37	IGC-S3	DLC-37
Molybdenum	0.00E+00	0.00E+00	0.0	0.0
Silicon	1.22E+00	1.58E+00	1.8	2.1
Manganese	7.97E-02	1.32E-01	0.1	0.2
Carbon	6.66E-02	1.09E-01	0.1	0.1
Boron-11	1.22E-04	4.00E-04	0.0	0.0
Boron-10	2.09E+01	2.05E+01	30.0	27.0
Chromium	1.69E+00	2.22E+00	2.4	2.9
Iron	1.00E+01	1.41E+01	14.3	18.6
Nickel	3.58E+01	3.71E+01	51.4	48.9
Total	6.97E+01	7.59E+01	0.0	0.0

Table - 2.15: Helium production contribution due to each element at the core centre

(n , α) reactions due to	Full		Above 1 MeV		Between 1MeV and 0.1 MeV		Between 0.1MeV and 100 eV		Less than 100 eV	
	IGC-S3	DLC-37	IGC-S3	DLC-37	IGC-S3	DLC-37	IGC-S3	DLC-37	IGC-S3	DLC-37
Molybdenum	0.00E+00	0.00E+00	0.00E+00	0.00E+00	0.00E+00	0.00E+00	0.00E+00	0.00E+00	0.00E+00	0.00E+00
Silicon	1.22E+00	1.58E+00	1.22E+00	1.58E+00	0.00E+00	0.00E+00	0.00E+00	0.00E+00	0.00E+00	0.00E+00
Manganese	7.97E-02	1.32E-01	7.97E-02	1.32E-01	7.46E-06	5.74E-06	0.00E+00	0.00E+00	0.00E+00	0.00E+00
Carbon	6.66E-02	1.09E-01	6.66E-02	1.09E-01	0.00E+00	0.00E+00	0.00E+00	0.00E+00	0.00E+00	0.00E+00
Boron-11	1.22E-04	4.00E-04	1.22E-04	4.00E-04	0.00E+00	0.00E+00	0.00E+00	0.00E+00	0.00E+00	0.00E+00
Boron-10	2.09E+01	2.05E+01	2.86E-01	2.93E-01	4.06E+00	4.43E+00	1.65E+01	1.58E+01	1.70E-03	1.76E-03
Chromium	1.69E+00	2.22E+00	1.69E+00	2.22E+00	0.00E+00	0.00E+00	0.00E+00	0.00E+00	0.00E+00	0.00E+00
Iron	1.00E+01	1.41E+01	1.00E+01	1.41E+01	3.41E-04	9.88E-05	0.00E+00	0.00E+00	0.00E+00	0.00E+00
Nickel	3.58E+01	3.71E+01	3.58E+01	3.71E+01	3.80E-02	3.07E-02	1.06E-04	4.87E-05	1.19E-13	1.04E-13
Total	6.97E+01	7.59E+01	4.91E+01	5.56E+01	4.10E+00	4.46E+00	1.65E+01	1.58E+01	1.70E-03	1.76E-03

Table - 2.16: Percentage helium production contribution at the core centre

(n , α) reactions due to	Above 1 MeV		Between 1MeV and 0.1 MeV		Between 0.1MeV and 100 eV		Less than 100 eV	
	IGC-S3	DLC-37	IGC-S3	DLC-37	IGC-S3	DLC-37	IGC-S3	DLC-37
Molybdenum	-	-	-	-	-	-	-	-
Silicon	100.0	100.0	0.0	0.0	0.0	0.0	0.0	0.0
Manganese	100.0	100.0	0.01	4.35E-03	0.0	0.0	0.0	0.0
Carbon	100.0	100.0	0.0	0.0	0.0	0.0	0.0	0.0
Boron-11	100.0	100.0	0.0	0.0	0.0	0.0	0.0	0.0
Boron-10	1.4	1.4	19.43	21.60	78.95	77.07	8.13E-03	8.59E-03
Chromium	100.0	100.0	0.0	0.0	0.0	0.0	0.0	0.0
Iron	100.0	100.0	0.0	7.01E-04	0.0	0.0	0.0	0.0
Nickel	100.0	100.0	0.11	8.27E-02	2.96E-04	1.31E-04	3.32E-13	2.80E-13
Total	70.4	73.3	5.88	5.88	23.67	20.82	2.44E-03	2.32E-03

Tables 2.15 and 2.16 give the values of helium production for different elements for different neutron energies and their percentage variations in core centre. Here more than 70 % of the helium production is from the neutrons above 1MeV. Except for B-10, percentage helium

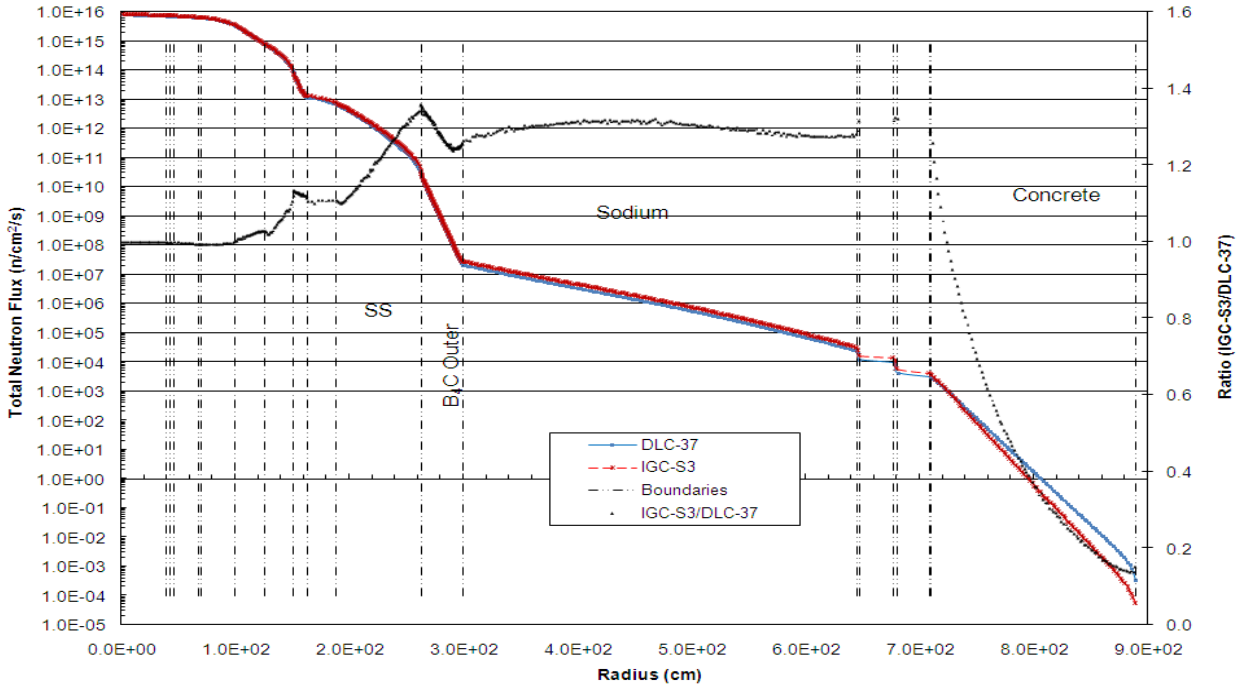

Fig-2.2: Total neutron flux along central radial direction

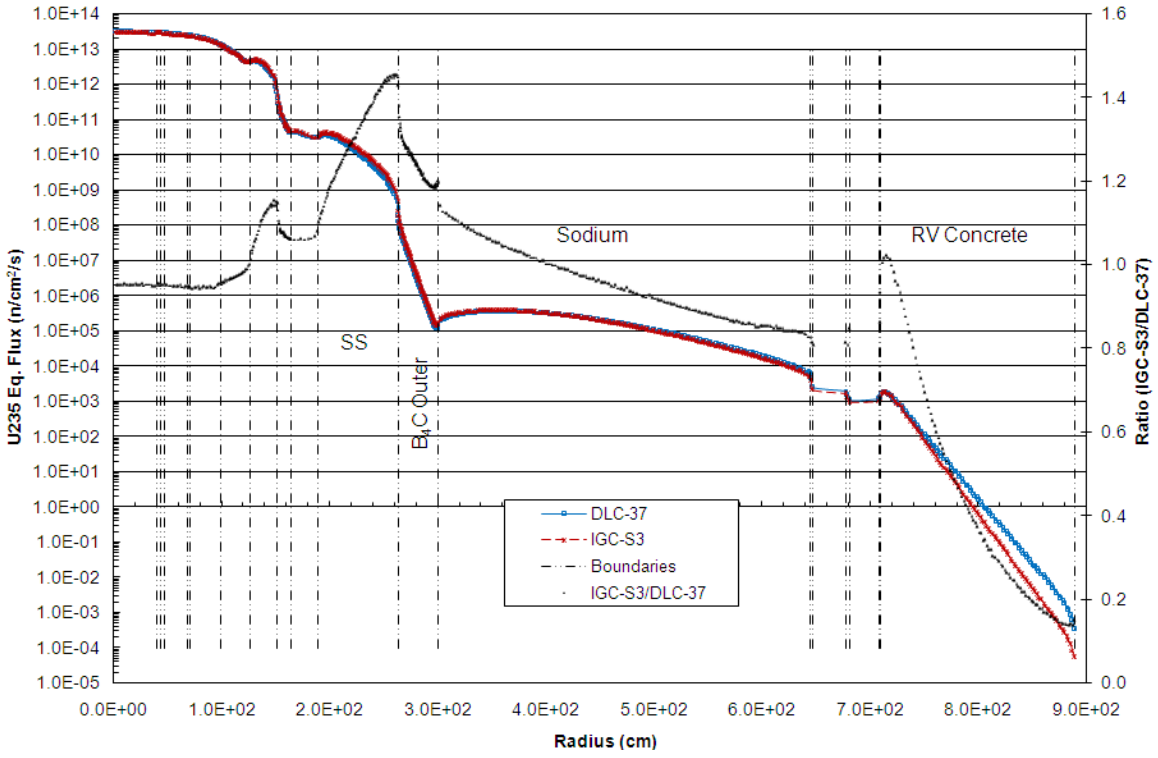

Fig-2.3: U235 equivalent flux along central radial direction

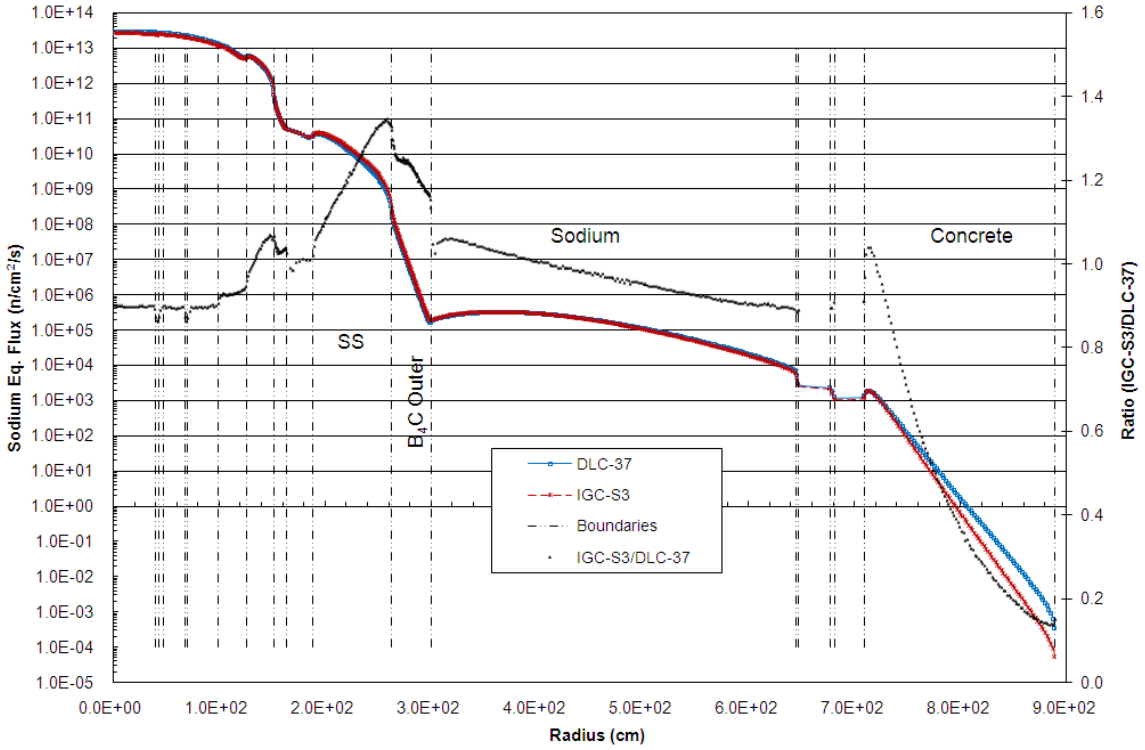

Fig-2.4: Sodium equivalent flux along central radial direction

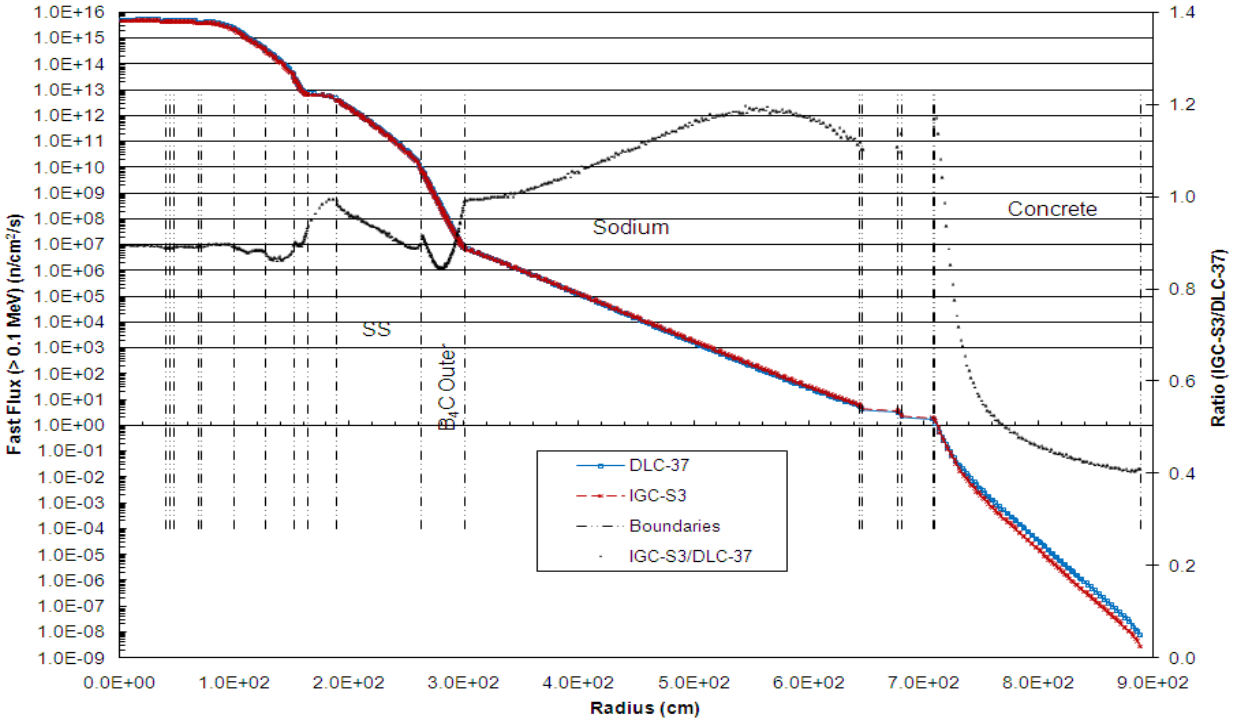

Fig-2.5: Fast flux (> 0.1 MeV) along central radial direction

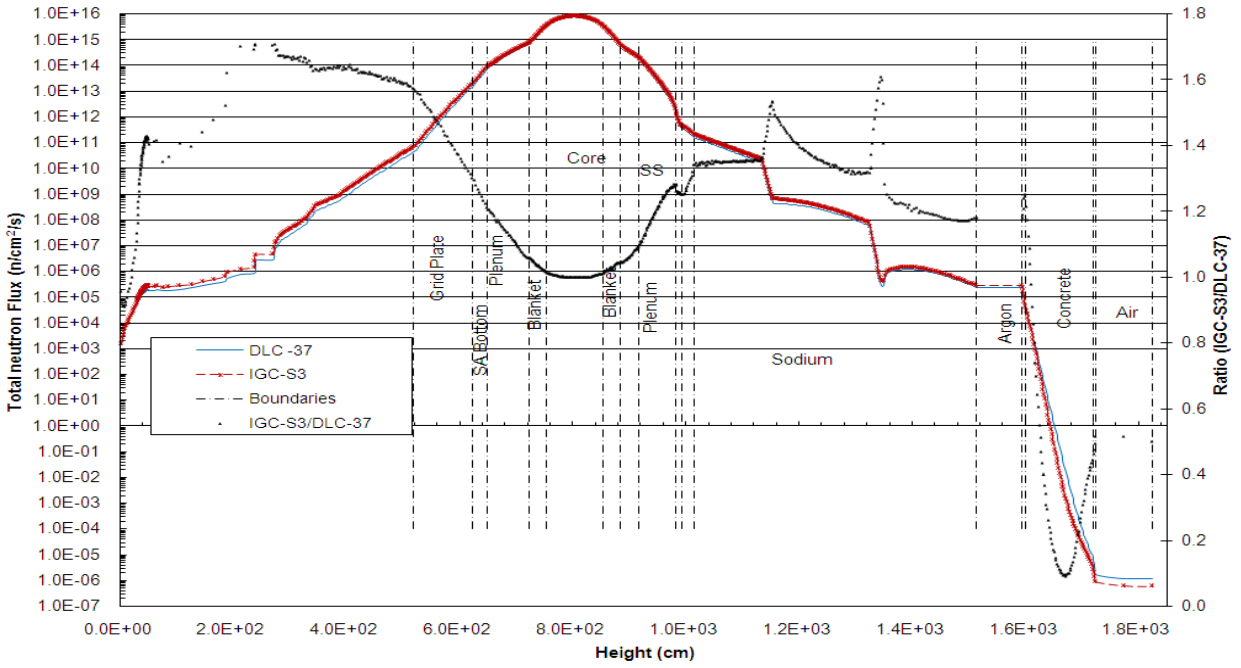

Fig-2.6: Total neutron flux along central axial direction

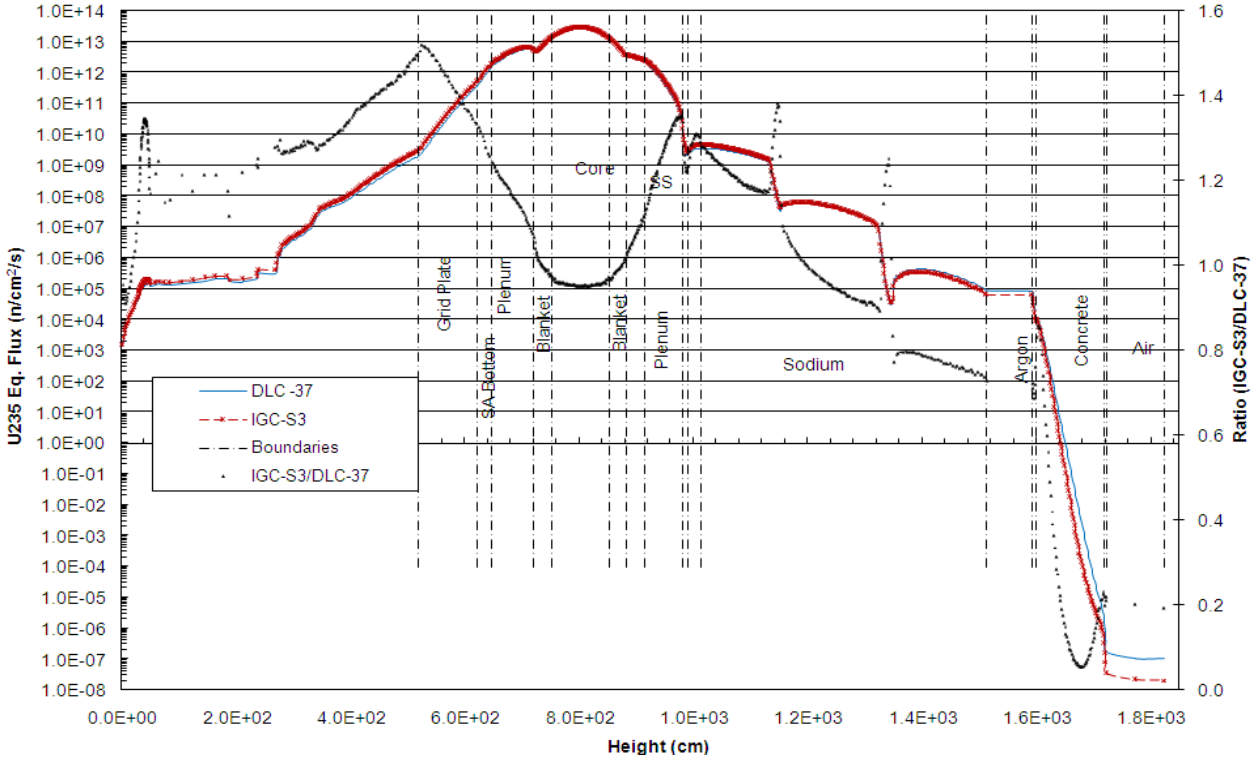

Fig-2.7: U235 equivalent flux along central axial direction

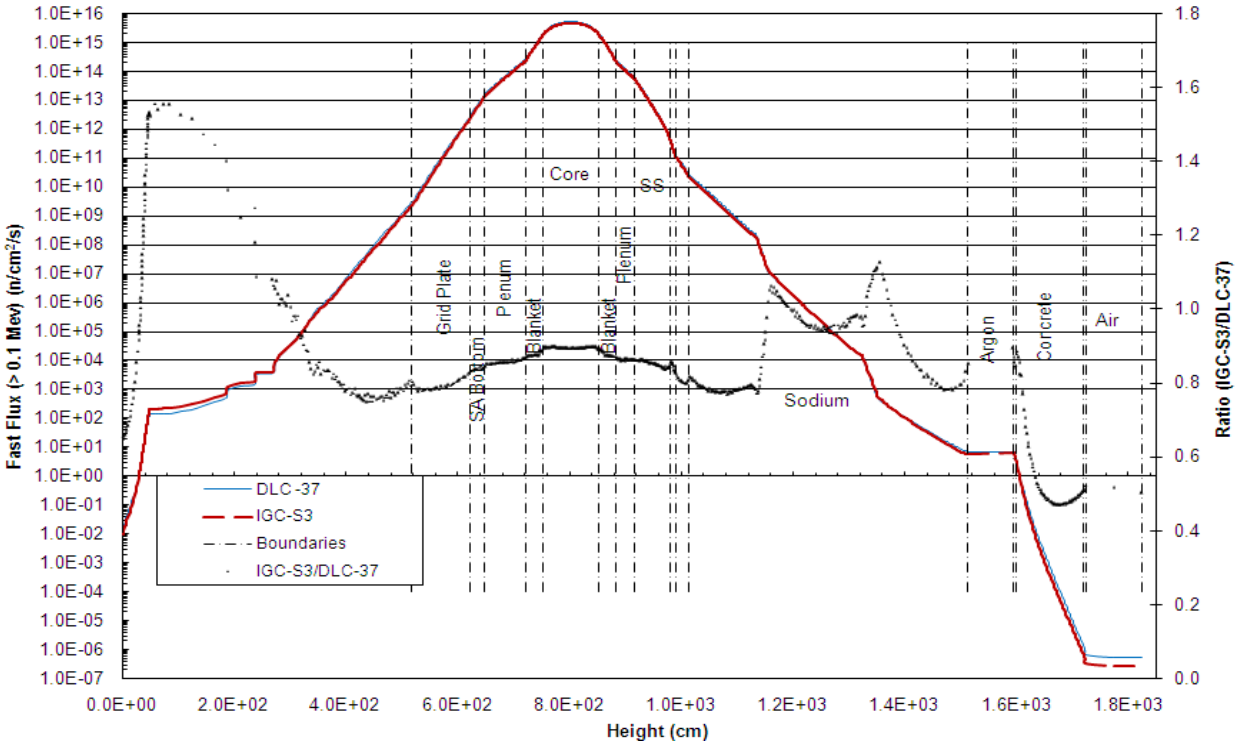

Fig-2.8: Fast flux (> 0.1 MeV) along central radial direction

production for individual elements are nearly 100 % above 1 MeV. For B-10, out of the total B-10 helium production the corresponding contributions above 1MeV, between 1 MeV and 0.1 MeV and between 0.1 MeV and 100 eV are 1.4 %, 20 % and 79 % respectively for IGC-S3. For the energy range less than 100 eV, helium production contribution from any of the elements from the steel are negligible.

DLC-37 is a standard cross section set and was the only one to perform fast reactor shielding calculations in IGCAR till IGC-S series became available. IGC-S3 has 175 neutron energy groups in VITAMIN-J structure which is internationally accepted choice for fast reactor shield calculations. And the neutron group boundaries are 14.9 MeV and 1.0E-4 eV in DLC-37 set whereas IGC-S3 group boundaries are from 19.6 MeV to 1.0E-5 eV. Likewise, the number of gamma energy groups in IGC-S3 is also higher covering 1 keV to 50 MeV as compared to 21

groups covering 10 keV to 14 MeV in DLC set. Therefore IGC-S3 is preferred for subsequent calculations.

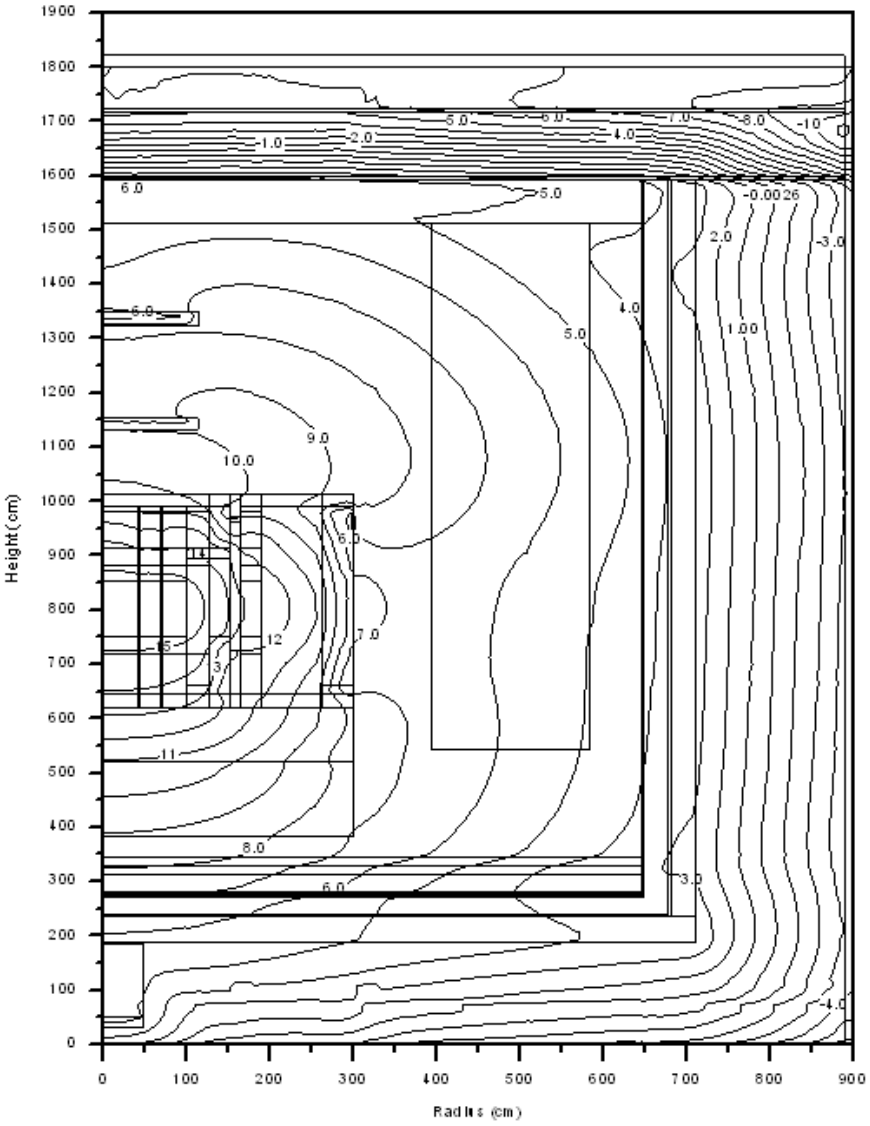

Fig-2.9: Total neutron flux contours

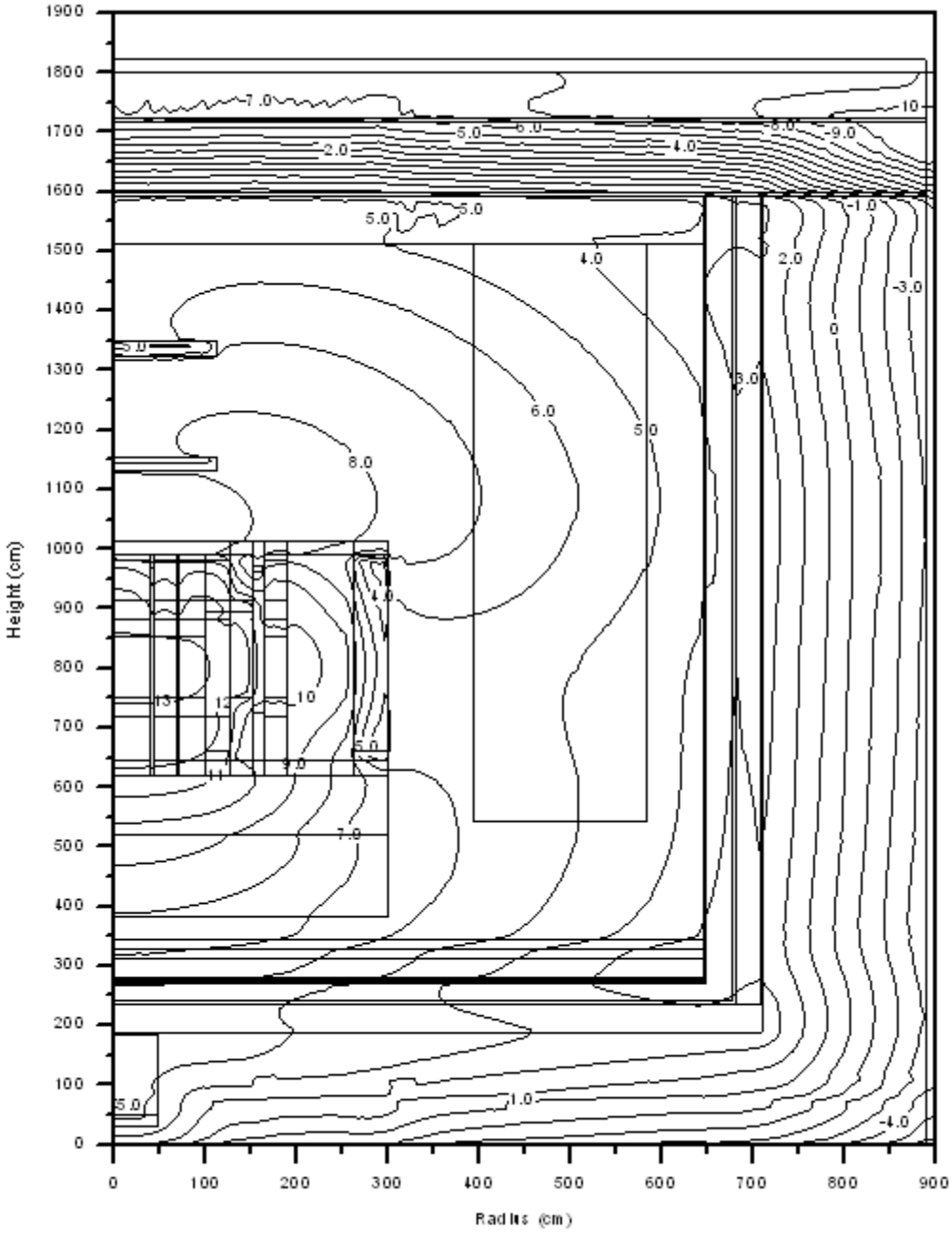

Fig-2.10: Total U235 equivalent flux contours

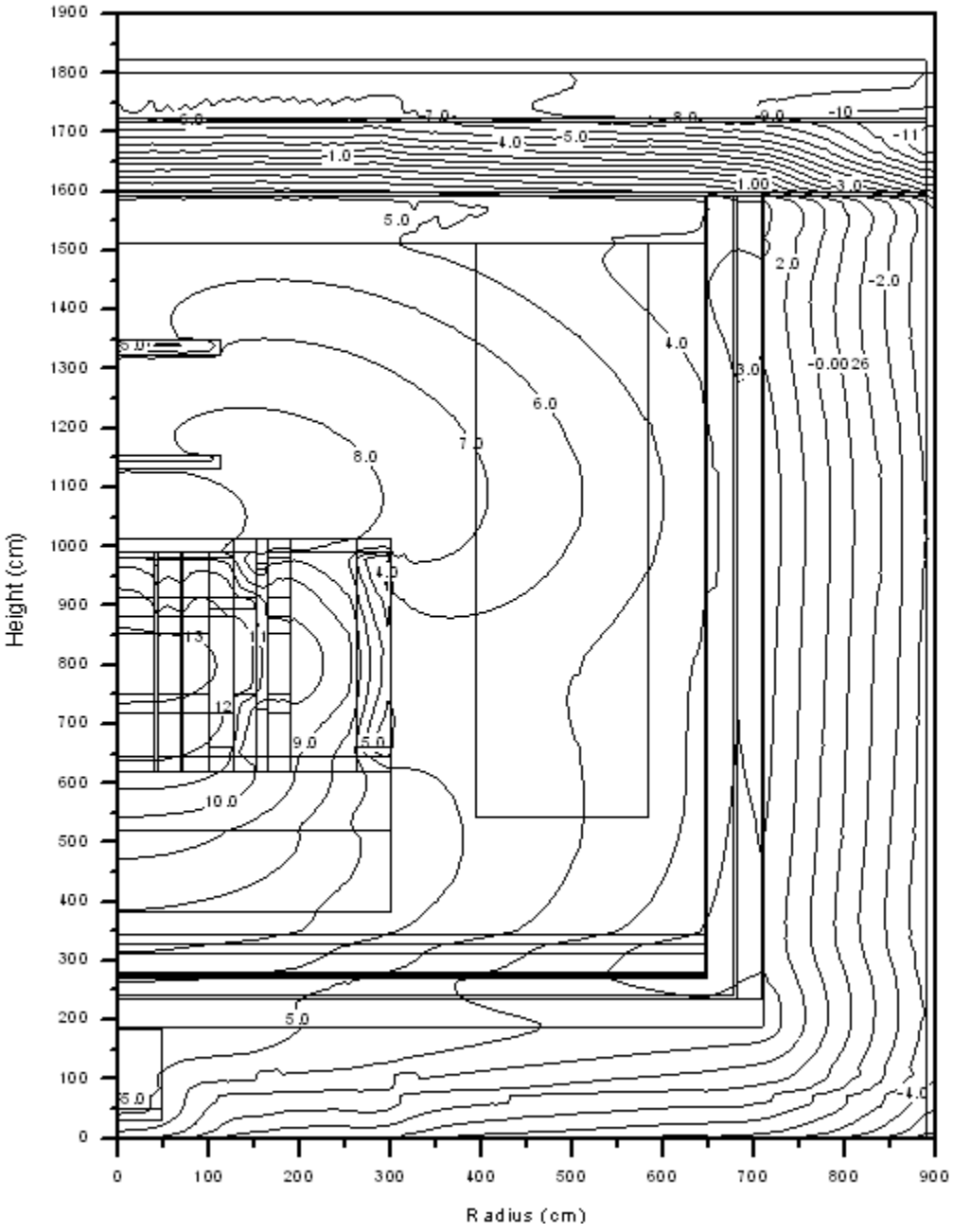

Fig-2.11: Sodium equivalent flux contours

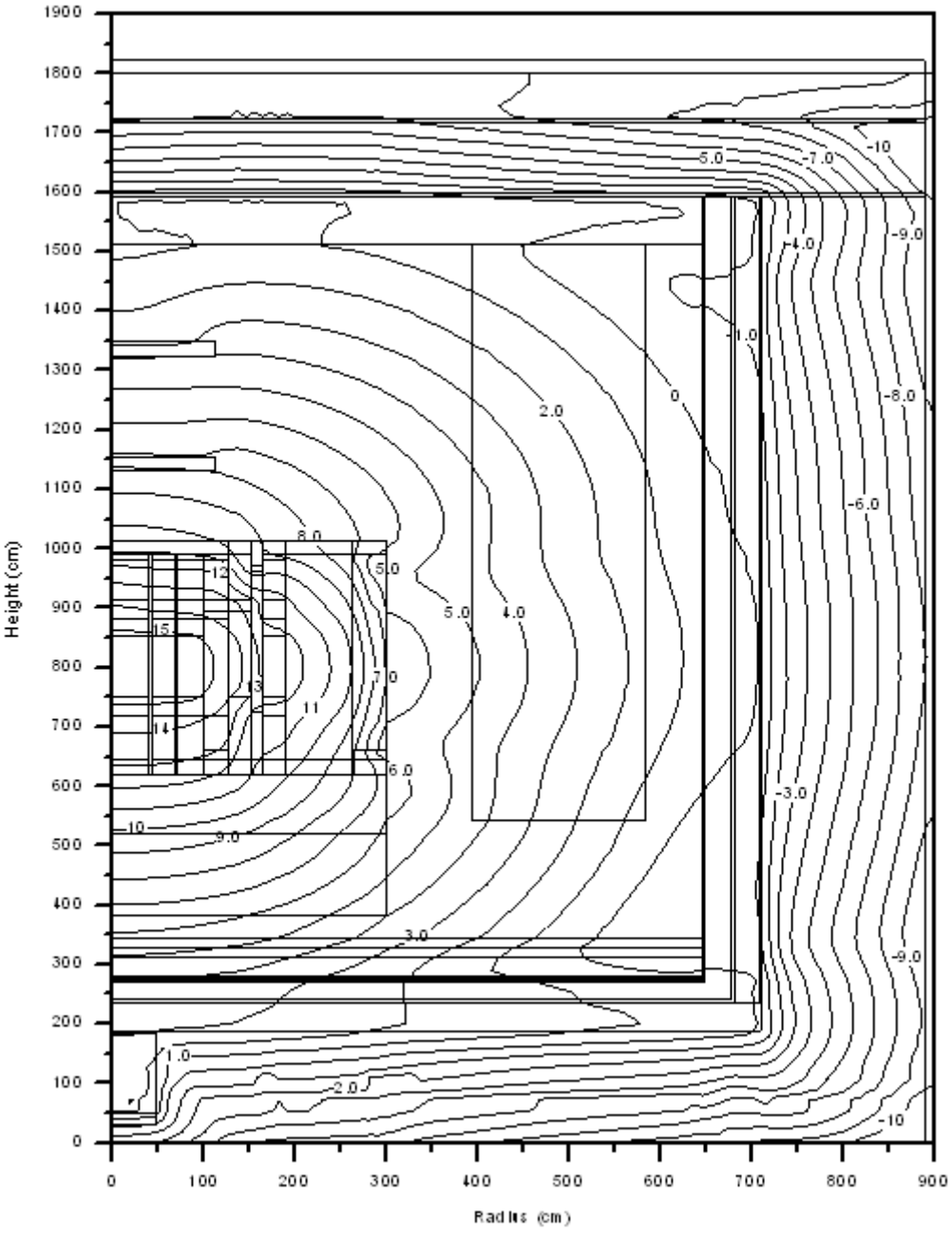

Fig-2.12: Fast flux (> 0.1 MeV) contours

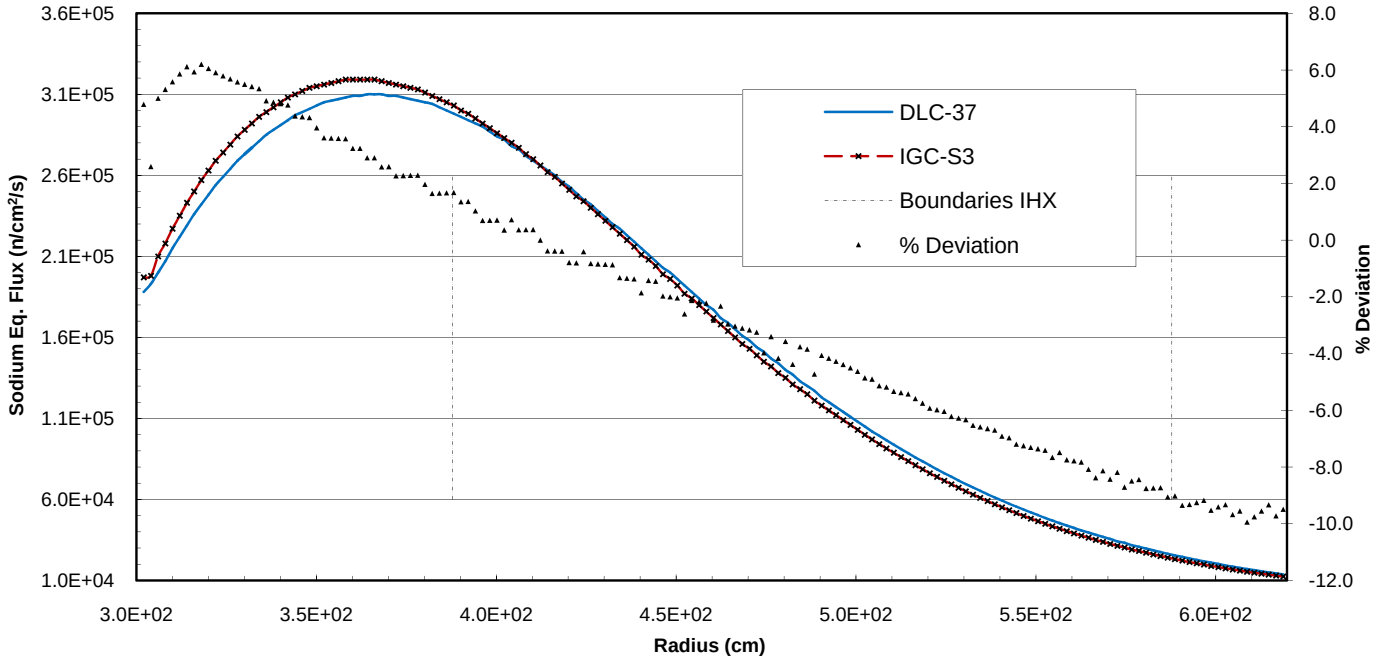

Fig-2.13: Sodium eq. flux in IHX region along central radial direction

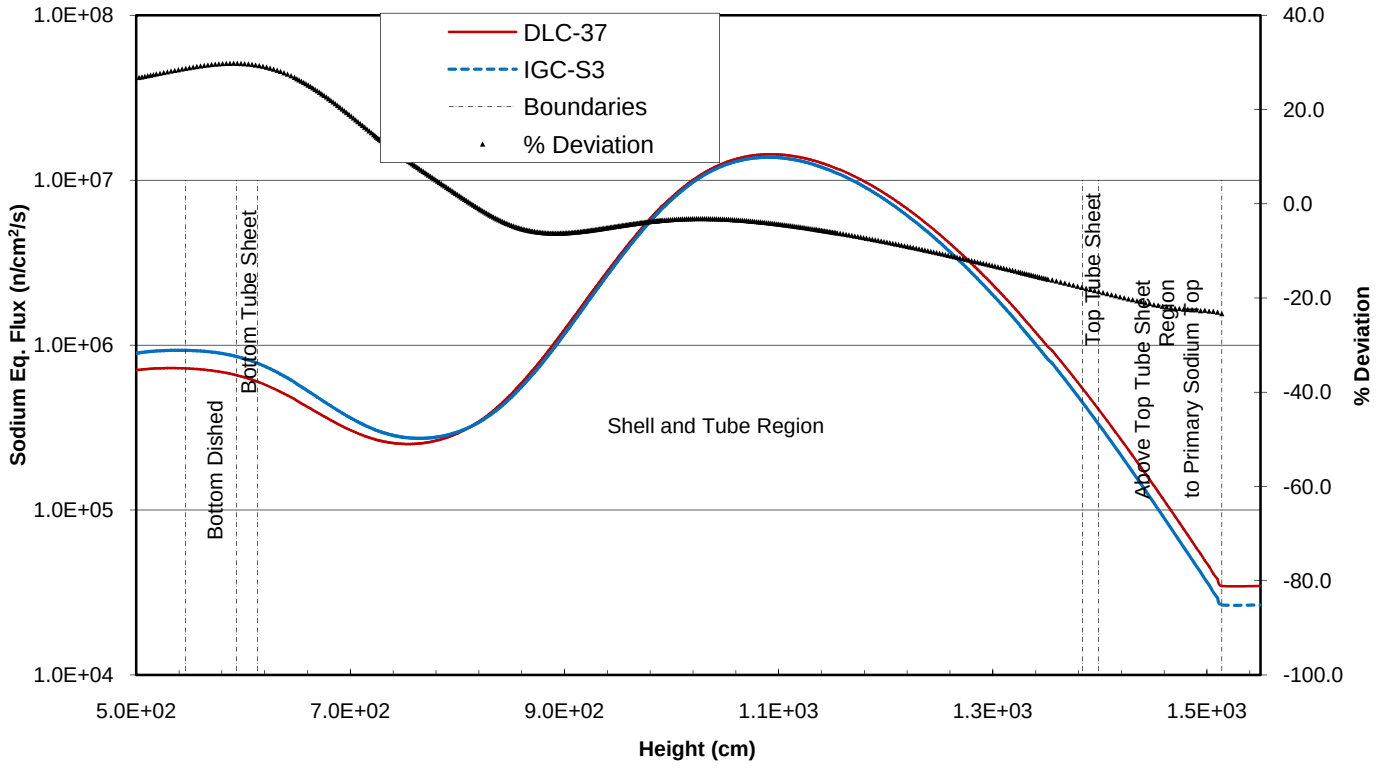

Fig-2.14: Sodium eq. flux (axial) at the left boundary of IHX

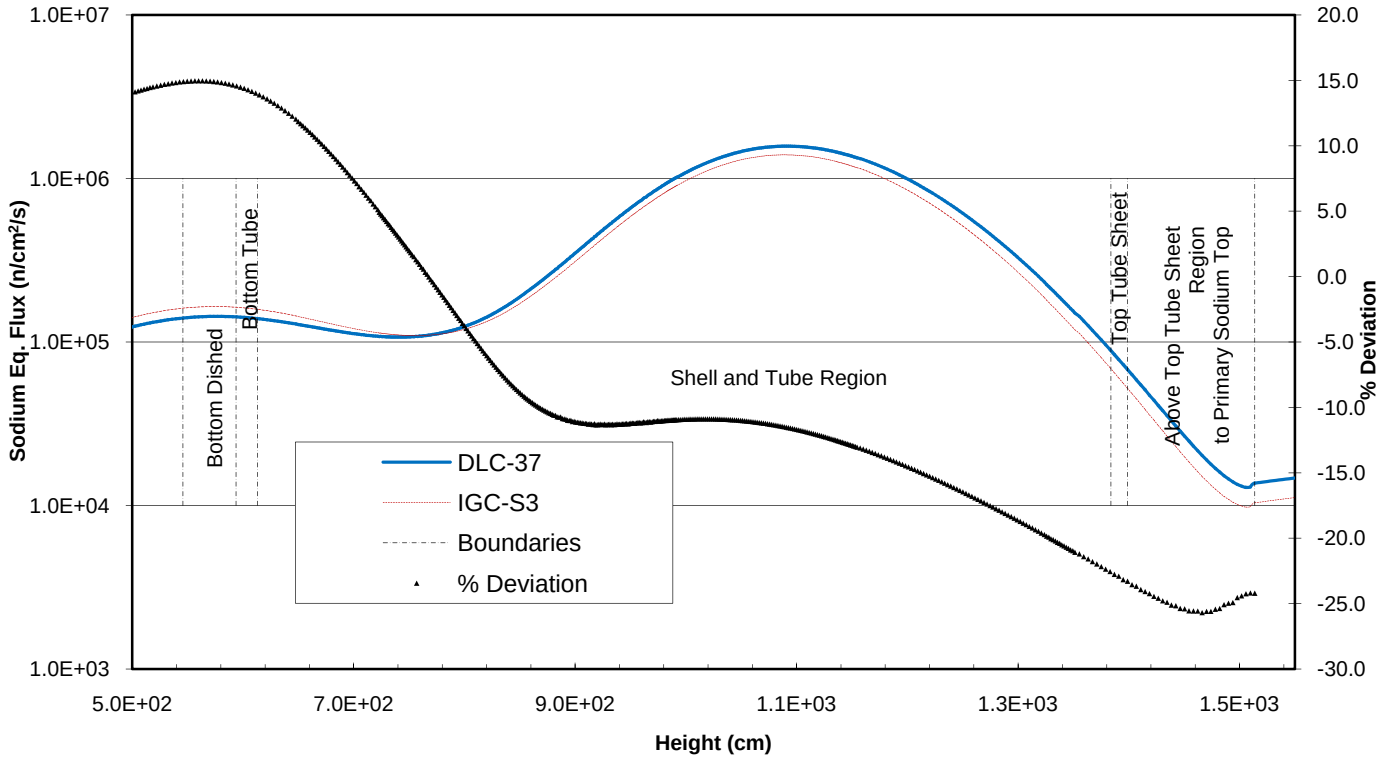

Fig-2.15: Sodium eq. flux (axial) in the centre of IHX

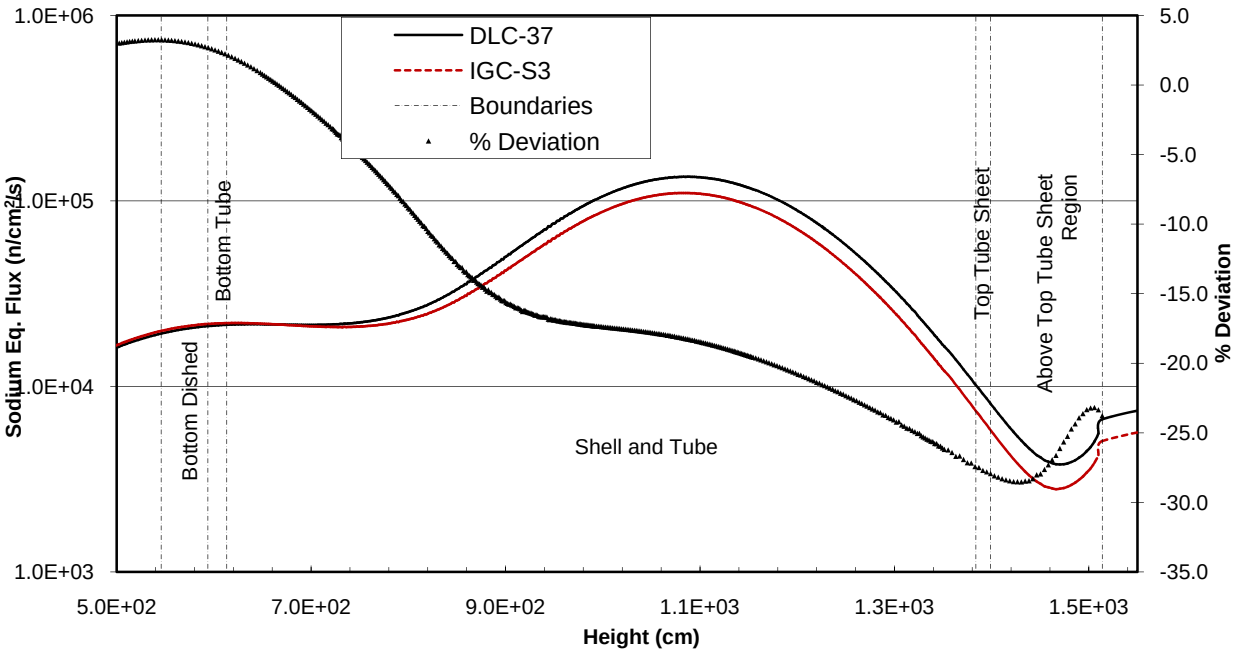

Fig-2.16: Sodium eq. Flux (axial) at the right boundary of IHX

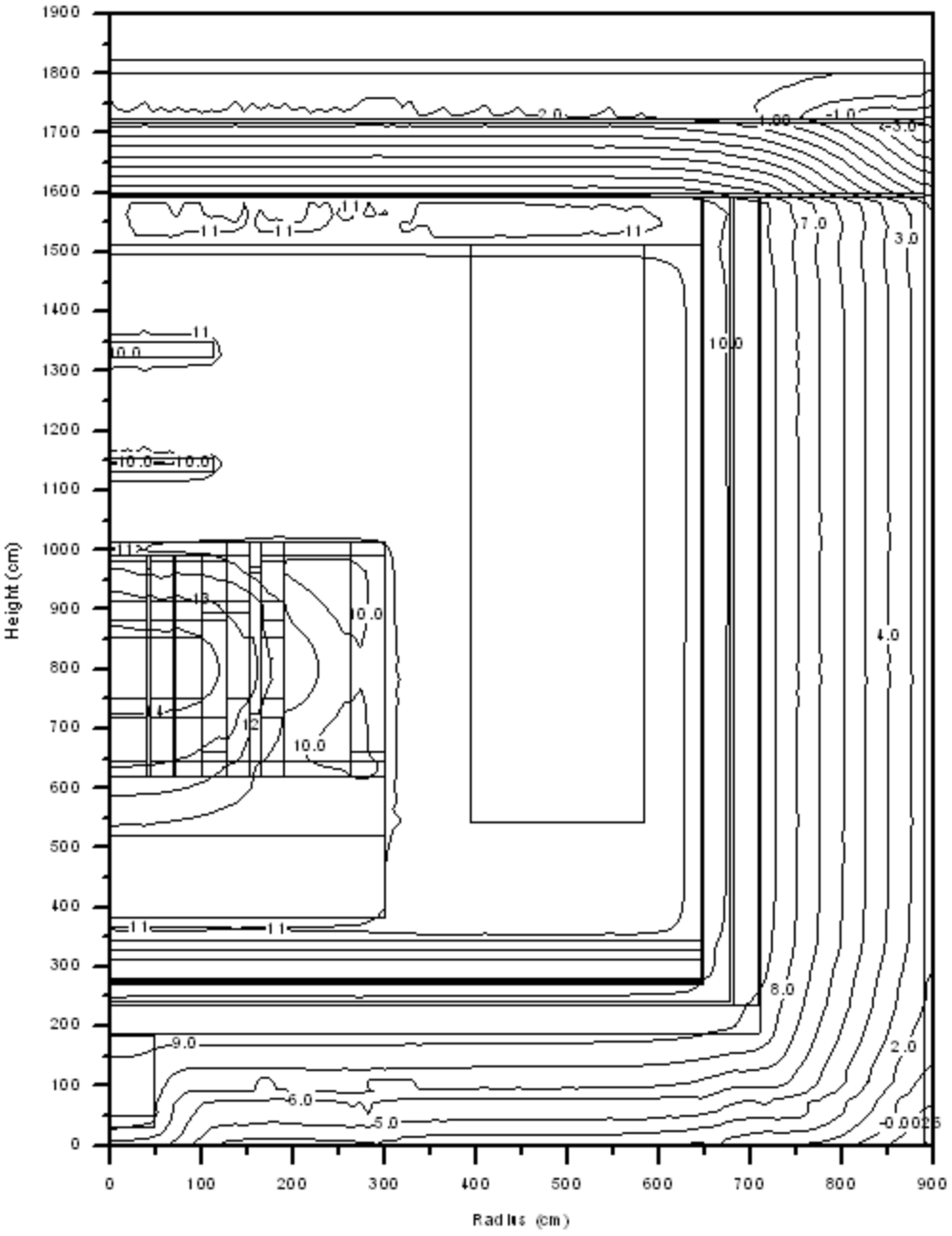

Fig-2.17: Total gamma flux contours

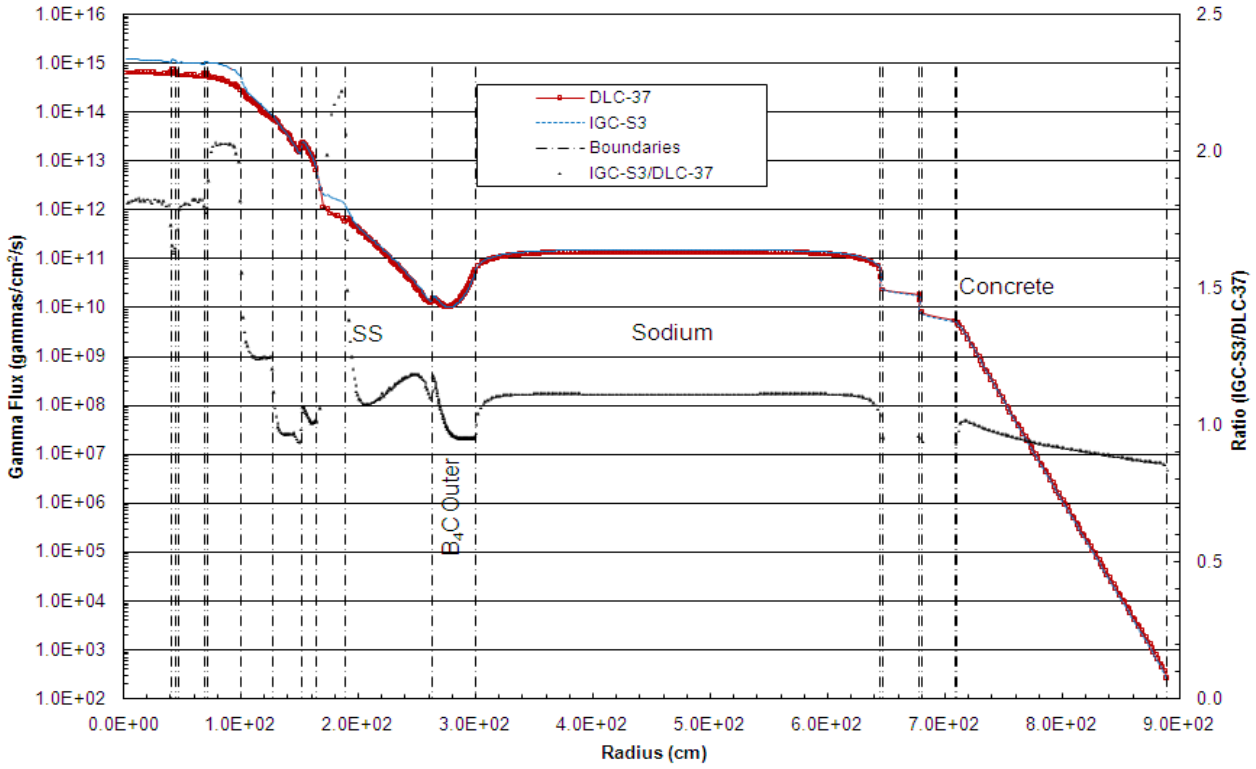

Fig-2.18: Total gamma flux along radial direction

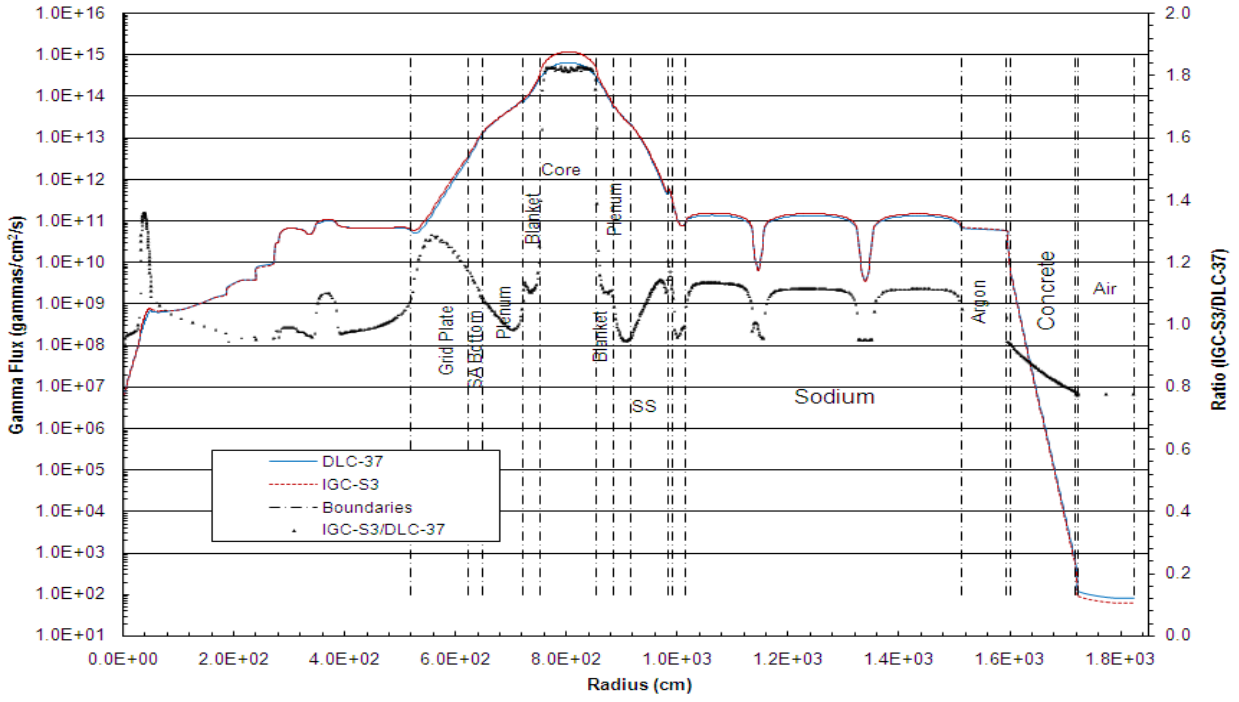

Fig-2.19: Total gamma flux along axial direction

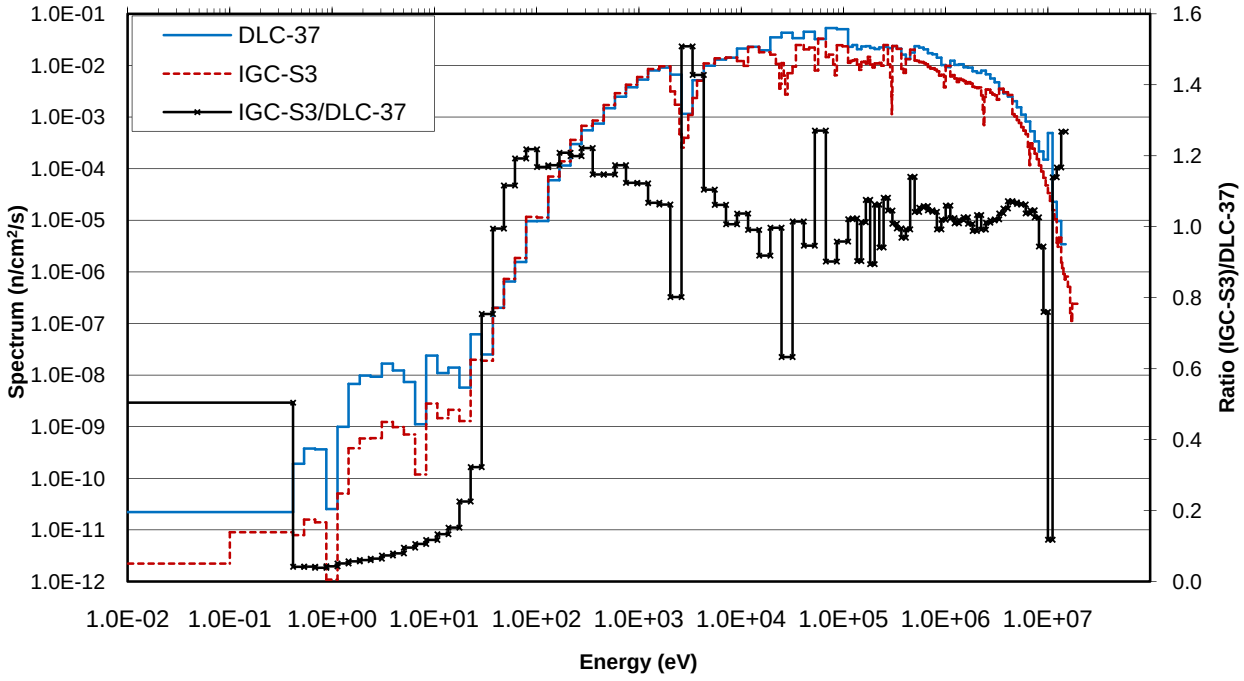

Fig-2.20: 175 and 100 group neutron spectrum in core centre

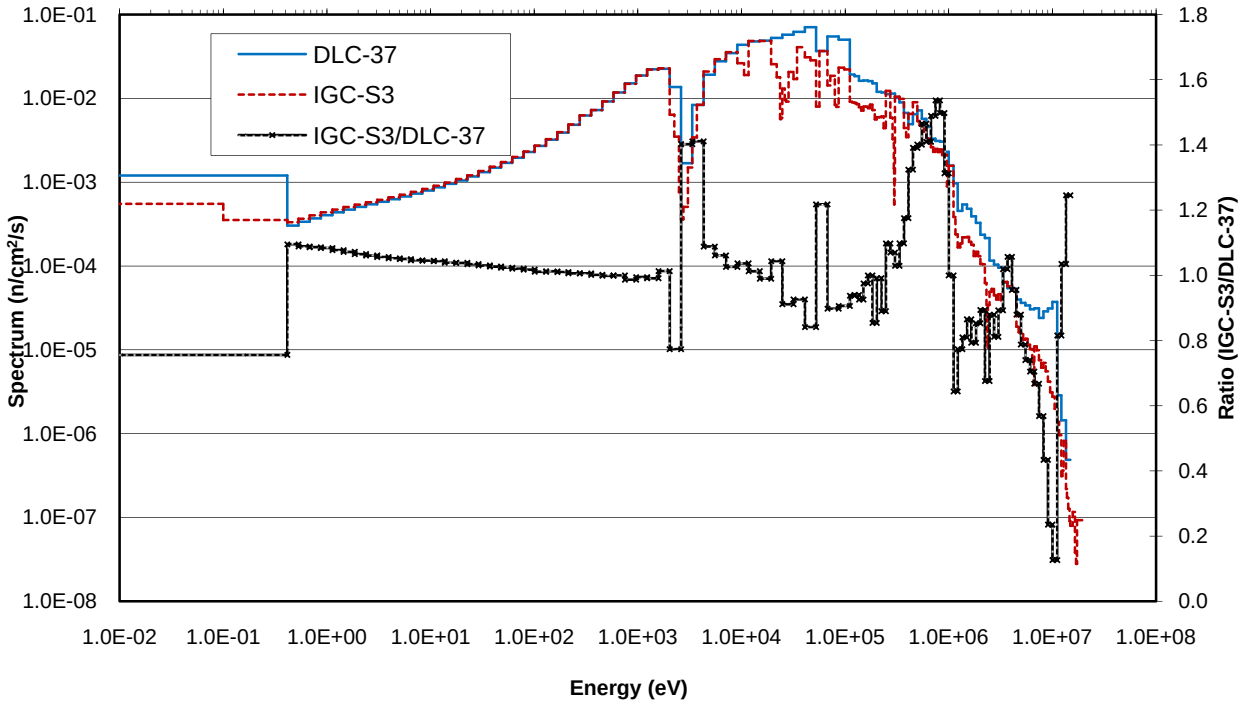

Fig-2.21: 175 and 100 group neutron spectrum at the B_4C exit region

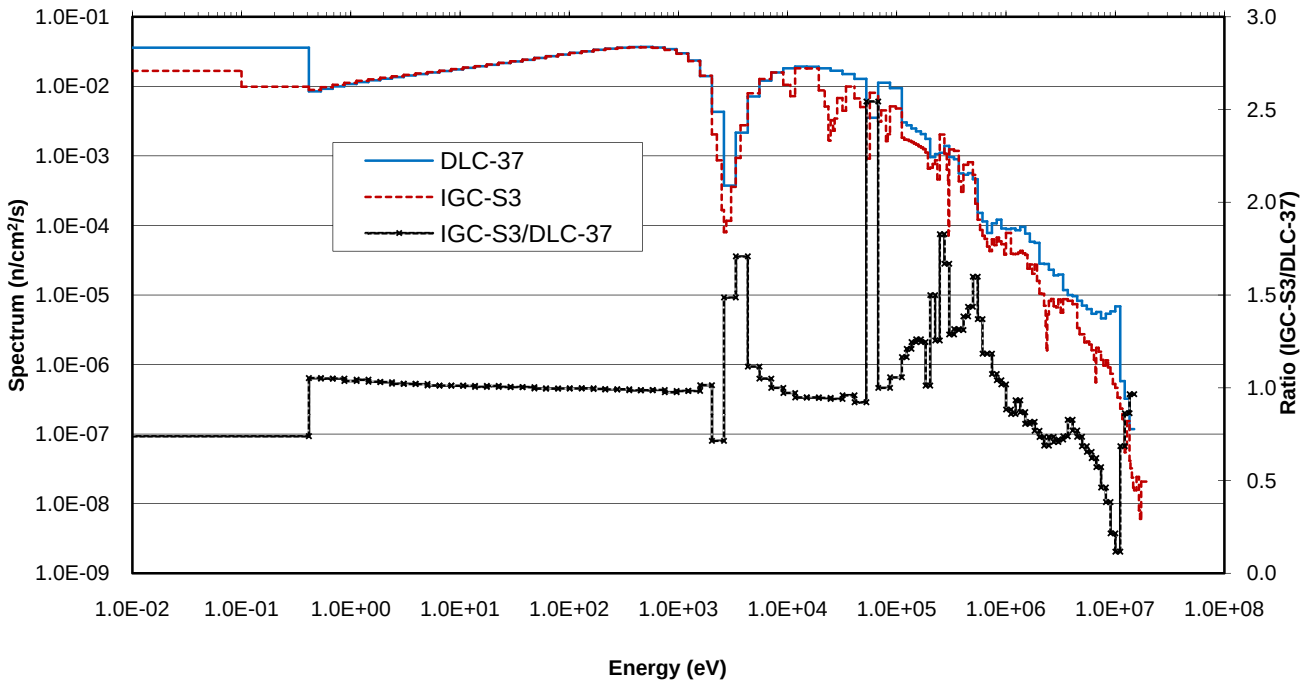

Fig-2.22: 175 and 100 group neutron spectrum at the IHX left location through core centre

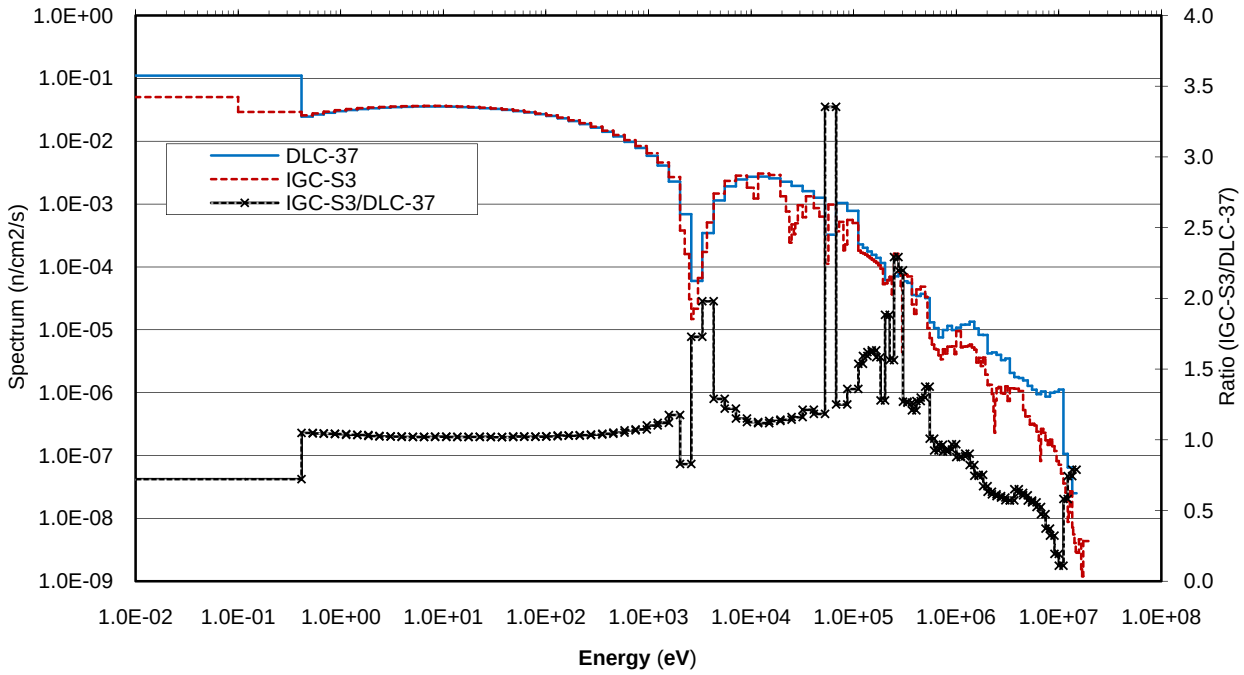

Fig-2.23: 175 and 100 group neutron spectrum at the IHX middle location through core centre

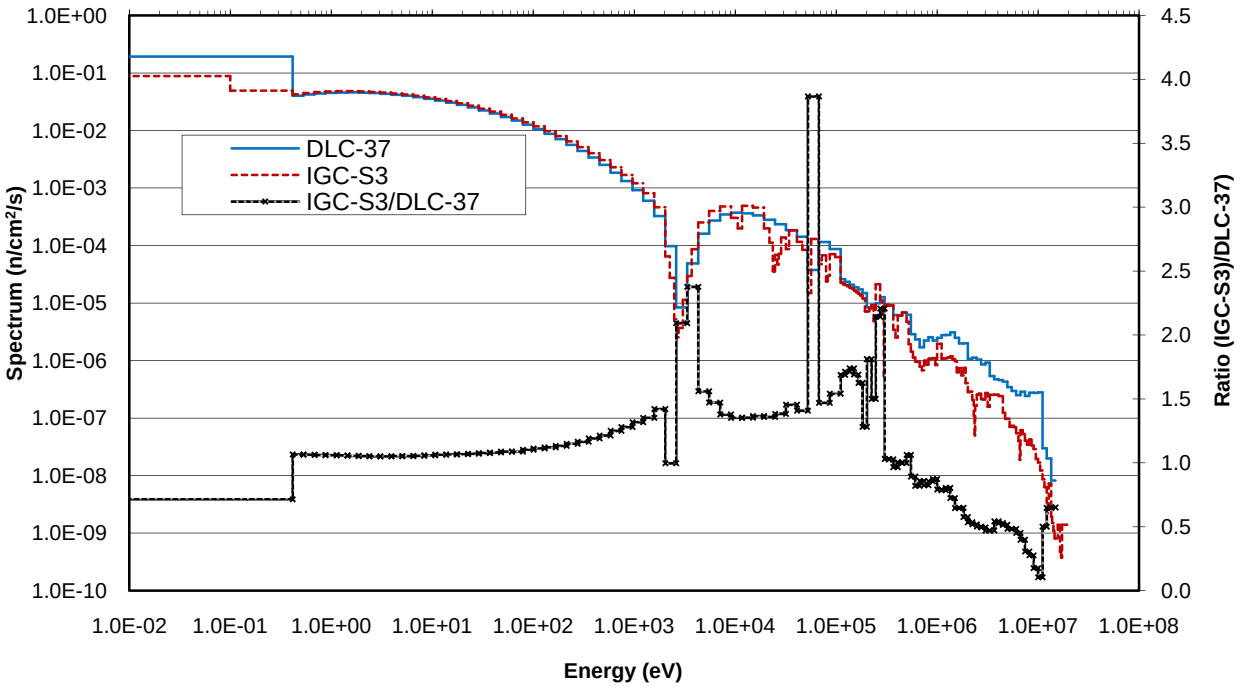

Fig-2.24: 175 and 100 group neutron spectrum at IHX exit location through core centre

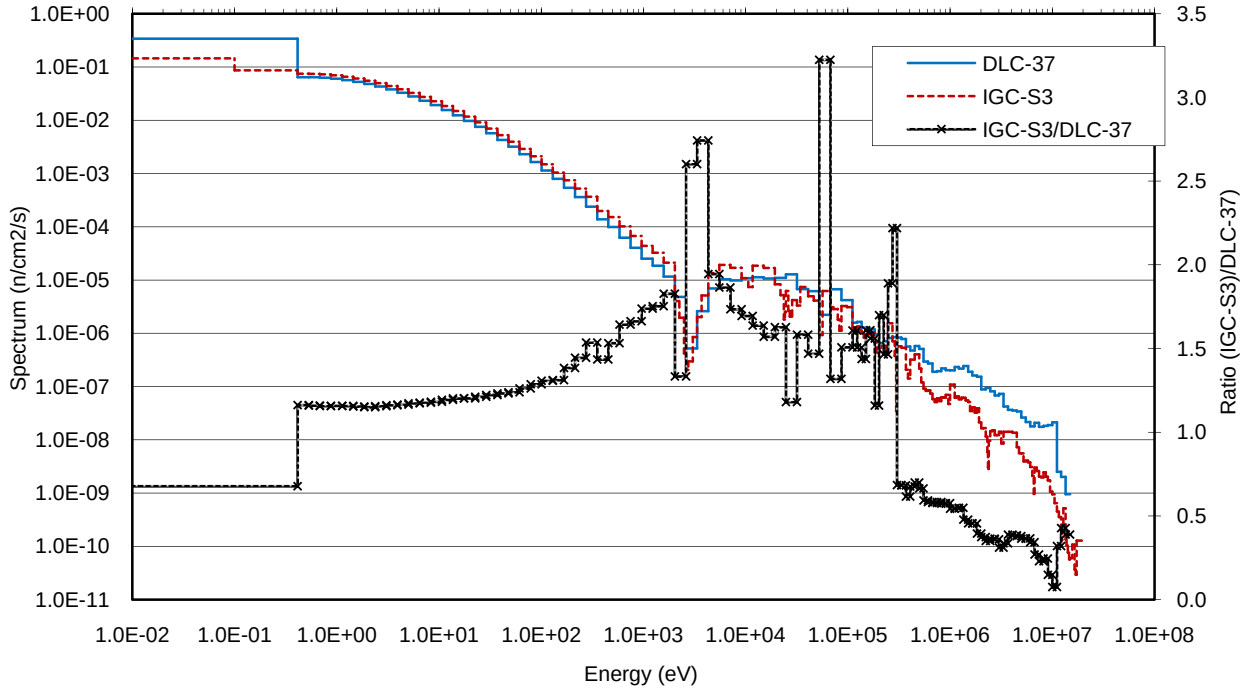

Fig-2.25: 175 and 100 group neutron spectrum at the IHX beginning location along primary sodium top

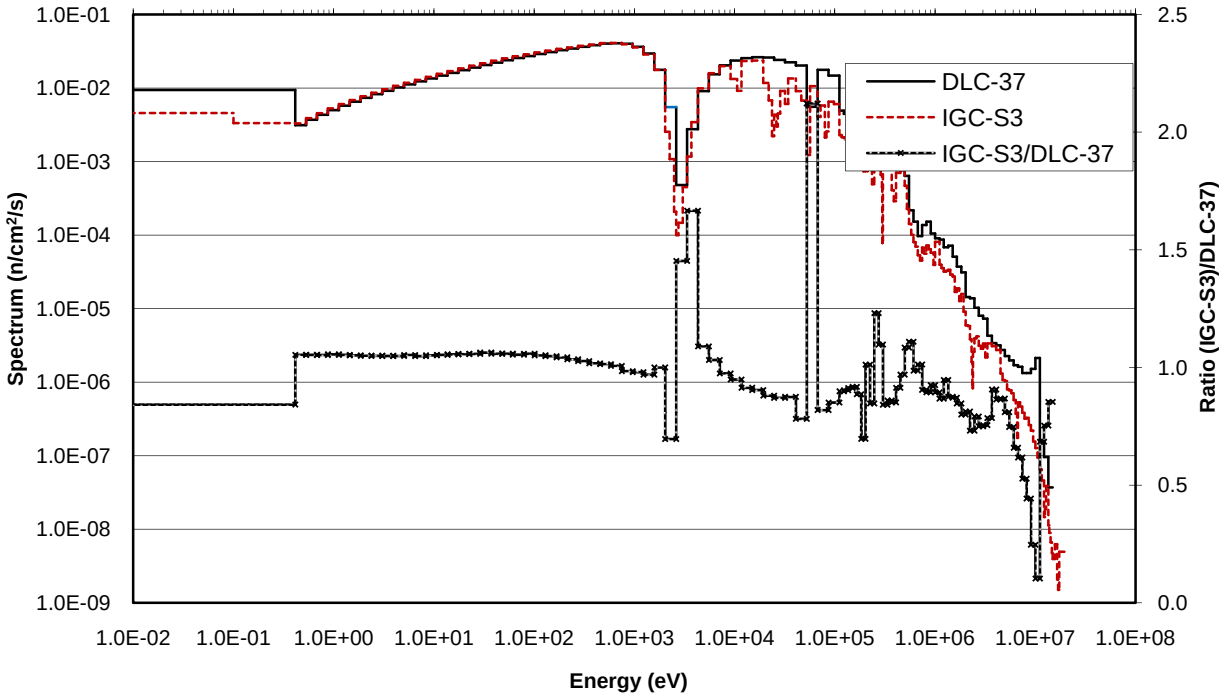

Fig-2.26: 175 and 100 group neutron spectrum at the top detector location

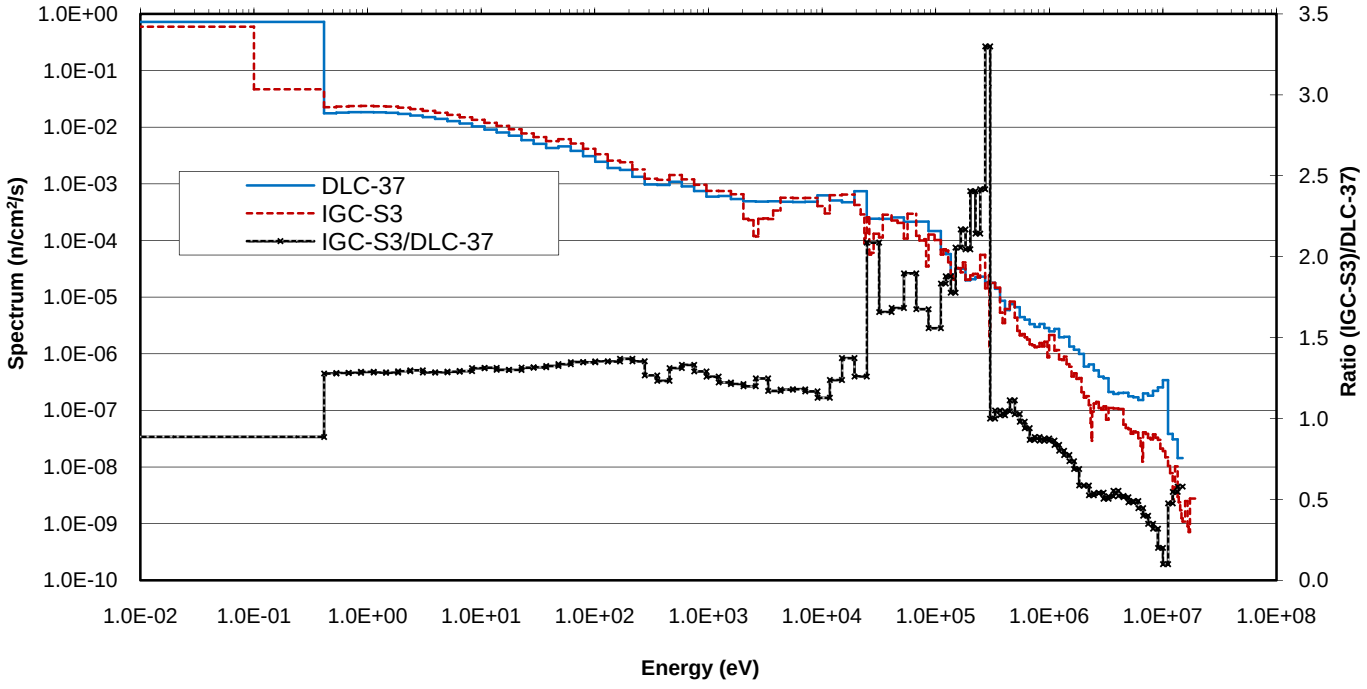

Fig-2.27: 175 and 100 group neutron spectrum at the under vessel detector location

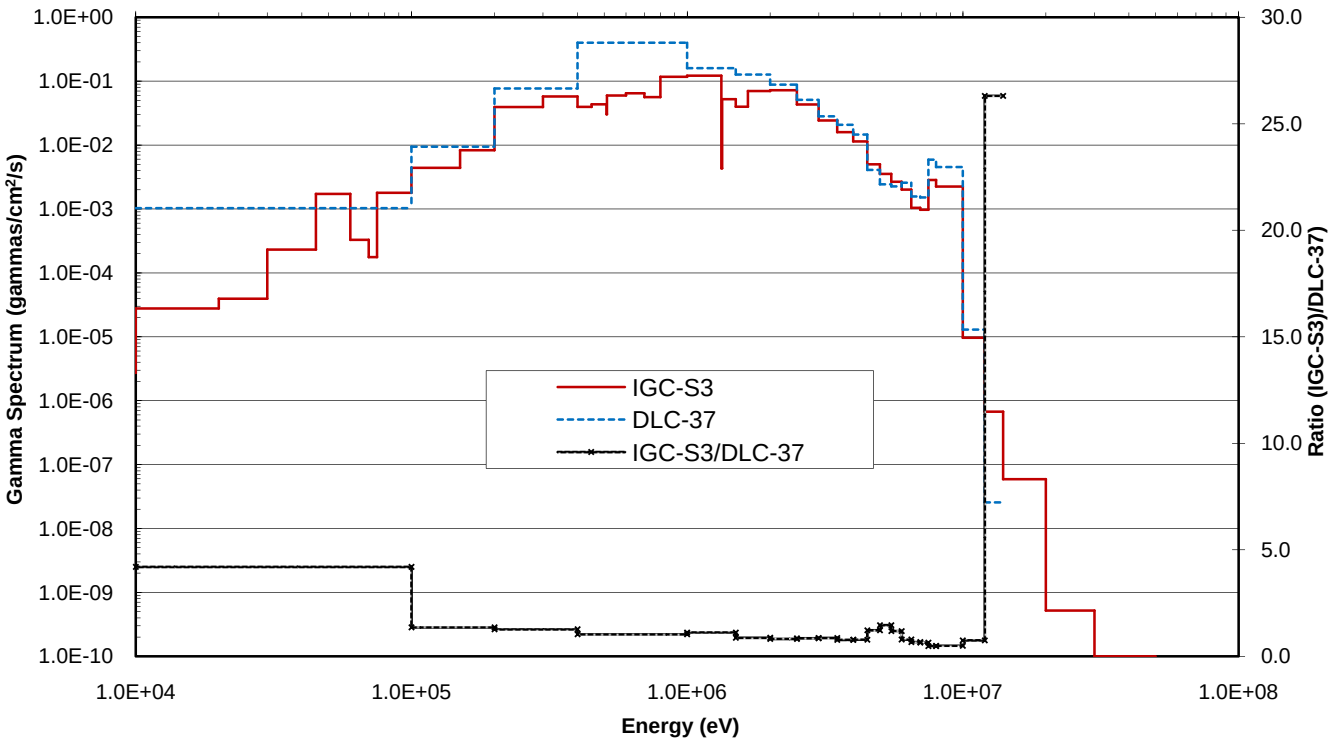

Fig-2.28: Gamma spectrum at core centre

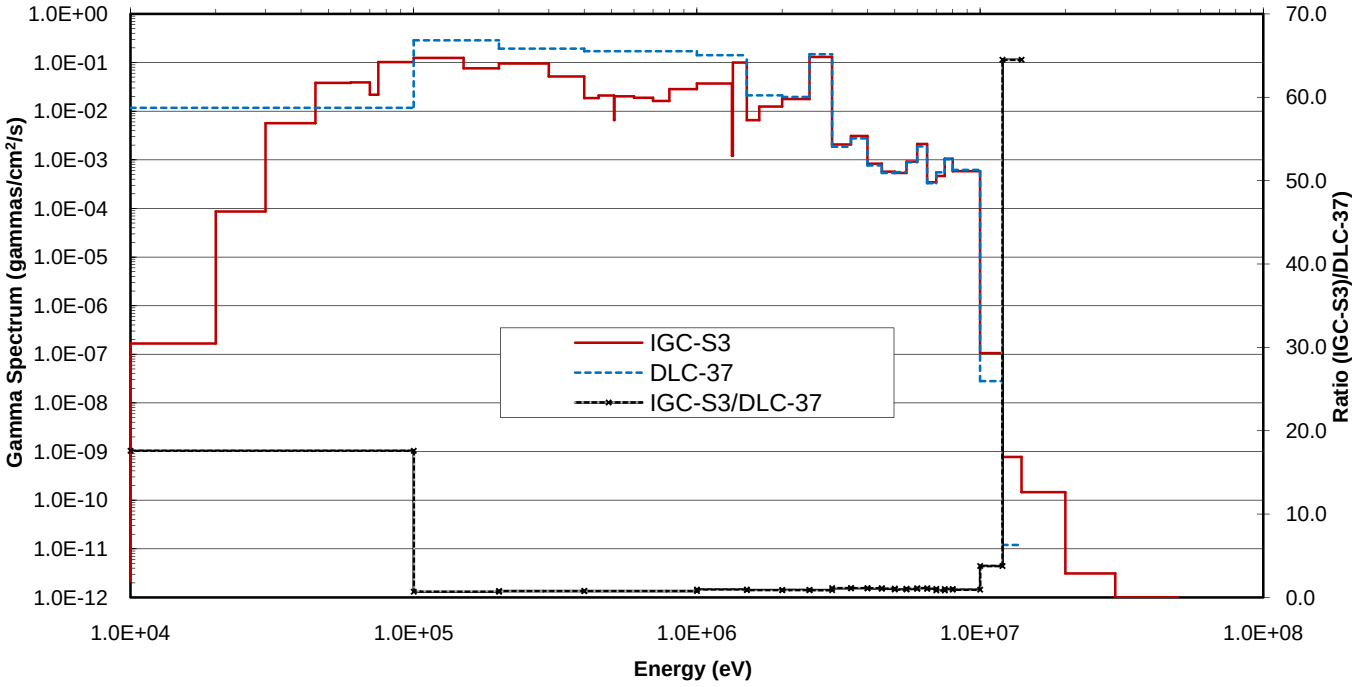

Fig-2.29: Gamma spectrum at top detector position

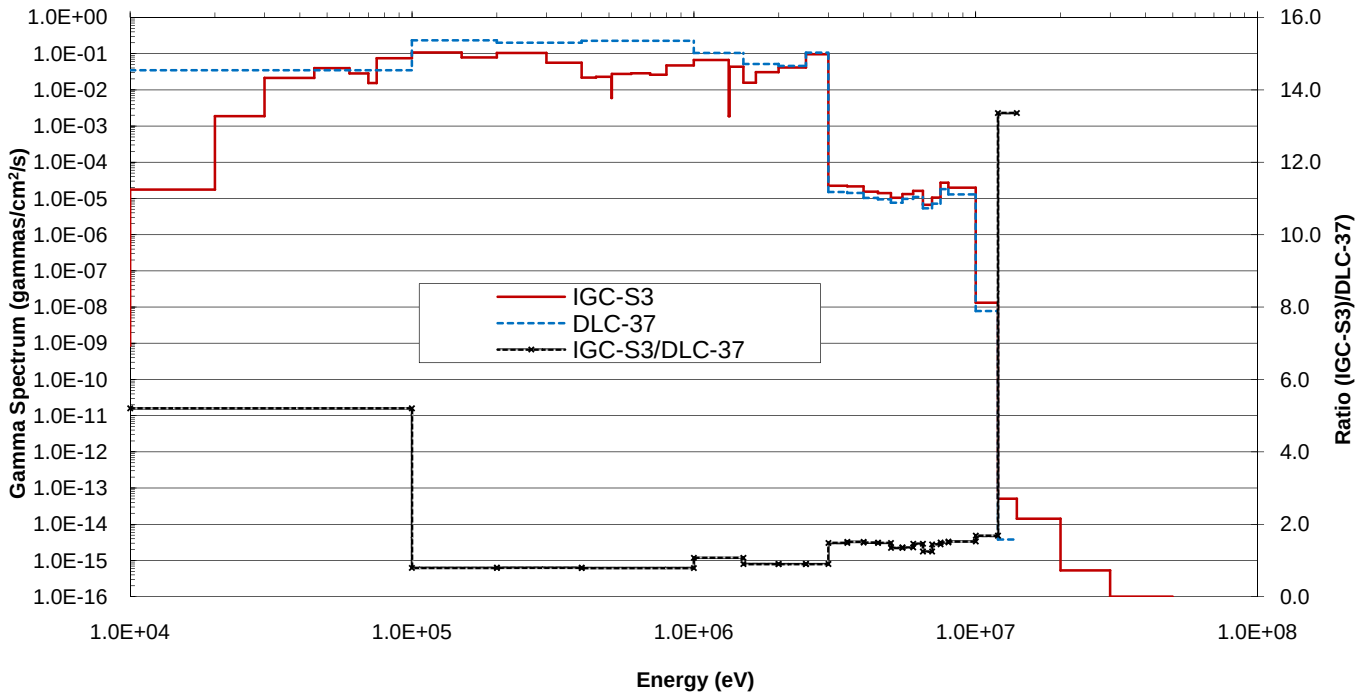

Fig-2.30: Gamma spectrum at bottom detector position

2.5 Computation of Secondary Sodium Activity

Sodium flowing through the secondary loop gets activated by neutron irradiation during its transit in the IHX. The nuclear reaction $Na^{23}(n, \gamma)Na^{24}$ is the dominant one based on activation cross section, half life and threshold energy. This emits two gammas of energy 2.76 and 1.38 MeV with half life 15 h. Secondary sodium is the most important parameter which decides the in-vessel shields like radial and upper axial shields. Accurate estimation of secondary sodium activity is essential to find out the radiation levels and accessibility along the secondary sodium pipelines. Secondary sodium pipe lines with varying pipe diameters pass through the Steam Generator Building (SGB) which mostly contributes to the radiation dose levels in the SGB.

IHX in PFBR is tube and shell type as given in Fig.2.31. The geometry of the IHX cannot be represented exactly in R-Z geometry. For the computation of secondary sodium activity,

cross sectional area of IHX of radius R is divided into many strips by drawing arcs corresponding to the radial mesh widths as shown in Fig. 2.32. The coordinates of the point of intersection of the i^{th} radial mesh circle with the IHX circle is denoted by (x_i, y_i). It is easily seen after some algebra, that the angles θ_i and θ_{i+1} shown in Fig. 2.32 are given by

$$\theta_i = \cos^{-1}(\frac{x_i}{r_i}) = \cos^{-1}(\frac{r_i^2 - R^2 + D^2}{2Dr_i})$$

$$\theta_{i+1} = \cos^{-1}(\frac{x_{i+1}}{r_{i+1}}) = \cos^{-1}(\frac{r_{i+1}^2 - R^2 + D^2}{2Dr_{i+1}}) \qquad (2.1)$$

The volume element corresponding to full circle in R-Z geometry is $\pi(r_{i+1}^2 - r_i^2)(z_{j+1} - z_j)$. A good approximation to the total capture reaction rate in secondary sodium passing through IHX is given by

$$R = \sum_i \sum_j \sum_{k=1}^{175} \Sigma(k)\ \varphi(i,j,k) F_{SS}(i,j)(2\theta_{i+1/2}/2\pi)\pi(r_{i+1}^2 - r_i^2)h_j \qquad (2.2)$$

where $\Sigma(k)$ is the macroscopic cross section for the reaction ^{23}Na(n, γ)^{24}Na, $\varphi(i,j,k)$ is the k^{th} energy group neutron flux at mesh (i, j) and F_{SS}(i, j) is the secondary sodium volume fraction in the mesh (i, j). Summation over radial mesh i and axial j mesh is for the entire region of IHX where secondary sodium is present. The distance D between the core centre and centre of IHX is 488 cm. The angle $\theta_{i+1/2}$ is the average angle given by

$$\theta_{i+1/2} = (\theta_i + \theta_{i+1})/2 \qquad (2.3)$$

The secondary sodium activity is computed using (2.2).

Secondary sodium is circulated through IHX with a circuit time t_C of 68.5 s and irradiation time (over one circuit) t_i of 7.2 s in the reactor considered. Thus the secondary sodium activity per cm^3 of sodium is calculated using the standard formula

$$SSA/cm^3 = R\frac{(1-e^{(-\lambda t_I)})}{(1-e^{(-\lambda t_C)})} \qquad (2.4)$$

2.5.1 Dose on pipes in SGB

The steam generator building will have controlled access and the design dose rate criteria for accessibility is 10 μSv/h in the general areas and 25 μSv/h at 1m distance from the surface of the secondary sodium pipelines (Indira, 2001).

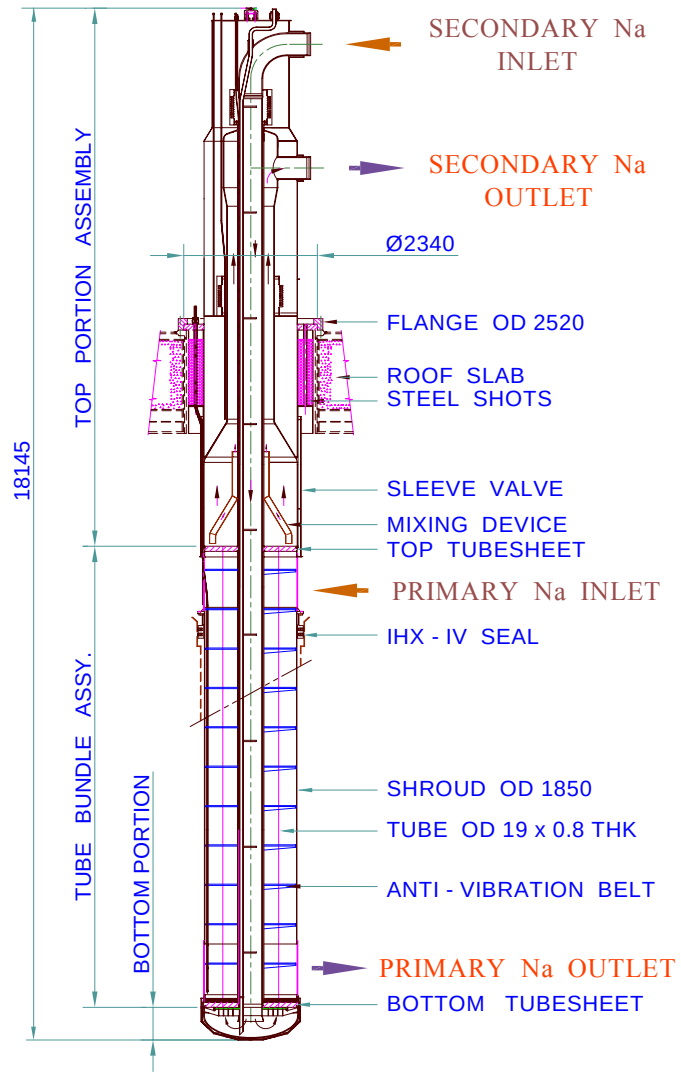

Fig-2.31: Intermediate heat exchanger

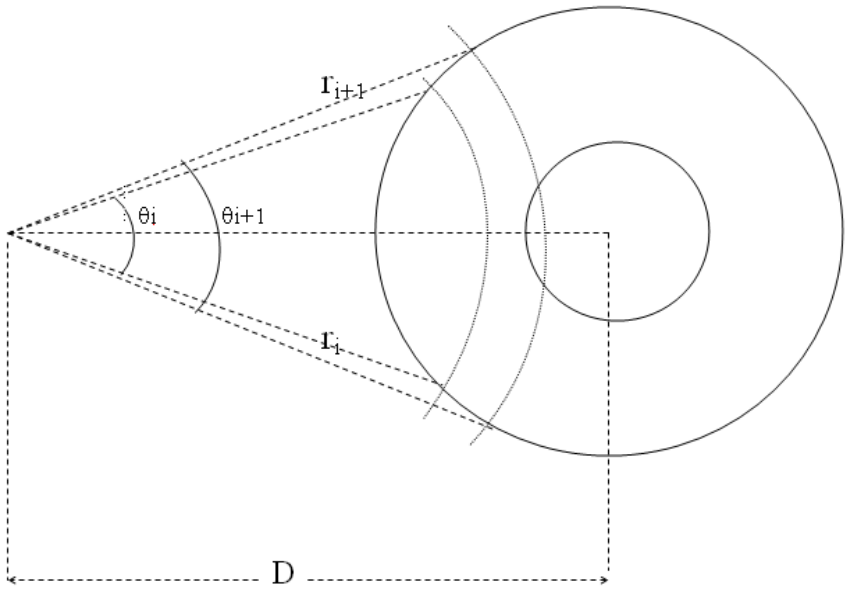

Fig-2.32: Geometry of IHX (not to scale)

Table 2.17 gives secondary sodium activity computed using IGC-S3 and DLC-37 cross section sets.

Table - 2.17: Secondary Sodium Activity (Bq/cm^3) computed with IGC-S3 and DLC-37

Energy Range	IGC-S3	DLC-37	Dose Rate (μSv/h) in Steam Generator Building	
			IGC-S3	DLC-37
Below 0.4 eV	3.89E+02	4.90E+02	17.0	17.7
0.4 eV to 1eV	1.28E+02	9.29E+01		
1eV to 10 eV	1.27E+02	9.27E+01		
10 eV to 0.1MeV	2.45E+01	1.79E+01		
0.1 MeV to 1 MeV	5.44E-03	3.43E-03		
Above 1MeV	2.75E-05	2.99E-05		
Total	6.68E+02	6.94E+02		

2.6 Summary

Methodology of computation is presented in this chapter. Boltzman Transport Equation and current methods adopted for solving the equation are briefly explained. Nuclear data used in

the calculations are presented. The reference case is fully described. The rationale for using the 2-D deterministic code is given. The problem is solved using the 2D code DORT in RZ geometry model of PFBR. All the relevant neutron and gamma fluxes are generated using both DLC-37 and IGC-S3 cross section sets. DLC-37 is a standard cross section set and was the only one to perform fast reactor shielding calculations in IGCAR till IGC-S series became available. IGC-S3 has 175 neutron energy groups in VITAMIN-J structure which is internationally accepted choice for fast reactor shield calculations. It is found the results qualitatively agree well. Hence the future calculations will be carried out with IGC-S3 which has higher number of energy groups in its structure. Because of non compatibility of IHX geometry with RZ calculation geometry of the code, a new method for accurate estimation of secondary sodium activity is developed and thereby the dose rate in the steam generator building computed. All the parameters obtained will serve as reference values in studies presented in the next chapters.

Chapter – 3

SCOPING STUDIES FOR NEW ALTERNATIVE SHIELD MATERIALS

3.1 Introduction

Scoping studies are required to identify prospective shield materials that could be effective with respect to cost and volume reduction. From the preliminary literature survey, the basic shield materials identified for scoping studies are SS, B_4C, Ferro-Boron (Fe-B), Borated Steel, tungsten carbide, gadolinium, gadolinium oxide, calcium boride, gadolinium boride, silicon boride, iron boride, aluminium boride and zirconium boride. Transport calculations using 2-dimensional transport code DORT (Rhoads and Childs, 1988) are carried out for the core and blanket surrounded by the candidate shield material in the radial direction. In this scoping study, single material is assumed in all the shield rows. The reference case is the PFBR shield configuration described in the previous chapter. The 1D- model for radial shield used for PFBR is given in Fig. 2.1.

3.2 Scoping Studies

As described in the previous chapter the PFBR has six rows of SS and 3 rows of B_4C outer shields. The calculations are done by replacing SS and B_4C in the outer shield regions of PFBR with different shield materials by using the same volume fractions. Calculations are performed with DORT code and IGC-S3 cross section set. Total neutron flux and sodium equivalent fluxes are calculated at different points in the different shield regions and the values are given Table 3.1 and 3.2. Since secondary sodium activity is a very important parameter for in-vessel shield design, comparison of fluxes are done in the IHX location also.

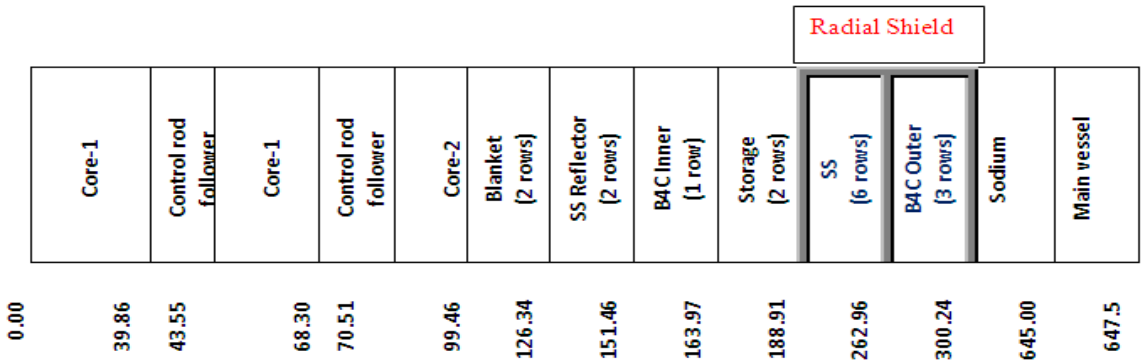

Fig-3.1: Radial Model of PFBR

3.3 Comparison between Different Shield Materials

The calculations show that a) all borides are as effective or even more effective than the reference case. Their efficacy essentially depends on the boron atom density. b) Many of the absorbers like Gadolinium are not as effective for fast neutrons as the reference shield combination. This is clearly due to low absorption cross sections for fast neutrons and c) tungsten and tantalum are found to be very effective than the reference case. The other factors to be considered are availability and cost as compared to the reference case. The cost is very high in the case of tungsten and tantalum compounds. In the case of borides of Al, Gd, Si, Zr and Ca, availability itself is in doubt though many of them show good prospects.

Table - 3.1: Performance of different shield materials with respect to total flux (n/cm^2/s) and sodium capture rate (/cm^3/s) at IHX location. PFBR is taken as reference case

	Neutron Flux	Location				Ratio w.r.t. reference case at IHX location
		SS Beginning	B_4C Outer	IHX-Beginning		
PFBR (B_4C- 2.2 g/cc)	Tot Flx	7.49E+12	2.24E+07	1.68E+06		1.00
	Sod. C Rate	1.43E+10	7.05E+04	1.19E+04		1.00
SS (7.76 g/cc)	Tot Flx	7.50E+12	2.32E+09	1.49E+08		89.56
	Sod. C Rate	1.44E+10	1.94E+07	2.58E+06		220.74
Fe-B (3.8 g/cc)	Tot Flx	4.63E+12	6.11E+07	4.88E+06		2.90
	Sod. C Rate	6.94E+09	1.45E+05	3.17E+04		2.66
Ferro-Tungsten (6.51 g/cc)	Tot Flx	6.18E+12	5.66E+09	3.82E+08		226.93
	Sod. C Rate	1.03E+10	2.11E+07	3.32E+06		278.46
Borated Steel (1.2 % Boron)	Tot Flx	6.56E+12	8.41E+08	5.72E+07		34.02
	Sod. C Rate	1.15E+10	3.54E+06	5.30E+05		44.53
Tungsten Carbide (15.63 g/cc)	Tot Flx	6.02E+12	2.94E+04	1.79E+03		1.07E-03
	Sod. C Rate	1.09E+10	1.68E+02	1.64E+01		1.38E-03
Tungsten (18.5 g/cc)	Tot Flx	6.11E+12	2.47E+06	1.57E+05		9.33E-02
	Sod. C Rate	9.15E+09	7.62E+03	1.43E+03		1.20E-01
Silicon Boride (2.47 g/cc)	Tot Flx	4.05E+12	1.63E+06	1.58E+05		9.40E-02
	Sod. C Rate	5.90E+09	2.47E+03	7.38E+02		6.20E-02

Table - 3.2: Performance of different shield materials with respect to total flux (n/cm^2/s) and sodium capture rate (/cm^3/s) at IHX location.

	Neutron Flux	Location				Ratio w.r.t. reference case at IHX location
		SS Beginning	B_4C Outer	IHX-Beginning		
Zirconium Boride (3.6 g/cc)	Tot Flx	4.75E+12	7.43E+07	6.17E+06		3.67
	Sod. C Rate	6.94E+09	1.51E+05	3.65E+04		3.06
Calcium Boride (2.45 g/cc)	Tot Flx	3.98E+12	2.80E+06	2.58E+05		0.15
	Sod. C Rate	5.58E+09	4.08E+03	1.30E+03		0.11
Aluminium Boride (1.9 g/cc)	Tot Flx	4.36E+12	5.12E+07	4.38E+06		2.60
	Sod. CRate	6.26E+09	9.83E+04	2.51E+04		2.11
Gadolinium (4.74 g/cc)	Tot Flx	4.96E+12	3.13E+08	2.45E+07		14.53
	Sod. C Rate	6.47E+09	5.00E+05	1.74E+05		14.60
Gadolinium Oxide (7.407 g/cc)	Tot Flx	5.29E+12	6.64E+08	4.65E+07		27.62
	Sod. C Rate	7.90E+09	1.99E+06	3.71E+05		31.14
Gadolinium Boride (5.31 g/cc)	Tot Flx	4.12E+12	2.21E+07	1.95E+06		1.16
	Sod. C Rate	5.71E+09	3.39E+04	1.07E+04		0.90
Tantalum (16.69 g/cc)	Tot Flx	6.11E+12	2.47E+06	1.57E+05		9.33E-02
	Sod. C Rate	9.15E+09	7.62E+03	1.43E+03		1.20E-01
B_4C (2.4 g/cc)	Tot Flx	4.06E+12	3.56E+06	3.40E+05		0.20
	Sod. C Rate	5.93E+09	5.52E+03	1.62E+03		0.14

3.4 Neutron Flux Spectra

The neutron flux spectra at various location of PFBR is given in Fig 2.2. The comparisons of neutron spectra with different shield materials at the exit of shield region are given in the figures (Fig. 3.2a. to Fig. 3.2i.).

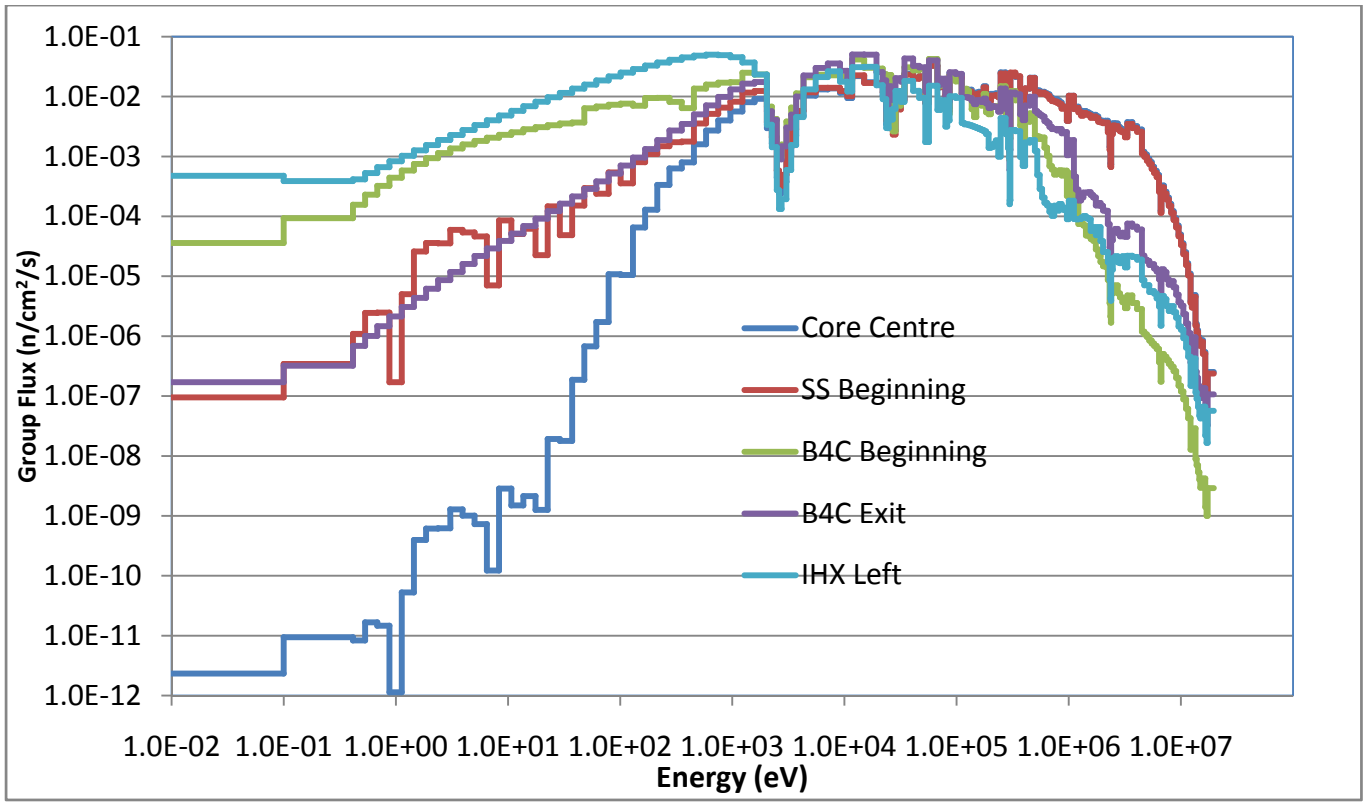

Fig-3.2a: Neutron flux spectra at different locations of PFBR

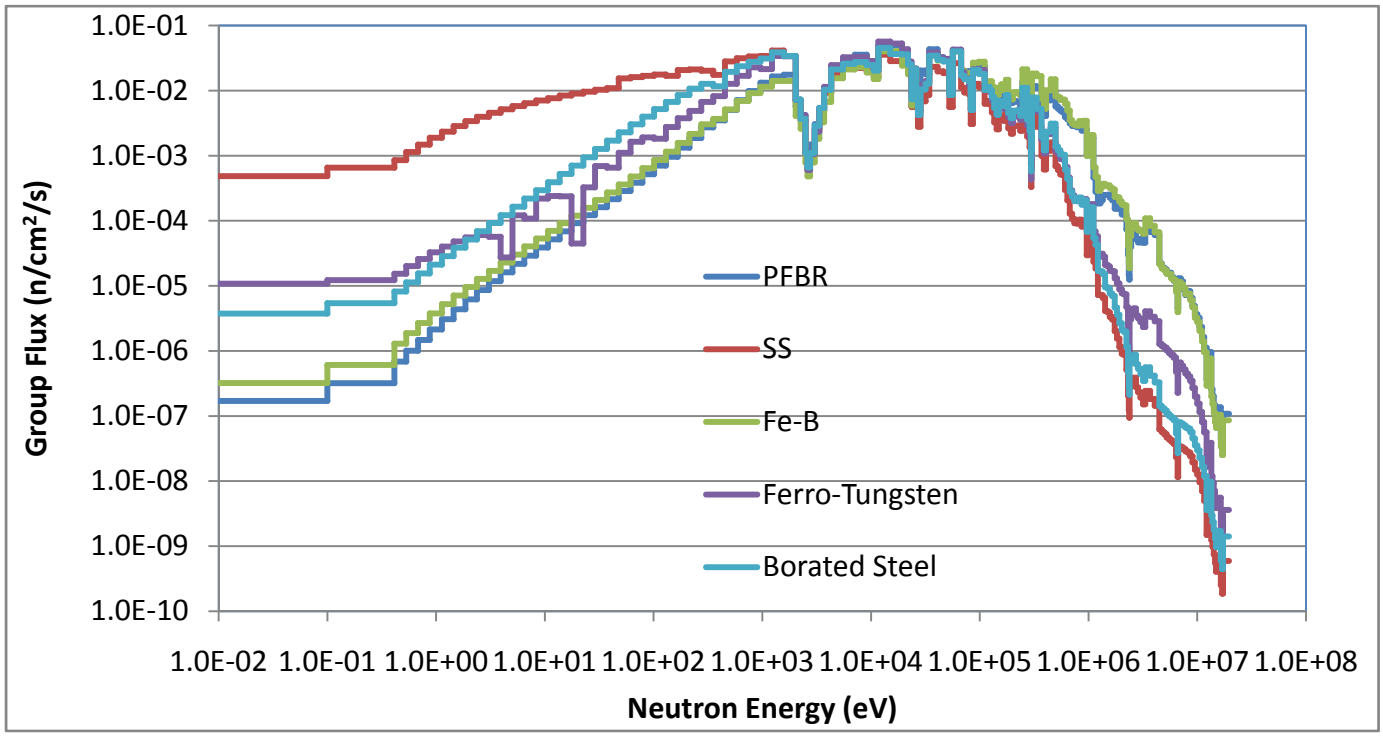

Fig-3.2b: Neutron flux Spectra at the exit of various shield materials

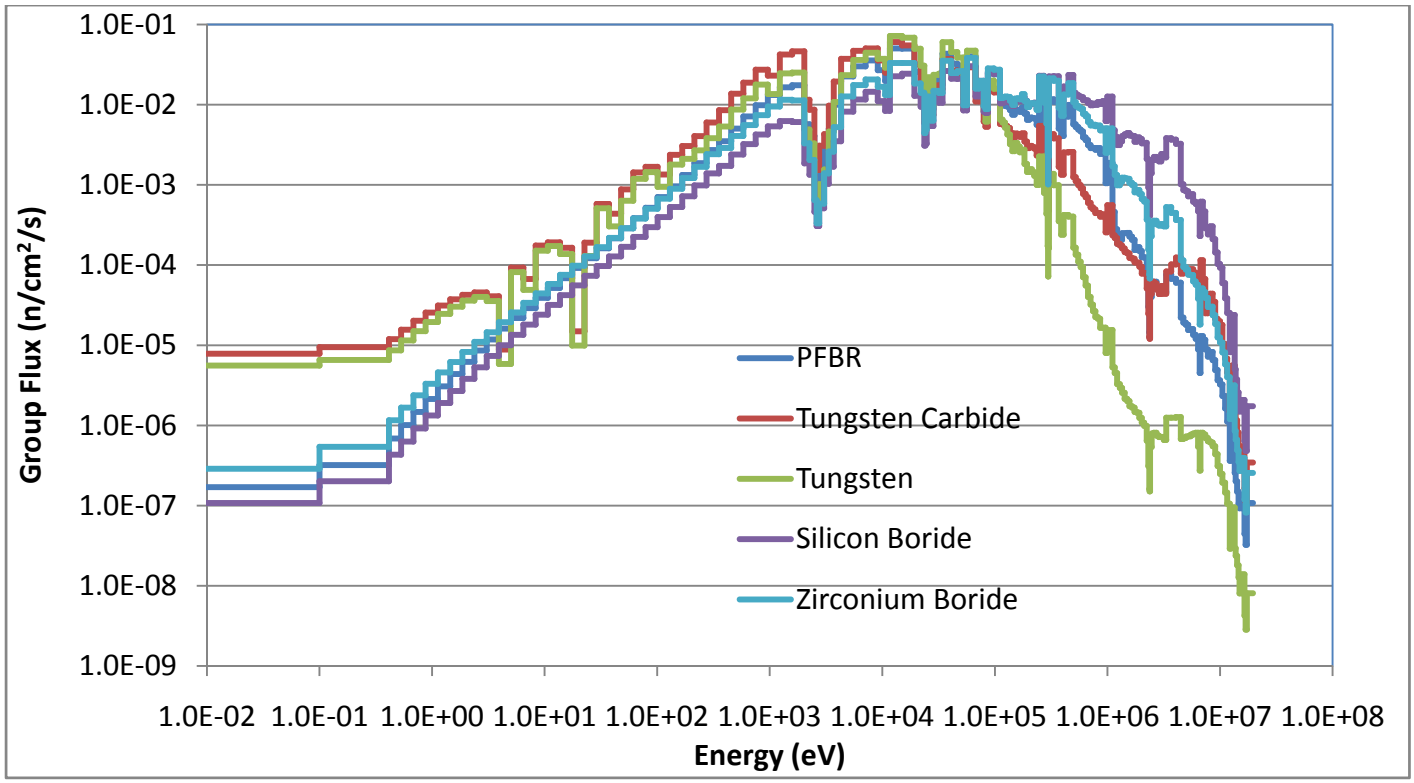

Fig-3.2c: Neutron flux Spectra at the exit of various shield materials

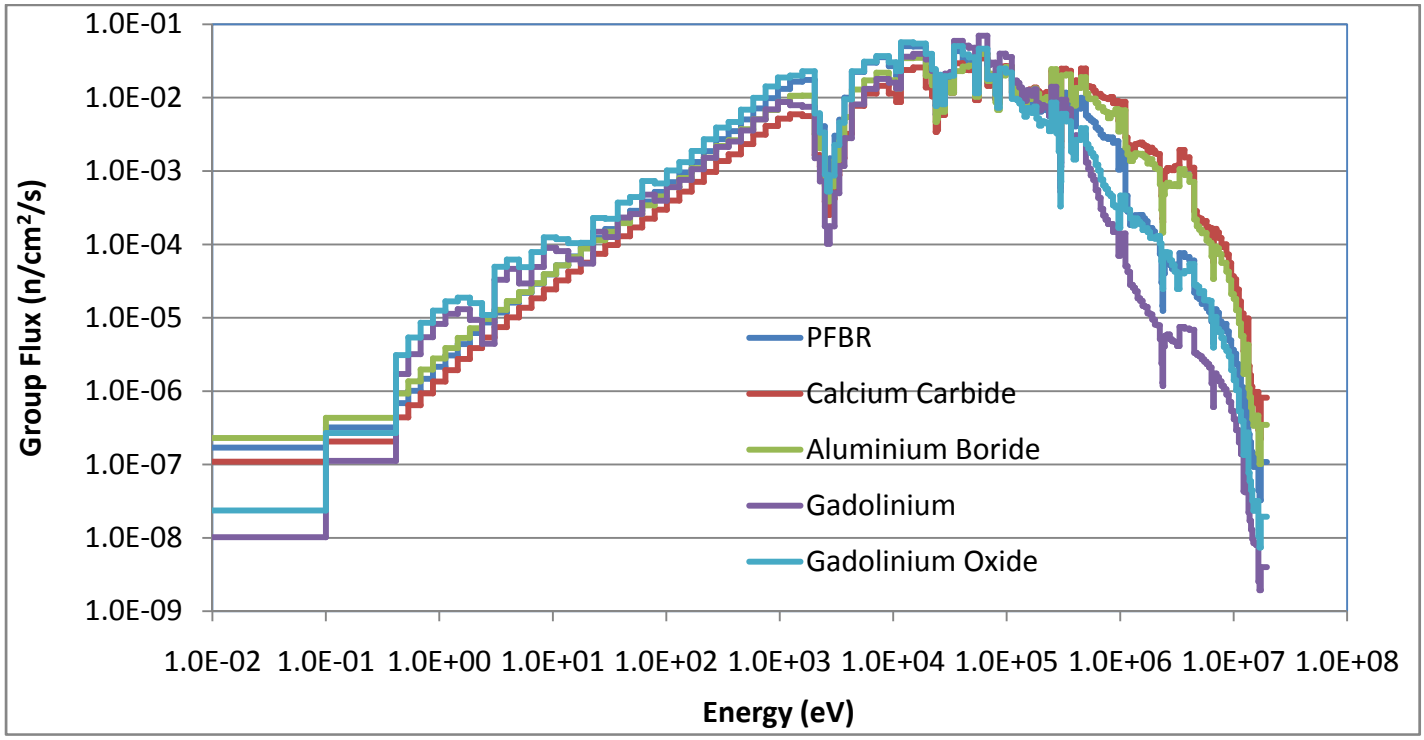

Fig-3.2d: Neutron flux spectra at the exit of various shield materials

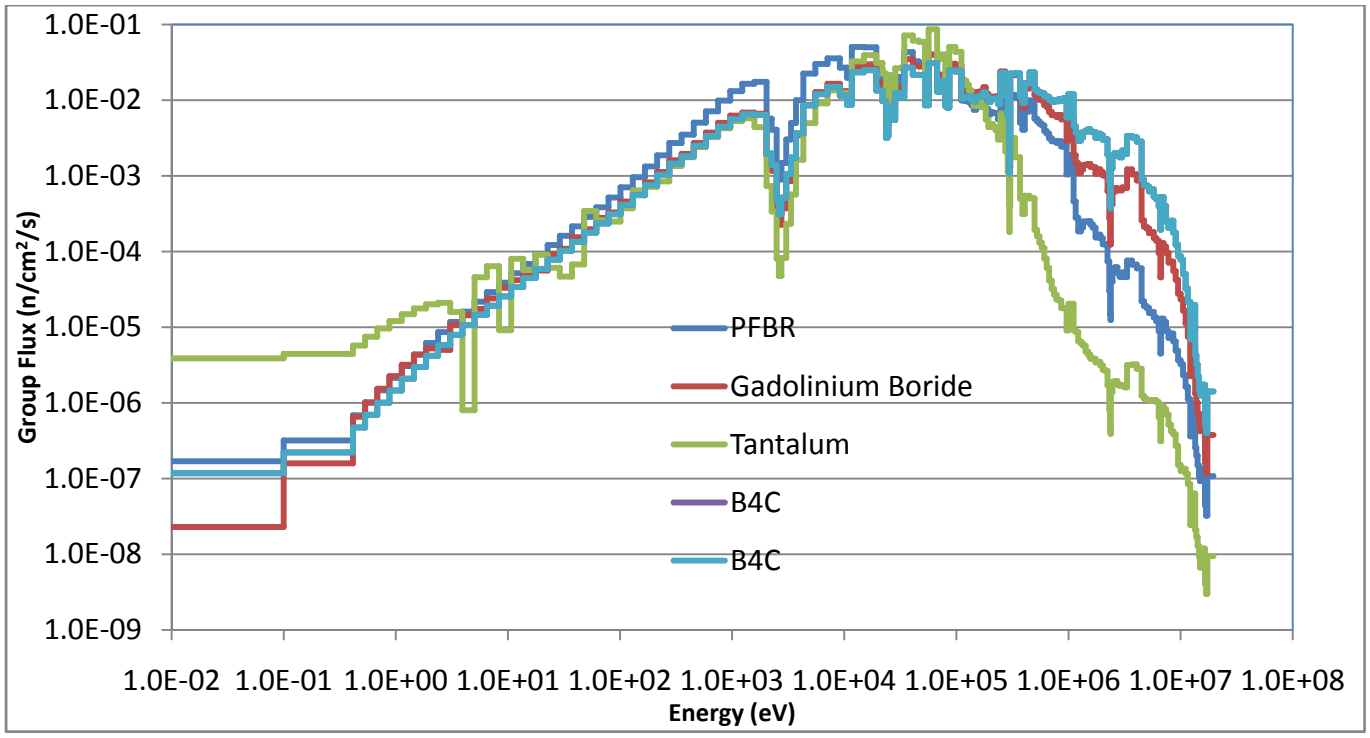

Fig-3.2e: Neutron flux spectra at the exit of various shield materials

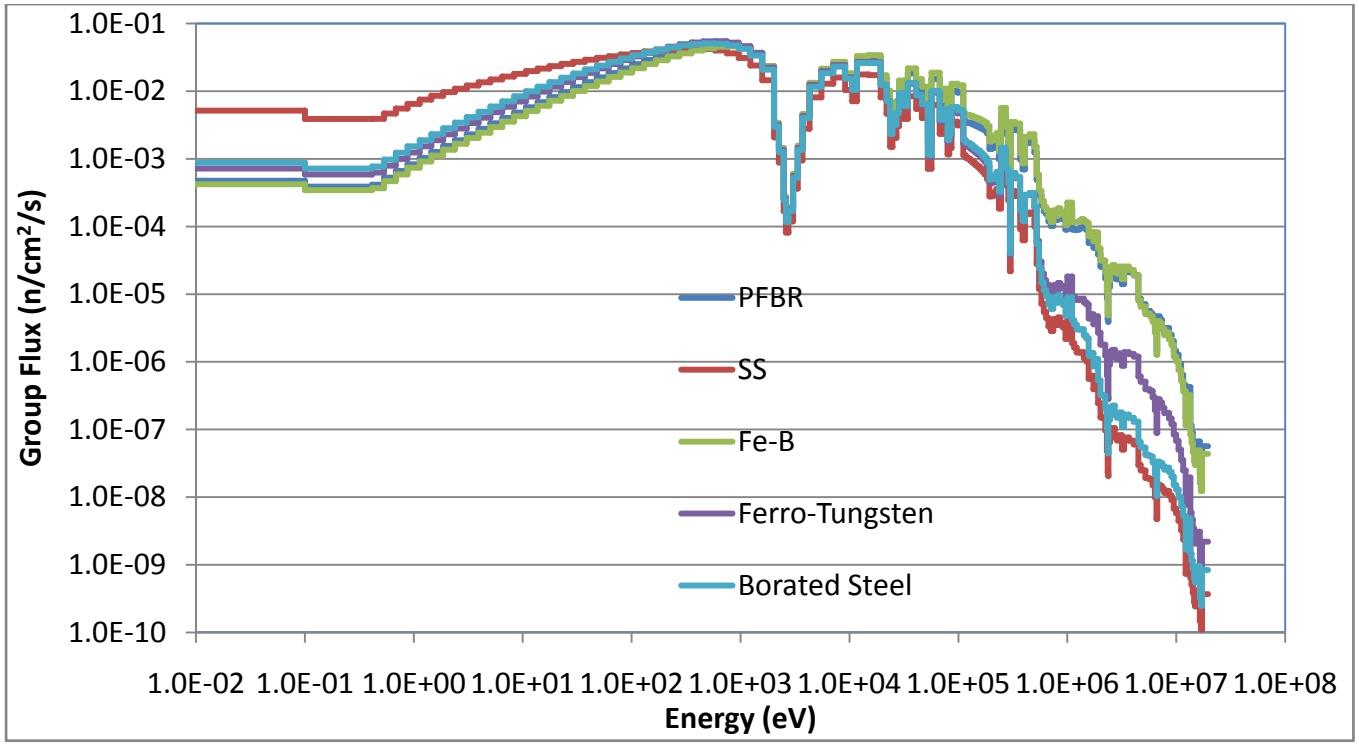

Fig-3.2f: Neutron flux spectra at the beginning of IHX location for different shield materials

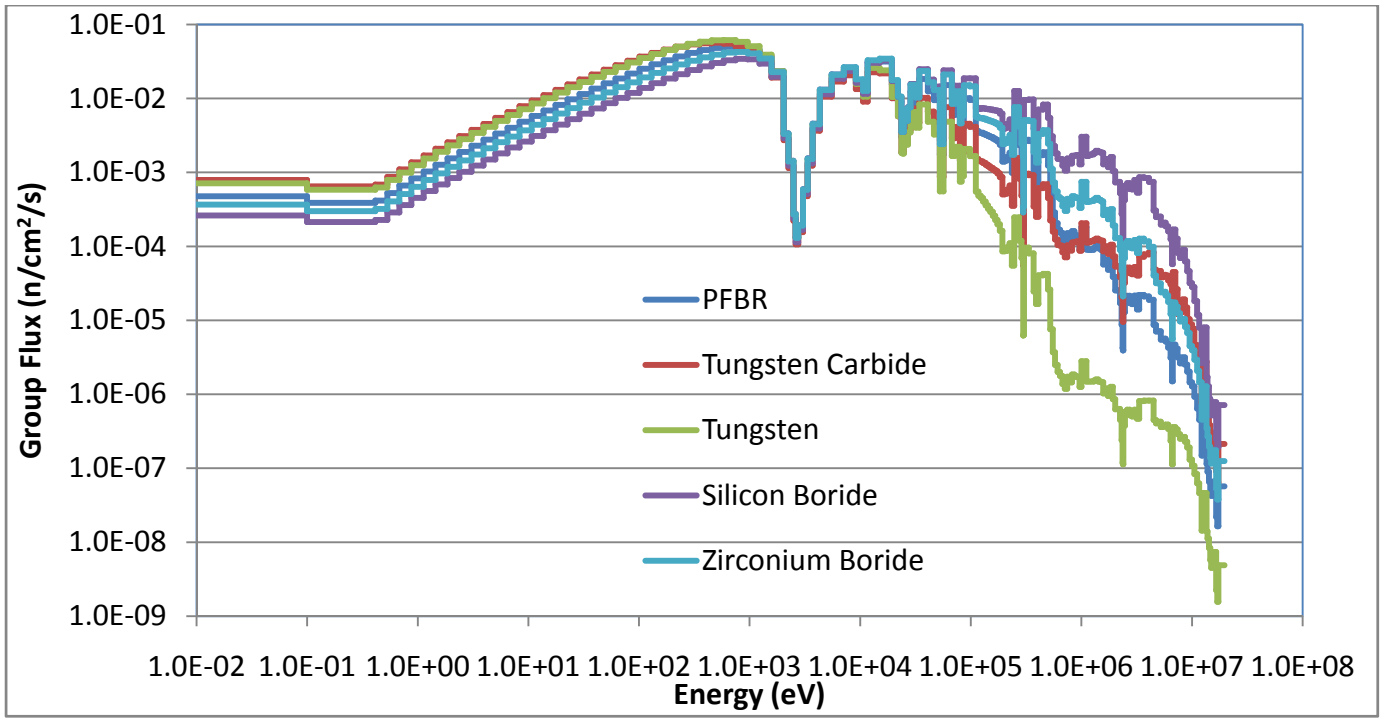

Fig-3.2g: Neutron flux spectra at the beginning of IHX location for different shield materials

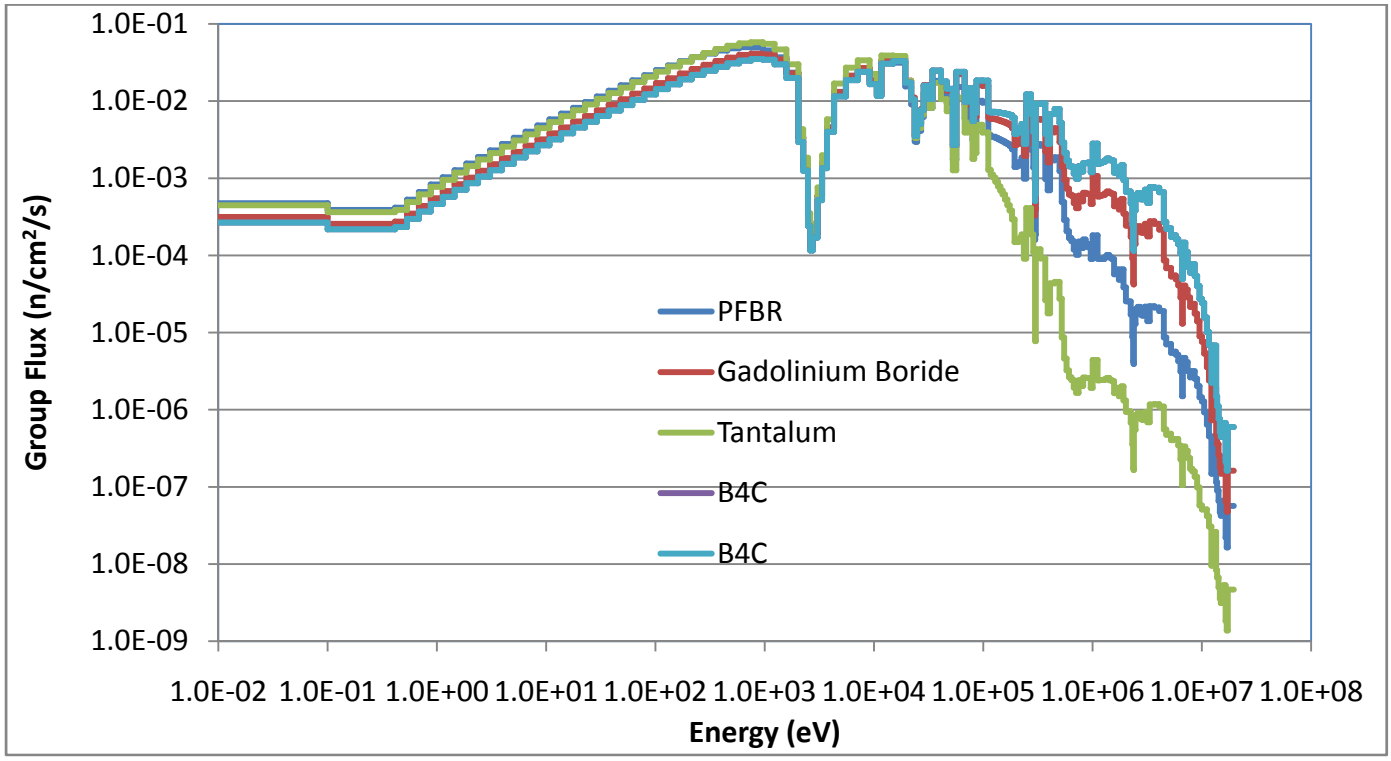

Fig-3.2h: Neutron flux spectra at the beginning of IHX location for different shield materials

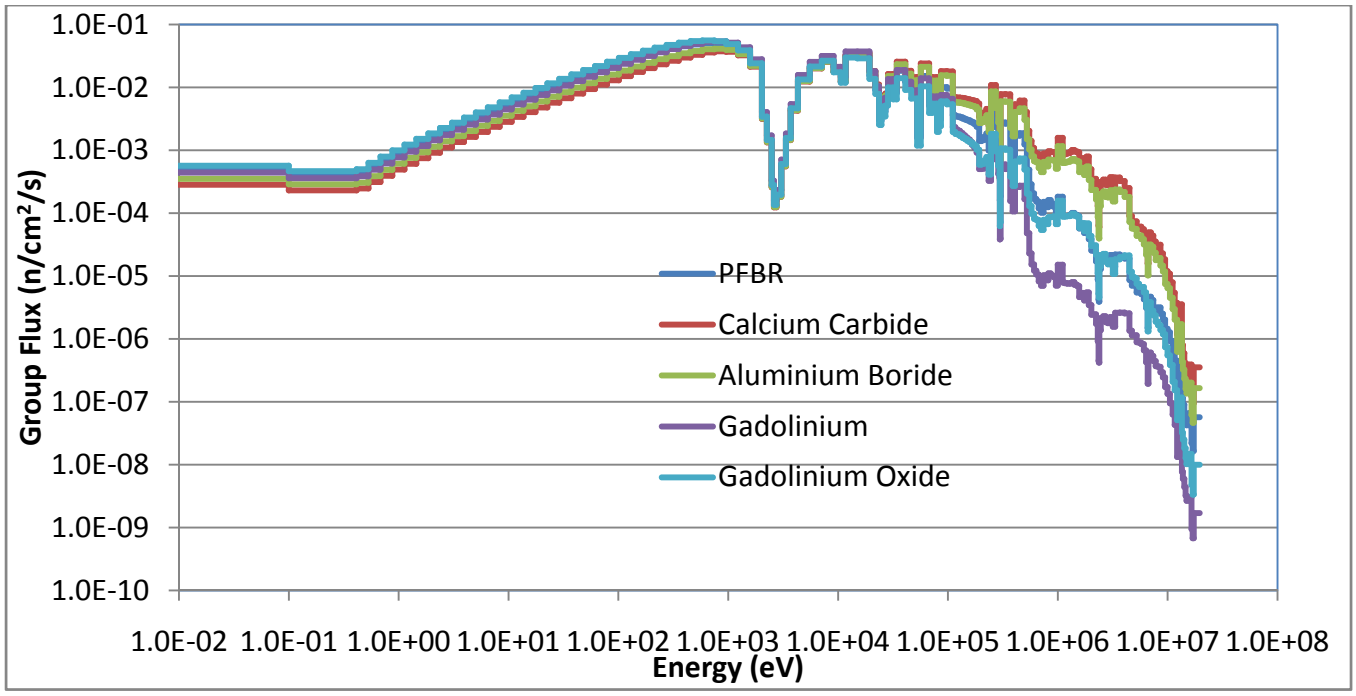

Fig-3.2i: Neutron flux spectra at the beginning of IHX location for different shield materials

Out of all the materials studied, with regard to neutron attenuation properties and cost, Fe-B is found to be a promising alternate shield material as a replacement for SS and B_4C shield combination in PFBR. Therefore more detailed studies are carried out with Fe-B. As a single material, studies have shown that, it is as effective as the reference case. It also happens to be commercially available in large quantities and cheap. Another advantage is the lower radioactive waste generation over a period of irradiation because of the absence of cobalt in Fe-B as impurity (Keshavamurthy et al., 2013). Fe-B is much less expensive as compared to SS and B_4C and the cost and weight of shielding is shown to be significantly lower.

3.5 Properties of Fe-B

3.5.1 General details

Commercial grade Fe-B with density around 6.7 g/cc has been traditionally used as a master alloy addition in steel industry. It contains about 15-18 wt% boron, besides a lot of impurities like carbon, oxygen, silicon, phosphorous etc. The commercial material is generally available in lumps, granules and coarse powder forms with a price that is only about 10 % of B_4C powder. Typical elemental composition of Fe-B is shown in Table 3.3. It must be added that for use of Fe-B (Bruno Merk and Jörg Konheiser, 2014) in fast reactor cores, there should be a tight control over free oxygen content. Further, the presence of unreacted 'boron' as such should be avoided, since it aggravates the SS clad attack at high temperatures (unbound boron diffuses fast into SS clad at temperatures exceeding 650 ^{o}C). The presence of carbon to the extent of 0.2 wt.% is not a serious issue in the current application, as SS 304L clad carburisation at typical operating temperatures is not a restricting factor, especially with twin type of containers planned for PFBR shield assemblies. On the other hand, boronization of SS clad needs to be investigated, if Fe-B with significant free boron content has to be used.

Table - 3.3: Typical elemental composition of Fe-B

Element	Boron	Silicon	Aluminium	Carbon	Sulphur	Phosphorous	Oxygen	Iron
Typical Composition (wt. %)	15-18	0.89	0.17	0.29	0.006	0.005	0.1	Balance

For experimentally proving the effectiveness of Fe-B as a good neutron shield material, neutron attenuation in Fe-B using KAMINI reactor were undertaken (Venkatasubramanian and Rajeev Ranjan Prasad et al., 2009; Venkatasubramanian and Haridas et al., 2009; Keshavamurthy et al., 2011).

3.5.2 Attenuation experiments in KAMINI

KAMINI (KAlpakkam MINI) Reactor located at Indira Gandhi Centre for Atomic Research (IGCAR), Kalpakam, India is a U-233 fuelled, low power research reactor and functions as a neutron source facility (Pasupathy et al., 1993; Mohapatra et al., 2004; Mawutorli Nyarku et al., 2013). The core of KAMINI comprises of nine rectangular fuel subassemblies, arranged in a 3 x 3 array. Each Subassembly has eight flat plates of uranium aluminum alloy. Each fuel plate has a central meat section of 1 x 55 x 250 mm. The shutdown mechanism of the reactor consists of the Safety Control Plate (SCP) assemblies with a cadmium stroke length of 300 mm. The reactor power is also regulated by the SCPs. The reactor has three horizontal hollow beam tubes (north, south, and west) that extract neutrons from the core-reflector interface. Centre lines of two of these beam tubes (west and south) are at an elevation of core centre and extend close to the core, while the centre line of the third one (north) is located at a higher elevation of 151.95 mm above the core centre and facing the top axial reflector to reduce the gamma dose. At the inner ends of the north and south beam tubes, aperture-control plates are provided to obtain a pencil beam of neutrons.

KAMINI spectra includes 35% fast, 33% thermal and 32% epithermal flux as the south beam tube exit spectra (Mohapatra, et al., 1998; 2004; Mohapatra, 2004). Experiments were conducted (Keshavamurthy, 2011; Sunil Kumar et al., 2004) in the southern end neutron beam (slit source of dimension 220mm x 70 mm) of KAMINI reactor with the Fe-B with a bulk

density of ~ 4 g/cm^3. Commercial Fe-B with different content of (11.8% and 15.2%) natural boron was taken up for studies. For comparison purposes, experiments were also carried out with natural boron carbide powder of density 2.4 g/cm^3 (Keshavamurthy et al., 2011; Rajeev Ranjan Pasad, 2008). Shield material filled in rectangular aluminium boxes (of two different sizes 300mm x 150mm x 50 mm and 300mm x 150mm x 60mm) was placed in front of the neutron beam. Provision of foil holders was made to keep the activation foils in front of the beam as well as in between aluminum boxes containing shield material. The foils were so selected that their neutron activation charecterestics cover the energy spectra from epithermal to fast neutron region.

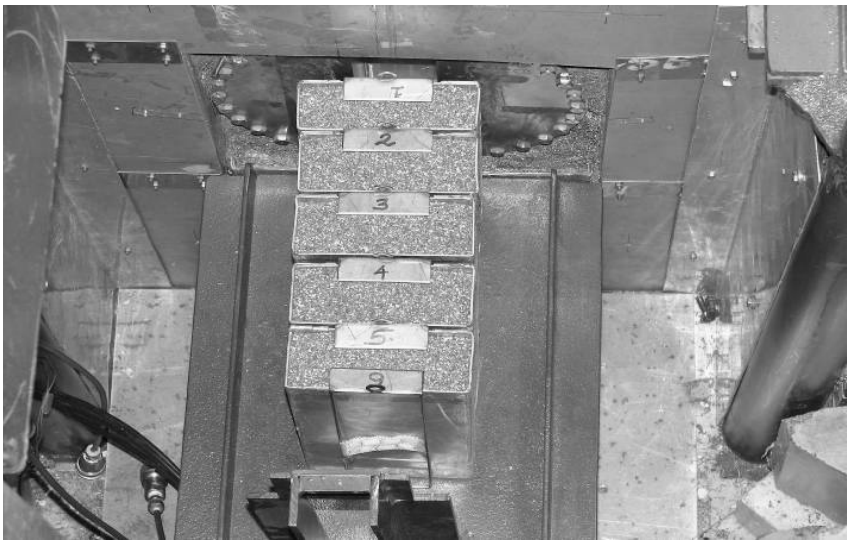

Fig-3.3: Arrangement of Fe-B filled boxes and foil holders at south beam of KAMINI

The measured attenuation of thermal and epithermal fluxes are represented by reaction rates, ^{197}Au(n, γ) and ^{55}Mn(n, γ). It should be noted that Fe-B has 11.8 and 15.2% boron as compared to 78% in B_4C. Measured attenuation of fast flux is represented by the inelastic threshold reactions^{115}In(n, n') and ^{105}Rh(n,n'). With regard to the reaction rates representing fast fluxes, the thicknesses of B_4C and Fe-B to achieve the same level of attenuation are

approximately the same. The neutron activation characteristics of elements irradiated are given in Table 3.4. Reaction rate attenuations are given in Table 3.5 and 3.6. The measured attenuation characteristics are illustrated in Figure 3.4.

Table - 3.4: Neutron activation foil characteristics

Foils/ Salt Used	Element of interest	Activation Reaction	Threshold Neutron energy	Half-Life of Product Nucleus	Gamma energy Measured(keV)
Au	Au	Au^{197} (n, γ) Au^{198}	~0.025 eV, 4.906 eV	2.69 d	411
$MnSo_4$	Mn	Mn^{55} (n, γ) Mn^{56}	~0.025 eV, 337 eV	2.57 h	846.75
Cu	Cu	Cu^{63} (n,γ) Cu^{64}	~0.025 eV, 580 eV	12.8 h	511
NaCl	Na	Na^{23}(n, γ) Na^{24}	~0.025 eV, 1710 eV	15.06 h	1368.50
Cd	Cd	Cd^{111} (n, n') Cd^{111m}	~500-600 keV	48.6m	245.4
In	In	In^{115} (n, n') In^{115m}	~1.2 MeV	4.5 h	336.23
Rh	Rh	Rh^{103}(n, n') Rh^{103m}	~600 keV	57 m	22
Pt	Pt	Pt^{195} (n, n') Pt^{195m}	~500 keV	4.02 d	65.1, 66.8
Hf	Hf	Hf^{180} (n, n') Hf^{180m}	~300-600 keV	5.5 h	215,332,443

Table - 3.5: Attenuation of reaction rates sensitive to thermal and epithermal fluxes (normalized to first location (L1)) using different foils

Thickness (cm)	Au^{197} (n,γ) Au^{198}			Mn^{55} (n,γ) Mn^{56}			Cu^{63} (n,γ) Cu^{64}	
	Fe-B (11.8%)	Fe-B (15%)	B_4C	Fe-B (11.8%)	Fe-B (15%)	B_4C	Fe-B (15%)	B_4C
0 cm (L1/L1)	1.00	1.00	1.00	1.00	1.00	1.00	1.00	1.00
5.5 cm (L1/L2)	73.83	88.43	158.96	55.57	74.82	180.08	31.09	43.45
12.5 cm (L1/L3)	346.58	367.86	683.15	365.53	448.08	1161.61	113.46	190.09
19.5 cm (L1/L4)	909.64	924.27	1647.25	1086.55	1235.38	2744.32	234.61	495.42
26.5 cm (L1/L5)	1649.26	1711.89	426.29	2164.60	2185.26	759.77	530.71	277.36
33.5 cm (L1/L6)	376.74	361.10	#	435.24	520.29	#	356.59	#

Table - 3.6: Attenuation of reaction rates sensitive to fast flux (normalized to first location) using different foils

Thickness (cm)	In^{115} (n, n') In^{115m}			Rh^{103}(n, n') Rh^{103m}			Hf^{180} (n, n') Hf^{180m}	
	Fe-B (11.8%)	Fe-B (15%)	B_4C	Fe-B (11.8%)	Fe-B (15%)	B_4C	Fe-B (15%)	B_4C
0 cm (L1/L1)	1.00	1.00	1.00	1.00	1.00	1.00	1.00	1.00
5.5 cm (L1/L2)	1.43	1.38	1.54	1.42	1.65	2.01	20.55	23.48
12.5 cm (L1/L3)	2.89	2.88	3.55	2.76	5.09	5.75	59.33	75.50
19.5 cm (L1/L4)	6.63	6.81	8.98	10.12	12.46	9.99	152.08	206.45
26.5 cm (L1/L5)	14.95	16.33	26.45	18.84	39.21	37.91	362.19	290.51
33.5 cm (L1/L6)	39.92	42.91	#	#	#	#	238.22	#

Measurements not done, L1, L2, L3, L4, L5, L6 Foil Location numbers

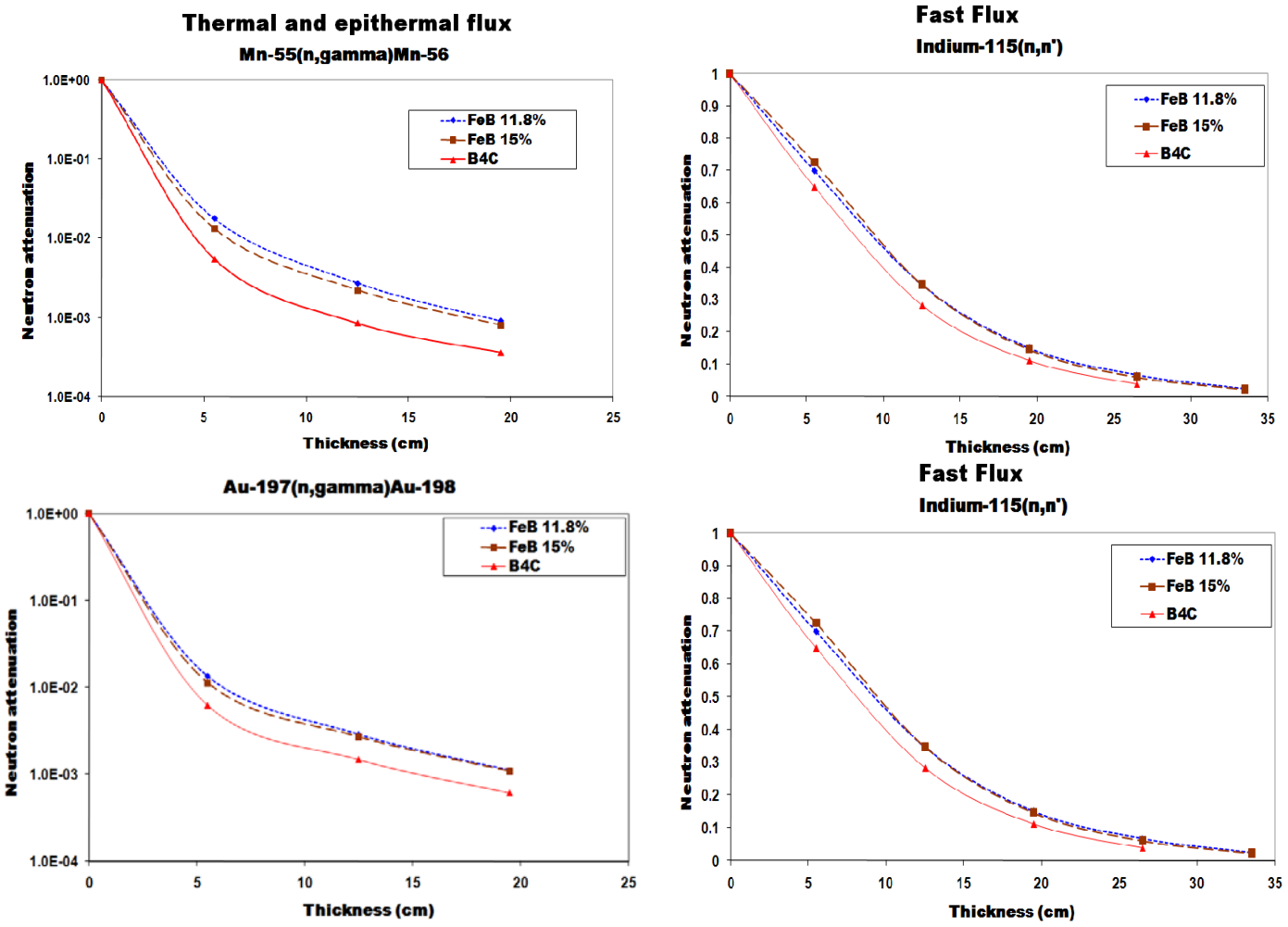

Fig-3.4: Measured neutron attenuation characteristics of Fe-B as compared to B_4C

3.5.3 Metallurgical investigations

Insufficient information is available in the open literature with regard to qualifying the metallurgical compatibility of Fe-B with austenitic stainless steels at high temperatures. In view of this a comprehensive metallurgical characterisation of the high temperature stability of Fe-B was undertaken at IGCAR (Raju et al., 2011).

3.5.3.1 X-ray Studies

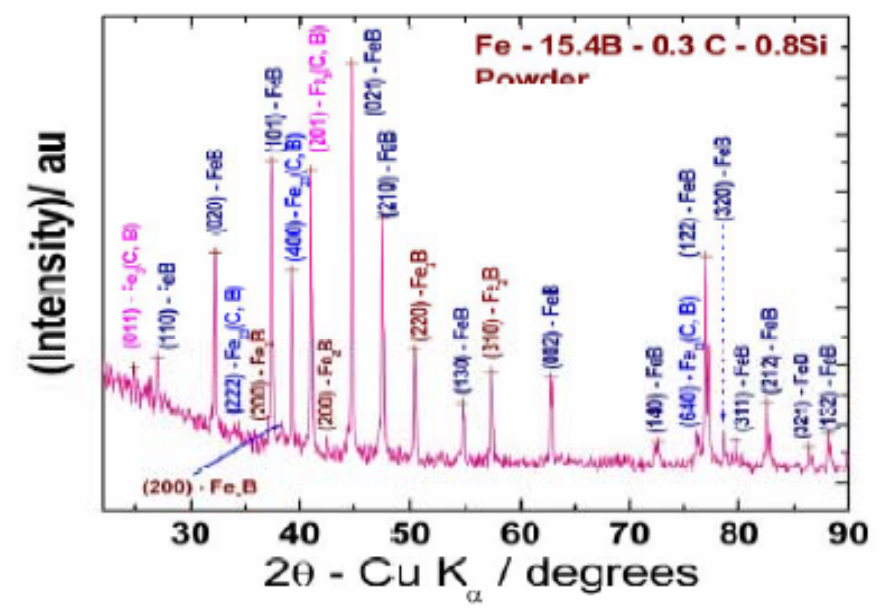

Fig-3.5: X-ray diffraction profile of Fe-B

The powder x-ray diffraction profile of Fe-B [Raju; 2011] is presented in Fig. 3.5. As can be seen, the Fe-B contains a mixture of three intermetallic compounds, namely Fe-B, Fe_2B and $Fe_3(B,C)$. It was found that no free iron or boron was highlighted and the entire boron is present in the combined form. The orthorhombic Fe-B constitutes the major phase, the other two being present in smaller volume fractions, especially the $Fe_3(B,C)$ - boro cementite phase. This latter phase is present due to the presence of carbon (0.3 wt %), which together with boron forms the cementite phase [Ohtani et al., 1998]. According to the current assessed Fe-B binary phase

diagram [Okamoto et al., 2004], the alloy with about 15 to 17 wt.% B should contain some amount of Fe_2B, the lower boride phase.

However, this phase dissolves back into the Fe-B phase at high temperatures. In a similar manner, the $Fe_3(B,C)$ boro cementite phase is also unstable at high temperatures, and it dissolves into the Fe-B and Fe_2.B at high temperatures. Presently, reliable information on phase diagram features of boron rich Fe-B-C ternary is rather limited and does not cover the compositional range of our interest. Measurements made on Fe-B (Arun Kumar Rai et al., 2011) are briefly reported below.

3.5.3.2 Thermal properties

The thermal stability of Fe-B powder was investigated (Arun Kumar Rai et al., 2011) using differential thermal analysis (DTA) carried out in flowing pure argon atmosphere. The corresponding DTA thermogram obtained during both heating and cooling cycle is shown in Figure 3.6 and the following major results obtained:

(i) The Curie temperature (T_c) was found to be 725 ^oC.

(ii) The dissolution of boro cementite $Fe_3(B,C)$ occurs at about 1104 ^oC.

(iii) The dissolution of Fe_2B in the γ-austenite phase was found to occur at 1227 ^oC.

(iv) Finally, the melting of Fe-B begins at 1359 ^oC. It is found to be almost complete at 1450 ^oC.

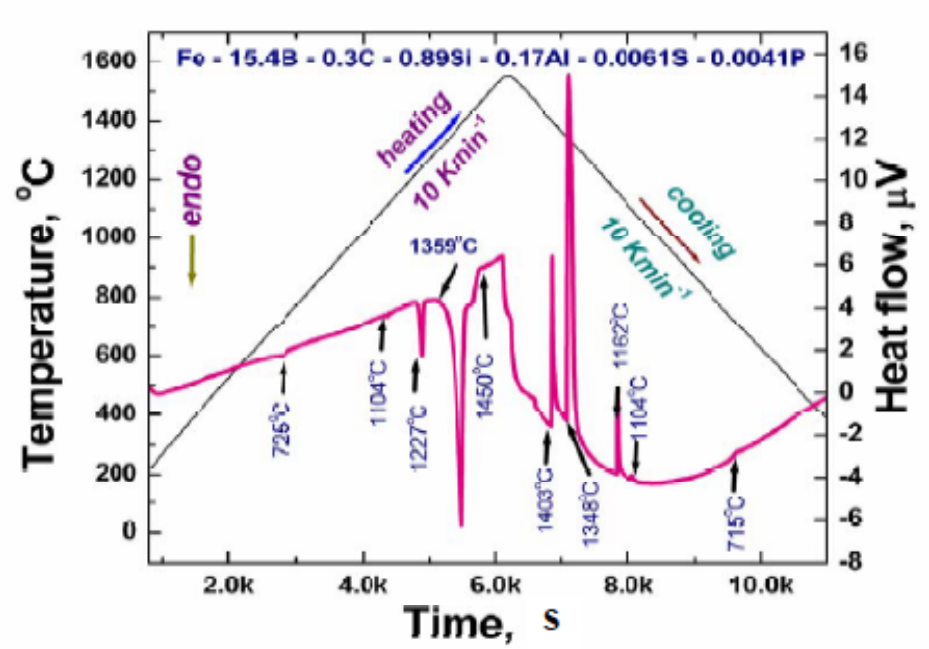

Fig-3.6: DTA Thermogram of Fe-B powder recorded during heating and cooling.

This later temperature may be taken as the melting point or the liquidus point of Fe-B. An estimate of the latent heat associated with the melting was made by making a comparison

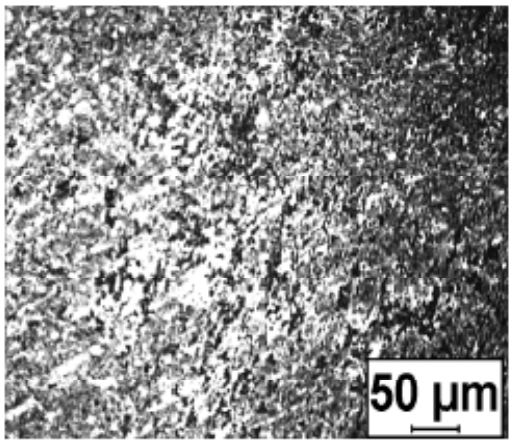

Fig-3.7: Microstructure of fine Fe-B powder

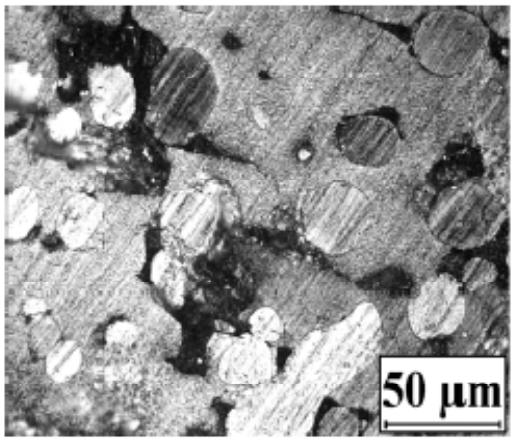

Fig-3.8: Microstructure of bulk Fe-B block

experiment under identical experimental conditions with pure iron and was found to be 356

kJ/kg. Fe-B releases a large quantity of heat of solidification as compared to other boron compounds.

3.5.3.3 Metallographic characterization

The optical and scanning electron microscopy investigations of Fe-B have also been carried out to support the results of thermal stability. The relevant results are shown in Fig. 3.7. and 3.8., and more details on metallographic constitution of Fe-B can be obtained from the published literature (Arun Kumar Rai et al., 2011).

3.5.3.4 High temperature compatibility studies

The estimated life time of the shielding subassembly is about 60 years with the anticipated

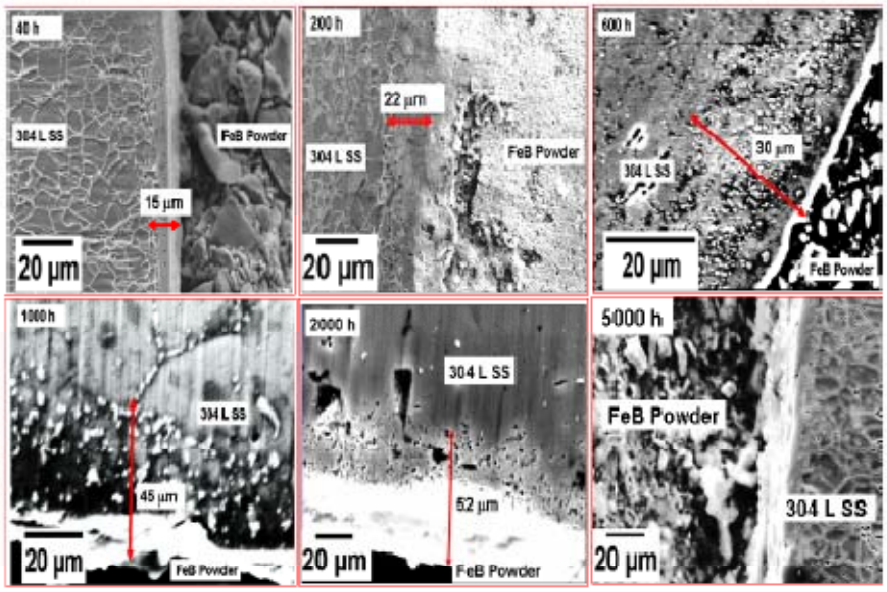

Fig-3.9: Clad –Fe-B interaction at elevated temperature of 700°C

service temperature of 550°C. Accelerated tests for shorter time spans at successively higher temperatures, namely 550 °C, 600 °C, 700°C and 800°C, have been conducted for long time durations of up to 10000 h, for investigating the high temperature clad integrity in contact with

Fe-B shield (Raju et al., 2011). The results of metallographic characterization of Fe-B/304L reaction couples at 700 ^{o}C are presented in Fig. 3.9. These investigations revealed that the loss of clad thickness due to boron diffusion induced attack is rather insignificant, as compared to clad thickness of 2150 microns. There is also a 5000 micron thick outer clad provided acting as an additional barrier. The estimated upper bound for clad attack thickness is about 250 microns over a period of 60 years at the design service temperature of 550^{o}C. This is only about 12% of the primary clad thickness and 3.4% of total clad wall thickness and further, no loss of ductility of clad or cracking has been found at the end accelerated testing.

3.5.4 Chemical compatibility

Extensive chemical compatibility experiments were carried out at IGCAR by equilibrating Fe-B with SS304L in presence of sodium at various temperatures (Sudha, 2013; Keshavamurthy et al., 2013). SS 304L samples used for the chemical compatibility studies of Fe-B in sodium environment were analysed using SEM and EDX after several equilibration in sodium at 973 K for 1000, 2000, 3000, 4000 and 5000 h. Microhardness of the above specimens was also measured using a Vickers microhardness tester. It was observed that the reaction layer is clearly delineated (Fig. 3.10). It is found that the zone of chemical interaction increased with time. The thickness of Ni depleted layer as a result of sodium corrosion also increases with time of exposure in sodium.

The clad thinning is seen to be around 250 microns at this elevated temperature of 973 K over 5000 h. It has been established that at the normal service temperatures, the general and in-sodium compatibility is good and do not pose constraints for the use of Fe-B up to about 1000 K. It must also be mentioned here that sodium is extremely unlikely to come into contact with the material as it is provided with double containment.

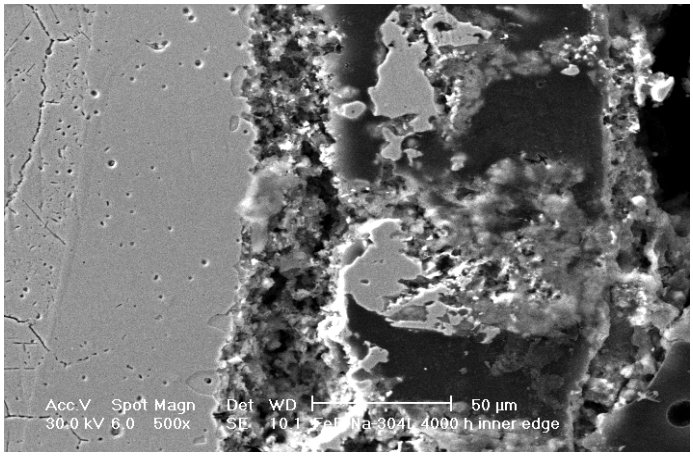

Fig-3.10: SEM image of clad interaction with hot sodium and Fe-B clearly delineated on the right.

3.5.5 Fe-B Irradiation Capsules Fabrication and Testing in FBTR

In view of the good compatibility of Fe-B with SS clad and sodium in out of pile tests, design and fabrication of Fe-B irradiation test capsules was planned. Two types of Fe-B capsules were developed: one for conducting an irradiation test in FBTR and the other one being a 1:1 scale version of actual PFBR, as part of technology development.

3.5.5.1 Irradiation capsule

The irradiation test capsule (Fig. 3.11) consists of an inner capsule with an outer diameter, OD, of 14 mm and an inner diameter, ID, of 12 mm containing fully vibropacked Fe-B granules under argon atmosphere in five separate partitions.

There is an outer tube (OD: 16 mm and ID: 14.5 mm) serving as secondary containment for preventing the release of Fe-B powder into hot sodium, in the unlikely event of breach of the inner capsule. The central three partitions of irradiation capsule are in line with the fuel column of the driver fuel pins during irradiation in FBTR. The fabrication involved intricate thin section welds under argon glove box atmosphere, and suitable weld qualification procedures have been devised for ensuring proper quality of welds. The welding of the secondary containment was

done at site in IGCAR followed by due quality inspection protocols. High purity helium was filled in the annular gap between the inner capsule and the outer containment tube for ensuring good heat transfer characteristics.

For filling helium, an innovative helium filling arrangement was designed and fabricated. An intermediate plug was welded to the outer containment tube with provision to evacuate and fill the annular gap with helium and close the filling path. Leak-tight ring type containment with separate connections to vacuum pump and the helium gas cylinder was designed and fabricated to facilitate evacuation and gas filling operations (Fig. 3.12). Neutron radiography (NR) of the capsule was carried out to get pre-irradiation data and as part of the qualification (Fig. 3.13).

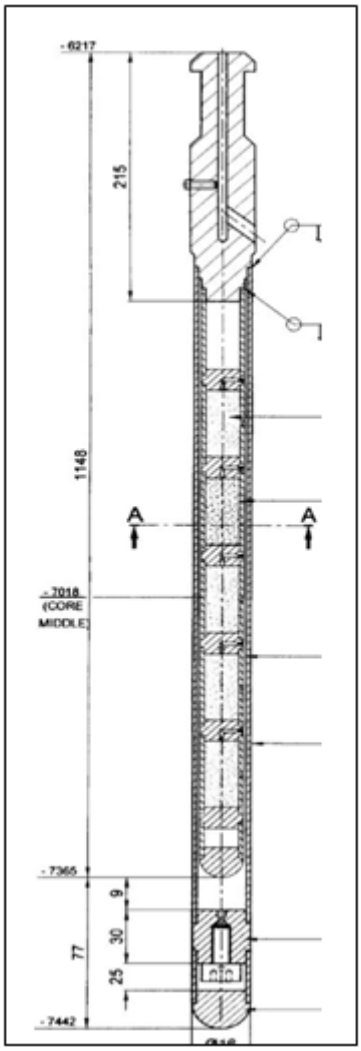

Fig-3.11: Capsule fabricated for Irradiation test in FBTR

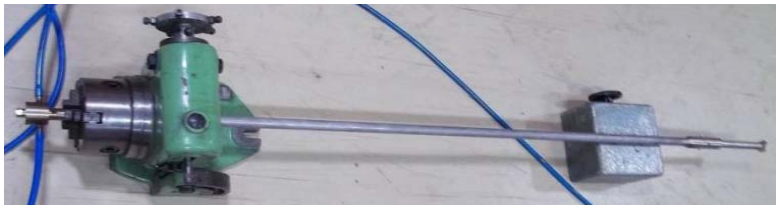

Fig-3.12: Device to fill helium filling in secondary containment

3.5.5.2 Irradiation in FBTR

The in-vessel shield in future FBRs will sustain 60 years of irradiation with an assumed load factor of 75 %. To simulate this, it was found necessary to load the capsule in the 4th ring location of FBTR and irradiate it for 45 effective full power days at a flux level of 1.0x10^{15} n/cm^2/s. As part of pre-irradiation data, neutron radiography of the capsule was carried out using

KAMINI neutron source reactor to measure the length of the Fe-B column for comparing the same with post irradiation data to evaluate the consolidation of stack if any.

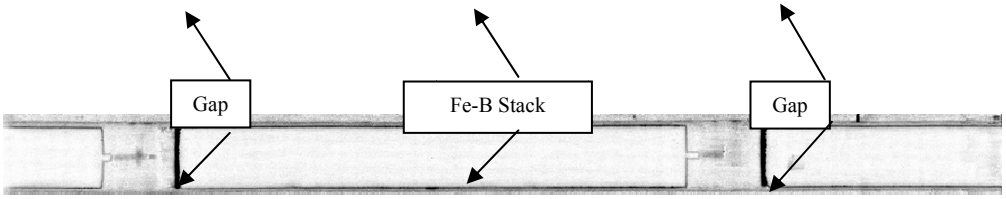

Fig-3.13: Neutron radiography image of Fe-B capsule before irradiation (Middle sub-capsule - No.3)

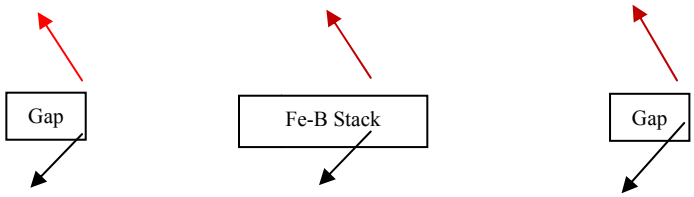

Fig-3.14: Neutron radiography image of Fe-B capsule after irradiation (Middle sub-capsule- No.3)

The Fe-B capsule was irradiated in FBTR in 4th ring for 66 effective full power days. During irradiation, the reactor was operated with an inlet temperature of 390°Cand outlet temperature of 475ºC. There are five sub-capsules filled with compacted Fe-B powder with a density of 4.2 gm/cc. The capsule material was SS 304L. Maximum total *dpa* was about 2.96 at near the middle of the Fe-B capsule.

Pre and post irradiation data obtained by NR have been compared. It was observed that the integrity of the subcapsule is maintained and there is no visible reaction of Fe-B powder with

the capsule material. Further post-irradiation tests for determination of amount of Helium gas produced, and the microstructural examination of the inner surface of the capsule will be carried out in future.NR image of the capsule post-irradiated capsule is shown in Fig. 3.14.

3.6 Summary

The calculations show that all borides are as effective or even more effective than the reference case. For many borides the availability and cost is a problem. Many of the absorbers like Gadolinium are not as effective for fast neutrons as the reference shield combination. Out of all the materials studied with regard to attenuation and cost Fe-B is found to be a promising alternate shield material as a replacement for SS and B_4C shield combination in PFBR. Neutron attenuation characteristics of Fe-B has been investigated both theoretically and experimentally and has been found to be favorable for use in FBRs. Its use will result in significant savings in cost, without impairing shielding capabilities. Extensive and in-depth out of pile characterization thermo physical properties and high temperature metallurgical compatibility tests with SS 304L clad was carried out. These, as well as studies of interaction of sodium and Fe-B together on clad at high temperature, show excellent compatibility with the clad. Material irradiation tests planned and conducted in FBTR simulating 60 years of neutron fluence were also presented.

Chapter – 4

FERRO-BORON AS IN-VESSEL SHIELD MATERIAL

4.1 Introduction

Reactor core shielding constitutes an important and large part of reactor assembly. Improved shield configurations with advanced shield materials with an objective of reducing shield volumes and improved economics are important. As described in the previous chapter, Fe-B is identified as a promising shield material through scoping calculations and experiments. Though, the efficacy of Fe-B as a neutron shield material is identified based on the neutron attenuation experiments in the KAMINI reactor, detailed reactor physics analyses and transport calculations using realistic combinations of Fe-B (Sunil Kumar, et al., 2010), are necessary to demonstrate its cost effectiveness to achieve the same level of radiological safety as the reference case combination. In this chapter, in-vessel shield calculations for a 500 MWe reactor, same in all respects to PFBR except the in-vessel shield part, are performed. The in-vessel shield part of the reactor consists of Fe-B shields. The core is taken as same as in PFBR with (Pu-U) oxide. Axial shields in the core region are also unaltered. Only the radial shields consisting of 6 SS and 3 B_4C assemblies are replaced by Fe-B assemblies. PFBR is taken as the reference case.

The volume fraction of the Fe-B taken is as that of the B_4C volume fraction in the outer shield assemblies of PFBR. The composition of Fe-B corresponds to what is available in the market and taken from an analysis of it which is supplied. The chemical composition of the Fe-B is already given in the Chapter-3. This composition with the proper volume fractions of steel and sodium are used for the macroscopic cross section preparation.

The detailed transport calculations are done with DORT code (Rhoads and Childs, 1988) and IGC-S3 cross section set. Modelling of computation of secondary sodium activity passing through IHX and the dose computation in the SGB is already presented in Chapter-2.

4.2 Neutron Monitoring In PFBR

The core status is monitored in all states of the reactor i.e., shutdown, fuel handling, start-up, intermediate and power ranges, through neutron flux monitoring system. In PFBR core flux is monitored through the neutron detectors (Nagaraj, 2006; Sivaramakrishna, 2008) kept both at the control plug location and at the bottom of the reactor vessel. In order to monitor the core during the initial fuel loading operation, High Temperature Fission Counters (HTFCs) in control plug locations are replaced by Boron-10 coated proportional counters. At reactor power above 5 % of the nominal power (1250 MWt), monitoring is carried out by the HTFCs below safety vessel where six such detectors are located. The U-235 equivalent neutron flux at control plug detector location varies from 22 $n/cm^2/s$ at shut down to $2.0x10^9$ $n/cm^2/s$ at nominal power. To have an efficient reactor start-up, the shut down count rate is to be kept at minimum of 3 counts per second (cps) per unit U-235 equivalent flux for the control plug detectors (Nagaraj, 2006). Reduction of axial shields in the core will increase the detector counts. However it has the penalty of increasing secondary sodium activity and hence dose in SGB. Therefore axial shields have to be provided judiciously.

4.3 Geometry of Model Cores with Shields

4.3.1 Reference case

The Reference case is PFBR. The details of the modelling and calculations have already been given in Chapter-2.

4.3.2. Proposed core with Fe-B shields

In this core, all the 9 outer rows have Fe-B shield assemblies. The core plan is shown in Fig.4.1. The composition is typical of commercially available material. The density of Fe-B powder or granules is taken as 4 g/cm^3, which is about 60 % of the theoretical density. It is packed in SS 304L tubes of ID 110.0 mm and OD 114.3 mm. Double containment is also provided by an outer 304L tube of ID 120.0 mm and OD 130.0 mm. Sketch of a Fe-B assembly is shown in Fig.4.2.

In the calculations, 2-D R-Z cylindrical geometry was employed as in the reference case. The equivalent radii were worked out by volume conservation. The R-Z configuration for calculation with Fe-B shield is shown in Fig.4.3. The corresponding material volume fractions are given in Table 4.1.

4.4. Calculations

4.4.1. Nuclear data

The cross section set IGC-S3 (Devan et al., 2002) is used in the calculations. The set is a 217- group coupled library as described in Chapter 2.

4.4.2. Transport calculations

Calculations are performed by 2 dimensional transport code DORT using IGC-S3 cross section set. The criterion used for flux convergence is 1.0E-04 and that for the fission convergence is 1.0E-03. The angular quadrature approximation used is S_8 and the order of scattering cross section anisotropy used is P_3. Total 571 meshes are taken in the radial direction and 718 meshes are taken in the axial direction. These are identical to the input data used for reference case.

Table - 4.1: Material volume fractions of regions of CFBR

Region No	Mixture Name	Na (%)	S. Steel (%)	B_4C (%)	Blanket (%)	Fuel (%)	Fe-B (%)
1	SA Bottom	56.31	43.69				
2	Plenum	40.75	24.17				
3	SA Head	68.08	31.92				
4	Blanket- bottom S.S.	41.36	58.64				
5	Blanket- Plenum	27.92	20.22				
6	Blanket- top SS	90.25	9.75				
7	S.S. Reflector and B_4C Inner	53.96	46.04				
8	Reflector	20.97	79.03				
9	S.S.Reflector	91.87	8.13				
10	S.S. Reflector -top	73.64	26.36				
11	B_4C inner- Plenum	22.78	15.77				
12	B_4C outer -bottom S.S.	22.41	77.59				
13	B_4Couter- bottom S.S.	15.9	84.1				
14	B_4Couter- top S.S.	79.2	20.8				
15	S.S. Shield- bottom SS	46.9	53.1				
16	S.S. Shield -top SS	79.2	20.8				
17	S.S. Shield	28	72				
18	Axial Blanket	40.75	24.17		33.26		
19	Core 1	40.75	24.17			33.26	
20	Core 2	40.75	24.17			33.26	
21	Radial Blanket	27.92	19.74		50.52		
22	B_4C Inner (Pellet)	22.78	15.72	60.28			
23	Sodium at $500^{O}C$	100					
24	CR Absorber	52.3	19	28.7			
25	CR Follower	83.3	16.7				
26	B_4C Outer (Powder)	15.9	21.52	60.21			
27	Sodium at $400^{O}C$	100					
28	B_4C Region	50.2	18.5	31.3			
29	SS Shield	50.2	49.8				
30	SS structural		100				
31	Grid Plate	68.42	31.58				
32	Core Support Structure	92.44	7.56				
33	Fe-B	15.9	21.52				60.21

Flux convergence was achieved after 20 outer iterations. Inner iterations were varied between 20 to 25 for the groups. The computations were performed in a 64 bit Bull Nova Cluster

machine with 16 nodes. The clock speed of a node is 1.5 GHz. The total cpu time taken by the computations was 700 hours. Reaction rates were also monitored for convergence simultaneously.

4.5. Results

4.5.1 Neutron spectrum

The neutron spectra hold the key for differences in reaction rates. They are evaluated at nodal points like shield beginning, shield exit and IHX locations in the central radial direction are generated for core with Fe-B shields as well as the reference core. Comparison of spectra for reference and Ferro-Boron cases at flux peaking position of IHX is also given. The spectrum comparisons are given in Fig.4.4, 4.5, 4.6 and 4.7. In the beginning of the shields for reference case spectrum is softer compared to the core with Fe-B shields. This can be attributed to the reflection of neutrons from SS subassemblies in the reference case whereas the neutrons are getting absorbed in Fe-B all through. At the exit of the shields as shown in Fig. 4.6 both the spectra are almost similar. In the IHX location in the central radial direction, spectrum is slightly harder compared to PFBR case.

4.5.2. Fluxes and reaction rate distributions

The 2-D total flux contours for the configuration are given in Fig. 4.8. The contour plot of capture reaction rate $^{23}Na\ (n,\gamma)\ ^{24}Na$ is plotted in Fig. 4.9. The shielding surrounding the core and blankets in pool type of reactors is, in fact, dictated mostly by radiological criterion for dose in Steam Generator Building (SGB) arising due to secondary sodium activity. The computed neutron fluxes are given in Tables 4.2 and 4.3. Variation of maximum sodium capture rate is plotted along IHX in Fig. 4.10 for the reference as well as the Fe-B case. In both the cases, it

reaches a maximum at a level about a metre below IHX window. Peaking at this location occurs due to the absence of effective shields to stop streaming through the upper plenum regions in the

Table - 4.2: Comparison of Neutron Fluxes (n/cm^2/s) along Central Radial Direction

No	Region	Radius (cm)	mesh	Total Neutron Flux			U235- Eq. Flux		
				PFBR	CFBR	Ratio	PFBR	CFBR	Ratio
1	Core Centre	0.00E+00	1	8.00E+15	8.00E+15	1.00	2.85E+13	2.85E+13	1.00
2	Core-1 (39.6 cm)	3.79E+01	20	7.23E+15	7.23E+15	1.00	2.71E+13	2.71E+13	1.00
3	Radial Shield -Beginning	1.85E+02	136	7.63E+12	4.57E+12	1.67	3.14E+10	1.57E+10	2.00
4	Radial Shield- First Row	2.00E+02	148	4.24E+12	1.28E+12	3.31	3.91E+10	4.16E+09	9.40
5	Radial Shield- Second Row	2.13E+02	160	2.21E+12	4.14E+11	5.34	2.68E+10	1.36E+09	19.71
6	Radial Shield- Third Row	2.25E+02	172	1.05E+12	1.29E+11	8.14	1.49E+10	4.35E+08	34.25
7	Radial Shield- Fourth Row	2.37E+02	184	4.67E+11	3.91E+10	11.94	7.36E+09	1.34E+08	54.93
8	Radial Shield- Fifth Row	2.50E+02	196	1.87E+11	1.14E+10	16.40	3.12E+09	4.00E+07	78.00
9	Radial Shield- Sixth Row	2.62E+02	208	4.08E+10	3.24E+09	12.59	4.50E+08	1.16E+07	38.79
10	Radial Shield- Seventh Row	2.75E+02	236	2.64E+09	8.60E+08	3.07	1.13E+07	3.12E+06	3.62
11	Radial Shield- Eigth Row	2.87E+02	264	2.27E+08	2.30E+08	0.99	9.62E+05	8.48E+05	1.13
12	Radial Shield- Ninth Row	3.00E+02	292	2.69E+07	7.30E+07	0.37	1.67E+05	4.53E+05	0.37
13	(Sodium) (344.76 cm)	6.43E+02	464	2.81E+04	7.05E+04	0.40	4.66E+03	1.04E+04	0.45
14	Main Vessel (2.5 cm)	6.46E+02	466	9.63E+03	2.46E+04	0.39	1.27E+03	2.92E+03	0.43

Table - 4.3: Comparison of Neutron Fluxes (n/cm^2/s) along Central Radial Direction

	Region	Radius (cm)	mesh	Fast Flux (> 0.1 MeV)			Na Eq. Flux		
				PFBR	CFBR	Ratio	PFBR	CFBR	Ratio
1	Core Centre	0.00E+00	1	4.75E+15	4.75E+15	1.00	2.61E+13	2.61E+13	1.00
2	Core-1 (39.6 cm)	3.79E+01	20	4.16E+15	4.16E+15	1.00	2.42E+13	2.42E+13	1.00
3	Radial Shield -Beginning	1.85E+02	136	4.33E+12	2.75E+12	1.57	3.03E+10	1.44E+10	2.10
4	Radial Shield- First Row	2.00E+02	148	1.76E+12	7.57E+11	2.32	3.49E+10	4.19E+09	8.33
5	Radial Shield- Second Row	2.13E+02	160	7.36E+11	2.34E+11	3.15	2.30E+10	1.41E+09	16.31
6	Radial Shield- Third Row	2.25E+02	172	2.88E+11	6.97E+10	4.13	1.28E+10	4.64E+08	27.59
7	Radial Shield- Fourth Row	2.37E+02	184	1.06E+11	2.01E+10	5.27	6.31E+09	1.48E+08	42.64
8	Radial Shield- Fifth Row	2.50E+02	196	3.60E+10	5.61E+09	6.42	2.69E+09	4.54E+07	59.25
9	Radial Shield- Sixth Row	2.62E+02	208	8.97E+09	1.53E+09	5.86	4.32E+08	1.35E+07	32.00
10	Radial Shield- Seventh Row	2.75E+02	236	6.65E+08	3.89E+08	1.71	1.78E+07	3.73E+06	4.77
11	Radial Shield- Eigth Row	2.87E+02	264	5.95E+07	9.97E+07	0.60	1.54E+06	1.04E+06	1.48
12	Radial Shield- Ninth Row	3.00E+02	292	7.20E+06	2.59E+07	0.28	1.87E+05	4.12E+05	0.45
13	(Sodium) (344.76 cm)	6.43E+02	464	5.23E+00	1.76E+01	0.30	5.51E+03	1.22E+04	0.45
14	Main Vessel (2.5 cm)	6.46E+02	466	2.75E+00	9.21E+00	0.30	1.56E+03	3.54E+03	0.44

fuel and blanket subassemblies. B_4C shielding provided at the top portion of fuel assemblies is small due to the requirement that flux at detector location in the control plug must not be low for detection. The same sodium capture rates normalized to its peak value of the reference case are plotted in Fig. 4.11 for relative comparison. Maximum sodium capture rate is lower in the Fe-B case at all levels above core and the peak value is 93 % of the peak value of the reference case. The reason is that, though the spectral shapes at the peak position are similar as shown in Fig.4.8 total flux level is lower in the Fe-B case. This is due to the presence of boron in the upper parts of the shield assemblies in the neutron streaming paths. The figure also indicates that the contribution to secondary sodium activity is dominated by the region adjacent to the peak position. The maximum capture rate on IHX in the core mid plane is 50 % more compared to the reference case, but it is only 2.2 % of the peak value.

4.5.3 Secondary sodium activity and dose on pipes in SGB

The secondary sodium activity is computed using the method as already explained in Chapter-2. For Fe-B case it is marginally lower than that of the reference case for the reasons explained in sec. 4.1. Top parts of shield subassemblies in between core subassemblies and the IHX peak position have significant boron atom densities. In the reference case, the top portion of the first 6 SS rows does not have any boron and the neutrons are streaming above the last 3 rows of B_4C.

Secondary sodium is circulated through IHX with a circuit time t_C of 68.5 s and irradiation time (over one circuit) t_i of 7.2 s in the reactor considered. Thus the secondary sodium activity per cm^3 of sodium is calculated using the standard formula given in Chapter-2.

For the Fe-B case, the activity calculated is 71.3 Bq/cm^3. For the reference (PFBR) case, the value obtained for secondary sodium activity is 72.1 Bq/cm^3. The dose is computed to be 19.3 μSv/h on the pipe carrying secondary sodium activity in SGB.

4.5.4 Detector fluxes

Fe-B shields provided to reduce secondary sodium activity have minor impact on flux at detector location. The neutron detectors (Sivaramakrishanan, 2008) for core flux monitoring in PFBR consists of a set of detectors (both fission chambers and boron counters) on the control plug located at the level of lattice plate above the subassembly top. At the location of the detector position the fission rate and B-10 reaction rates are computed for the Fe-B case and compared with the reference case. Table 4.4 shows the comparison of these reaction rates over a distance of 200 cm radially in the lattice plate position both for fission chamber and boron counter. The results show that by replacing the shield assemblies with Fe-B, the neutron counts in the control plug detector location in Fe-B case is less than 5 % difference as compared to the reference case.

Table - 4.4: Boron detector (located 75 cm above core SA top) counts and fission chamber (45 cm above the core SA top) counts at different radial distances from core axis for Fe-B case. All counts normalized to the reference case

Radial Distance	U-235	B-10
0.0	9.95E-01	9.95E-01
50.0	9.94E-01	9.89E-01
100.0	9.93E-01	9.93E-01
125.0	9.92E-01	9.90E-01
150.0	9.90E-01	9.87E-01
200.0	9.87E-01	9.76E-01

4.5.5 Helium production in PFBR and CFBR shield assemblies

Shield assemblies have no arrangements of venting helium. But they are not removed over the entire life of the reactor. Future Fast Reactors in India are planned to be built to have a

life of 60 years. Another thing to be noted is that Fe-B is filled in all the 9 rows of shield assemblies. Consequently the innermost Fe-B assembly is nearer the core as compared to the B_4C shield assemblies in the reference case. Therefore it is important to show that helium produced over the life of the reactor does not pose problems of unacceptably high pressures. Towards this end, calculations of helium production have been carried out in the Fe-B and also in the outer three rows of B_4C assemblies in the reference case. The estimated helium production is given in Table 4.5. The quantity of helium produced in the first row of Fe-B shield assemblies in a CFBR would be about 45 times more compared to the pressure developed in the 7^{th} rows of B_4C subassemblies in the reference case. Even though the B-10 atom densities are less in the case of Fe-B subassemblies compared to B_4C subassemblies, the neutron flux seen by the first row of Fe-B subassemblies are more compared to the 7^{th} row of subassemblies in the reference case. However the absolute value of helium production is not high. At these levels of helium production, release fraction from granules is expected to be small as shown in earlier studies on helium release from B_4C. The maximum pressure due to helium produced over the life time of the reactor is estimated to be less than 10 bars. This is not high and much lower than the fission

Table - 4.5: Helium production in different shields of shield assemblies for 60 years of operation

PFBR	Average Helium Production (per cc)	CFBR	Average Helium Production (per cc)
1^{st} row of SS	-	1^{st} row of Fe-B Powder	2.11E+19
2^{nd} row of SS	-	2^{nd} row of Fe-B Powder	6.52E+18
3^{rd} row of SS	-	3^{rd} row of Fe-B Powder	2.17E+18
4^{th} row of SS	-	4^{th} row of Fe-B Powder	7.05E+17
5^{th} row of SS	-	5^{th} row of Fe-B Powder	2.22E+17
6^{th} row of SS	-	6^{th} row of Fe-B Powder	6.81E+16
1^{st} row of B_4C Powder	4.68E+17	7^{th} row of Fe-B Powder	1.92E+16
2^{nd} row of B_4C Powder	2.80E+16	8^{th} row of Fe-B Powder	6.97E+15
3^{rd} row of B_4C Powder	3.17E+15	9^{th} row of Fe-B Powder	4.79E+16

(Load factor 75 % assumed)

gas pressures exerted on the fuel clad which is much thinner. Hence it can be safely concluded that helium production in Fe-B shield assemblies will not cause problems.

4.6 Summary

Detailed calculations with Fe-B as neutron shields in the 500 MWe reactor was carried out. The reference case is 500 MWe PFBR. The proposed core has 9 rows of Fe-B shield assemblies and has the same material composition as PFBR in rest of the core. The study has shown that Fe-B shields are capable of satisfying the radiological safety criteria as good as the reference case. The secondary sodium activity and dose in SGB are marginally lower than the reference case. Though it has much lower boron atom densities as compared to B_4C, its effectiveness has stemmed from the fact that boron is spread throughout the shield region. The total shield material weight is lower by about 50 tonnes because of the lower density of Fe-B compared to stainless steel. The material cost for shielding is also lower by a factor 5 as compared to PFBR. Another advantage is the lower radioactive waste generation. Helium production in Fe-B assemblies over their entire life was computed and shown that it does not cause problems.

Further optimization analyses with modifications in shield configuration for axial shields in fuel and blanket assemblies are discussed in Chapter-5 towards achieving reduction of number of rows of outer shields without reducing detector counts at the monitoring location above subassembly top at the same time.

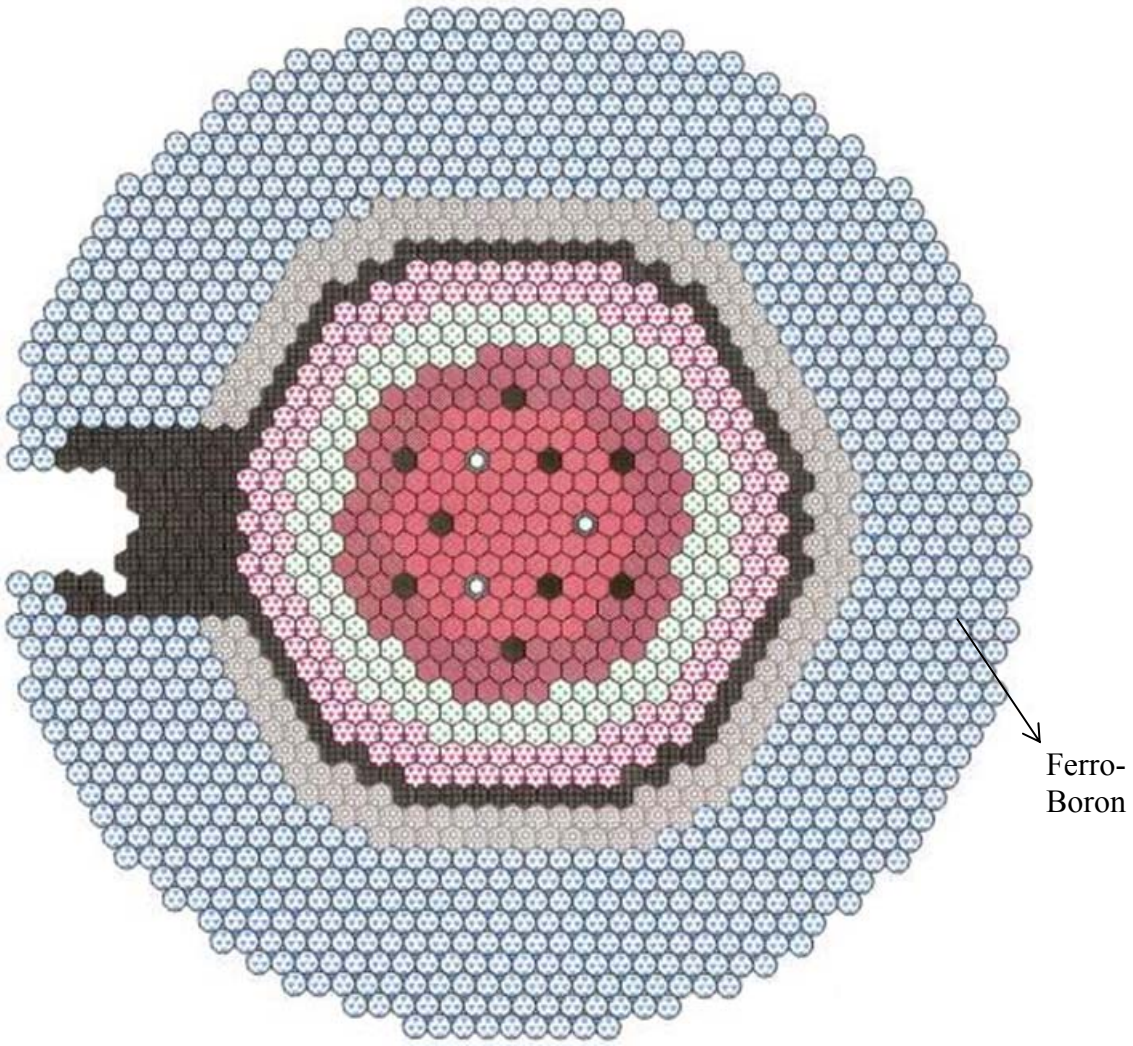

Fig-4.1: Core plan of reactor with Fe-B assemblies

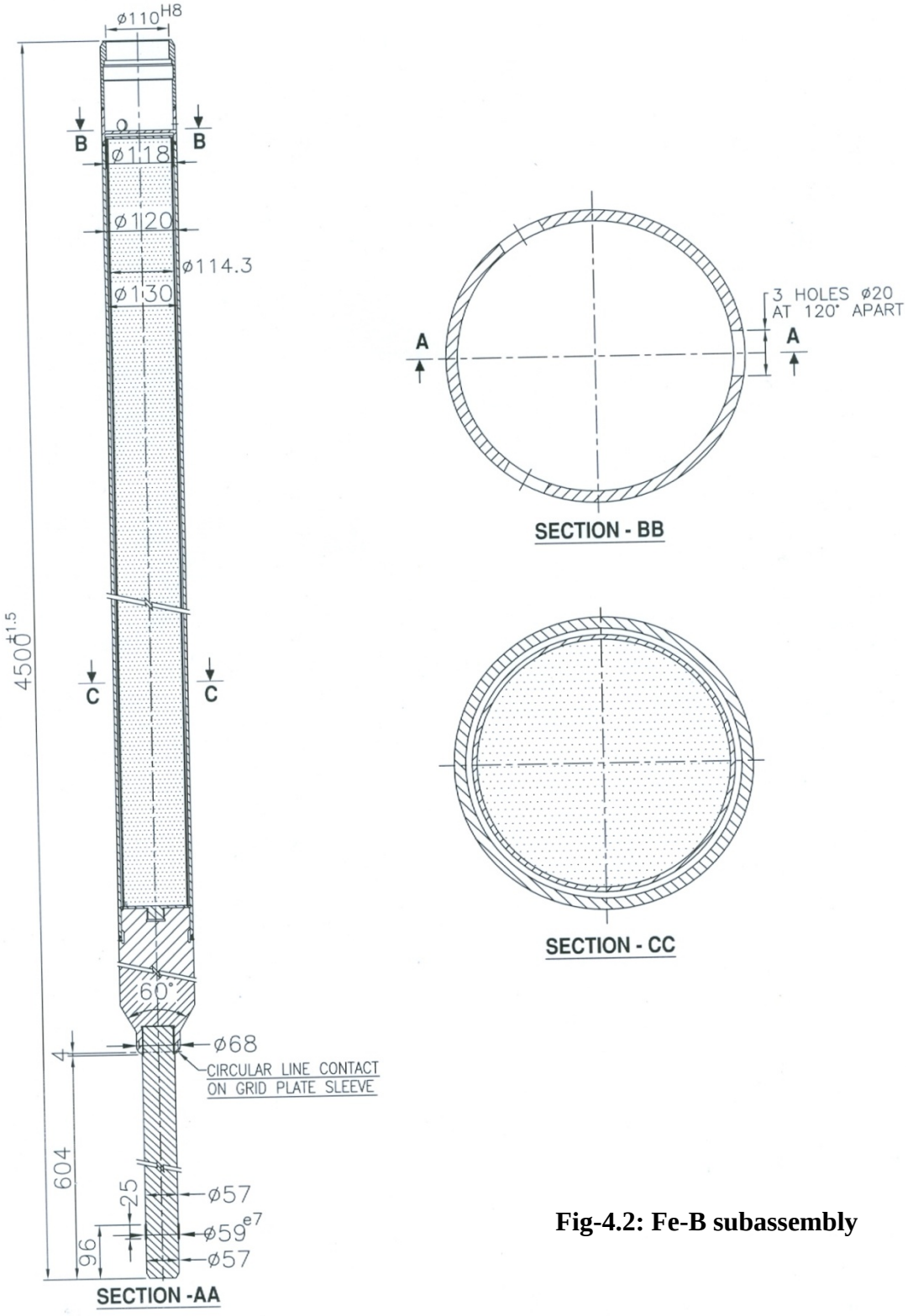

Fig-4.2: Fe-B subassembly

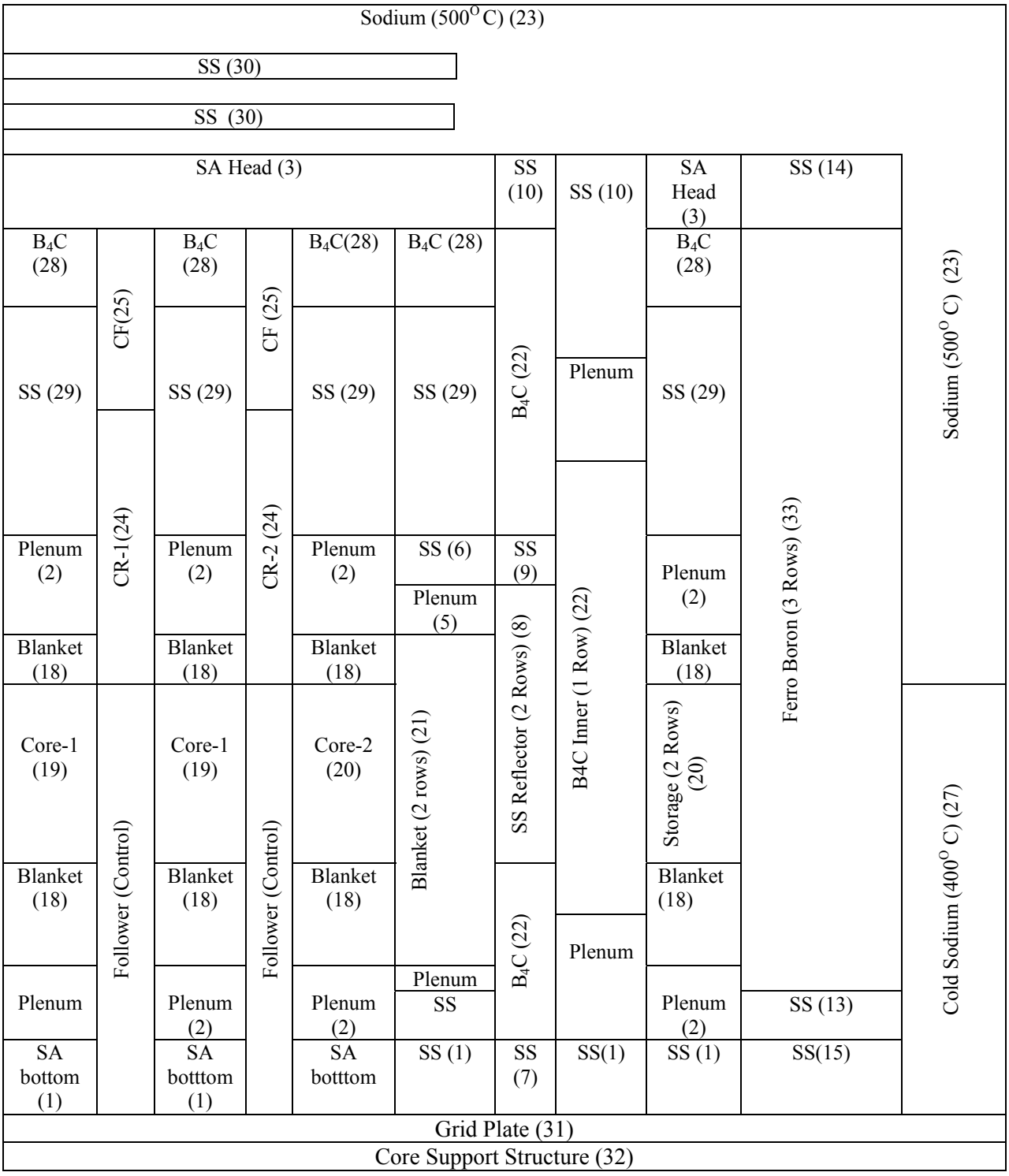

Fig-4.3: 2D R-Z Calculational model – Fe-B case

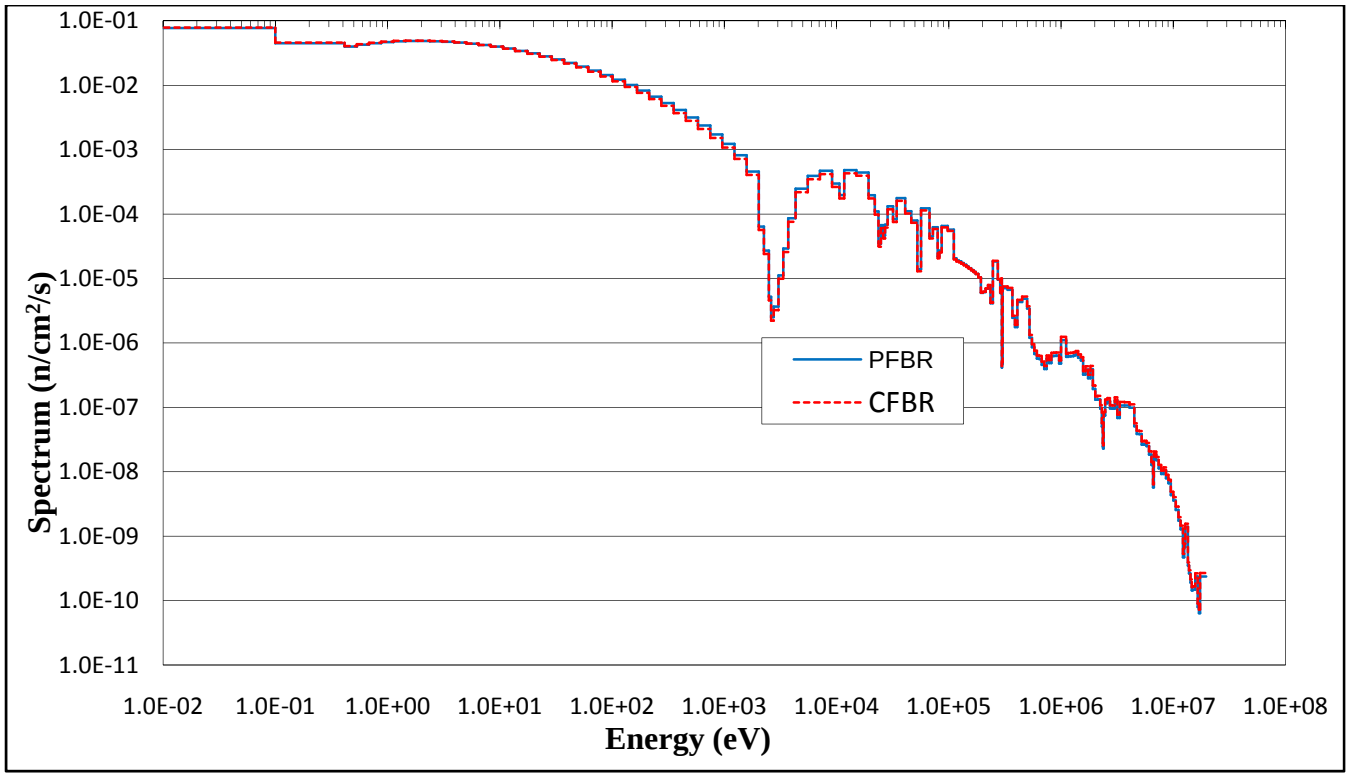

Fig-4.4: Comparison of spectra in IHX at flux peaking position along IHX for reference case and Fe-B case

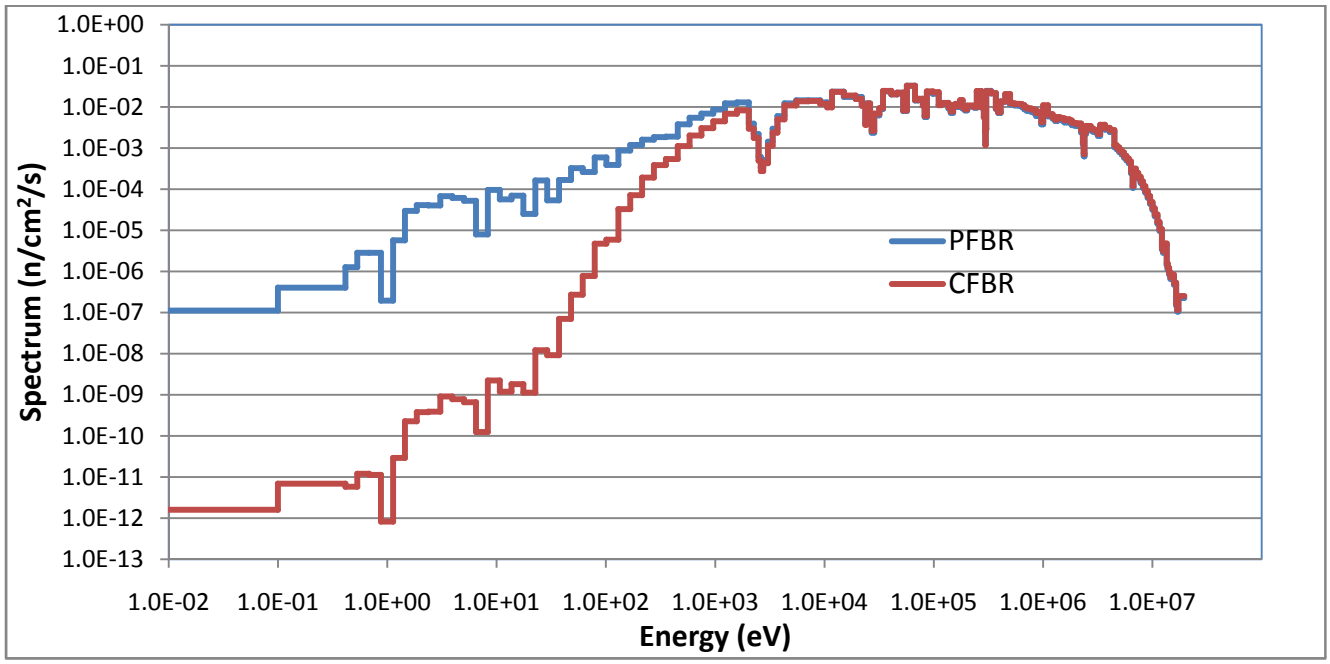

Fig-4.5: Comparison of neutron spectrum at the beginning of shields

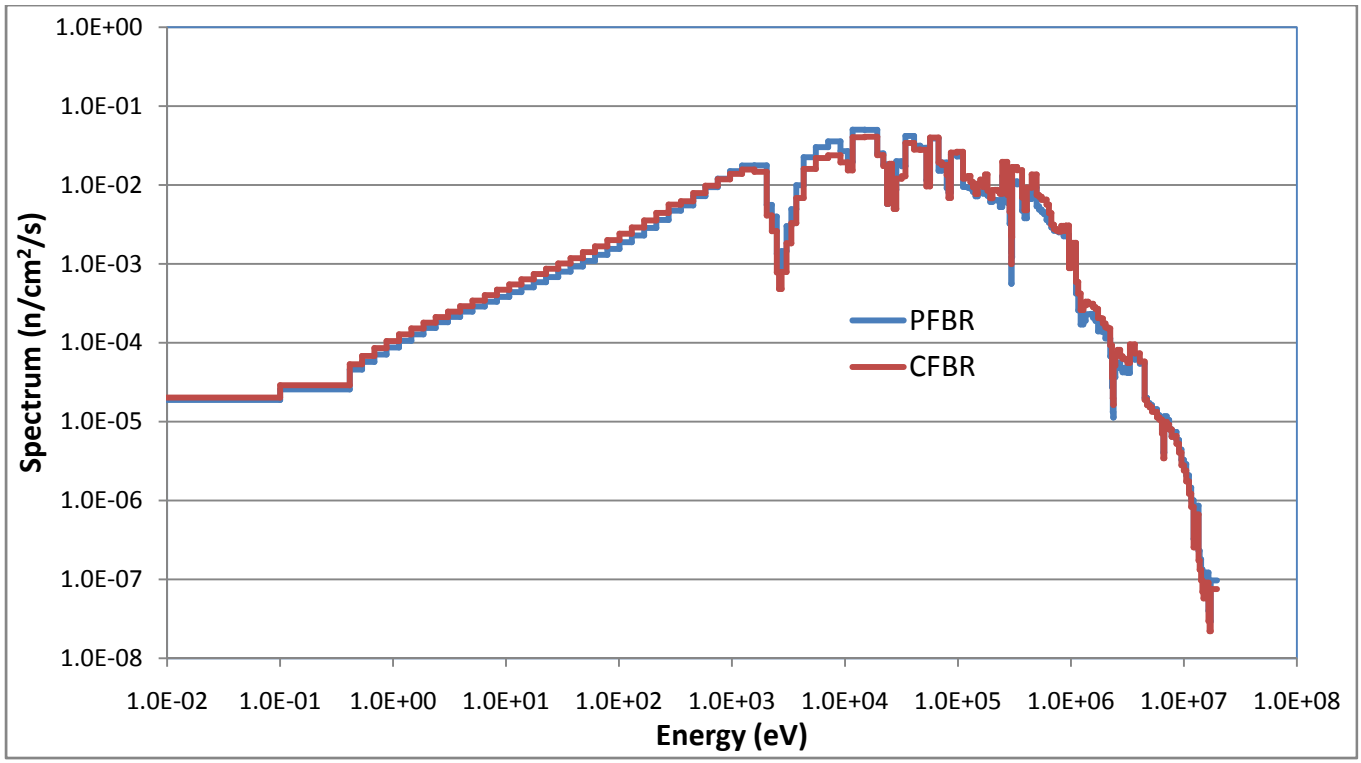

Fig-4.6: Comparison of neutron spectrum at the exit of shields

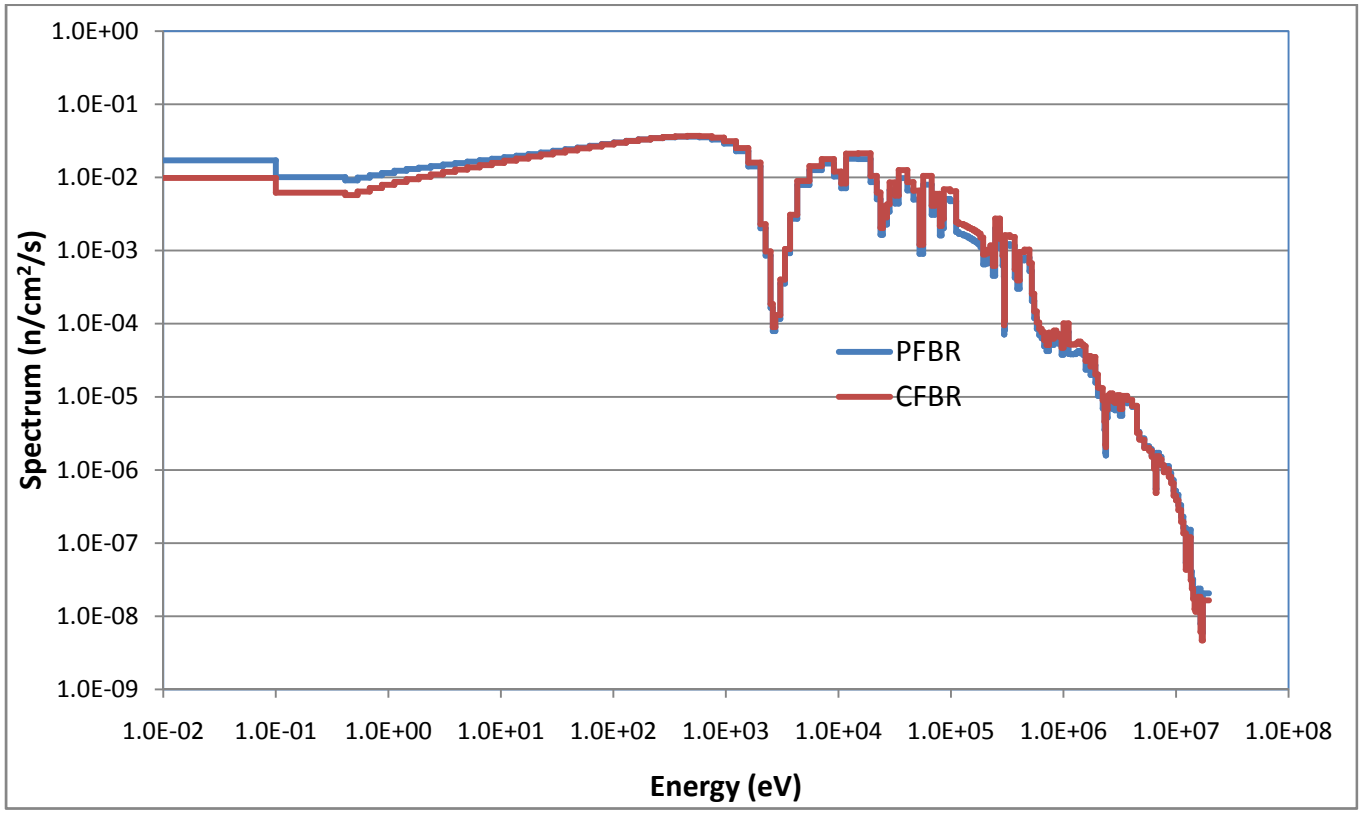

Fig-4.7: Comparison of neutron spectrum at the IHX location

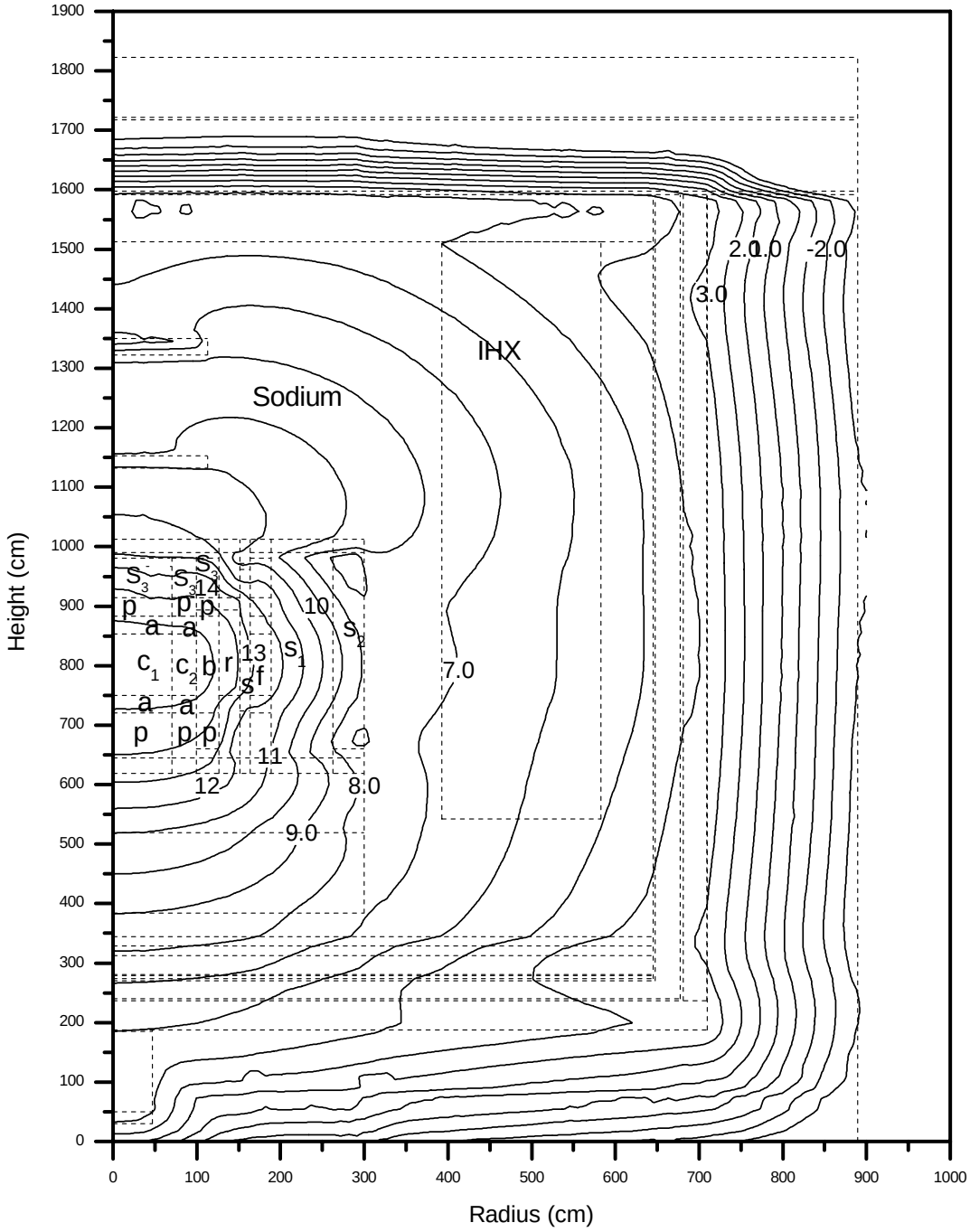

c_1- core1, c_2- core2, a- axial blanket, b- radial blanket, r- SS reflector,s- B_4C inner shield, f- storage, s1- radial SS shields, s2- radial B_4C shields, p- plenum, S_3- axial SS shields

Fig-4.8: Total neutron flux (n/cm^2/s) contours

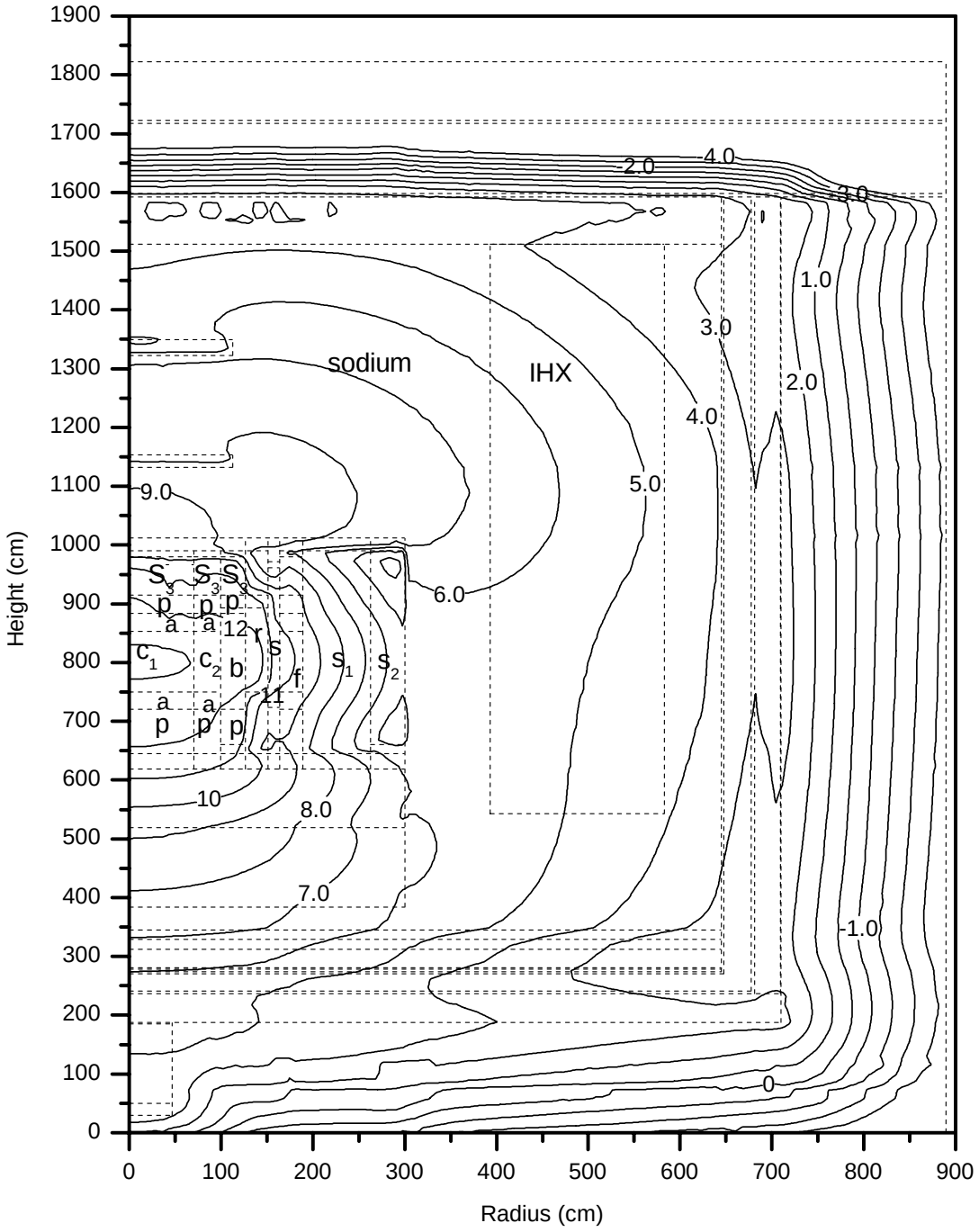

Fig-4.9: Sodium capture rate (10^{-24}Bq/atom) contours

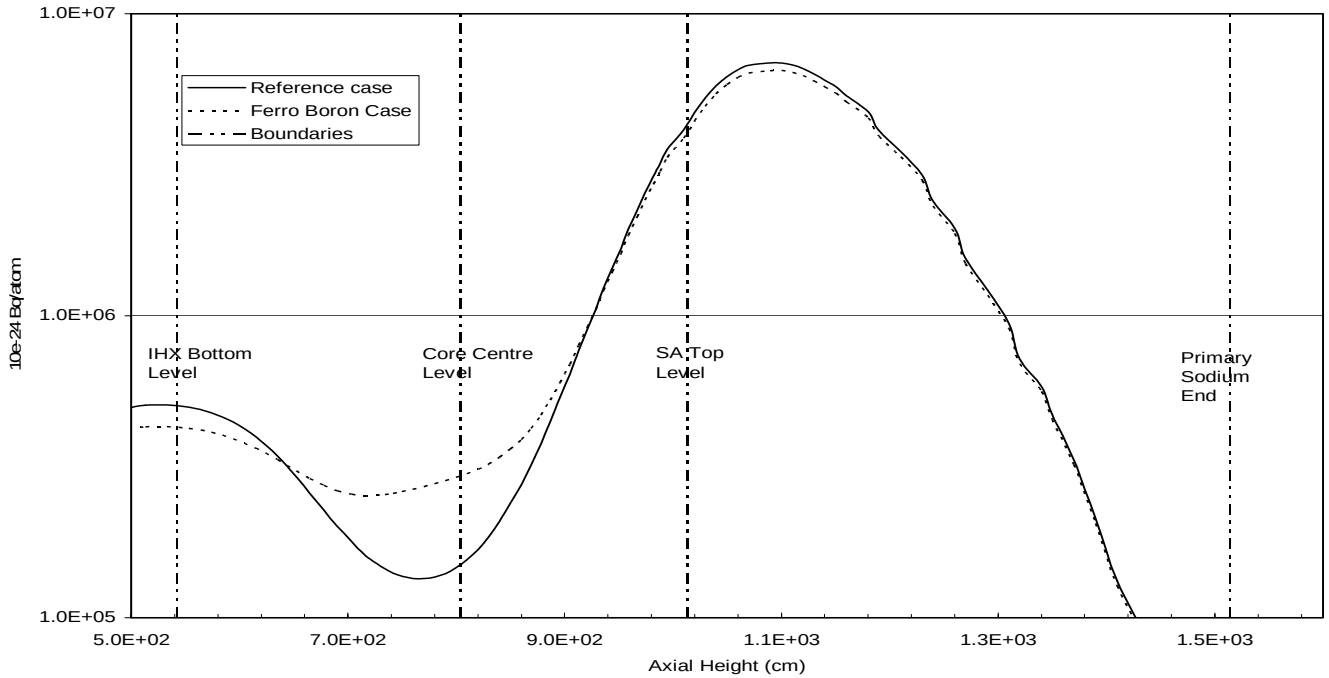

Fig-4.10: Maximum sodium capture rate along IHX

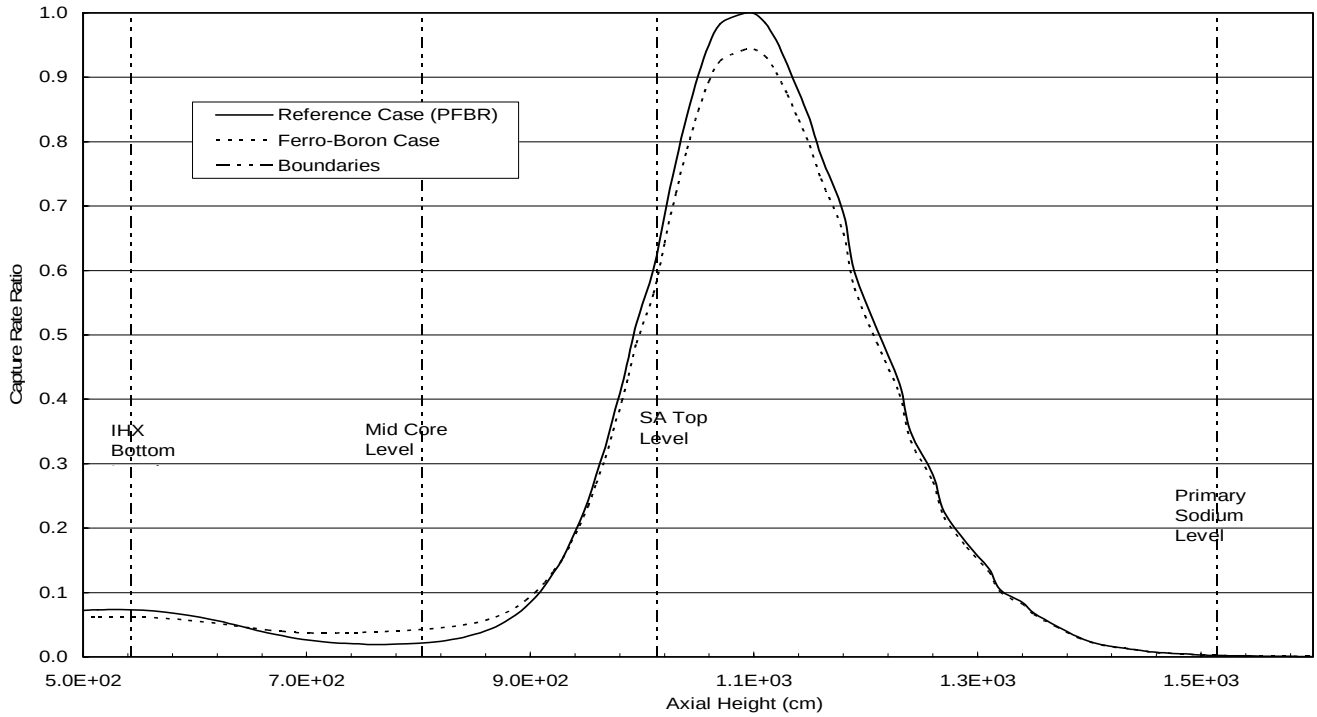

Fig-4.11: Sodium capture rate normalized to the peak value

Chapter – 5

AXIAL AND RADIAL SHIELD OPTIMIZATION FOR CFBRS WITH FERRO-BORON

5.1 Introduction

A series of Commercial Fast Breeder Reactors (CFBRs) are planned to be constructed in India (Chellapandi et al.,2010). Fe-B is proposed as in-vessel neutron shield in these reactors. Efficacy of radial shield subassemblies replaced by Fe-B subassemblies were discussed in Chapter-4. Size of the reactor vessel in a pool type fast reactor depends on the number of rows of radial shield assemblies. The reduction of number of rows of radial shields makes it possible to bring the IHX closer to the core, and hence reduction of reactor vessel size which is expected to bring down the overall cost. For achieving reduced number of shield rows, many axial and radial shield optimization studies are done. Shields provided in the upper axial part help in preventing of neutrons streaming towards IHX. Reduction in shield rows may increase the secondary sodium activity due to increased streaming. To offset this increase appropriate axial shields can be provided. But these may affect the neutron counts in the control plug detectors. Safety issues dictate the minimum count rate required to be measured at any power level. Therefore provision of more axial shields can cause detector counts to go below the allowed limit at low power operations. Reduction in axial shields give more counts in the detector location but the penalty one has to pay is that secondary sodium activity will go up. Therefore optimization studies are required for both axial and radial shield configurations. The studies carried out in this chapter take care of the twin aims of not sacrificing count rates but at the same time restricting secondary sodium activity below the allowed limit.

Calculations performed with eight rows of Fe-B assemblies instead of nine rows of shield assemblies as in the reference case, show an increase in secondary sodium activity. Therefore some changes in the axial shields are required to offset increase in sodium activity. Many axial shield configurations are studied (Sunil Kumar et al., 2013; 2009) for improving the detector counts and each time secondary sodium activity is also calculated. These studies include the replacement of a) axial B_4C in the core -1 and core -2 assemblies of PFBR with SS, b) axial B_4C in the core-1 subassemblies alone with SS, c) replacement of axial B_4C with Fe-B, d) replacement of both SS and B_4C with Fe-B. These options are investigated in core -1 and core-2 subassemblies separately and together also. The reference case is PFBR. The effectiveness is seen through two parameters 1) secondary sodium activity and dose in steam generator building (SGB) 2) detector counts at the above core monitoring location.

5.2 Geometry of Different Configurations of Cores with Shields

Comparative studies are made with respect to PFBR as reference core which is given in Fig.5.1. Three configurations with Fe-B shields are considered.

5.2.1 Reference case

The details of the modelling and calculations are given in Chapter-2. The RZ model of reference case is given in Fig.5.1.

5.2.2 Studies with Fe-B shields in the radial direction alone

Three configurations with Fe-B shields are considered. The different radial and axial configurations with FE-B studied are given below.

5.2.2.1 Case-1

In this configuration all the outer radial shield assemblies of reference case are replaced with Fe-B shield assemblies. But the total number of shield assemblies is reduced to 8 rows instead of 9 rows. The RZ model of case-1 is given in Fig.5.2.

5.2.2.2 Case-2

This is same as in case-1 so far as the outer radial shields are concerned. The axial SS shields at the top of the two rows of blankets are replaced with B_4C shielding. Same shielding is provided at the top of reflector assemblies. The density of B_4C pellets is taken at 2.4 g/cm^3. The RZ model of case-2 is given in Fig.5.3.

5.2.2.3 Case-3

This is same as case-2 except that the B_4C axial shield in core-1 subassemblies are replaced with stainless steel. The RZ model of case-3 is given in Fig.5.4.

5.3 Transport Calculations

5.3.1 Nuclear data

The cross section set IGC-S3 (Devan et al., 2002) is used in the calculations. The set is a 217- group coupled library as described in Chapter 2.

5.3.2 Calculations

Calculations are performed by 2 dimensional transport code DORT using IGC-S3 cross section set. The criterion used for flux convergence is 1.0E-04 and that for the fission convergence is 1.0E-03. The angular quadrature approximation used is S_8 and the order of scattering cross section anisotropy used is P_3. All the calculations are performed with 571 meshes in the radial direction and 718 meshes in the axial direction. Flux convergence was

achieved after 20 outer iterations. Inner iterations were varied between 20 to 25 for the groups. Reaction rates were also monitored for convergence simultaneously.

5.4 Results

5.4.1 Neutron spectra

The computed spectral shapes at the peak position for all cases including the reference case are almost similar as shown in Fig. 5.5. This is because of the contribution of the streaming neutrons towards flux peaking position in the IHX region. The spectral shape at the detector position in the control plug is shown in Fig.5.6. The spectrum shows that case-3 is more thermalised. This is attributed to the absence of B_4C in the axial portion of core-1 subassemblies. More thermal neutrons reach the detector region. Also the presence of 10 cm extra SS also contributes additionally for thermalization of neutrons.

5.4.2 Secondary Sodium Activity and Dose on Pipes in SGB

The secondary sodium activity is computed using the method explained in Chapter-2. When all the nine rows are Fe-B assemblies, secondary sodium activity is marginally lower than that of the reference case for the reasons explained earlier. Top parts of shield subassemblies in between core subassemblies and the IHX peak position have significant boron atom densities. In the reference case, the top portion of the first 6 rows of Stainless Steel shield assemblies does not have boron.

Secondary sodium is circulated through IHX with a circuit time t_C of 68.5 s and irradiation time (over one circuit) t_i of 7.2 s in the reactor considered. The secondary sodium activity per cm^3 of sodium is calculated using the standard formula which already described in the previous chapters.

The shielding surrounding the core and blankets in pool type of reactors is dictated by radiological criteria for dose due to secondary sodium activity in SGB and the neutron detector counts at the control plug location. Along the axial height of IHX the sodium capture rate becomes a maximum at a level about a meter below the top IHX window in all the cases studied. Peaking at this location occurs due to the absence of effective shields to stop streaming through the upper plenum regions in the fuel and blanket subassemblies. B_4C shielding provided at the top portion of fuel assemblies is small due to the requirement that flux at detector location in the control plug must not be low for detection.

Sodium capture rates for all three cases normalized to the peak value of the reference case are plotted in Fig. 5.7. Maximum sodium capture rate is lower in case-1 at all levels above subassembly top and the peak value is 96 % of the reference case. Detector flux is also not changed appreciably as discussed in the earlier section. The capture rate is slightly lower due to the presence of boron in the upper parts of the shield assemblies in the neutron streaming paths. But in the core mid plane of IHX, the capture rate is much higher as compared to the reference case since the number of rows of shield assemblies is 8 compared to 9 in the reference case and the rise in secondary sodium activity is about 25 %. This rise is not very high as the contribution from the core mid plane region is not very significant as seen in Fig.5.7.

The axial B_4C shielding in blankets and SS reflectors in case-2 with slightly higher density by about ~ 10 % decreases secondary sodium activity by 16 %. The peak capture rate is lower by 50 % due to the presence of additional B_4C in the upper part of blanket subassemblies. Since the number of radial shielding subassemblies is same in case-1 and case-2, capture rate at the core mid plane is same in both the cases. But the modification in axial shields of blanket and SS reflector has a negative impact on detector fluxes.

In case-3 also the increase in sodium capture rate at core centre does not affect the secondary sodium activity much because the capture rate corresponding to core centre location is only 13 % that of the flux peaking position as in cases1 and 2 . The secondary sodium activity increases marginally by 5 % in case-3 compared to reference case.

Secondary sodium activity normalized to the reference case for all three cases are given in Table 1. The behaviour is same for the dose in SGB.

Table - 5.1: Secondary sodium activity for each case normalized to the reference case

Case Studied	Secondary Sodium Activity
Reference Case	1.00
Case-1	1.25
Case-2	0.84
Case-3	1.05

5.4.3 Detector counts

The neutron monitoring systems are as described in Chapter - 4. The positions of neutron detectors at above core location can vary within a radius of approximately 200 cm from central axial position. The reaction rates, U-235(n,f) and B-10 (n,α) are computed as a function of radius and are shown in Fig.5.8 and Fig.5.9 respectively for all the three cases relative to the reference case value.

Fe-B radial shields have only a minor impact on flux at detector location. The neutron detectors for core flux monitoring on the control plug are located at the level of lattice plate above core. Neutron counts are estimated by averaging U-235 fissions over the entire active length of the detector placed in control plug locations. The results show that by replacing the

shield assemblies with Fe-B, the neutron counts in case-1 are only 3 % lower as compared to the reference case. But when axial SS is replaced with B_4C at the top of the two rows of blankets (case-2) the detector counts are 22 to 46 % lower compared to the reference case. To overcome this reduction in flux in the control plug detector, 10 cm B_4C shield in the upper portion of the core-1 subassemblies alone are replaced with SS in case-3. This modification in axial shields increases the detector fluxes nearly 50 % as compared to the reference case. A comparison of detector counts with reference core is given in Table 5.2.

Table – 5.2: Boron detector (located 75 cm above core SA top) counts and fission chamber (located 45 cm above the core SA top) counts at different radial distances from core axis for different cases. All counts normalized to the reference case

	Case-1		Case-2		Case-3	
Radial Distance	U-235	B-10	U-235	B-10	U-235	B-10
0.0	1.00	1.00	0.79	0.74	2.18	2.08
50.0	1.00	1.00	0.75	0.72	1.91	1.89
100.0*	1.00	1.00	0.66	0.67	1.41	1.54
125.0	1.00	1.00	0.62	0.65	1.23	1.38
150.0	0.99	0.99	0.59	0.63	1.13	1.26
200.0	0.97	0.98	0.55	0.59	1.01	1.11

* Detector position in normal reactor operation

5.5 Fe-B in the Axial Region of Core Subassemblies

Fe-B was used only in the radial subassemblies till now in our studies. Use of Fe-B in axial shields in core subassemblies is studied now. All the axial modifications in core subassemblies are done considering only eight rows of radial shield assemblies with Fe-B. In all

cases, the volume fractions of Fe-B used in the axial region of core subassemblies are equal to the volume fractions of B_4C used in the axial region.

5.5.1 Case-4

Here 10 cm B_4C in the core-1 subassemblies alone are replaced with Fe-B.

5.5.2 Case-5

Both Stainless Steel (66.5 cm) and B_4C (10 cm)in the axial region of core-1 subassemblies are replaced with Fe-B.

5.5.3 Case-6

B_4C in the core-1 and core-2 subassemblies are replaced with Fe-B.

5.5.4 Case-7

Both SS and B_4C in the axial region of core-1and core-2 subassemblies are replaced with Fe-B.

5.6 Results for Fe-B in Axial Shield Region

The secondary sodium activity in case-4 is 97 % of the reference case. This reduction is due to the presence of B_4C in the axial region of Blanket subassemblies. The peak value of the sodium reaction rates in the IHX level also comes down to 68 % compared to the reference case even though along the central radial direction it goes up. But secondary sodium activity is higher than case-2 where it shows B_4C in the axial region of core-1 subassemblies is a better shield. However, compared to case-2 detector counts have improved.

Table 5.3: Secondary sodium activity for each case normalized to the reference case for axial modification with Fe-B

Cases Studied	Secondary Sodium Activity
Reference Case	1.00
Case-4	0.97
Case-5	1.11
Case-6	0.82
Case-7	0.83

The secondary sodium activity in case-5 is more than the reference value. Also compared to case-4 the peak value of sodium capture along IHX goes up. This offsets the advantage of detector flux going up compared to reference case. Both U-235 and B-10 count rates increase.

Table 5.4: Boron detector (located 75 cm above core SA top) counts and fission chambers (located 45 cm above the core SA top) counts at different radial distances from core axis for axial Fe-B shields. All counts normalized to the reference case

	Case-4		Case-5		Case-6		Case-7	
Radial Distance	U-235	B-10	U-235	B-10	U-235	B-10	U-235	B-10
0.0	1.27	1.17	1.41	1.33	2.18	2.08	2.18	2.08
50.0	1.17	1.12	1.34	1.29	1.91	1.89	1.91	1.89
100.0*	0.98	1.01	1.17	1.19	1.41	1.54	1.41	1.54
125.0	0.90	0.96	1.08	1.14	1.24	1.38	1.24	1.38
150.0	0.84	0.91	1.03	1.09	1.13	1.26	1.13	1.26
200.0	0.79	0.85	0.96	1.03	1.01	1.11	1.01	1.11

* Detector Position in normal reactor operation

In case-6 where B_4C and SS in core -1 assemblies are replaced with Fe-B, the secondary sodium activity decreases to 82 % of the reference case. But in case-7 secondary sodium activity is almost same as that of case-6. This can be seen in Fig.5.10 where the sodium reaction rates are overlapping each other. But the detector counts are higher compared to any other case. Increase in detector counts by 41 to 54 % is observed in the normal operation condition in these cases. The reduction of secondary sodium activity and at the same time increase of detector counts gives scope for reduction of height of subassemblies in future (CFBR) reactors when both SS and B_4C in core-1 or core-1 & core-2 subassemblies are replaced with Fe-B. The ratio with respect to the reference case for secondary sodium activity is given in Table 5.3 and the ratio of the detector counts in the control plug location are given in Table 5.4.

5.7 Summary

Optimization studies with the use of the shield material Fe-B was carried out with reference to a) reduction of radial shields and b) axial shields to improve flux at control plug detector location without affecting secondary sodium activity. Three shield configurations were considered with reduced number of shield assemblies with Fe-B instead of SS and B_4C used as in the reference case of PFBR. With the modifications introduced in the radial shields and axial shields of blanket, core and reflectors, the secondary sodium activity in all the three cases is not significantly different from the reference case. The changes in shields made in CFBR bring about the following improvements over PFBR shields:

- The choice of Fe-B as radial shield results in economy of the use of shield material. The weight reduction of the outer rows of in-vessel shields is by about 50 % of PFBR outer shields and the cost is down to approximately 17 % of the shields in the reference case.

- Out of the three, the best axial shield configuration is where axial SS shielding is provided over core-1 and axial B_4C shielding is provided over blanket and reflector subassemblies. This increases the detector counts by about 50 % for CFBR without affecting secondary sodium activity.

- The reduction of number of rows of radial shields makes it possible to bring the IHX closer to the core, and hence reduction of reactor vessel size. The cost saving due to this is still to be worked out as it involves many complex parameters to be considered.

- Calculations have indicated that use of Fe-B in the axial shield region of PFBR can lead to reduction of Subassembly height.

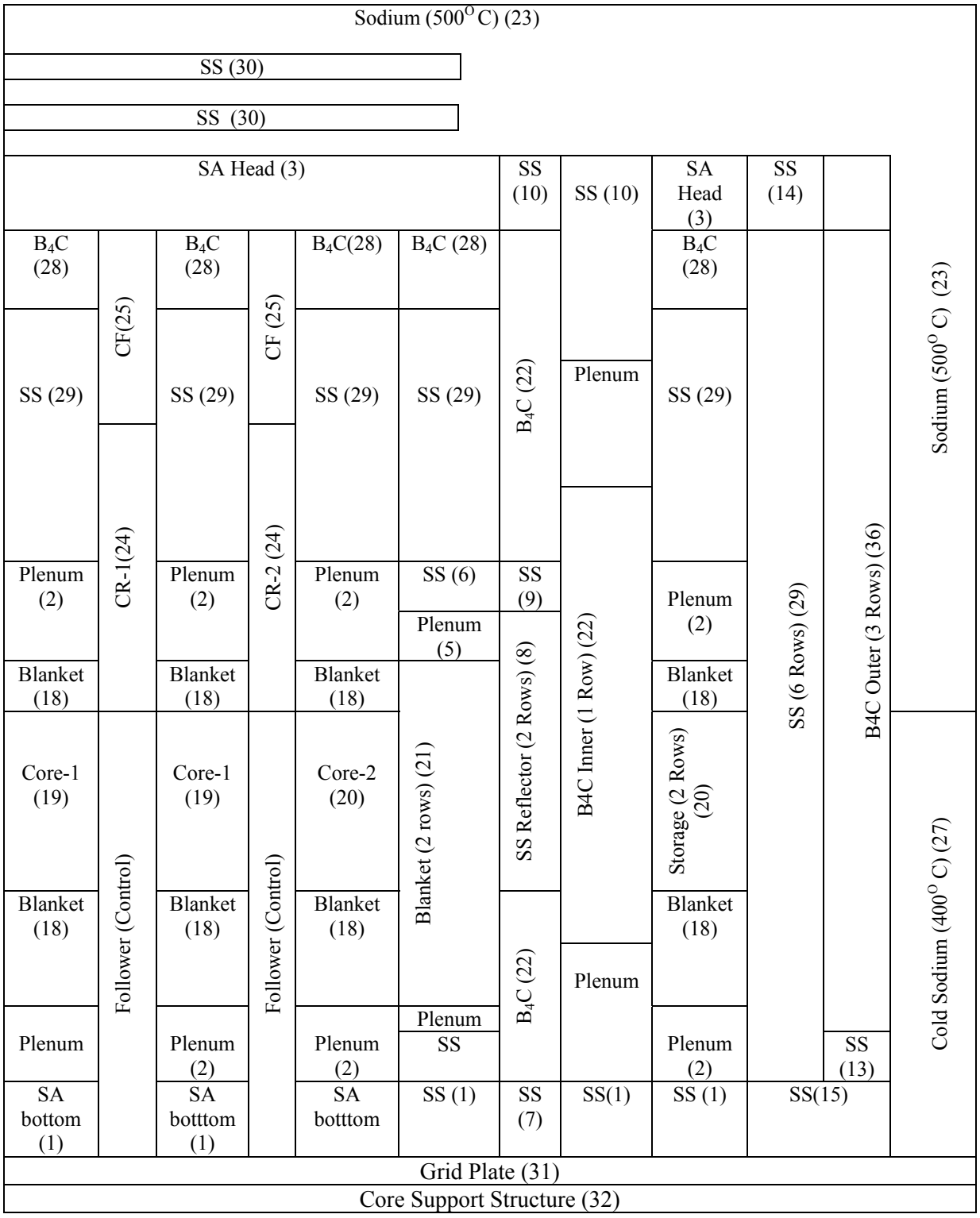

Fig-5.1: 2D R-Z Calculational model for reference case (PFBR)

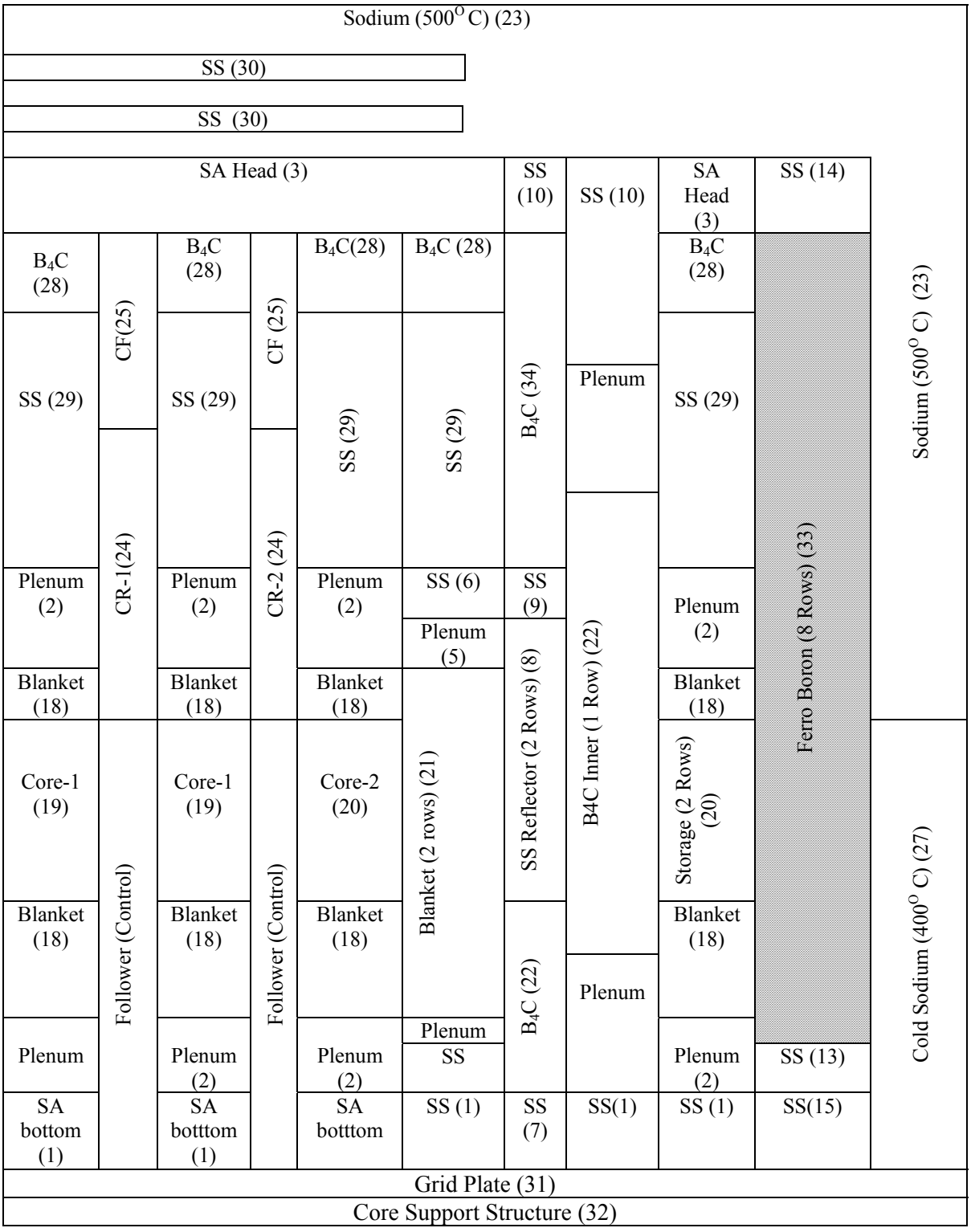

Fig-5.2: 2D R-Z Calculational model for case- 1

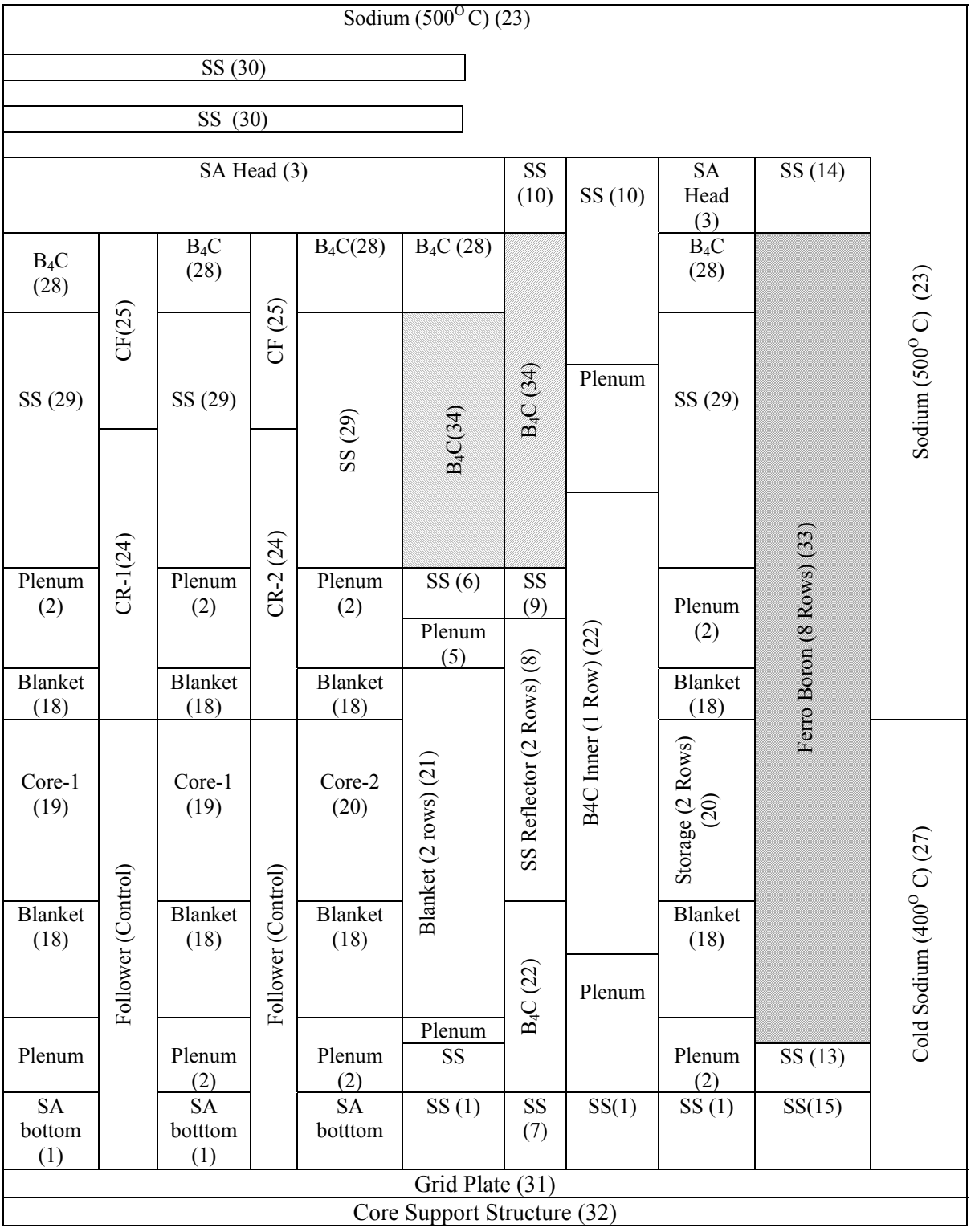

Fig-5.3: 2D R-Z Calculational model for case- 2

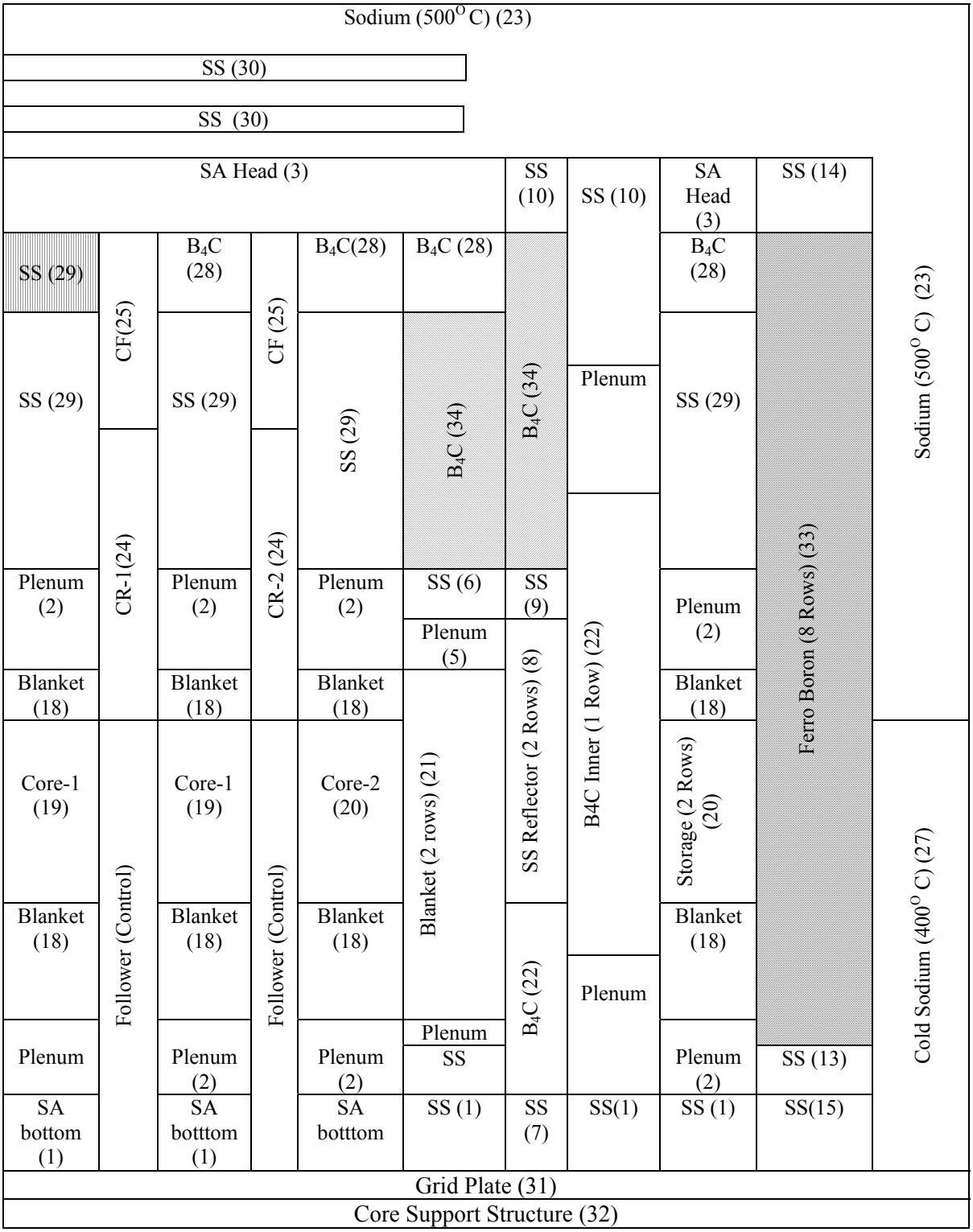

Fig-5.4: 2D R-Z Calculational model for case- 3

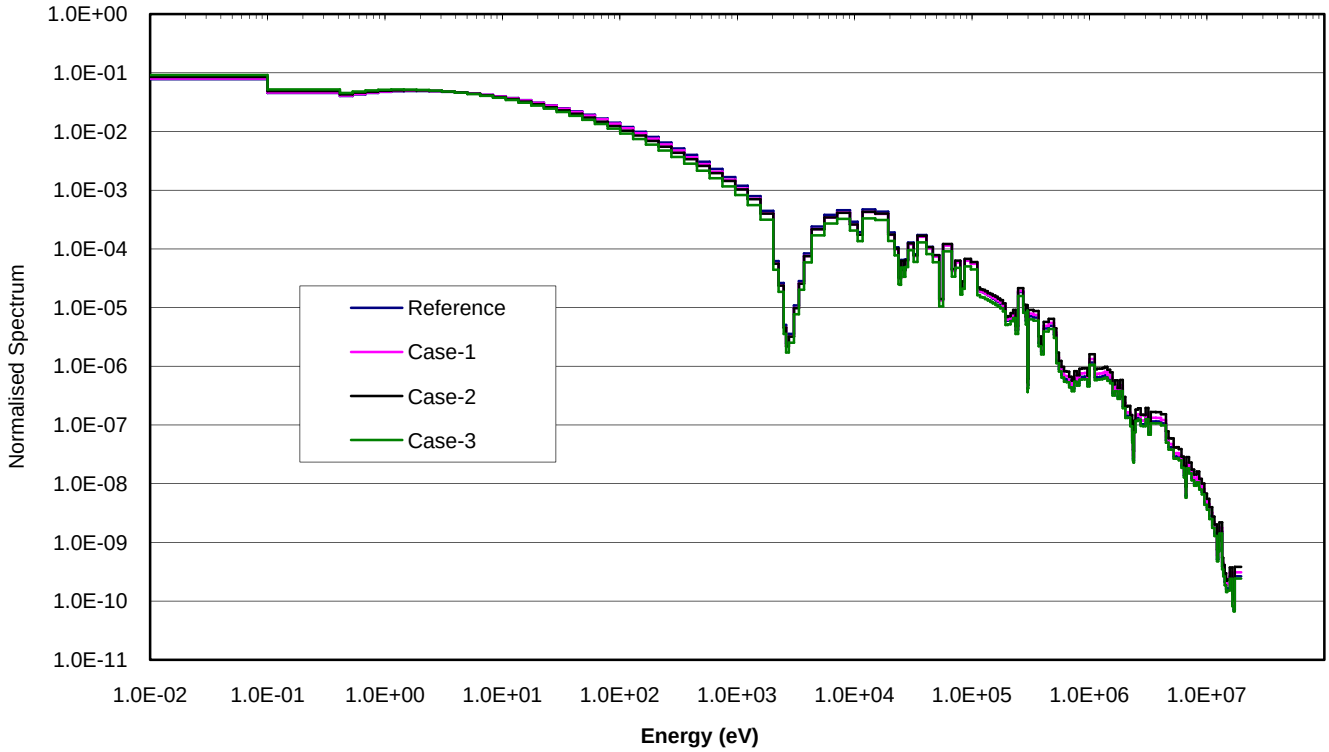

Fig-5.5: Comparison of spectra at flux peaking position of IHX

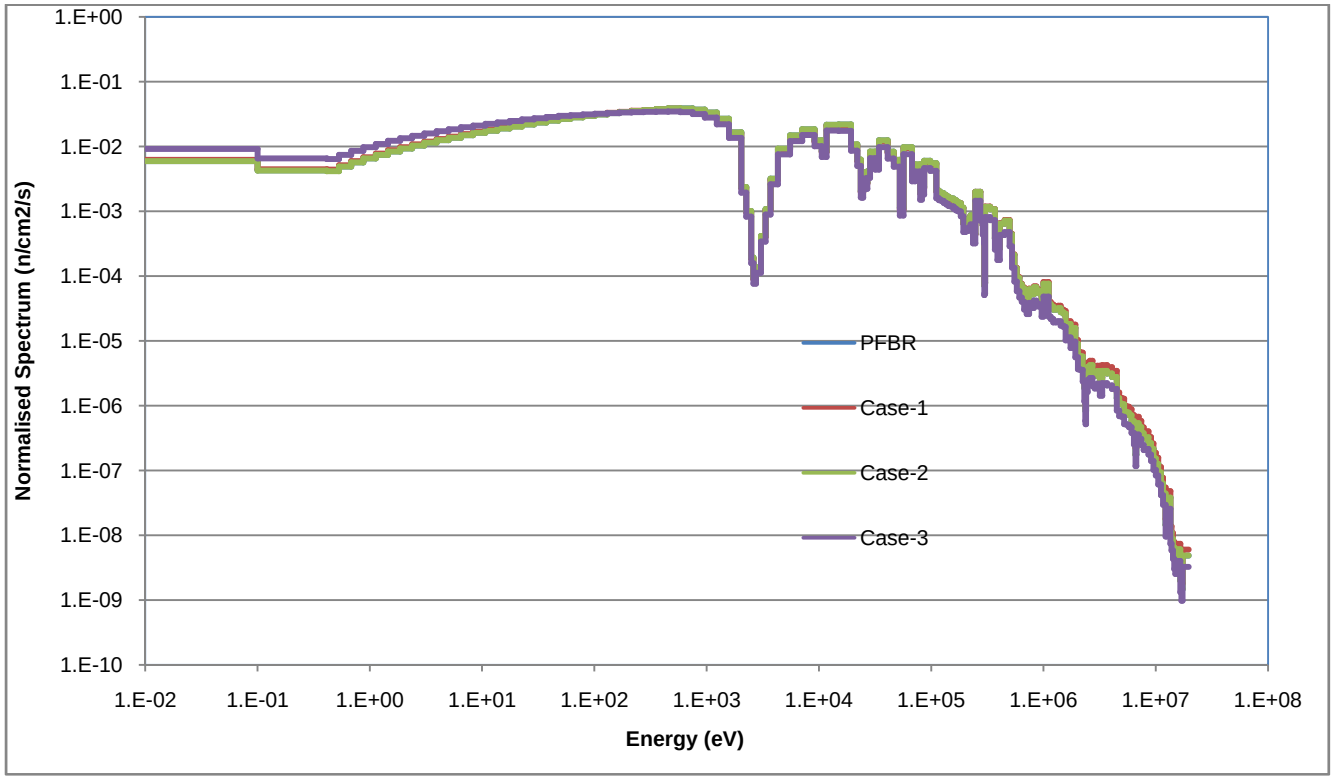

Fig-5.6: Neutron spectra at control plug detector location for various cases

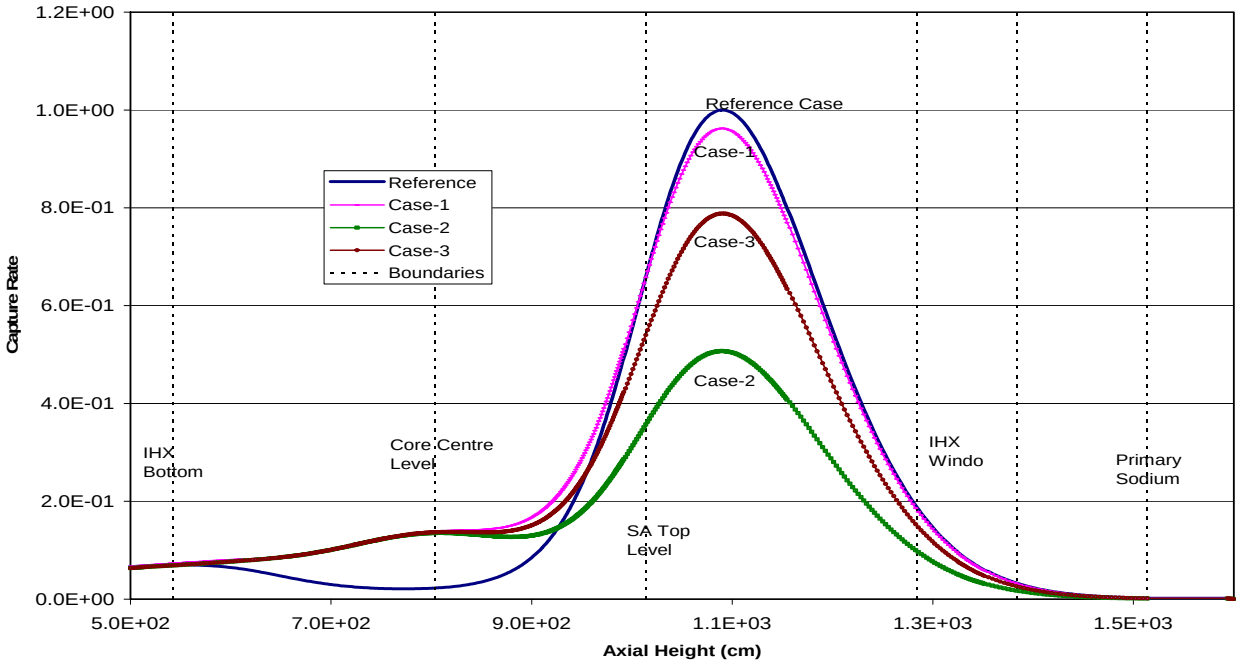

Fig-5.7: Maximum sodium capture rate (along IHX) normalised to the peak value of reference case

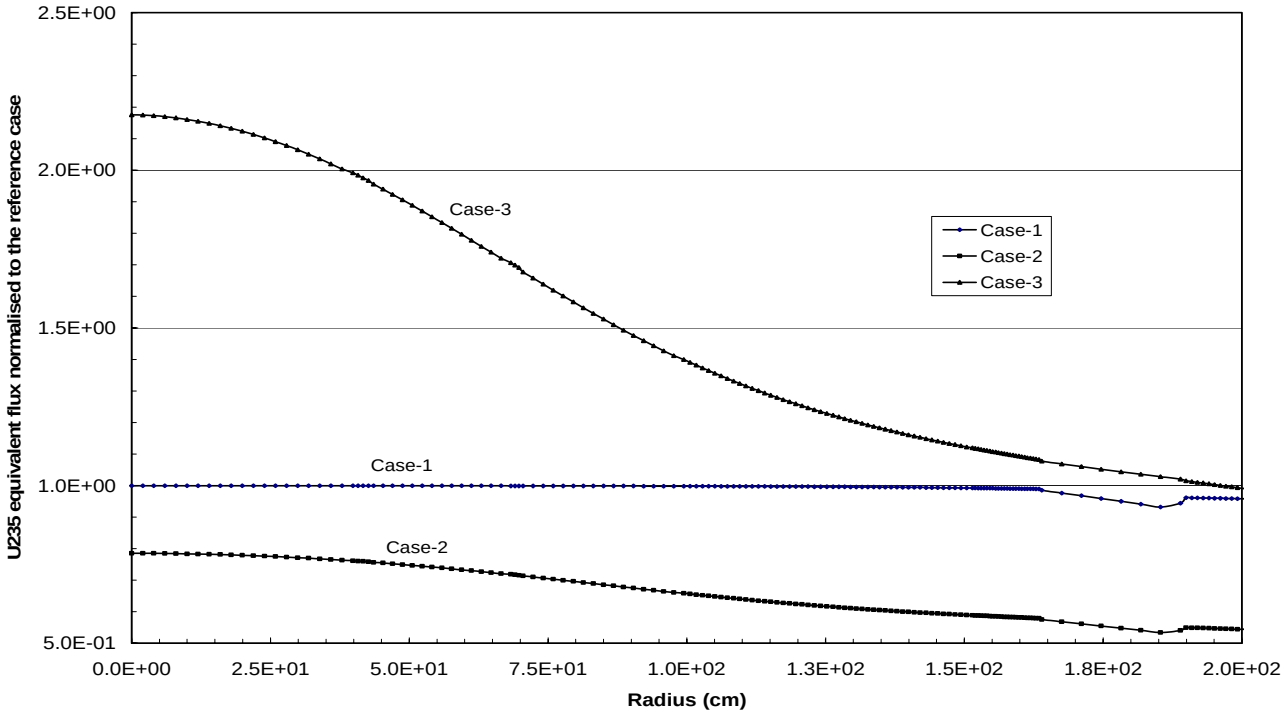

Fig-5.8: Radial variation of U-235 equivalent fluxes in the control plug location.

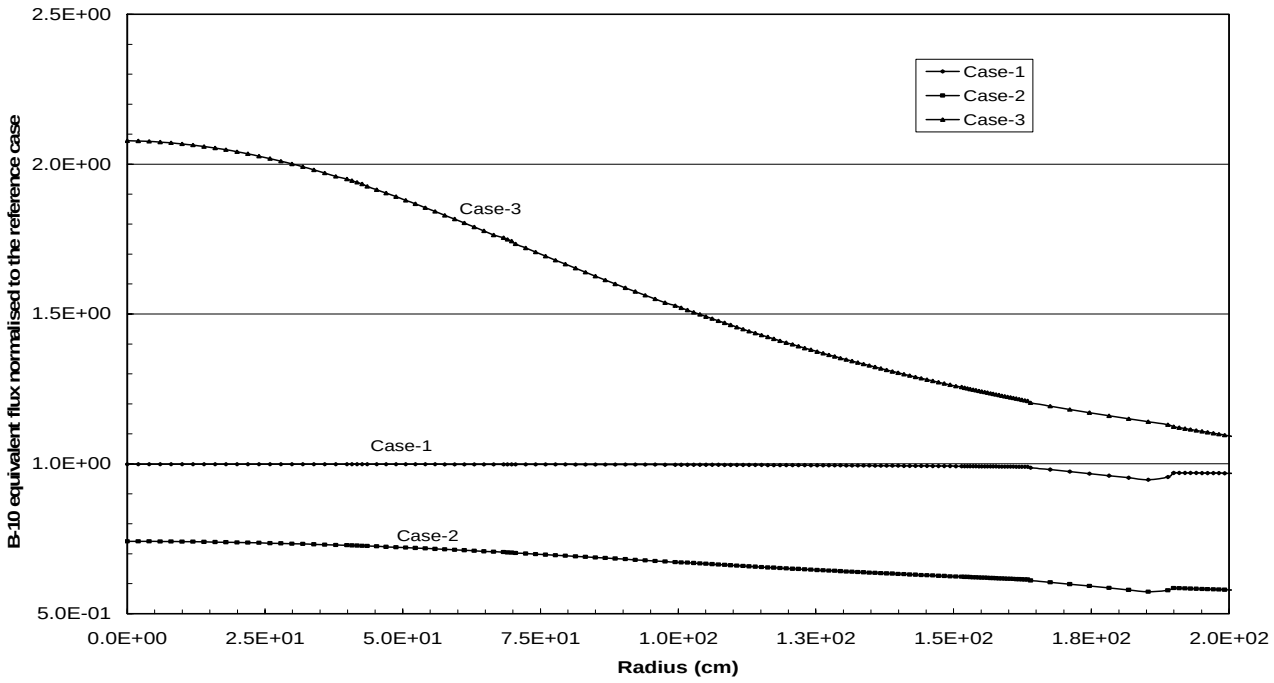

Fig-5.9: Radial variation of ratio of B-10 equivalent fluxes in the control plug location

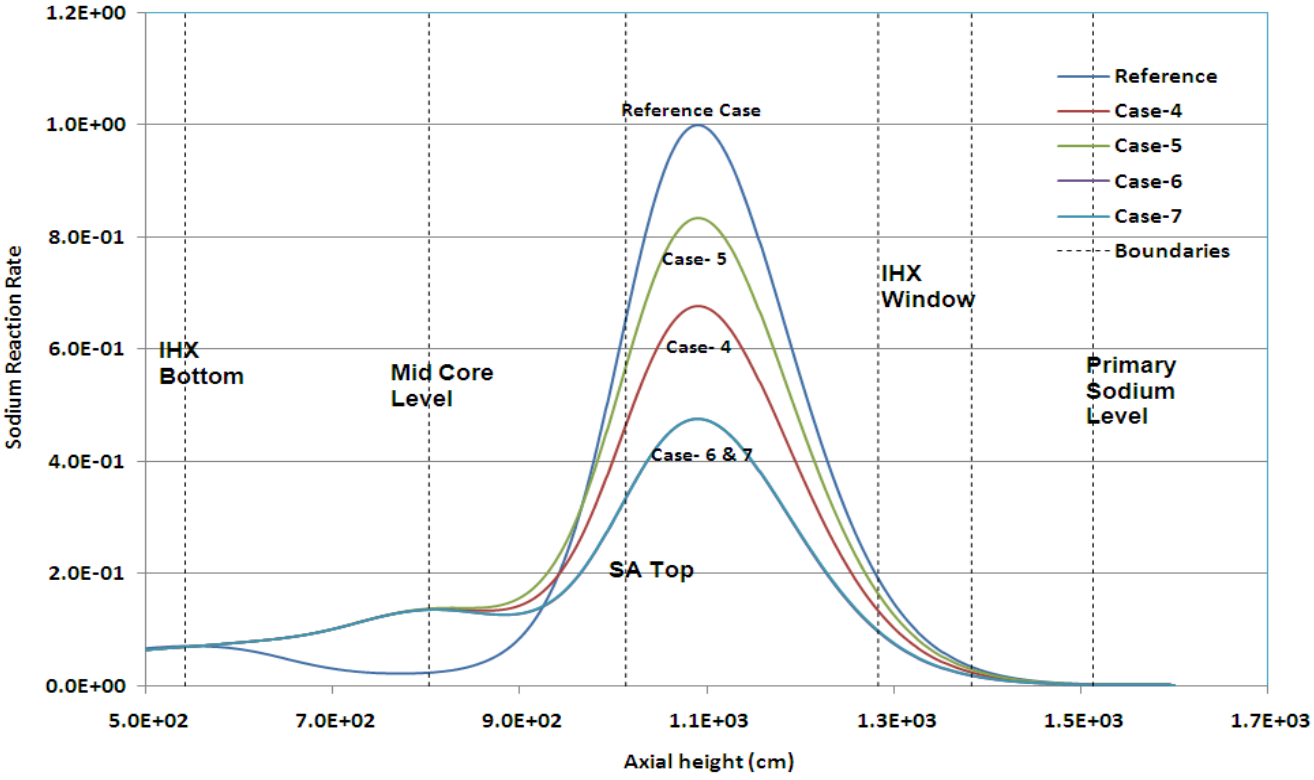

Fig-5.10: Maximum sodium capture rate (along IHX) normalised to the peak value of reference case for axial Fe-B cases

Chapter – 6

STUDIES ON AXIAL SHIELDS IN FBTR AND RADIATION DAMAGE TO GRID PLATE

6.1 Introduction

FBTR has been successfully operating since 1985 (Srinivasan, G., 2006). It has seen more than 1300 days of effective full power operation and has been a workhorse for irradiation experiments. This is the only high flux, high temperature fast spectrum reactor in India. In the recent campaigns, Fe-B and Sphere-pac fuel were irradiated and currently it is undergoing metal fuel irradiations to study neutronic and thermal hydraulic properties of metal fuel for fast reactors. Some of the important irradiation experiments in the past which gave valuable information were irradiation of Zircolloy, test subassembly with PFBR fuel composition, and varieties of structural and clad materials.

The core of FBTR was originally designed with 65 SA of MOX with 30 % PuO_2 & 70% UO_2 (enriched to 85 %). Due to certain constraints on fuel, the reactor was made critical with 22 SA of MK-I SA (70 % PuC+30 % UC). The resulting power was only 10.6 MWt as against the original design power of 40 MWt. However, the peak flux for the 65 SA MOX core and the MK-I core are comparable. The spectrum of the MK-I core is harder, and the flux incident on the grid plate is also higher since the MK-I SAs are only provided with steel reflectors. The reactor core has been progressively enlarged by adding MK-II SA and high Pu MOX SA. The core in the 21st campaign has 29 MK-I, 11 MK-II and 8 MOX subassemblies. Though the reactor power has been lower as compared to the original design power level of 40 MWt, the neutronic fluence and the *dpa* levels seen by the Grid Plate are comparable to what would be seen if the reactor has

operated with the originally envisaged 65 SA MOX core. FBTR grid plate is a permanent core structure subjected to irradiation over the life time of the reactor. The grid plate material is a modified version of Type 316 stainless steel, identified as Type 316 SS (FBTR quality), and has more stringent composition specifications than the corresponding ASTM grade. The data on the change in mechanical properties of this material due to exposure to radiation is not available.

An assessment of life of grid plate was made at the end of 18th campaign (Reddy et al., 2012]. An irradiation experiment was carried out in FBTR to determine the change in mechanical properties of specimens made of grid plate material at the desired low fluence irradiation conditions. Based on analysis of experiments and flux measurements at grid plate location, the residual life of FBTR was estimated to be 6.52 effective full power year (EFPY) at the end of 18th campaign [Reddy et al., 2012]. It was also planned that fresh specimens be irradiated up to ~6 *dpa* before the end of 3.5 EFPY since the results were based on linear extrapolation from 2.5 *dpa* to 4.5 *dpa*.

In view of the unique nature of FBTR as a fast flux facility for material and fuel irradiation experiments, radiation damage to grid plate and the consequent effect on life of FBTR have become important issues. It was contemplated by the plant to go for a hybrid core with MOX and MK-II assemblies (Srinivasan et al., 2005). This involves increased length of outer MOX core assemblies. If such a core changes are contemplated, it is important to estimate the effect of increased length of subassemblies on the grid plate. In this chapter we present studies carried out on radiation damage of grid plate. Section 6.2 is concerned with radiation damage due to proposals such as above of converting FBTR into a hybrid core with MOX and MK-II subassemblies to verify whether such cores can give rise to higher radiation damage. The studies

on suitable axial shields with dimensional constraints to reduce radiation damage to grid plate are presented in section 6.3.

6.2 Hybrid Core with MOX and MARK-II Subassemblies

The option of using more MOX assemblies was considered by the plant. If the dimensions of the subassembly have to be retained, higher Plutonium content has to be considered. However reports in open literature indicate that MOX with PuO_2 content only up to the extent of 45 % (Sengupta et al., 2006) is compatible with sodium. It is not possible to reach criticality, in FBTR, with a full core of MOX with this PuO_2 content, since the core has to be confined within the area covered by the core cover plate mechanism, which limits the core size to 85 subassemblies. But with MOX core alone the reactor cannot become critical with this enrichment of Plutonium. An alternate strategy of having hybrid core with Mark-I fuel at the centre and MOX fuel at the periphery was thought of (Srinivasan et al., 2005). This hybrid core is capable of giving 30 MWt power.

The MOX subassemblies would have a fissile column length of 43 cm which is higher than Mark-I subassemblies (32 cm). The lower position of these subassemblies would then be closer to the grid plate as seen in Fig.6.1. Hence a new calculation of radiation damage on grid plate was necessitated. There was a concern whether displacement per atom (*dpa*) of the top of the grid plate would be higher below the MOX fuel region. Increased *dpa* would again limit reactor life. Typically a limit of 1.3 *dpa* (Tavassoli Ali Asghar, 1990) has been quoted as grid plate cannot be inspected. Many full 2-D RZ transport calculation including all the shields were carried out for FBTR hybrid core using 175 group cross sections in the Vitamin - J structure (Sunil Kumar, et al., 2006; 2008).

Another option of going for a full Mark-II core was also contemplated (FBTR safety report, 1995). Mark-II subassemblies require lower plutonium content. Since radiation damage to grid plate is a critical issue for extension of FBTR life, it was of interest to compare the radiation damage (*dpa*) rate in grid plate between hybrid core and the present existing core with Mark-I core at the centre and Mark-II core at the periphery. The 2D RZ schematic of Mark-II core with thoria blanket is shown in Fig.6.2.

6.2.1 Nuclear Data

The cross section set IGC-S3 (Devan et al., 2002) is used in the calculations. The set is a 217- group coupled data set as described in Chapter 2.Transport calculations were carried out with self shielded cross sections generated in IGC-S3 format called IGCS3-S (Sujoy Sen and Gopalakrishnan, 2006).

6.2.2 Core geometry and model of calculation

Calculations were performed by 2 dimensional transport code DORT using IGC-S3 cross section set. Modelling is done in 2D RZ geometry is given in Fig.6.3. Table 6.1 gives the various volume fractions at different regions in transition zones. Totally 40 mixtures are used in the calculations and the atom densities in various regions are taken from Ref (Sunil Kumar et al., 2005). The criteria used for flux convergence and that for eigen value convergence are same as described in the earlier chapters viz., 1.0E-03 and 1.0E-04. This convergence was obtained in all groups at all spatial mesh points. The angular approximation used is S_8 and the order of scattering cross section anisotropy is P_5. The fluxes are normalised to a total of 2.96E+15 n/cm^2/s (for 30 MWt operation) at the core centre derived from the core calculations (Sivakumar et al., 2005).

Total 269 meshes are taken in the radial direction and 417 meshes are taken in the axial direction.

6.2.3 Neutron spectra

The core averaged neutron spectra obtained for the Hybrid and Mark-II cores are given in Fig. 6.4 in the 175 energy group structure. It is seen that hybrid core has a lightly harder spectrum.

6.2.4 Fluxes

The contour plots of total neutron flux for both hybrid core and Mark-II core are given in Fig.6.5 and Fig.6.6 respectively. The corresponding figures for fast flux (>0.1MeV) are shown in Fig. 6.7 and 6.8 respectively. Total neutron fluxes are normalized to the same value of 2.96E+15 $n/cm^2/s$ at core centre for both hybrid core and full Mark-II core and the corresponding reactor powers are 30MWt and 33.83 MWt respectively. Tables 6.2 and 6.3 show the behaviour of total neutron flux, U235 equivalent flux, fast flux above 0.1 MeV and fast flux above 1 MeV along the central axial line for hybrid core and Mark-II core respectively using IGCS3-S cross section set. Axially the total flux above 0.1 MeV is 4.92E+13 $n/cm^2/s$ and that above 1 MeV is 2.16E+12 $n/cm^2/s$ respectively above the grid plate for hybrid core. The corresponding values for Mark-II core in this location are 4.19E+13 $n/cm^2/s$ and 2.15E+12 $n/cm^2/s$. Thus the fast fluxes are only slightly larger for hybrid core. These fluxes above cover gas as incident on control plug bottom are 2.84E+09 $n/cm^2/s$ and 1.27E+08 $n/cm^2/s$ respectively for hybrid core case. The respective flux values are lower in the case of Mark-II core and are 2.08E+09 $n/cm^2/s$ and 0.86E+08 $n/cm^2/s$.

Table 6.4 and 6.5 show the behavior of these fluxes along the radial direction at the grid plate level.

6.2.5 Radiation damage and helium production

The radiation damage to the structural material depends on the neutron flux, neutron energy or energy spectrum, irradiation time, temperature and crystal and defect structure. Evaluation of radiation damage is made in terms of displacement per atom (*dpa*). The value of *dpa* due to neutrons at position (i, j) are calculated by integrating the neutron flux with displacement cross section:

$$(dpa/s)_{i,j} = \sum_{x}\sum_{k=1}^{NG} f_x \sigma_x^k \phi(i,j,k) \qquad (6.1)$$

where$f_x$is the fraction of the isotope x present in steel, σ_x^k is the damage cross section (Gopalakrishnan , 1994) and ϕ is the energy dependent flux at position (i, j).

The computed *dpa* values decrease continuously from core centre to the boundary. The radiation damage along the radial direction through the grid plate top is shown in Fig.6.9. The maximum *dpa/s* experienced at the grid plate top is 1.34E-08 and 1.24E-08 respectively for hybrid core and Mark-II core. The maximum *dpa/year* on the grid plate below the hybrid core is 0.43 whereas in the case of Mark-II core the maximum value on the grid plate is 0.39. The *dpa* experienced on the grid plate corresponding to the beginning of the MOX fuel is 0.38 and the corresponding value at the end of the MOX fuel is 0.30. The corresponding values at the same radial positions on the grid plate are 0.34 and 0.26 for Mark-II core. On top of the grid plate, the *dpa* falls monotonically from the core centre to nickel reflector despite the longer MOX fuel region. FBTR being an experimental reactor, capacity factor is low. A limit of 1.3 *dpa* for grid

plate will correspond to 3 and 3.33 full power years of reactor operation for hybrid and Mark-II core respectively. Therefore from the radiation damage due to longer MOX fuel subassembly does not restrict reactor life when compared with only MARK-II core (Sunil Kumar et al., 2005).

Calculations of helium productions were also carried out using the (n,α) cross sections in 100 groups as well as in 175 groups (Sujoy Sen et al., 2005). The helium production along the radial direction through grid plate is shown in Fig. 6.10. The maximum helium production experienced on the grid plate for Hybrid core and MARK-II core are 1.30E+09 cm^3/sand 1.46E+09 cm^3/s respectively. The maximum values of helium production for Hybrid core and MARK-II for one year are 0.32 appm (atoms parts per million) and 0.38 appm and the minimum values are 0.26 appm and 0.33 appm respectively. The limit specified for the internal structures of fast breeder reactors is 3 appm (Tavassoli Ali Asghar, 1990). Helium production restricts reactor life to about 9 efpy and 8 efpy for Hybrid and Mark-II core respectively. This is less restrictive as compared to radiation damage to the grid plate.

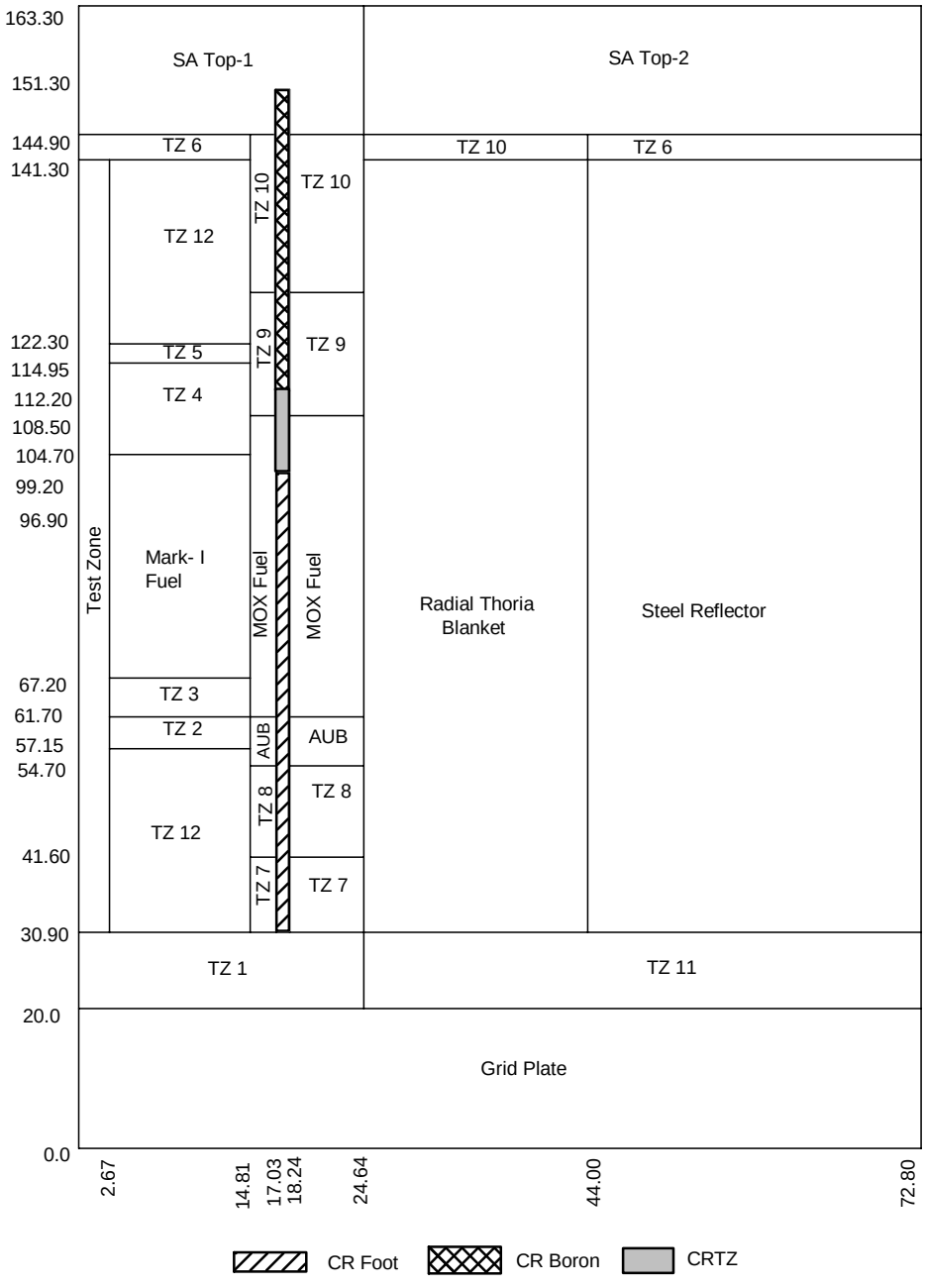

Fig-6.1: 2D R-Z Schematic model of FBTR (Hybrid Core)

* The regions marked as TZ in the figures are Transition Zones (Steel, Na and Void) and the volume fractions of these zones are given in Table 6.1.

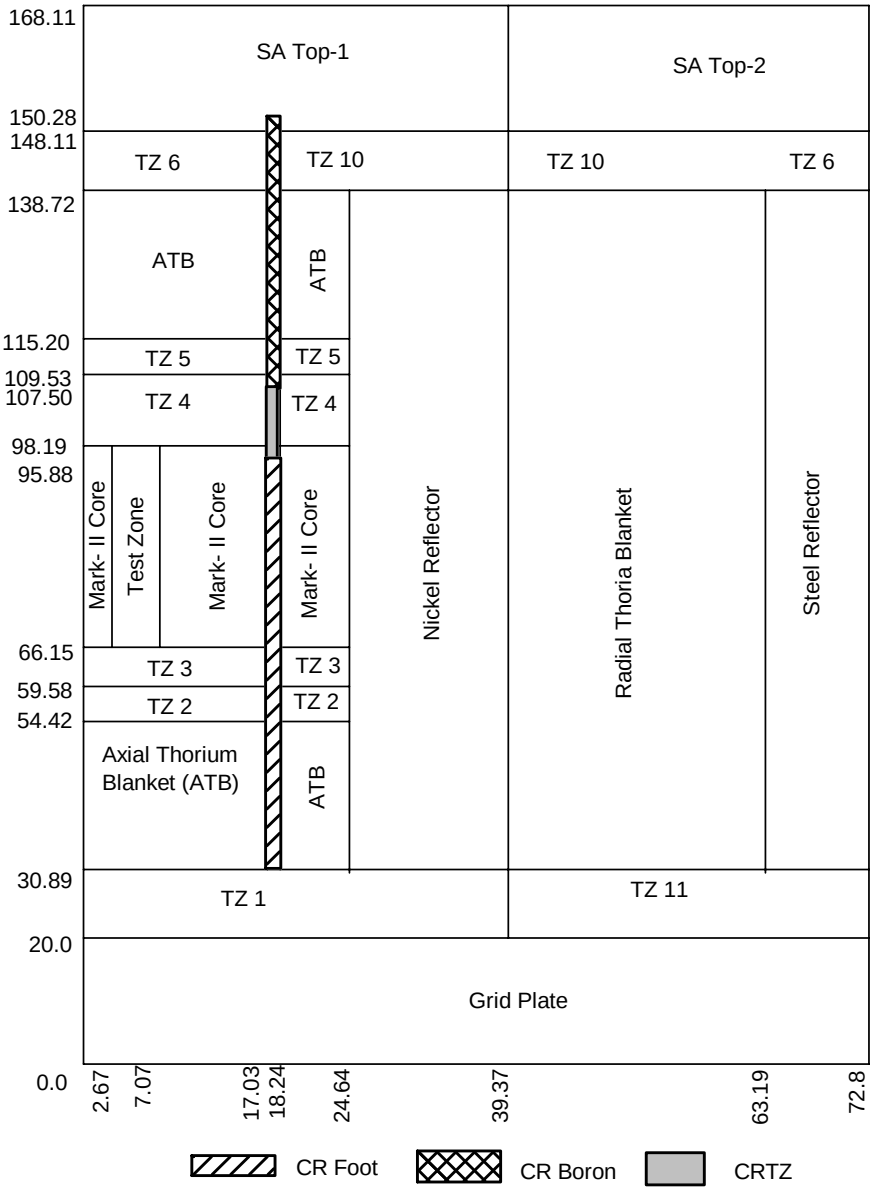

Fig-6.2: 2D R-Z Schematic model of FBTR (Mark-II Core)

* The regions marked as TZ in the figures are Transition Zones (Steel, Na and Void) and the volume fractions of these zones are given in Table 6.1.

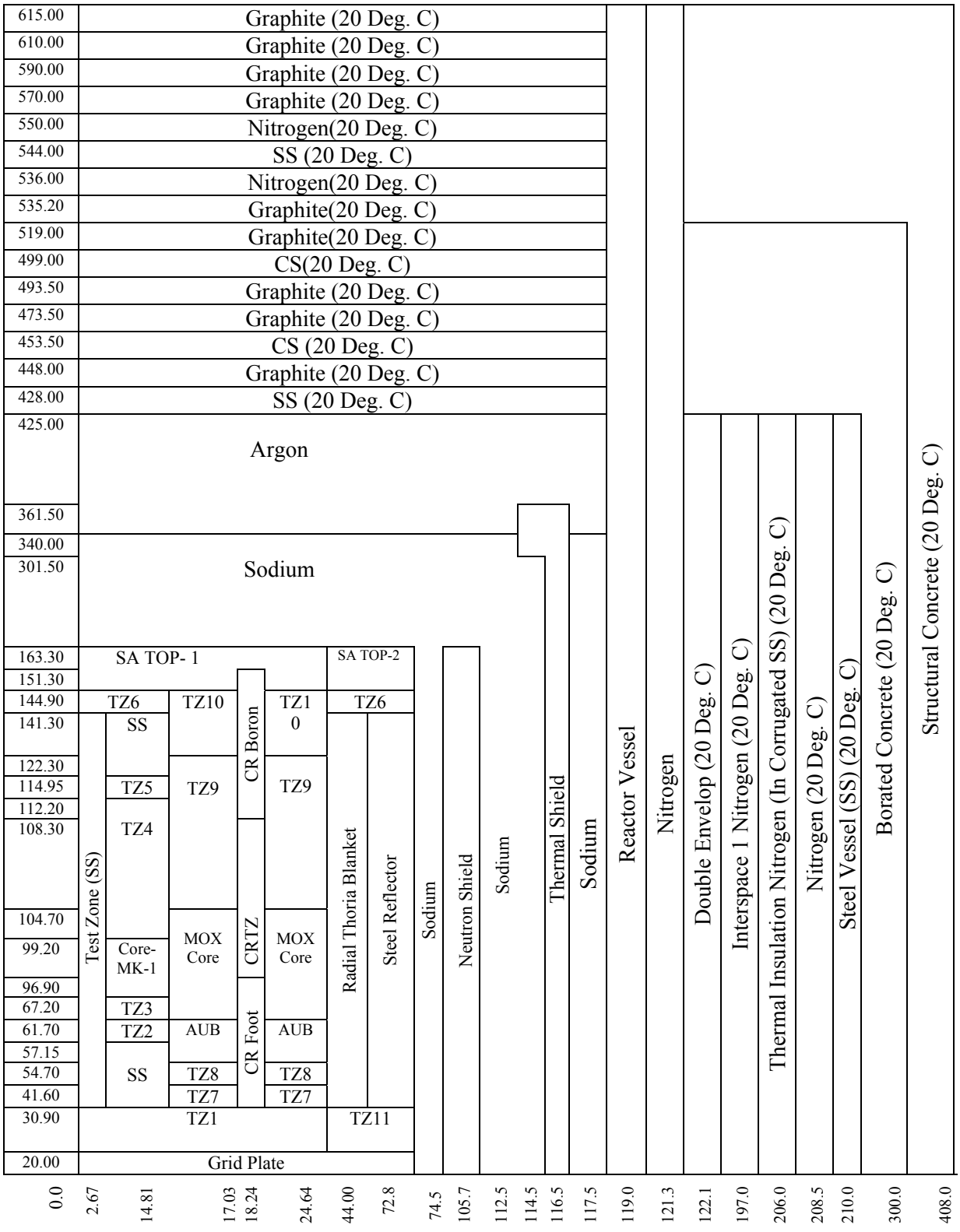

Fig-6.3: 2D R-Z Calculational model of FBTR –Hybrid Core

(Numbers in brackets denote Region Numbers)

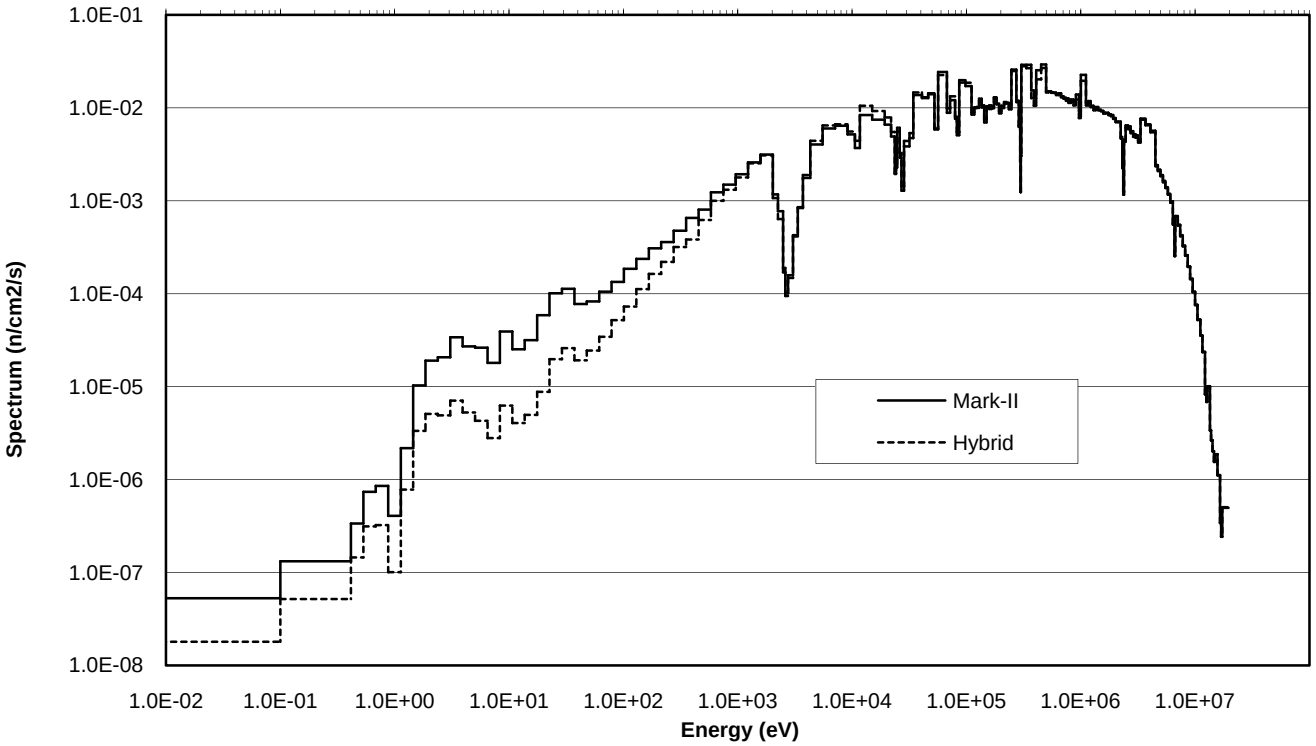

Fig-6.4: Core averaged spectrum for hybrid core and Mark-II core

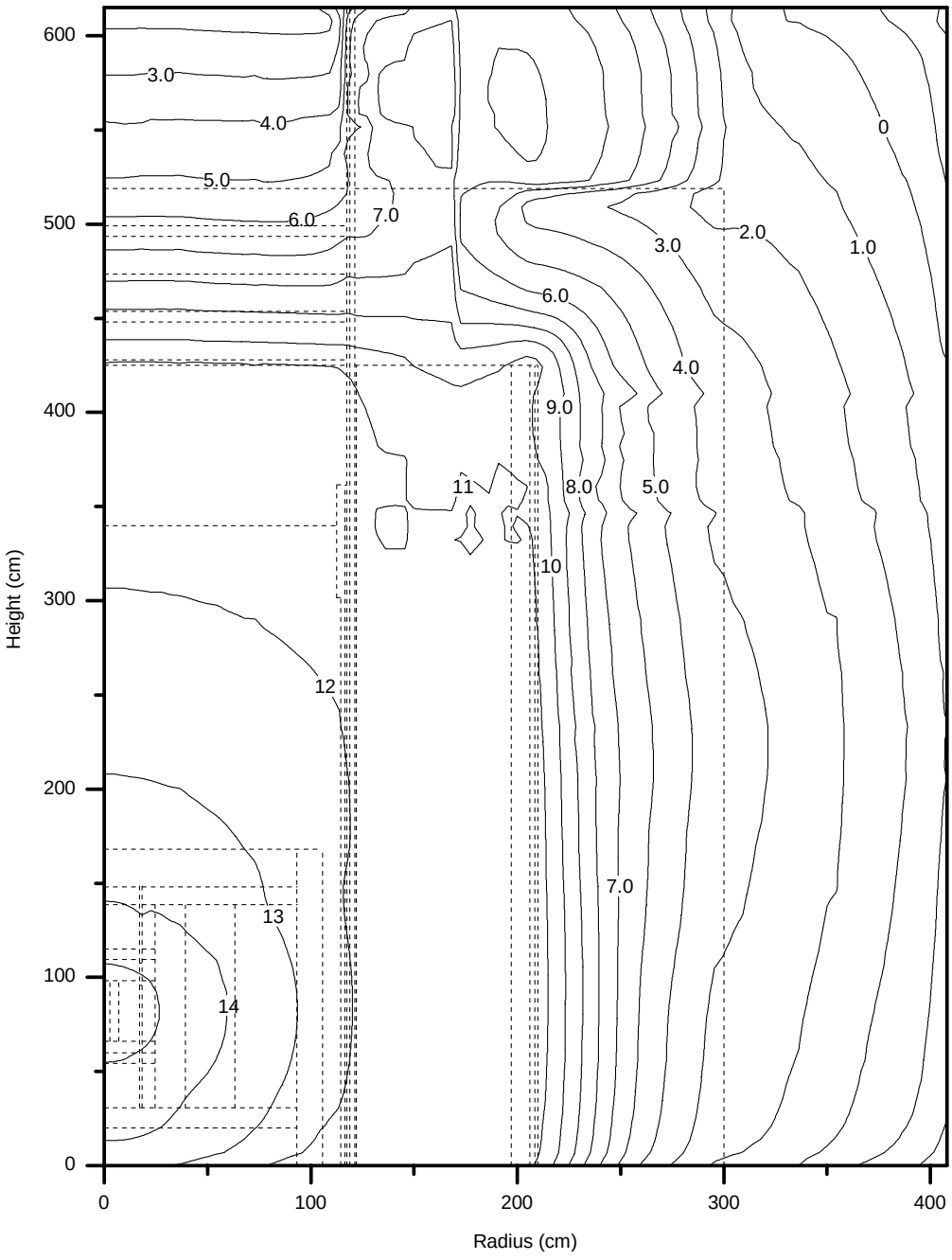

Fig-6.5: Total neutron flux contours of hybrid core

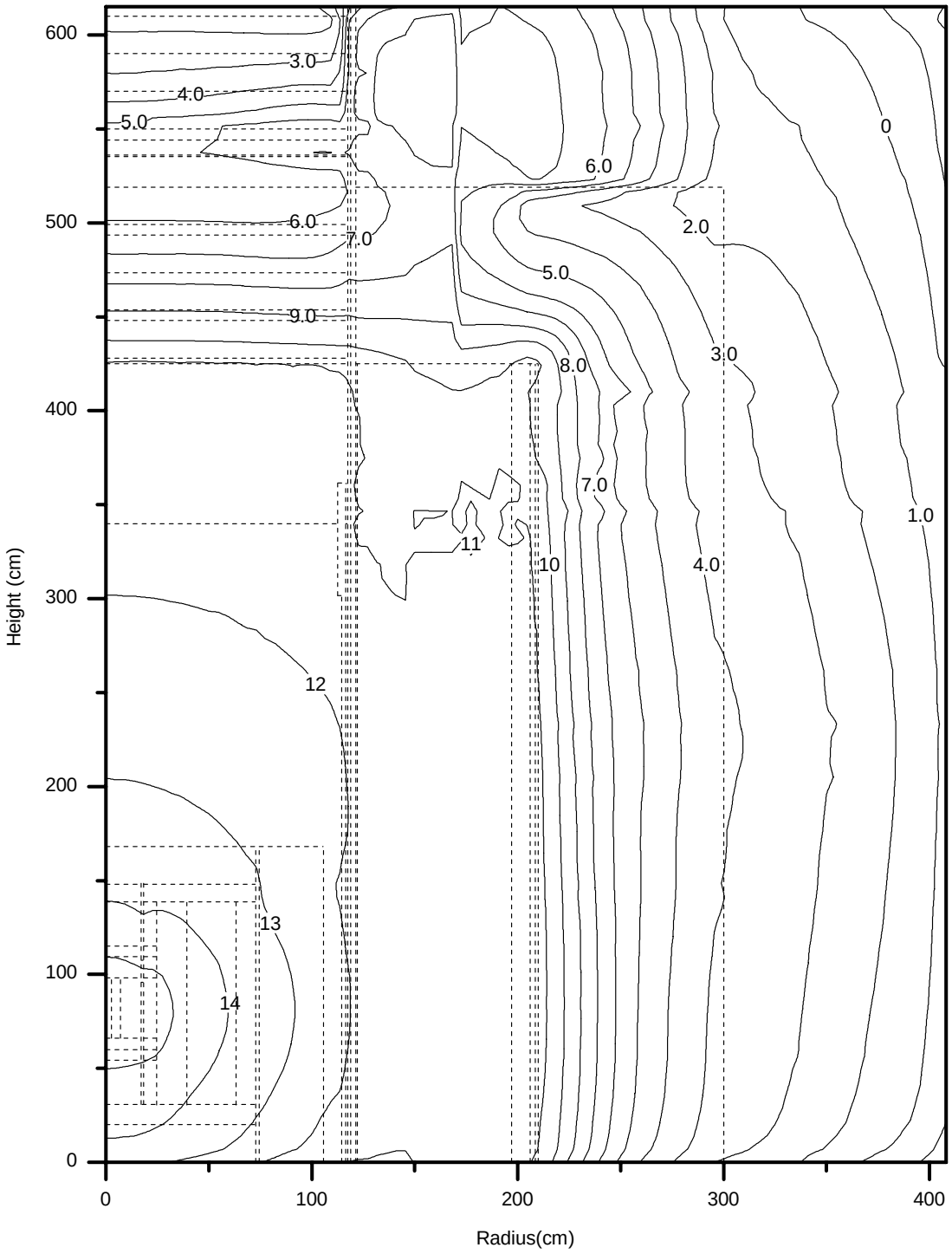

Fig-6.6: Total neutron flux contours of Mark-II core

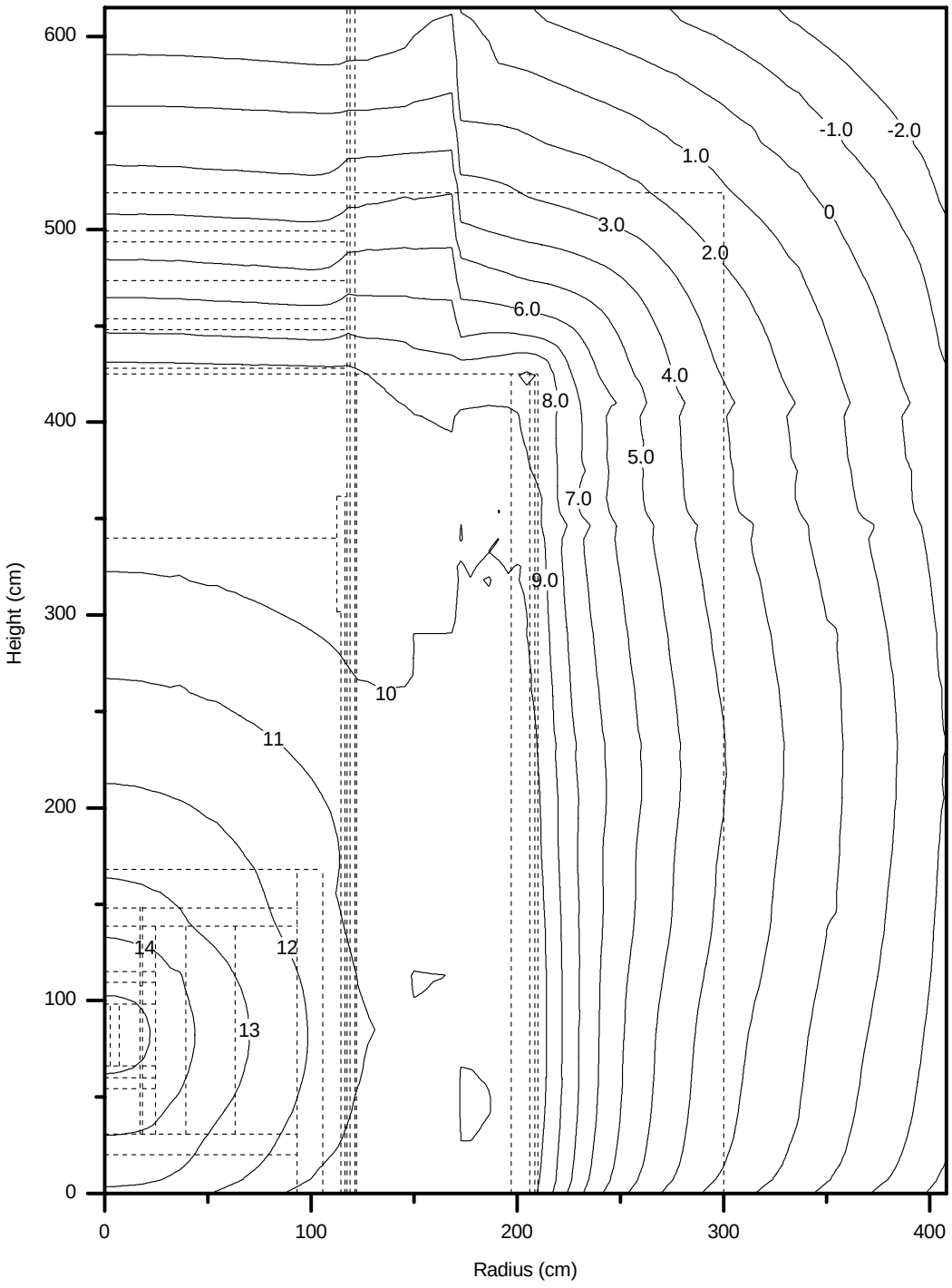

Fig-6.7: Fast flux (> 0.1 MeV) contours of hybrid core

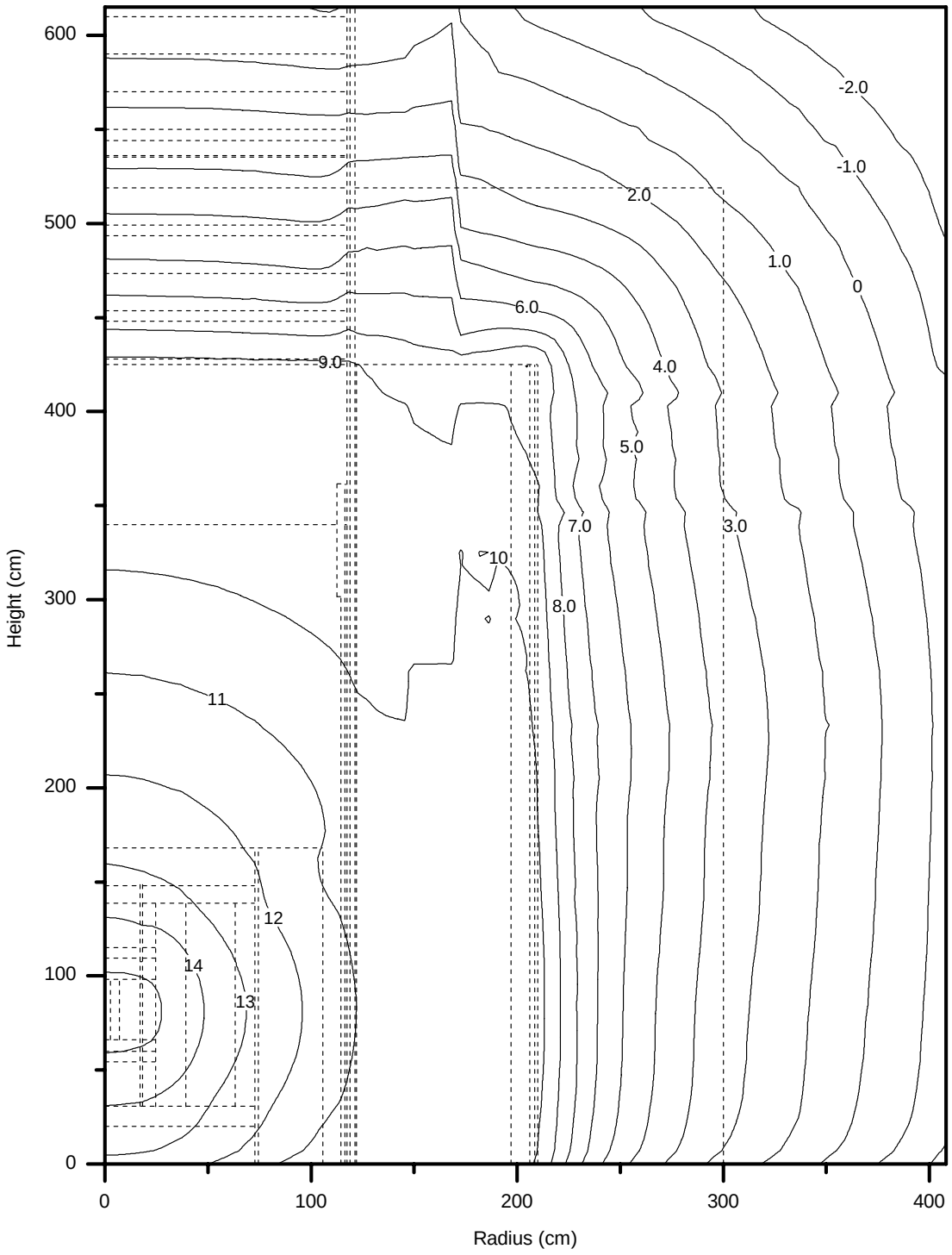

Fig-6.8: Fast flux (> 0.1 MeV) contours of Mark-II core

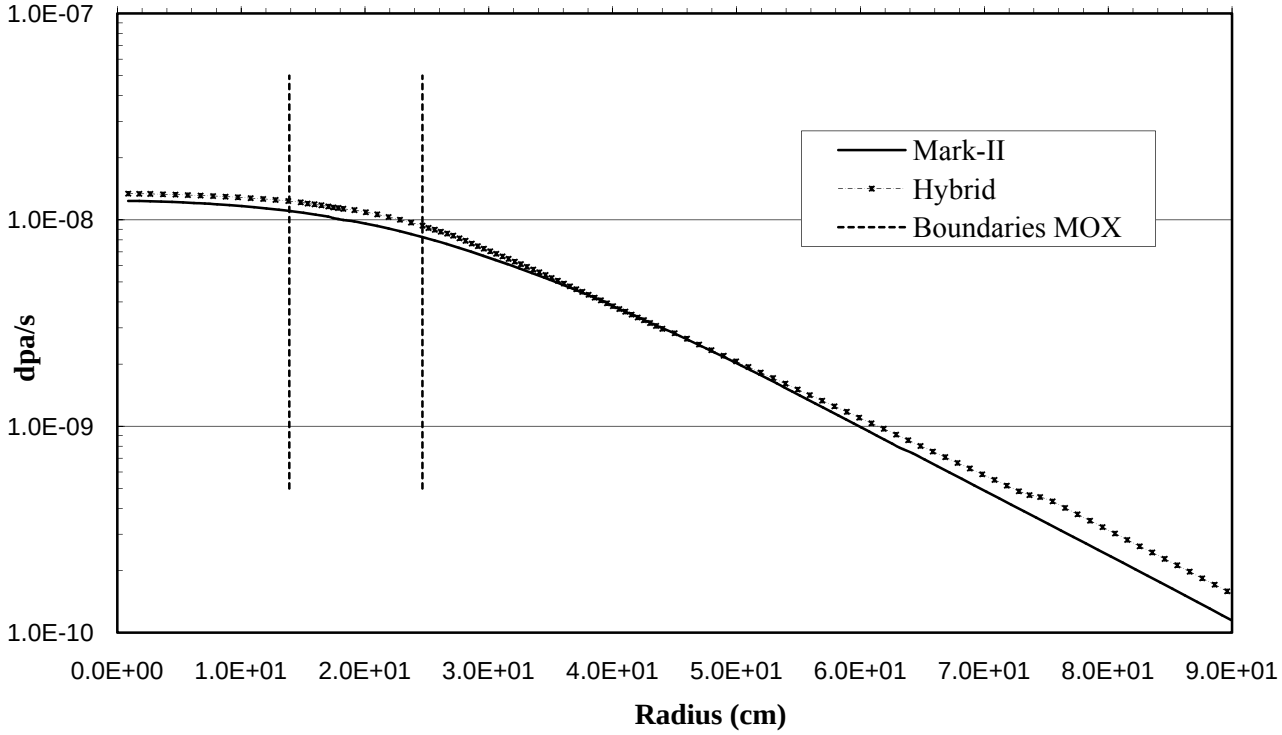

Fig-6.9: Comparison of *dpa* on grid plate for Mark-II core and hybrid core

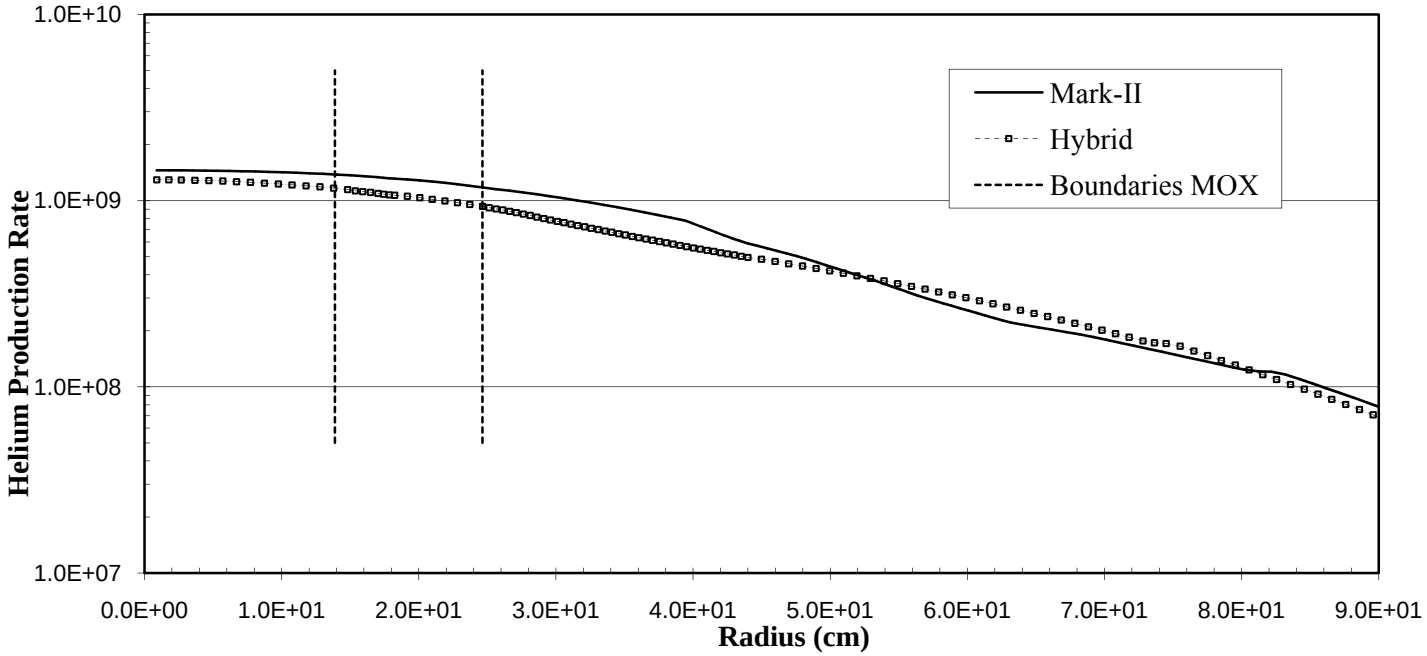

Fig-6.10: Comparison of helium production on grid plate for Mark-II core and hybrid core

Table - 6.1: Volume fractions at different regions in transition zones

Hybrid Core			Mark-II Core		
Regions	SS	Na	Regions	SS	Na
TZ –1	43.45	56.16	TZ –1	43.45	56.16
TZ –2	55.48	40.71	TZ –2	48.13	51.87
TZ –3	33.6	25.65	TZ –3	32.00	35.42
TZ –4	33.6	33.90	TZ –4	35.20	35.42
TZ –5	85.14	14.48	TZ –5	42.47	57.53
TZ –6	85.54	14.46	TZ –6	47.32	52.68
TZ –7	85.54	14.46	TZ-11	43.45	56.11
TZ –8	32.85	36.56			
TZ –9	32.85	35.19			
TZ –10	58.79	22.44			
TZ –11	43.45	56.16			
TZ -12	61.55	38.45			

Table - 6.2: Axial fluxes (n/cm^2/s) at different regions of FBTR hybrid core

No	Region *	Height (cm)	Tot Neutron Flux	U-235 eq. flux	Flux above 0.1MeV	Flux above 1MeV
1	Grid Plate Entry	1.00	1.63E+13	2.16E+11	5.82E+12	1.96E+11
2	Grid Plate	20.91	1.54E+14	2.23E+12	4.92E+13	2.16E+12
3	TZ-1	31.39	2.74E+14	3.35E+12	1.02E+14	6.00E+12
4	TZ-12	57.95	1.15E+15	5.51E+12	7.50E+14	1.44E+14
5	TZ-2	62.16	1.39E+15	5.44E+12	9.75E+14	2.21E+14
6	TZ-3	67.70	1.86E+15	5.75E+12	1.44E+15	4.05E+14
7	Core Centre	82.55	2.96E+15	7.81E+12	2.47E+15	7.84E+14
8	Core exit	99.66	1.64E+15	4.85E+12	1.28E+15	3.51E+14
9	TZ-4	112.67	7.60E+14	2.99E+12	5.06E+14	8.58E+13
10	TZ-5	115.46	6.61E+14	2.76E+12	4.27E+14	6.67E+13
11	TZ-12	141.90	9.22E+13	5.73E+11	4.51E+13	2.85E+12
12	TZ-6	145.43	7.64E+13	4.99E+11	3.61E+13	2.26E+12
13	SA-Top	163.80	3.10E+13	4.06E+11	1.00E+13	5.64E+11
14	Sodium	350.75	2.37E+11	1.59E+10	3.57E+09	1.85E+08
15	Argon	425.75	1.88E+11	1.19E+10	2.84E+09	1.27E+08
16	SS	429.00	6.87E+10	3.33E+09	1.71E+09	9.14E+07
17	Graphite	448.92	3.02E+09	1.05E+08	8.62E+07	1.11E+07
18	CS	454.50	1.04E+09	3.18E+07	4.77E+07	5.37E+06
19	Graphite (493 cm)	494.42	4.63E+06	1.43E+05	4.61E+05	1.07E+05
20	CS (499 cm)	500.00	1.84E+06	4.72E+04	2.81E+05	5.45E+04
21	Graphite (535.2 cm)	535.60	4.67E+04	9.39E+02	9.52E+03	2.97E+03
22	Graphite (615 cm)	611.25	1.67E+02	2.42E+00	5.94E+01	2.85E+01

* Values are given at upper boundary of each region except for the first region.

Table - 6.3: Axial fluxes (n/cm^2/s) at different regions of FBTR Mark -II core

No	Region *	Height (cm)	Tot Neutron Flux	U-235 eq. flux	Flux above 0.1MeV	Flux above 1MeV
1	Grid Plate Entry	1.00E+00	1.65E+13	2.26E+11	4.78E+12	1.79E+11
2	Grid Plate	2.00E+01	1.58E+14	2.15E+12	4.19E+13	2.15E+12
3	TZ-1	3.09E+01	2.86E+14	2.67E+12	9.39E+13	6.10E+12
4	ATB	5.44E+01	1.30E+15	6.20E+12	7.93E+14	1.25E+14
5	TZ-2	5.96E+01	1.57E+15	6.71E+12	1.04E+15	2.04E+14
6	TZ-3	6.62E+01	1.96E+15	6.71E+12	1.42E+15	3.53E+14
7	Core Centre	8.10E+01	2.96E+15	8.35E+12	2.33E+15	6.54E+14
8	Core exit	9.82E+01	1.65E+15	5.13E+12	1.22E+15	2.81E+14
9	TZ-4	1.10E+02	9.81E+14	3.35E+12	6.67E+14	1.12E+14
10	TZ-5	1.15E+02	7.74E+14	2.72E+12	4.98E+14	6.77E+13
11	ATB	1.39E+02	9.55E+13	4.99E+11	4.07E+13	3.03E+12
12	TZ-6	1.48E+02	5.44E+13	4.06E+11	2.06E+13	1.51E+12
13	SA-Top	1.68E+02	2.51E+13	3.92E+11	6.12E+12	3.92E+11
14	Sodium	3.40E+02	2.15E+11	1.52E+10	2.61E+09	1.27E+08
15	Argon	4.25E+02	1.71E+11	1.15E+10	2.08E+09	8.64E+07
16	SS	4.28E+02	6.12E+10	3.08E+09	1.24E+09	6.24E+07
17	Graphite	4.48E+02	2.42E+09	8.74E+07	6.03E+07	7.77E+06
18	CS	4.54E+02	8.14E+08	2.56E+07	3.25E+07	3.75E+06
19	Graphite (493 cm)	4.94E+02	3.19E+06	9.96E+04	3.25E+05	7.93E+04
20	CS (499 cm)	4.99E+02	1.35E+06	3.56E+04	1.97E+05	4.04E+04
21	Graphite (535.2 cm)	5.35E+02	2.14E+07	7.62E+05	4.47E+05	4.50E+03
22	Graphite (615 cm)	6.10E+02	2.48E+03	1.04E+02	7.15E+01	2.73E+01

* Values are given at upper boundary of each region except for the first region.

Table - 6.4: Radial fluxes (n/cm^2/s) at different regions of FBTR hybrid core at the level of grid plate

No	Region *	Radius (cm)	Tot Neutron Flux	U-235 eq. flux	Flux above 0.1MeV	Flux above 1MeV
1	Core Centre	0.0	1.58E+14	2.22E+12	4.93E+13	2.21E+12
2	Test Zone (SS)	3.18E+00	1.57E+14	2.21E+12	4.89E+13	2.19E+12
3	Mark-I Fuel	1.43E+01	1.42E+14	1.96E+12	4.41E+13	2.20E+12
4	Mox Fuel	1.72E+01	1.35E+14	1.85E+12	4.15E+13	2.11E+12
5	CR Foot	1.87E+01	1.31E+14	1.79E+12	4.00E+13	2.09E+12
6	Mox Fuel	2.49E+01	1.10E+14	1.52E+12	3.21E+13	1.78E+12
7	Radial Thoria Blanket	4.45E+01	4.56E+13	7.84E+11	9.45E+12	3.33E+11
8	Steel Reflector	7.32E+01	1.04E+13	2.46E+11	1.51E+12	1.86E+10
9	Sodium	7.50E+01	9.85E+12	2.36E+11	1.41E+12	1.66E+10
10	Neutron Shield	1.06E+02	9.31E+11	2.25E+10	1.22E+11	4.37E+08
11	Sodium	1.15E+02	6.84E+11	1.83E+10	8.18E+10	2.98E+08
12	Thermal Shield	1.17E+02	5.45E+11	1.47E+10	6.62E+10	2.49E+08
13	Sodium	1.18E+02	4.37E+11	1.20E+10	5.43E+10	2.16E+08
14	Reactor Vessel	1.20E+02	3.54E+11	9.66E+09	4.65E+10	1.97E+08
15	Double Envelope	1.41E+02	2.39E+11	7.01E+09	3.20E+10	1.78E+08
16	Steel Vessel	2.11E+02	1.76E+11	5.62E+09	2.01E+10	1.22E+08
17	Borated Concrete	3.01E+02	2.54E+03	2.54E+02	1.16E+03	6.15E+02
18	Structural Concrete	4.05E+02	1.74E+00	1.29E+00	1.78E-01	9.49E-02

* Values are given at the outer boundary of each region.

Table - 6.5: Radial fluxes (n/cm^2/s) at different regions of FBTR mark-II core at the level of grid plate

No	Region *	Radius (cm)	Tot Neutron Flux	U-235 eq. flx	Flux above 0.1MeV	Flux above 1MeV
1	Core Centre	0.00E+00	1.67E+14	2.44E+12	4.20E+13	2.15E+12
2	Core	2.67E+00	1.66E+14	2.44E+12	4.17E+13	2.12E+12
3	Test Zone	7.07E+00	1.62E+14	2.40E+12	4.05E+13	2.04E+12
4	Core	1.70E+01	1.41E+14	2.19E+12	3.49E+13	1.67E+12
5	CR Foot	1.82E+01	1.36E+14	2.14E+12	3.36E+13	1.59E+12
6	Core	2.46E+01	1.12E+14	1.85E+12	2.76E+13	1.21E+12
7	Ni Reflector	3.94E+01	5.68E+13	9.60E+11	1.32E+13	3.70E+11
8	Radial Thoria Blanket	6.32E+01	1.44E+13	2.82E+11	2.31E+12	3.54E+10
9	Steel Reflector	7.28E+01	7.81E+12	1.66E+11	1.16E+12	1.37E+10
10	Sodium	7.45E+01	7.34E+12	1.58E+11	1.07E+12	1.24E+10
11	Neutron Shield	1.06E+02	7.05E+11	1.72E+10	8.87E+10	3.78E+08
12	Sodium	1.15E+02	5.22E+11	1.41E+10	5.98E+10	2.68E+08
13	Thermal Shield	1.17E+02	4.18E+11	1.15E+10	4.84E+10	2.24E+08
14	Sodium	1.18E+02	3.36E+11	9.39E+09	3.97E+10	1.93E+08
15	Reactor Vessel	1.19E+02	2.73E+11	7.65E+09	3.41E+10	1.77E+08
16	Double Envelop	1.22E+02	1.88E+11	5.70E+09	2.36E+10	1.56E+08
17	Steel Vessel	2.10E+02	1.37E+11	4.49E+09	1.49E+10	1.09E+08
18	Borated Concrete	3.00E+02	2.84E+03	2.46E+02	1.34E+03	7.14E+02
19	Structural Concrete	4.04E+02	1.77E+00	1.28E+00	1.96E-01	1.05E-01

* Values are given at the outer boundary of each region.

6.3 Extension of life of FBTR with Alternate Lower Axial Shields

Currently, shielding against neutrons is provided by lower axial stainless steel rods. Life of FBTR can be extended by providing suitable alternate shield material which can reduce the radiation damage. Based on cross section behaviour of materials, we chose the candidate materials B_4C, Fe-B, tungsten metal, tungsten carbide (WC), tantalum, molybdenum and many combinations of these materials for life extension. The studies covered their effectiveness of shielding the grid plate and helium production.

6.3.1 Calculations

For purposes of the present study, use of R-Z geometry described in the latest report (Safety Report of FBTR, 2010; Raghukumar and Radha, 2012) is used. Fig.6.11 gives the R-Z geometry. IGC-S3 cross section set containing neutron cross section data has been used in the calculations. The reference case is the core with stainless steel shields. The results of the calculations are given in Table 6.6.

dpa is mainly contributed by the neutrons of energy above 0.1 MeV. The energy spectrum at the central axial grid plate location is given in Fig.6.12. For comparison, the core centre energy spectrum is also given. The variation of *dpa* along the radial surface of grid plate is given in Fig.6.13.

Table - 6.6: *dpa* values of grid plate for different axial shield combinations

Cases Studied	*dpa* for one year	Reactivity Change (pcm) with respect to reference case
FBTR-steel (26 cm) (Reference case)	0.33	-
Fe-B	0.253	-815.29
Tungsten Carbide	0.1427	-329.03
B_4C	0.104	-1077.23
Tungsten Carbide (13 cm) + Fe-B (13 cm)	0.2181	-474.60
Tungsten Carbide + B_4C	0.102	-584.90
SS+ Fe-B	0.258	-384.78
SS+ B_4C	0.118	-524.04
Tungsten Carbide (21 cm) +Fe-B (5 cm)	0.154	-333.07
Molebdenum	0.204	-24.05
Tungsten	0.16	-275.77
Nickel	0.33	27.24

MARK-I and MARK-II subassemblies of FBTR are designed with 26 cm stainless steel in the lower axial shield. The calculated *dpa* with SS shields on the grid plate is found to be 0.33 for 1 year. The maximum flux experienced by the grid plate surface with different shield materials for different lower axial shields are given in Table 6.7. Among the materials, Fe-B,

tungsten carbide and B_4C, the maximum reduction is seen in the case of B_4C for both total and fast flux. Total flux is only 22 % and the fast flux above 0.1 MeV is 29 % of the flux in the reference case. Combination of tungsten carbide and B_4C is better than any other material studied including pure B_4C material as lower axial shield for getting fast flux more than 0.1 MeV. The results of calculations are given in Table 6.8. Reactivity changes are also given alongside.

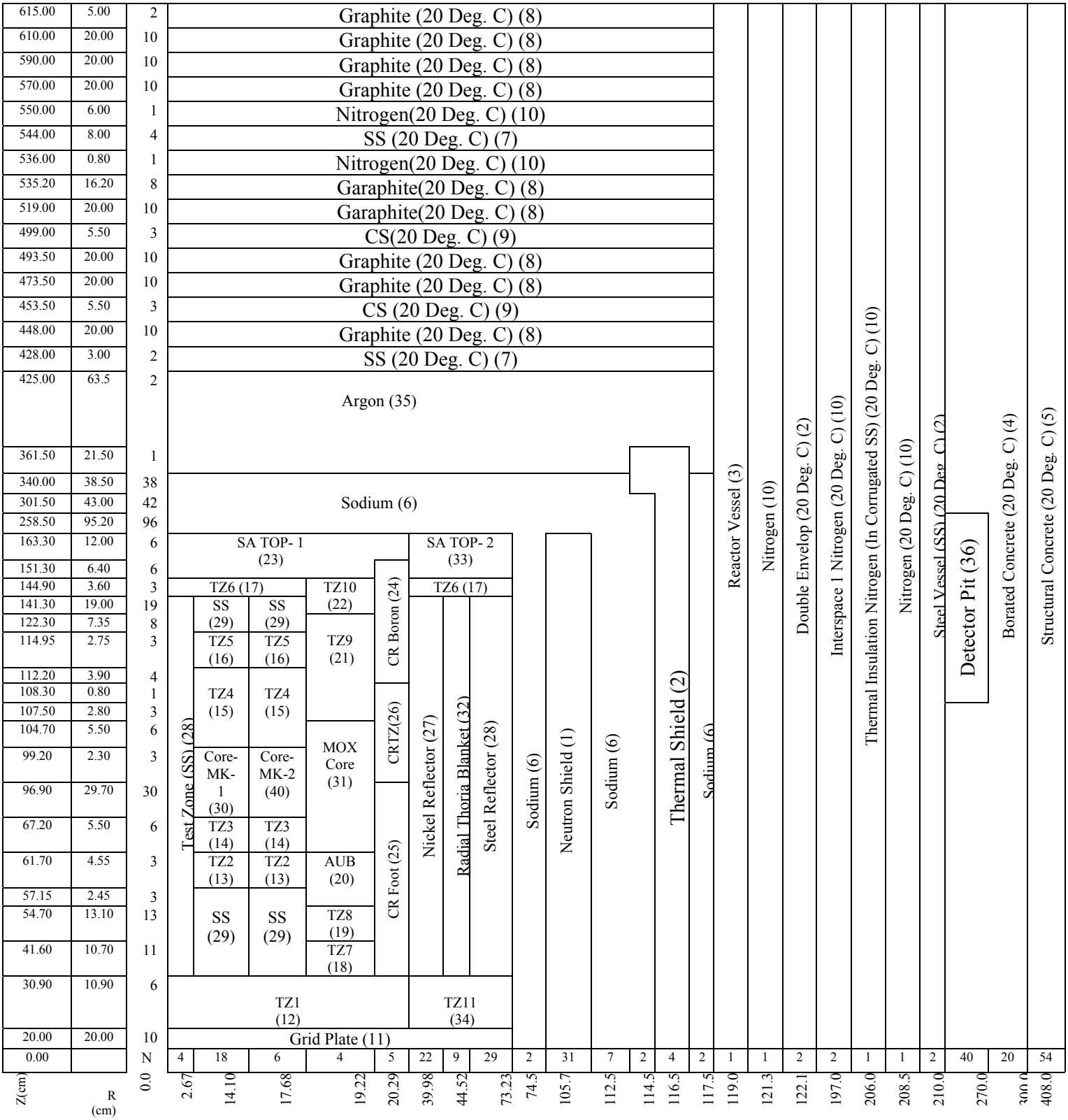

Fig-6.11: 2D R-Z Calculational model of FBTR –Present Core

(Numbers in brackets denote Region Numbers)

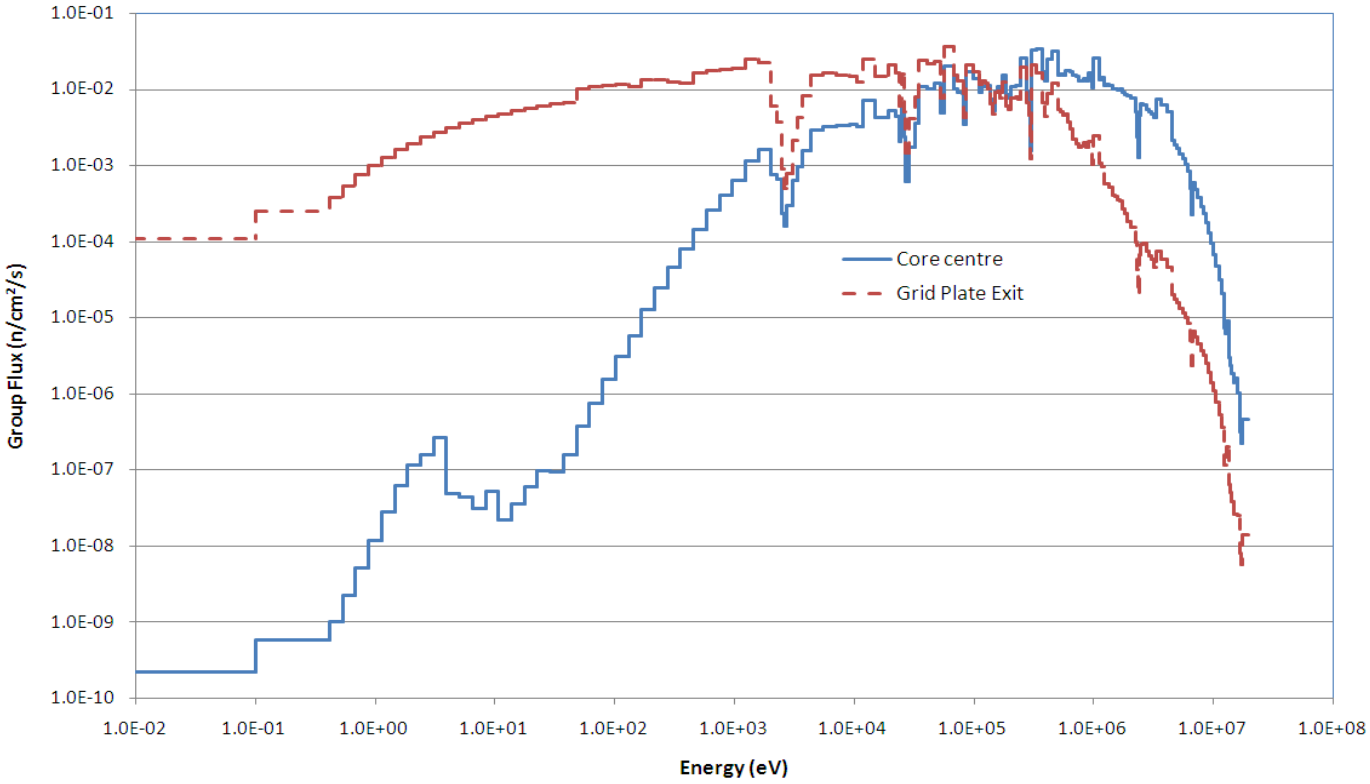

Fig-6.12: Variation of Neutron Spectrum at Core centre and Grid Plate

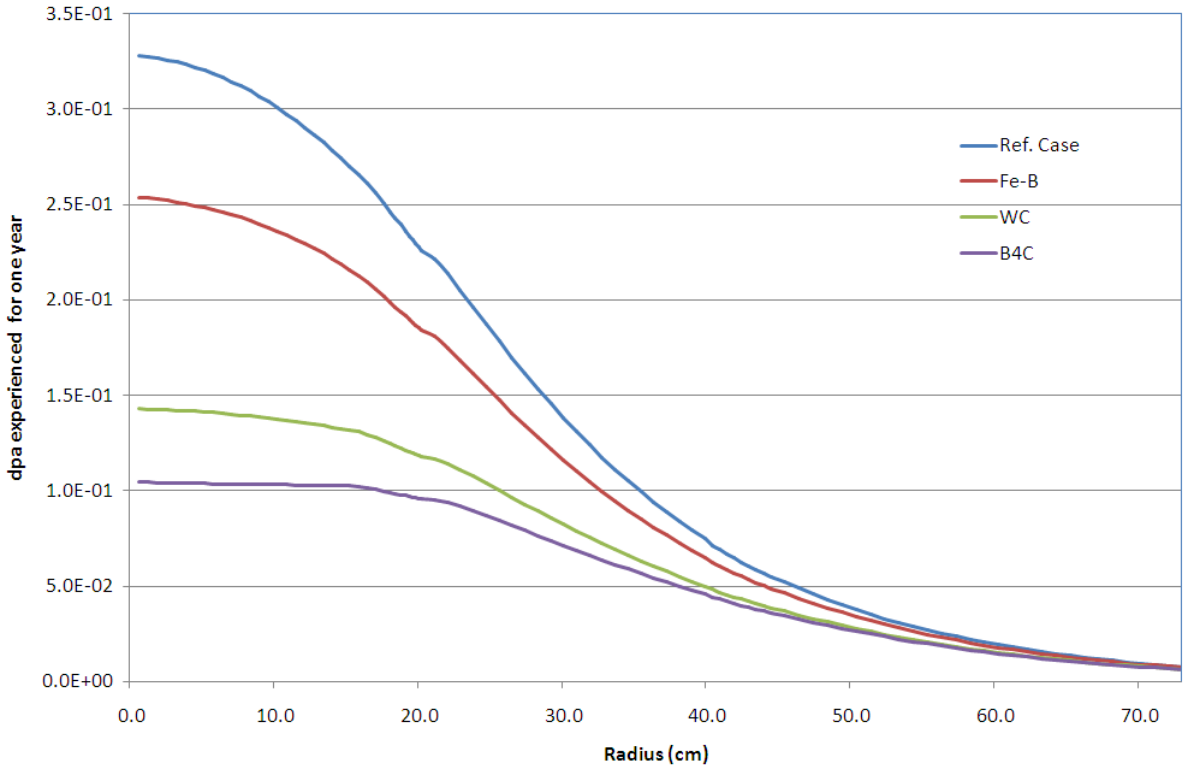

Fig-6.13: Variation of *dpa* along the grid plate surface.

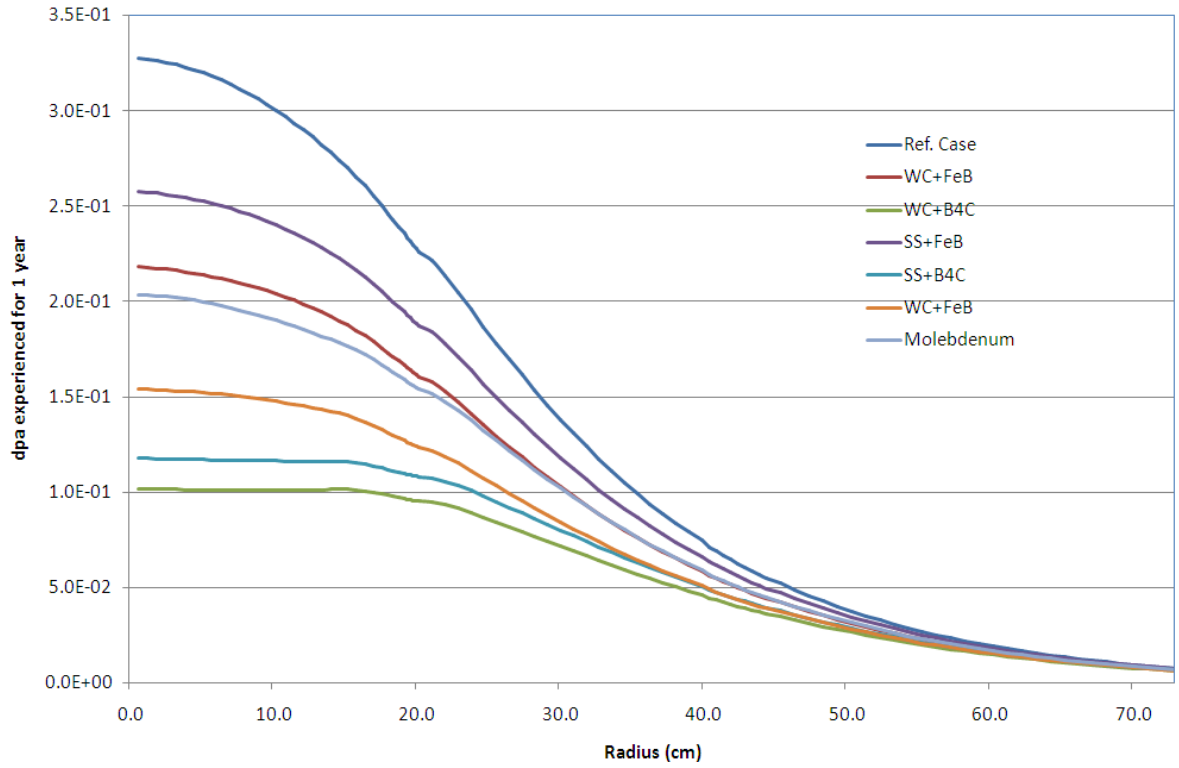

Fig-6.14: Variation of *dpa* along the grid plate surface.

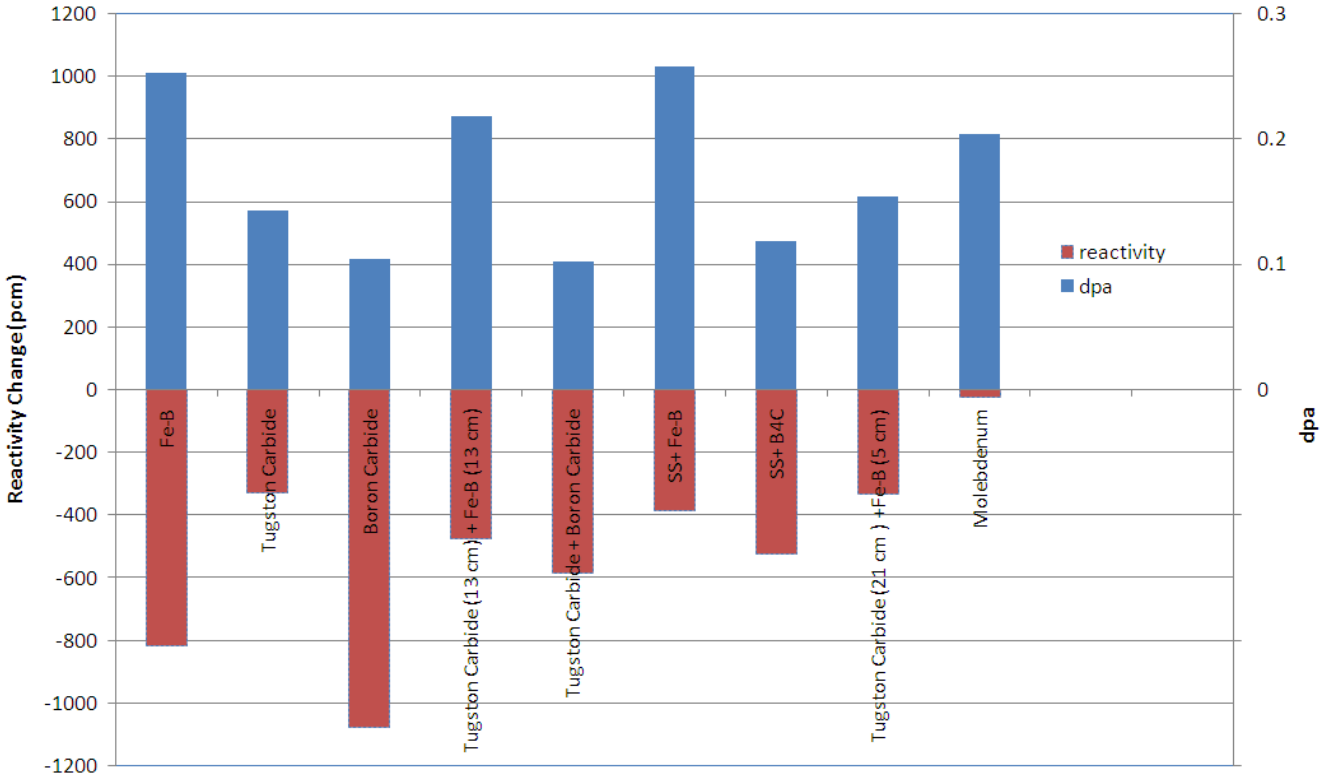

Fig-6.15: *dpa* values at the grid plate for different shield materials and the corresponding change in reactivity

Table - 6.7: The maximum flux experienced by the grid plate surface with different shield materials

Cases	Total Flux	0.1 MeV	1 MeV	U235
Reference Case	1.39E+14	4.44E+13	1.62E+12	1.93E+12
Fe-B	8.06E+13	3.29E+13	2.16E+12	6.54E+11
WC	6.86E+13	1.73E+13	7.03E+11	7.63E+11
B_4C	3.12E+13	1.29E+13	1.14E+12	2.71E+11
WC+FeB	7.44E+13	2.81E+13	1.71E+12	6.36E+11
WC+B_4C	3.27E+13	1.26E+13	1.01E+12	2.95E+11
SS+ FeB	8.52E+13	3.37E+13	1.99E+12	7.03E+11
SS + B_4C	3.73E+13	1.47E+13	1.14E+12	3.28E+11
WC(18.5 cm) +FeB	6.61E+13	1.92E+13	8.74E+11	6.65E+11
Molebdenum	8.69E+13	2.62E+13	8.68E+11	8.84E+11
Tungsten	7.02E+13	1.97E+13	4.47E+11	6.61E+11

Table - 6.8: Maximum *dpa* experienced by the grid plate

No	Cases	*Dpa*	No	Cases	*Dpa*
1	Ref. Case	0.33	7	SS+FeB	0.26
2	FeB	0.25	8	SS+B_4C	0.12
3	WC	0.14	9	WC(18.5 cm) +FeB	0.15
4	B_4C	0.10	10	Molebdenum	0.20
5	WC+FeB	0.22	11	Tungsten	0.16
6	WC+B_4C	0.10			

Similar trends are also seen in the case of radiation damage.B_4C in the lower axial shield gives lower *dpa* value as given in Table 6.8. Tungsten carbide- B_4C combination also give low *dpa*. Out of the different combinations studied SS and Fe-B gives the maximum *dpa* of 0.26. Fe-B singly does not reduce *dpa* much compared to other combinations. The *dpa* variation along the grid plate in the radial direction for different shield materials are given in Figs.6.13. and 6.14.

Reduction in reactivity is also observed with different shield materials. The maximum reactivity change is seen when B_4C is used as the lower axial shield, which is about -1077 pcm. In the case of tungsten carbide, reduction in reactivity is 329 pcm. The minimum reactivity change is seen in the case of molybdenum, which is a mere 24 pcm. Fig.6.15 shows

reactivity and *dpa* for different shield materials and their combinations. It is seen that tungsten carbide –B_4C combination is a good option where the *dpa* is approximately 0.1. The reduction in reactivity is ~584 pcm.

6.3.2 Row-wise *dpa* calculations

Since the removal of all core subassemblies in a single campaign is difficult, the possibility of removal of subassemblies ring-wise is also studied. To start with, SS shields in the first row core subassemblies alone are replaced with B_4C and tungsten carbide. Values of *dpa* are calculated. Then calculations are carried out with SS shields of both first and second row of core assemblies replaced by alternate shields. The values are given in Table 6.9. Values are also given for the first ring and second ring boundaries.

When B_4C is given as the lower axial shield for all the core subassemblies maximum reduction seen on the grid plate corresponding to core centre is 68 %. But the reduction is lower at 26.5 and 49.4 % when one row and two rows of B_4C shields are used. When tungsten carbide is given as the lower axial shield for all the core subassemblies maximum reduction seen on the grid plate corresponding to core centre is 52.4 %. But the reduction is 17.1 and 36.6 % corresponding to replacement of one row and two rows of SS by tungsten carbide shields. The *dpa* variation along the grid plate in the radial direction for first ring and second ring of core subassembly lower axial shields replaced with B_4C and tungsten carbide are given in Fig.6.16.

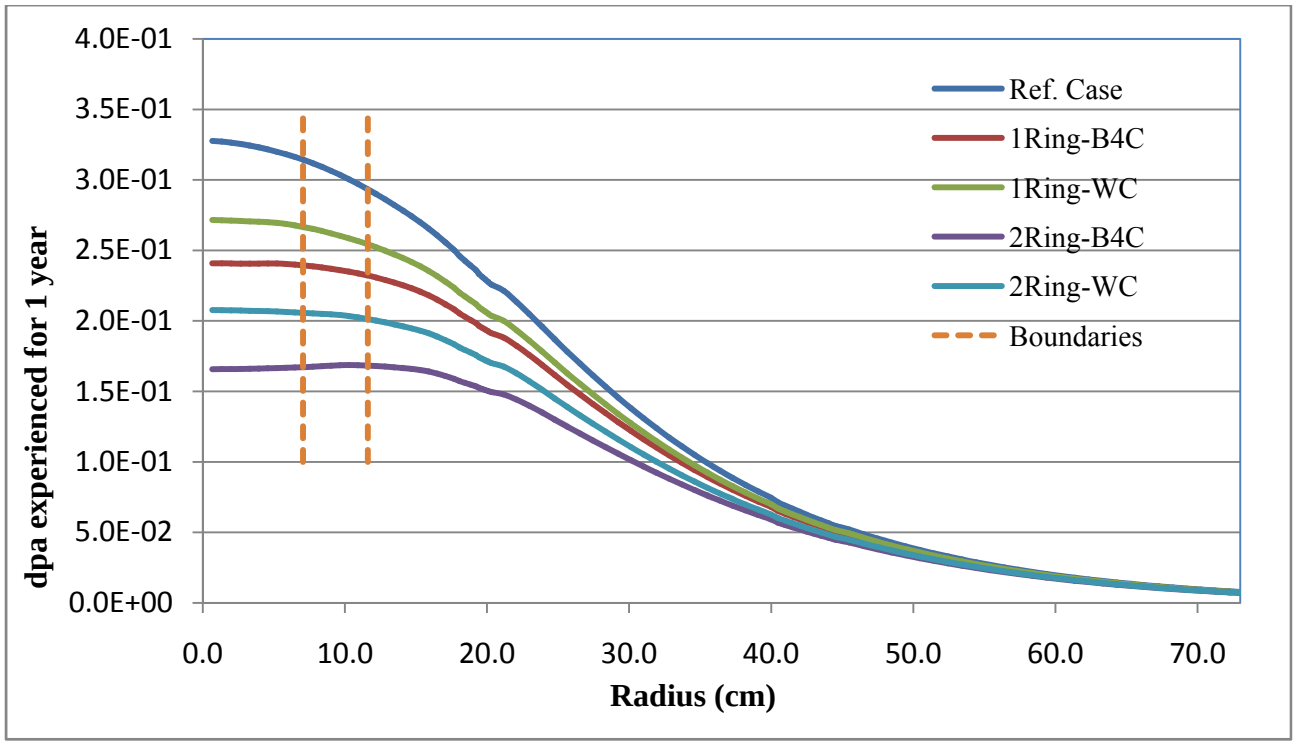

Fig-6.16: *dpa* variation when shield materials are used ring-wise.

Table - 6.9: Comparison of *dpa* values ring-wise for 1 year for different shield materials

Cases Studies	Centre	1st ring Boundary	2nd ring Boundary
Reference Case	3.28E-01	3.14E-01	2.94E-01
Full-B_4C	1.04E-01	1.03E-01	1.03E-01
1st ring alone B_4C	2.41E-01	2.39E-01	2.32E-01
Both 1st and 2nd ring B_4C	1.66E-01	1.67E-01	1.68E-01
Full-WC	1.56E-01	1.52E-01	1.47E-01
1st ring alone WC	2.72E-01	2.67E-01	2.54E-01
Both 1st and 2nd ring WC	2.08E-01	2.06E-01	2.01E-01

6.4 Summary

Radiation damage was assessed in the case where the core has longer MOX subassemblies by carrying out by 2-D R-Z transport calculations. The radiation damage to grid

plate below MOX fuel is found to be lower than that below MARK-I fuel centre in spite of longer fissile column length. Similar behaviour is seen for helium production as well.

In the case of a full Mark-II core, helium production is found to be higher as compared to hybrid core but radiation damage is more for hybrid core. But the new core is not expected to restrict reactor life from the point of view of radiation damage and helium production as compared to Mark-II Core.

The neutron transport calculations carried out with materials alternate to Stainless Steel in the lower axial part have shown that B_4C, tungsten carbide and tungsten carbide-Fe-B combination are effective in reducing radiation damage by about 50 % or more. Ring-wise removal of *dpa* results in reduction of about 17 % when only the first row of core subassembly lower axial shields are replaced with tungsten carbide whereas when two rows are replaced, the reduction is ~ 37 %.

The study has demonstrated that the life of FBTR can be extended by the use of alternate shield materials. In fact B_4C shows the greatest reduction. However, reactivity loss is also maximum in that case. In addition, the consequences of helium production in the case of B_4C may result in some modification of the lower axial part of the subassembly, such as providing a plenum. Therefore use of B_4C requires further investigations. Use of tungsten carbide reduces radiation damage by more than 50 % and the consequent reactivity loss is also not very significant. Therefore the study has concluded that tungsten carbide is the most optimal choice.

Chapter – 7

CONCLUSIONS AND SCOPE FOR FUTURE STUDIES

The main focus of the present thesis is core optimization of shielding in fast reactors with novel shield material combinations. The thesis started off with a description of the statement of the problem (stemming from the hard nature of the neutrons leaking out of core and blankets), commonly used shield materials in the decommissioned/existing fast reactors and methodology adopted for calculations. The widely used shield materials in the current fast reactors are SS and B_4C. The thesis has brought out the following points:

- Through extensive scoping calculations done on other prospective materials Fe-B, Borated Steel, tungsten carbide, gadolinium, gadolinium oxide, calcium boride, gadolinium boride, silicon boride, iron boride, aluminium boride and zirconium boride, Fe-B was identified as a shield material with good potential.
- Neutron measurements were carried out on Fe-B in KAMINI reactor, using the activation foil method, to get its neutron attenuation characteristics.
- Transport calculations with Fe-B shields in PFBR replacing its existing shields of 6 rows of SS and 3 rows of B_4C (This combination of shields was used as reference for purposes of comparing effectiveness of new shield material combinations). The calculations demonstrated that Fe-B is as good as the reference case in terms of radiological effectiveness.
- Shield weight and cost are lower if Fe-B is used. The weight will be reduced by about 50 tonnes in PFBR like reactors and cost will be about 5 times lower. Another advantage is generation of long lived Co-60 waste over the life of the reactor is absent as Fe-B does not have Co-60.

It is recognized that reduction of reactor vessel size is linked to reduction in cost in future FBRs (also called CFBRs) planned in India. The critical parameter for determining the size of the reactors has been the volume of the shields provided around the core and blankets, which is actually represented by the number of shield rows provided. The thesis undertook studies on reduction of number of rows. The conclusions of the study are

- Activation of secondary sodium activity, for a given number of radial shield rows, is determined more by axial streaming of neutrons towards regions around IHX window.
- Provision of axial shields would decrease the secondary sodium activity. However, it will have undesirable consequences on the crucial aspect of neutron monitoring, particularly at low power. Neutron detector counts should not be lower than reference case values.
- The choice of Fe-B as radial shield results in economy of the use of shield material. One row of shields can be reduced. The weight reduction of the outer rows of in-vessel shields is by about 50 % of PFBR outer shields and the cost is down to approximately 17 % of the shields in the reference case.
- The best axial shield configuration is where axial SS shielding is provided over core-1 and axial B_4C shielding is provided over blanket and reflector subassemblies. This increases the detector counts by about 50 % for CFBR without affecting secondary sodium activity.
- The reduction of number of rows of radial shields makes it possible to bring the IHX closer to the core, and hence reduction of reactor vessel size. The cost saving due to this is still to be worked out as it involves many complex parameters to be considered.

- Calculations have indicated that use of Fe-B in the axial shield region of PFBR can also lead to reduction of subassembly height.

The thesis dealt with another problem of radiation damage to grid plate of the Fast Breeder Test Reactor, currently in operation in Kalpakkam. Life of FBTR is critically linked to radiation damage suffered by grid plate. Currently, the lower axial shield provided in FBTR is Stainless Steel. Several lower axial shield options were considered in the thesis.

The main conclusions of the study are

- The study has demonstrated that the life of FBTR can be extended by the use of alternate lower axial shield materials.
- Out of the different materials studied B_4C shows the greatest reduction. However, reactivity loss is also maximum in that case. In addition, the consequences of helium production in the case of B_4C may result in some modification of the lower axial part of the subassembly, such as providing a plenum.
- Use of tungsten carbide reduces radiation damage by more than 50 % and the consequent reactivity loss is also not very significant. Therefore the study has concluded that tungsten carbide is the most optimal choice.

7.1 Scope for future work

There are significant differences in neutron spectra for various types of reactors. There is recently an immense interest in metal reactors, lead cooled reactors and accelerator driven systems all having their own characteristic neutron spectra where neutron spectra differ a lot from one another. These spectral differences lead to strong variations between various reactors in the neutron's ability to displace atoms and to cause transmutation. Depending on the reactor

size and its construction details there can also be significant variations in neutron spectra and radiation damage, especially where more energetic neutrons can leak out of the core.

India has also plans for research and development of metallic fuel fast breeder reactors as they have shorter doubling time. The neutron spectra in metallic core reactors are harder. Neutron streaming in metallic reactors from upper axial parts will also be more due to higher plenum provided. This will have the consequence of increase in the secondary sodium activity. Hence Optimization studies of shield thickness, both radial and axial can be challenging in achieving economy in volume, weight and cost of the shields.

We have planned to take up studies for such nuclear systems.

REFERENCES

1. Arun Kumar Rai., Raju, S., Jeya Ganesh, B., Panneerselvam, G., Vijayalakshmi, M., Jayakumar, T., and Baldev Raj., 2011. Investigation of high temperature phase stability, thermal properties and evaluation of metallurgical compatibility with 304L stainless steel, of indigenously developed Ferro-Boron alternate shielding material for fast reactor applications, Nuclear Engineering and Design 241, 2787– 2801.
2. Baldev Raj et al., 2005. A perspective of fast reactor fuel in India, Prog. Nucl. Energy, 47, 360-369.
3. Bell, G. I., and Glasstone, S., 1985. Nuclear reactor theory, Robert E. Krieger Publishing CO. Inc., Malabar, FL, USA.
4. Bruno Merk and Jörg Konheiser, 2014. Neutron shielding studies on an advanced molten salt fast reactor design, Annals of Nuclear Energy., 64, 441–448.
5. Cabrillat, J. C., Crouzet, J., Misrakis, J., and Salvatores, M., 1983. Shielding design methods for LMFBR validation on the PHENIX reactor. In: Proc. of the 6th Int. Conf. on Radiation Shielding, Japan, Vol. I.
6. Carlson, B. G., and Lathrop, K. D., 1965. Discrete ordinates angular quadrature of the neutron transport equation, Los Alamos Scientific Laboratory Report, LA-3186.
7. Carlson, B. G., and Lathrop, K. D., 1968. Transport theory, the method of discrete ordinates in computing methods in reactor physics, Greenspan H, Kelber CN, Okrent D,eds. New York: Gordon and Breach; 171–266.
8. Carlson B. G., 1970. Transport Theory: Discrete ordinates quadrature over the unit sphere, Los Alamos Scientific Laboratory Report, LA-4554.

9. Chellapandi, P., Puthiyavinayagam, P., Balasubramaniyan, V., Ragupathy, S., Rajanbabu, V., Chetal, S.C., and Baldev Raj., 2010. Design concepts for reactor assembly components of 500 MWe future SFRs, Nuclear Engineering and Design 240, 2948–2956.

10. Chetal, S.C., Balasubramaniyan, V., Chellapandi, P., Mohanakrishnan, P., Puthiyavinayagam, P., Pillai, C. P., Raghupathy, S., Shanmugham, T. K., and Sivathanu Pillai, C., 2006.The design of prototype fast breeder reactor. Nuclear Engineering and Design **236** (7–8), 852–860.

11. Chetal, S.C., 2009. A perspective on development of future FBRs in India. In: Int. Conf. Fast Reactors and Related Fuel Cycles (FR09)- Challenges and Opportunities, December 7-11, Tokyo, Japan.

12. Devan, K., Pandikumar, G., Gopalakrishnan, V., and Mohanakrishnan, P., 2002. IGC-S3: A 217 group (175n, 42γ) coupled cross section set from ENDF/B-VI. Report RPD/NDS/99, Indira Gandhi Centre for Atomic Research, Kalpakkam, India.

13. Devan, K., Pandikumar, G., Gopalakrishnan, V., and Mohanakrishnan, P., 2003. Effects of cross sections and quadrature orders on neutron fluxes and on secondary ^{24}Na activation rate of pool type 500 MWe FBR, Annals of Nuclear Energy. 30, 1181-1197.

14. Duderstadt, J. J., and Martin, W. R., 1979. Transport theory. New York: Wiley Interscience.

15. Duderstadt, J. J., and Hamilton, L. J., 1976. Nuclear reactor analysis, John Wiley & Sons, Inc., USA.

16. Fast Breeder Test Reactor Safety Report on Mark-II Core, March 1995., India

17. Fast Breeder Test Reactor, Chapter 2 of PSR, June 2010.

18. Garber, D., 1975. ENDF-201-ENDF/B Summary documentation (ENDF/B-IV), BNL-NCS-17541. Brookhaven National Laboratory, New York, USA.

19. Gopalakrishnan V., 1994. 100 Group displacement cross sections from RECOIL data base, RPD/NDS/54.

20. Gourdon, J., Mesnage, B., Voitellier, J., L., and Suescun, M., 1990. An overview of superphenix commissioning tests, Nuclear Science and Engineering. 106, 1-10.

21. Hammersley, J.M., and Handscomb, D.C., 1964, Monte Carlo Methods, John Wiley & Sons, New York.

22. IAEA, 2006. Fast reactor database, International atomic energy agency, Vienna (Austria). TECDOC-1531.

23. Indira, R., 2001. Shield design specification, PFBR/01115/DN/1074, IGCAR report, Kalpakkam.

24. John F. Crew and Gabriel Zamonsky, 1999. Uniform Positive-weight Quadratures for Discrete Ordinate Transport Calculations. Nuclear Science and Engineering, 131, 199-207

25. John F. Crew, Kai Hu and Gabriel Zamonsky, Uniform Gauss-Weight Quadratures for Discrete Ordinate Transport Calculations, 2000. Nuclear Science and Engineering, 136, 282-293.

26. Kenneth Shultis J. and Richard E. Faw., 2005. Radiation shielding technology. Health Phys. 88(4):297–322.

27. Keshavamurthy, R. S., Venketa Subramanyan, D., Rajeev Ranjan Prasad, Adish Haridas, Mohanakrishnan P., and Chetal S. C., 2011. Experimental measurements of neutron attenuation in the advanced shield material Ferro- Boron in KAMINI reactor, Energy Procedia 7, 273–278.

28. Keshavamurthy, R. S., Raju, S., Anthonysamy, S., Murugan, S., Sunil Kumar, D., Rajan Babu, V., Ravi Chandar, S. C., Venkiteswaran, C. N., and Chetal, S. C., 2013. Experimental and theoretical investigations of Ferro- Boron as in-vessel shield material in FBRs, FR-13 Paris.

29. Lathrop K. D., 1968. Ray effects in discrete ordinates equations. Nuclear Science and Engineering, 32, pp. 357-369.

30. Lathrop K. D., 1971. Remedies for ray effects. Nuclear Science and Engineering, 45, pp. 255-268.
31. Lamarsh, J. R., 1983. Introduction to nuclear engineering, Addison-Wesley Publishing Company.
32. Lathrop, K. D., 1972. Discrete ordinates methods for the numerical transport solution of equation, Reactor Technology, 15, 107-134.
33. Lawrence R Greenwood and Robert K Smither, 1985. SPECTER: Neutron damage calculations for material irradiations, ANL, FTP, TM-197.
34. Lewis, E. E., and Miller, W. F., 1984. Computational methods of neutron transport theory, Wiley, New York.
35. Lewis, E. E., and Miller, W. F. Jr., 1993. Neutron transport, American Nuclear Society, La Grange Park, IL.
36. Mohapatra, D. K., Sivakumar, S., Reddy, C. P., and Mohanakrishnan, P., 1998. Initial neutron flux measurements in KAMINI reactor, NSRP-12.
37. Mohapatra, D. K., 2004. 'Experimental and theoretical investigations in a thermal neutron research reactor KAMINI', PhD thesis.
38. Mohapatra, D. K., Sunil Sunny, C., Mohanakrishnan, P., and Subbaiah, K. V., 2004. Monte Carlo modeling of KAMINI, Annals of Nuclear Energy, 31, 2185-2194.
39. Masayuki Naganuma., Takashi Ogawa., Shigeo Ohki., Tomoyasu Mizuno., and Shigenobu Kubo., 2008. Development of advanced loop-type fast reactor in Japan: Minor actinide containing oxide fuel core design study for the JSFR. Proceedings of ICAPP '08, Anaheim, CA USA.

40. Mawutorli Nyarku, Keshavamurthy, R. S., Subramanian, D.V., Adish Haridas, and Eric T. Glover, 2013. Experimental neutron attenuation measurements in possible fast reactor shield materials, 53, Pages 135–139.
41. McLane, V., Dunford, C. L., and Rose, P. F. (Eds.), 1997. ENDF-102 Data formats and procedures for the evaluated nuclear data file ENDF-6, Report BNL-NCS-44945 Rev. 2/97. Brookhaven National Laboratory, New York, USA.
42. Mynatt, P. R., Gpxen, N. M., and Engle, W. W. Jr., 1966. On the application of discrete -ordinates transport theory to deep-penetration fast -neutron-dose calculations in water, Trans. Am. Nucl. Soc. 9, 366-367.
43. Mynatt, F. R., 1967. A user's manual for DOT, ReportK-1694, Union Carbide Corporation.
44. Nagaraj, C. P., 2006. Design note on neutron flux monitoring system, PFBR/66200/DN/1020, Rev. B., IGCAR Report, Kalpakkam.
45. Ohtani, H., Hasebe, M., Ishida, K., Nishizawa, T., 1998. Calculation of Fe-C-B ternary phase Diagram, Trans. ISIJ, Vol. 28, pp1043-1050.
46. Okamoto, H., 2004. Fe-B Phase Diagram- Supplementary literature Review, Journal of Phase Equilibria and Diffusion, 25, 297.
47. Pasupathy, C. S., Rasheed, K. K., Srinivasan, M., Patil, R. K., Govindarajan, G., Jose Joseph, Anandkumar, V., Venkatesan, E., and Shekar, K.R., 1993. Safety Assessment of KAMINI Reactor Section – A, Design Description," BARC/1993/1/022, Bhabha Atomic Research Centre.
48. Plaster, D. M., et al., 1975. Coupled 100 group neutron and 121 group gamma- ray cross sections for EPR calculations", ORNL-TM-4872.
49. Puthiyavinayagam, P., Pillai, C. P., Raghupathy, S., Shanmugham, T. K., and Sivathanu Pillai, C., 2006. The design of prototype fast breeder reactor. Nucl. Eng. Des., 236, 852–860

50. Raghukumar, G., and Radha, E., 2012. Calibration of control rods in the irradiation campaign 22A. ROMG/FBTR/RPD/S-RS-2/31400, IGCAR Report, Kalpakkam.

51. Rajeev Ranjan Prasad., 2008. Project report on neutron attenuation behaviour of Ferro-Boron in KAMINI, IGCAR Report, Kalpakkam.

52. Raju, S., Arun Kumar Rai, Jeyaganesh, B., Vijayalakshmi, M., Jayakumar, T., and Baldev Raj., 2011.Characterisation of high temperature phase stability and evaluation of metallurgical compatibility with SS 304L, of indigenously developed alternate shielding material Ferro-Boron for fast reactor applications, Energy Procedia 7, 264–272.

53. Reddy, C. P., Raghu Kumar, G., Murugan, S., and Varadharajan, S., Feb 2012. Residual life assessment of FBTR grid plate, ROMG/FBTR/S-RS-02/31400/TN-869, IGCAR Report, Kalpakkam.

54. Rhoads, W.A., and Childs, R. L., 1988. The DORT- two dimensional discrete ordinates transport code, Nucl. Sci. Engg. 99, 88.

55. Rose, P. F., 1991. ENDF-201-ENDF/B Summary Documentation (ENDF/B-VI) (BNL-NCS-17541). Brookhaven National Laboratory, New York, USA.

56. Satori, E., 1990. Standard energy group structures of cross section libraries for reactor shielding, reactor cell and fusion neutronics applications: VITAMIN-J, ECCO-33, ECCO-2000 and XMAS. JEF/DOC-315 Revision 3.

57. Sengupta, A.K., and Kamath, H.S., 2006. High Plutonia mixed carbide and mixed oxide fuels for LMRs: Thermo physical properties and out-of-pile fuel-clad-coolant compatibility, IGCAR CEA meeting on fuel safety.

58. Sivakumar, S., 2005. Zone averaged worth of fuel and structural material for proposed hybrid core, FBTR/TSD/RPS, IGCAR Report, Kalpakkam.

59. Sivaramakrishna M., 2008, Design specifications for neutronic channels, Report PFBR/66200/SP/1002, IGCAR Report, Kalpakkam.

60. Spanier, J., and Gelbard, E.M., 1969. Monte Carlo principles and neutron transport problems, Addison Wesley publishing company, LTK.

61. Srinivasan, G., Varatharajan, S. Reddy, C.P., Clement Ravichandar, S., and Puthiavinayagam, P., 2005. Proposal for a hybrid core for FBTR (Report ROD/FBTR/S-RS-02/31410/SCPRO-009) IGCAR Report, Kalpakkam.

62. Srinivasan, G., Suresh Kumar K.V., Rajendran B., and Ramalingam P.V., 2006, The Fast Breeder Test Reactor-Design and Operating Experiences, Nuclear Engineering and Design ., 236, Issues 7-8.

63. Stevens, P. N., 1970. Use of the discrete ordinates S_N method in radiation shielding calculations, Nuclear Engineering and Design, 13, pp 395-408.

64. Sudha, R., Chandran, K., Lavanya, M., Anthonysamy, S., and Ganesan V., 2013. Chemical compatibility studies of SS 304L with Fe-B in presence of liquid sodium, International conference on electron microscopy and XXXIV Annual Meeting of the Electron Microscope Society of India (EMSI), Kolkata, India.

65. Stacey, W. M., 2001. Nuclear reactor physics, John Wiley & Sons, USA.

66. Sujoy Sen, and Gopalakrishnan, V., 2005. Activation cross sections from reference neutron activation library, RPD/NDS/112, IGCAR Report, Kalpakkam.

67. Sujoy Sen., and Gopalakrishnan, V., May. 2006. Self-Shielded Fine group cross sections for shielding applications, RPD/NDS/123, IGCAR Report, Kalpakkam.

68. Sunil Kumar, D., Keshavamurthy, R.S., and Adish Haridas, 2004. Effectiveness of different shield materials in the outer in-vessel shield and sodium regions of PFBR – Possible use of KAMANI, REG/RPD/RSS/188, IGCAR Report, Kalpakkam.
69. Sunil Kumar, D., 2005. 2D-RZ transport calculations for FBTR with hybrid core, radial thorium blanket and shields, FBTR/RSS/DN/78, IGCAR report, Kalpakkam.
70. Sunil Kumar, D., Keshavamurthy, R. S., and Mohanakrishnan, P., 2006. Radiation damage to structural materials in FBTR with hybrid core, radial thorium blanket and shields, NSRP 16, India.
71. Sunil Kumar, D., Sujoy Sen., Keshavamurthy, R.S., and Mohanakrishanan, P., 2008, Comparison of FBTR hybrid Core and Mark-II (Carbide) core design and neutron irradiation in in-vessel shields, Annals of Nuclear Energy. 35, 937-946.
72. Sunil Kumar, D., Keshavamurthy, R. S., and Mohanakrishnan, P., 2009. Reduction of Radial Shields in PFBR Using Ferro-Boron. National Symposium on Radiation Physics, NSRP-18, Udaipur, India.
73. Sunil Kumar, D., Anthonysamy, S., Raju, S., Clement Ravichandar, S., Rajan Babu, V., Keshavamurthy, R.S., 2010. Studies on Ferro-Boron in-vessel shields in CFBR, TF-ASM/2010/REPORT/1, IGCAR Report, Kalpakkam.
74. Sunil Kumar, D., Keshavamurthy, R.S., Mohanakrishanan, P., and Chetal, S. C., 2010, A feasibility study of Ferro-Boron as in-core shield material in fast breeder reactors, Nuclear Engineering and Design. 240, 2972–2980.
75. Sunil Kumar, D., Keshavamurthy, R. S., Mohanakrishnan, P., and Chetal, S. C., 2013. Axial and radial shield optimization for CFBRs with Ferro-Boron, 2013, Nuclear Engineering and Design., 265, Pages 1159– 1165.

76. Tavassoli Ali Asghar, 1990. Effect of neutron radiation on mechanical properties of permanent near core structures, effects of radiation on materials: 14th International Symposium (Volume II), ASTM STP 1046, Philadelphia.

77. Venkatasubramanian, D., Adish Haridas and Keshavamurthy, R. S., 2009. KAMINI Shielding experiments: Experimental measurements of neutron attenuation in boron carbide powder, KAMINI/0115/KS/7/R-0, IGCAR Report, Kalpakkam.

78. Venkatasubramanian, D., Rajeev Ranjan Prasad, Adish Haridas and Keshavamurthy, R. S., 2009. KAMINI shielding experiments: Measurements of neutron attenuation in Ferro-Boron granules", KAMINI/0115/KS/6/R-0, IGCAR Report, Kalpakkam.

79. Venkatasubramanian, D., Haridas, A., Sunil Kumar, D., Keshavamurthy, R. S., and Mohanakrishnan, P., 2009. Experimental measurements of neutron attenuation through Ferro-Boron Slabs in the south end neutron beam of KAMINI Reactor, National Symposium on Radiation Physics, NSRP-18, Udaipur, India.

80. Walter, A. E., and Reynolds, A. B., 1981. Fast breeder reactors, Pergamon Press, New York.

APPENDIX

The definitions of different neutron fluxes are as follows:

(a) U235 Fission Equivalent Flux: $$\phi_f = \frac{\sum_{g=1}^{NG} \sigma_{f,g}\phi_g}{\sigma_{f,thermal}}$$

(b) B-10 (n,α) equivalent flux: $$\phi_{B-10} = \frac{\sum_{g=1}^{NG} \sigma_{\alpha,g}\phi_g}{\sigma_{\alpha,thermal}}$$

(c) Sodium capture (n,γ) Equivalent Flux:

$$\phi_{Na} = \frac{\sum_{g=1}^{NG} \sigma_{\gamma,g}\phi_g}{\sigma_{\gamma,thermal}} \equiv \frac{Sodium\ capture\ reaction\ rate}{\sigma_{\gamma,thermal}}$$

These are thermal equivalent fluxes at a location giving same reaction rate resulting from the spectrum of neutrons at that location. In the case of DLC-37 cross section set, NG is 100 and 175 in the case of IGC-S3 set.